PRODUCTION AND ANALYSIS OF POLYMER MICROCANTILEVER PARTS

A Thesis
Presented to
The Academic Faculty

by

Andrew W. McFarland

In Partial Fulfillment
of the Requirements for the Degree
Doctor of Philosophy

George W. Woodruff School of Mechanical Engineering
Georgia Institute of Technology
November 2004

PRODUCTION AND ANALYSIS OF POLYMER MICROCANTILEVER PARTS

Approved by:

Dr. Jonathan S. Colton,
Committee Chair
(George W. Woodruff School
of Mechanical Engineering)

Dr. F. Levent Degertekin
(George W. Woodruff School
of Mechanical Engineering)

Dr. David L. McDowell
(George W. Woodruff School
of Mechanical Engineering
and the School of Materials
Science and Engineering)

Dr. Marc K. Smith
(George W. Woodruff School
of Mechanical Engineering)

Dr. Lawrence A. Bottomley
(School of Chemistry
and Biochemistry)

Dr. John D. Muzzy
(School of Chemical and
Biomolecular Engineering)

Date Approved: November 19, 2004

ACKNOWLEDGEMENTS

I would like to first thank my advisor, Dr. Colton, for guiding me through this work. I feel that I have learned much working on this project and that would not have been possible without his help. Similarly, the collaboration with Dr. Bottomley and his students was fruitful and I am grateful to Dr. Bottomley for the exposure to the chemistry side of this work and for serving on my committee. Dr. Muzzy has always been available over the past four years for my polymer questions, and I would like to thank him for the help and for serving on my committee. Dr. Degertekin, Dr. McDowell, and Dr. Smith were all very helpful with suggestions about this project at the proposal stage and, although the proposal was somewhat different than the finished product, their input certainly shaped the final form of this work so I would like to thank them for serving on my committee and their general advice.

I have to thank the students in the Colton-Muzzy lab who I have worked with in my time at Tech, it was always a friendly environment to work in. Dr. Mark Poggi and future Dr. Meg Doyle both deserve large amounts of thanks for performing experimental work that is in this dissertation and putting up with my engineering practices (cantilevers falling on the floor and wiped off by hand– not acceptable apparently). My graduated friends (Erick and Young) made our time here enjoyable and I would like to thank them for that.

My family was a main factor in making this whole endeavor possible so I would like to thank them all and specifically my sister Missy, brother-in-law Dave, and now Samantha, who have been ridiculously accommodating when I visit. My parents both deserve thanks as they were completely supportive of this effort and always conscientiously believed in and encouraged my education.

TABLE OF CONTENTS

LIST OF TABLES

LIST OF FIGURES

SUMMARY

This dissertation presents work involving the manufacture and analytic modeling of microcantilever parts (length-width-thickness of roughly 500-100-10 μm). The manufacturing goals were to devise a means for and demonstrate repeatable production of microcantilevers from techniques not used in the integrated-circuit field, which are the exclusive means of current microcantilever production. The production of microcantilevers was achieved via a solvent casting approach and with injection molding, which produced parts from various thermoplastic polymeric materials (amorphous, semi-crystalline, fiber- and nanoclay-filled) in a repeatable fashion. Limits of the injection molding process in terms of the thinnest cantilevers possible were examined with 2 μm being the lower bound.

Subsets of the injection-molded parts were used in a variety of sensing applications, some results were successful (e.g., vapor-phase, resonance- and deflection-based sensing), while others showed poor results, likely due to experimental shortcomings (e.g., fluid-phase, deflection-based sensing). Additionally, microcantilever parts with integrated tips were injection-molded and showed to function at the same level as commercial, tipped, silicon-nitride parts when imaging an optical grating; this experimental work was the first demonstration of injection-molded parts for chemical sensing and force spectroscopy.

The scientific results were (*i*) the derivation of a length scale dependent bending stiffness and experimental evidence showing that such an effect was observed, (*ii*) the development of a new microcantilever experimental mode (surface stress monitoring via microcantilever bending resonant frequencies) and experimental validation of the technique, and (*iii*) a new method for determining microcantilever geometry

based upon measurement of a bending, lateral, and torsional mode and experimental validation of the procedure.

CHAPTER I

INTRODUCTION

1.1 Problem Description

In December of 1959, Richard Feynman stepped in front of the audience at the annual meeting of the American Physical Society and proceeded to deliver one of the most prophetic scientific speeches ever given, *There's Plenty of Room at the Bottom*, which foresaw tiny machines, nanodevices, and mankind's ability to manipulate materials atom by atom [78]. While his predictions were seen as optimistic and even ridiculous by some scientists of the time, many of those very same predictions were proven accurate as evidenced by today's MEMS, microfabrication, and microsystems technologies and markets. Feynman alluded to many possible applications of his nano-scale ideas but many eluded him, one being sensing at smaller characteristic length scales (Nobel laureates are due some reprieves).

Miniature sensing systems are, and will likely become, more ubiquitous in microelectromechanical systems (MEMS) and biological MEMS (BioMEMS) applications in part as a result of their high sensitivity and potential for scalability. The main topic of this thesis is one such sensing system which employs micron scale cantilever beams (hence dubbed microcantilever-based sensing); a generic microcantilever part is shown in Figure 1, detailing the base part and the six protruding microcantilevers (the number of cantilevers was chosen arbitrarily and usually spans from one to eight).

Figure 2 is a chart showing the cause-effect relationships of microcantilever sensing systems (as applied to this work) along with the measured values; the remainder of this paragraph will describe the terms used in this figure. Microcantilever sensing involves determination of microcantilever *resonance shift* (i.e., shifts in the frequency

of a resonance mode), detection of microcantilever *deflection*, or both. An *adsorption event* refers to the bonding of an analyte present in a fluid engulfing a microcantilever to the microcantilever itself (such as water condensing on the microcantilever from a humid air flow) or some type of analyte-induced change (such as analyte-induced change in the conformational state of DNA bonded to a microcantilever). The term *beam surface-field interaction* refers to the contact of a microcantilever with a surface or the interaction of a beam with a field quantity, such as the forces induced on a magnetic microcantilever due to an imposed magnetic field. These two events (i.e., adsorption and surface-field interaction) are termed primary causes, and they can induce a slew of effects. A *surface stress manifestation* may occur due to a difference in free energy between two surfaces of the microcantilever, for example, while the contact of a beam with a surface will cause *force loading of the beam* (e.g., transverse end-loading of the cantilever beam). The *environment change* group is self explanatory, but the *beam property change* group may require some elucidation through examples such as: temperature-dependent elastic modulii, resonance frequency variations due to tensile loading (similar to stretching a guitar string and increasing its stiffness), and adsorbed species which will change the effective microcantilever mass.

By realizing that the possible cause and effect relationships of Figure 2 cover many physical phenomena, microcantilevers have been used as sensors in numerous fields such as chemical sensing, calorimetry, rheology, infrared optics, probe microscopy, and magnetometery [23]. While this diversity is impressive, there are limitations currently present which restrict the potential of microcantilevers as listed below.

- **Limited feasible materials**– Nearly all microcantilevers are produced using conventional integrated circuit techniques (e.g., etching, lithography, deposition), which limit the possible materials to certain ceramics and a few photo- and fluoropolymers.

- **High cost**– Due to the limited production techniques, the cost of redesign and

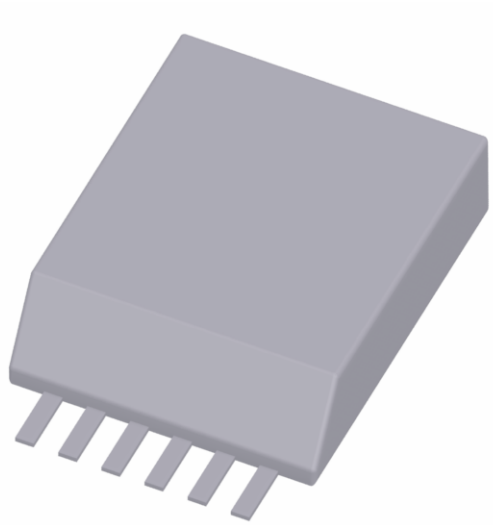

Figure 1: Generic microcantilever part, scale: — = 100 μm.

indeed production itself is quite high, mainly due to the need for cleanrooms and expensive associated equipment.

- **Limited production control**– Commercially available microcantilevers have large ranges on the stiffness and resonant frequencies of a particular beam (as high as $\pm 200\%$ of the nominal value in some cases). Consequently, the end user often must determine certain parameters each time a microcantilever is used, or employ the uncertain, manufacturer-provided parameter values.

- **Rudimentary mechanical understanding**– While conventional mechanics approaches (e.g., Euler-Bernoulli beam theory and the method of assumed modes) have proven relatively accurate in predicting the behavior of microcantilevers (e.g., stiffness and resonance frequency), more advanced theories have yet to be examined, and with the drive toward smaller devices (e.g., thinner microcantilevers to increase sensitivity [194]), the elementary theories may become inaccurate.

1.2 Project Goals and Contributions

In light of these shortcomings, this work seeks to advance the field of microcantilever sensing by creating sensing modes, new manufacturing processes enabling new sensing applications (e.g., use of polymeric beams as sensors), and by refining the fundamental understanding of the way microcantilever systems behave mechanically. Satisfaction of the following goals will accomplish this.

1.2.1 Manufacturing Goals and Contributions

The first manufacturing goal and contribution is to produce microcantilevers by employing techniques other than IC-based fabrication methods so as to circumvent their shortcomings. These new approaches will reduce cost, making microcantilever-based sensing platforms tenable to a larger audience, increase control of their production (i.e., reduce uncertainty in resonance behavior as compared to commercially-available microcantilever parts), and employ new materials to allow for sensing applications in which it is tedious and difficult to employ silicon-type beams, or where it is entirely impossible to use silicon-type beams. The second manufacturing goal and contribution is to examine the thinnest microcantilevers that can be made from a variety of polymers via injection molding. This minimum thickness parameter could be useful in future applications which employ very short (roughly 50-100 μm), very thin microcantilevers (roughly 10-100 nm) as sensors [57]. The third manufacturing goal and contribution is to produce microcantilevers from polymer composites with the same matrix material and varying filler types and fractions, which will prove that, for a given geometry, the microcantilever's mechanical behavior can be "tailored" via fillers. The final manufacturing goal and contribution is to use some of the injection molded microcantilevers as both deflection- and resonance-based sensors, and as contact mode scanning probe microscopy sensors; this will show that they are functional alternatives to silicon-type parts in a vast number of applications.

1.2.2 Scientific Goals and Contributions

The scientific goals, which lead to the scientific contributions of this work, are to (*i*) examine the influence of any effects that may become more influential as characteristic length scales decrease, (*ii*) develop a new microcantilever experimental mode, and (*iii*) develop a new microcantilever characterization technique. The first scientific goal and contribution specifically seeks to develop an analytic *length scale dependent* bending stiffness equation, which, if physically present at the micron scale, can be used to modify other equations, such as analytic resonance predictions to include a length scale dependence. The second scientific goal and contribution is to produce a relation between surface stress and its effect on microcantilever resonance frequency, hence allowing the observation of surface stress development solely by monitoring resonance behavior, which is a new experimental mode. The third and final scientific goal and contribution is to provide a new means to determine microcantilever geometry; the geometry makes the microcantilever stiffness and mass tenable, which are both important experimental parameters. With the current problems and limitations of microcantilever fabrication and usage discussed, along with the proposed goals and contributions which address these problems, the organization of this dissertation is now discussed.

1.3 Thesis Organization

The remainder of this dissertation describes the background materials, methods, and analysis associated with the achievement of the project goals. Specifically, Chapter 2 details the previous work on micron-scale and microcantilever part fabrication, and the manner by which these parts have traditionally and more recently been mechanically characterized. Chapter 3 thoroughly discusses the specific theoretical approaches adopted in this work to attain the scientific project goals of §1.2.2, while Chapter 4 discusses the experimental methods used to satisfy the manufacturing goals of §1.2.1,

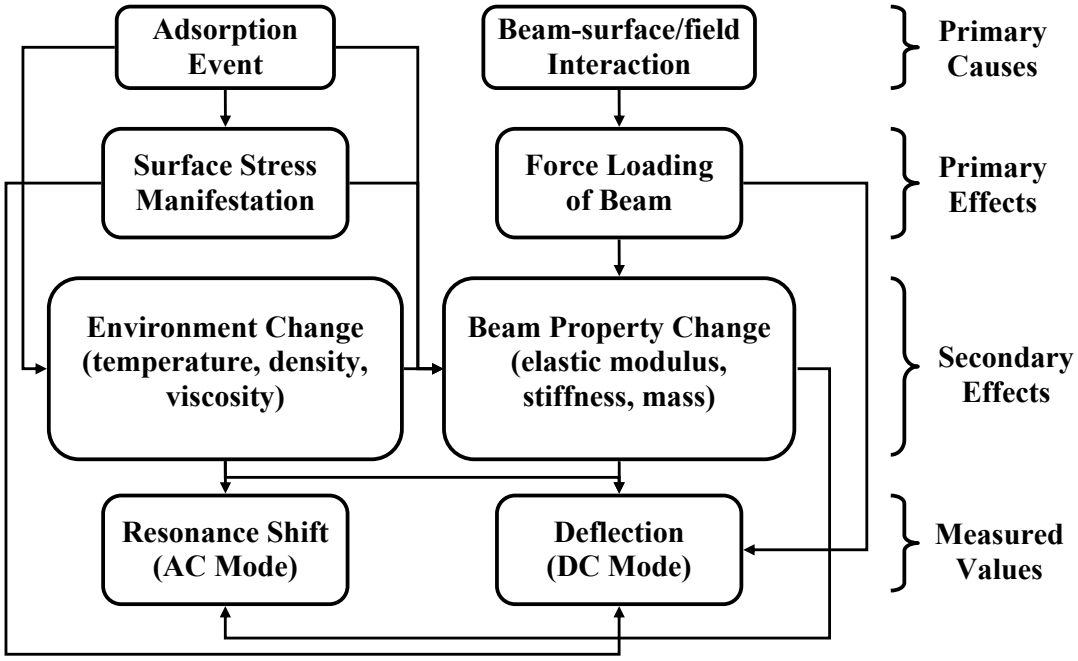

Figure 2: Flowchart of the causes and effects of microcantilever resonance and deflection behavior.

and the way microcantilevers are empirically evaluated for comparison to the theoretical formulae of Chapter 3. This comparison is presented in Chapter 5. The dissertation closes with the conclusions presented in Chapter 6, along with recommendations for future work.

CHAPTER II

BACKGROUND AND MOTIVATION

This chapter opens with an overview of microfabrication techniques (§2.1), a subset of which have been used to create microcantilevers (§2.2). After the microcantilever production schemes are covered, attention turns to the operation of microcantilevers as sensors (§2.3) and mechanical characterization and operation of microcantilevers (§2.4). An introduction to the simulation procedures which can (and will as seen in Chapter 5) be used to predict the behavior of the microcantilever sensing is then given (§2.5). This chapter concludes with the summary of §2.6. Chapter 3 rigorously examines a subset of the theories and techniques discussed in this chapter, while Chapters 4 and 5 detail the experimental setup and validation of the topics covered in Chapter 3.

2.1 Microfabrication Overview

This section covers some of the various microfabrication techniques which have been used to create microparts. The subsections detail the mechanisms of how each technique functions and also give examples of what previous work has produced using the various approaches. Numerous techniques are covered and, while not all are relevant to microcantilever sensing systems, many could be used to produce microcantilever parts either directly (e.g., micro-stereolithography) or indirectly (e.g., micromachining to produce injection molding micromolds). Nonetheless, the techniques have all been used to produce microparts. The topics of microcantilever systems, their function, and their fabrication begin in §2.2.

2.1.1 Silicon Micromachining

Thorough coverage of silicon micromachining and the associated developments is well beyond the scope of this work but it is hoped that this subsection gives an understandable yet brief review of the more prevalent developments and techniques that are germane to this dissertation– the reader may consult reference material for a more thorough explanation [83, 149, 227, 150].

Undoubtedly, the silicon micromachining field was born with the rise in computing power, and especially by the development of the transistor by Shockley, Bardeen, and Brattain at Bell Labs in 1947, and the later refinement by Bardeen and Brattain [19].[1] What followed was an explosion of transistor usage (vis-à-vis the exponential predictions of Moore's Law [188]) and along with it, rapid advancement of the technologies used to produce transistors– specifically, silicon micromachining which involves the following three processes.

- **Lithography**– a process of exposing a photosensitive material (e.g., positive and negative photoresists) to radiation (usually light) in a controlled fashion so that a master pattern may be transferred to the photosensitive material (and possibly scaled in dimension). After transfer of the pattern, areas of the photoresist exposed (unexposed) to light will be removed (unremoved) by a developer solution leaving the, possibly scaled, master pattern (inverse master pattern) in cured positive (negative) photoresist.
- **Etching**– a material removal process accomplished in many ways, such as: dissolution of the base material in liquid medium (wet etching), physical bombardment of the base material with ions (reactive ion etching, RIE, or focused ion beam etching, FIB), dissolution of the base material by a gaseous phase fluid (vapor phase etching), and erosion of the base material by bombardment

[1] Bell Labs is a research and development subsidiary of the American Telephone and Telegraph Company (AT&T) located in Murray Hill, NJ.

with other particles (e.g., sputter etching or laser ablation).

- **Deposition**– an additive process whereby material can be deposited onto large surfaces or controlled areas of the substrate (via masking). Some techniques include electrolytic processes, chemical vapor deposition, physical vapor deposition, and electroless processes.

Clever application of these three basic procedures allows for production of various types of MEMS for use in a wide array of scientific and commercial fields. The use of these techniques almost exclusively requires a cleanroom and expensive associated equipment. As IC-based microcantilever production is not used whatsoever in this work, the coverage is brief with attention now turning to non-IC based techniques, some of which were employed for this work.

2.1.2 Non-IC based Micromachining

The title of this subsection refers to machining of materials using scaled-down versions of conventional machining equipment and tools (e.g., milling, drilling, turning). The first step in this process is to make a stage apparatus which is capable of precise positional control of the workpiece, as the depths of cut are vastly smaller than in the conventional setting.

Several groups have developed complex assemblies that incorporate more than one machining process with accuracies on the micron scale. An aspheric generator (mainly used in the optics field) was made by the Cranfield precision group with a linear resolution on the order of nanometers [176]. Nakao *et al.* made a manufacturing setup that incorporated ion etching and a multidirectional SEM control system [191]. Mishima *et al.* produced a system with a micro-press, micro-lathe, and micro-mill (among other capabilities), which successfully manufactured a ball bearing [183]. Takeuichi *et al.* developed an impressive five-axis machining center with translational resolution (three axes) of 1 nm and rotational resolution of 1×10^{-5} degrees [237].

Once a feasible stage is produced, one must look to miniaturizing the tools and some of the the early attempts of Schaller *et al.* produced end mills with diameters as small as approximately 50 μm using mechanical grinding techniques [221]. To produce smaller end mills, focused ion beam techniques (discussed in §2.1.6) have proven to be quite successful in recent works, some showing that end mills have been produced with dimensions down to 15 μm [8, 81, 203]. Many works have shown that the tooling requirements lag behind the positioning capabilities currently available [260]. This has led to the use of diamond tooling, which can be produced (usually with focused ion beam approaches) with lower cutting edge radii of curvature than metal tools, hence making diamond the tool material of choice in many micron- and submicron-scale machining situations [147, 199, 32, 49].

2.1.3 Soft Lithography

Soft lithography was invented by Xia and Whitesides at Harvard University and is a production technique which involves the use of an elastomeric stamp, which is fabricated using a master structure, to (*i*) selectively deposit various substances (usually polymer solutions) onto planar or curved surfaces, (*ii*) form structures using the elastomeric stamp as a mold, or (*iii*) a combination of (*i*) and (*ii*). The elastomeric mold usually is made by casting an uncured elastomer onto a (usually) ceramic master and allowing it to cure, where the master is created with silicon micromachining techniques, micromachining, or focused ion beam milling, for example. There are five different types of soft lithography, which are now discussed. It should be noted that the elastomeric molds are transparent to UV light making photocuring feasible as required by some of the methods.

2.1.3.1 Microcontact Printing (μCP)

In this technique, the elastomeric stamp is used just as a conventional stamp is, only the protruding features on the rubber stamp are usually much smaller. The stamp

is "inked" with a solution which will then be deposited on the surface of interest to produce a self-assembled monolayer (SAM), setting μCP apart from the other soft lithography techniques, which do not exclusively use SAMs. Self assembly is seen in biological systems (e.g., formation of proteins and DNA folding [55]) and hence microcontact printing is enticing for biological applications. The technique has produced structures ranging from the molecular scale [143, 261] to the macroscale [34, 239]. Cylindrical, rolling stamps have been used and could prove μCP to be incredibly scalable [264].

2.1.3.2 Replica Molding (REM)

Replica molding uses a mold similar to μCP, but instead of depositing materials on a substrate, the mold is filled with a photo- or thermosetting polymer, which is subsequently cured and removed to form the desired part. The mold can be either an elastomer or a more rigid form (such as a metal or themoplastic polymer). Compact disks, microtools [119], diffraction gratings [104], and holographic structures [190] have been made with REM. The technique is limited by the wetting behavior of the mold and photopolymer used.

2.1.3.3 Microtransfer Molding (μTM)

Microtransfer molding is somewhat of a mix between μCP and replica molding- the elastomeric mold is filled with a prepolymer (photo- or thermosetting polymer), the mold is pressed against a curved or flat surface, the prepolymer cured, and the mold removed leaving a part on the surface. Zhao *et al.* used μTM to make numerous optical parts such as waveguides, couplers, and interferometers [272, 271] and the technique can be used to form patterns from materials other than polymers such as glassy carbon and ceramics [224, 157].

2.1.3.4 Micromolding in Capillaries (MIMIC)

Micromolding in capillaries uses an elastomeric mold with channels in it to produce extruded-type structures on curved and flat surfaces. The mold is placed on the surface, a prepolymer droplet is placed at one end of the exposed channel(s), capillary action draws the prepolymer into and filling the channel. The prepolymer is cured and the mold removed leaving the structure(s) on the surface. MIMIC can be used with materials other than prepolymers such as sol-gels, inorganic salts, or biological molecules [248, 120, 58].

2.1.3.5 Solvent-assisted Micromolding (SAMIM)

SAMIM uses a stamp (usually elastomeric) to apply a solvent to a polymer film, hence selectively removing certain portions of the film leaving a relief structure in the film the same general shape as the stamp. SAMIM has been used to produce nanometer-scale relief structures in various polymers using different solvents [264].

2.1.4 Electrodischarge Machining

Electric discharge machining (EDM) is a thermal material removal technique whereby an electrode tool erodes a conductive workpiece by thermal ablation due to spark discharge. The workpiece and tool are immersed in a fluid during the process. Two general classes of EDM exist, wire and die sink. In wire EDM, a conductive wire (25-300 μm diameter) under modest tension is fed a through a hole in the workpiece from a feed spool above to a receptor spool below the workpiece. Translating the workpiece while continually feeding the wire (to prevent the wire from breaking due to thermal creep) in directions normal to the wire produces a through-workpiece cut. In die sink EDM, the tool has the shape of the desired cavity and is plunged into the workpiece, hence removing material and leaving a cavity with the shape of the tool. Masuzawa could truly be considered the father of this technique as his work has a long history of quality and innovation in all the EDM variants. Parts have been

made by Masuzawa and coworkers incorporating EDM ranging from micro-holes to micronozzles and true three-dimensional cavities [159, 128, 160, 134, 235, 236, 161, 269]. The main disadvantage of die sink EDM is that the tool degrades during use, reducing dimensional accuracy. However, the WEDG (wire electrodischarge grinding) process, created by Masuzawa, can retain a near constant tool shape and produce features with sub-5 μm dimensions [158]. Unfortunately, it is only possible to use the WEDG process with elementary tool geometries and hence it is not a feasible technique to produce complicated 3D mold cavities. EDM has many advantages including the ability to machine very hard materials, minimal bulk heating of the workpiece, and absence of contact stresses permitting use on fragile specimens [184]. Ultrasonic vibration assistance has increased the feasible material removal rates of the EDM process while concurrently reducing the roughness of the machined surface [125, 126, 110].

2.1.5 Electrochemical Machining

ECM, or electrochemical machining, involves a reaction where the workpiece behaves as an anode and the tool as a cathode while immersed in an electrolytic bath. Application of an electric field between the two will cause electrons to migrate from the workpiece to the tool. Due to the reactions taking place, the tool will not change shape significantly but the stock will approach the shape of the tool. ECM has advantages similar to EDM (e.g., the ability to machine very hard materials, little bulk heating of the workpiece, and lack of contact stresses allowing use on fragile specimens) but cannot be used on materials with insufficient corrosion resistance, as the chemical reactions and electrolyte bath used greatly increase corrosion rates [184].

2.1.6 Focused Ion Beam

Not surprisingly, focused ion beam techniques involve bombarding a surface with ions that are accelerated and focused from a source (usually a liquid metal from a vast

array of possible materials: Al, As, Au, B, Be, Cu, Ga, Ge, Er, Fe, H, In, and many more) to a surface [249]. Focused ion beam manufacturing comes in two flavors, one shoots a "pencil" of ions toward a single point on the surface (FIB), and the other bombards the entire surface with a collimated beam of ions that usually pass through a masking device– this is known as focused ion beam lithography (FIBL). In FIB, the ions are directed at the surface with enough energy to cause sputtering of the workpiece surface upon collision of the ions with the electrons or nucleii of the substrate atoms. For FIB, ions are preferred to other particle beams (e.g., electrons and photons) as they are heavier and can impart much larger energy densities– a property which allows FIB to mill and to implant the ions in some hard materials such as metals and ceramics, materials which photons and electrons cannot mill with any practicality. It should be noted that a focused ion beam can be used to image certain crystalline materials due to the preferential flow of ions in open columns of the lattice structure. Additionally, a focused ion beam can be used as the heat source for chemical vapor deposition with vastly improved resolution compared to LCVD at the expense of a lower deposition rate. FIB is a great option to prepare tunneling electron microscope samples, has been used to produce micorcantilevers with thickness on the order of 10 nm, and can make complex three dimensional (3D) shapes (with overhangs), such as cups and coils, with characteristic dimensions of the order of 100 nm [36, 30, 210].

2.1.7 Laser Ablation/Machining

Laser energy can be used in a variety of fashions for microfabrication purposes– the main idea is to impart energy to a surface via a laser to ablate or change the phase of a small volume of material. Controlled scanning of the laser can act as a milling tool as well (similar to the focused ion beam discussed in §2.1.6). Laser processes also have been used to grow grains in specific directions in ceramic films [137], for polymer

microoptic (waveguide) production [111], to deburring of previously cut surfaces (laser cut or otherwise) [138].

2.1.8 Rapid Prototyping Approaches

Rapid-prototyping (RP) refers to techniques which take as input a computer aided design (CAD) drawing, and then transform that drawing into a true, three dimensional object in a fashion that is rapid (generally less than a day) compared to conventional manufacturing techniques with only a modicum of operator skill required. However, RP approaches usually entail many iterations to get a successful result, so many people say that if one knows anything about RP, one knows that RP is not rapid. Nonetheless, RP offers some unique advantages and many flavors, each of which will now be discussed.

2.1.8.1 Stereolithography

Stereolithography (SLA), the first rapid prototyping technique developed, is a process in which a thin layer of photosensitive polymer resin is subjected to laser light in specific locations to produce a single cross section of the desired part [123]. Lowering and subsequent spreading of another thin resin layer on top of this section allows manufacture of the next cross section. Repetition of this process, for all cross sections, produces the final part. Due to the layering scheme of the machine and possible insufficient laser control, a stair stepping effect usually is observed in some areas of the parts. This technology was the first to receive a patent and has been used to produce injection molds and micromolds, microcantilever-type structures, and general 3D MEMS structures, to name some [103, 213, 212, 154, 252].

2.1.8.2 Super IH

The Super IH process creates a 3D object by pinpoint solidification of a photopolymer in 3D space by focusing one (or two different) light source(s) on the desired solidification point [106, 117]. This method *does not* employ the 2D to 3D cross-section stacking method and allows for creation of arbitrary 3D geometries and freely movable mechanisms (e.g., a tapered roller bearing) as no support structures are needed as they are with regular stereolithography. The resolution of this method is on the order of microns for the one photon approach and on the order of 100 nm for the two photon approach, while the production times for both methods are less than those of conventional stereolithography [24]. It should be noted that both stereolithography and the Super IH process can be used with a limited number of ceramic/polymer composite materials [24, 234, 187].

2.1.8.3 Laminated Object Molding (LOM)

LOM works similarly to SLA in that it recreates a three dimensional object by joining together two dimensional surfaces. These surfaces are created by cutting a film-like material (usually paper) with a laser (or a knife in the Paper Lamination Technology process), adding an adhesive over the material surface, applying a fresh "sheet" of material on this adhesive, and then cutting the subsequent cross section. Repetition of this process yields the 3D part. LOM has been used to fabricate ceramic preforms [11] and polymer composite structures [121].

2.1.8.4 Fused Deposition Modeling (FDM)

Fused deposition modeling also produces 3D objects via the addition of 2D surfaces, which are created by depositing a bead of melted polymer on a surface in a vector pattern, similar to a tube of toothpaste. A plastic filament is unwound from a feed spool and fed into a heated extrusion nozzle, which melts the filament and deposits it in the vector pattern. This technique permits creation of composite structures by

changing the material fed to the extrusion nozzle during various stages of the production process. A drawback of the method is that it cannot yield a full density part, which other processes such as LOM can, due to the geometry of the deposited polymer beads. FDM has been used to make mundane items such as dogbone specimens for mechanical testing [13] and elastomer structures (oxygen air masks) [66].

2.1.8.5 Laser Engineered Net Shaping (LENS)

Laser engineered net shaping uses localized heating of a metal powder which is injected into a laser stream.[2] The laser heating causes the powder to melt and be deposited in the neighborhood of the laser spot. A 2D scanning pattern creates cross sections and moving the laser away from that surface (or vice versa) allows creation of 3D structures. The process is appealing in that it can produce near full-density parts from various metals (e.g., aluminum, Inconel, copper, and titanium) at reasonable speeds. LENS can be used to produce tooling [93] and functionally graded materials [69]. LENS is the only rapid prototyping procedure available to make metal parts aside from laser chemical vapor deposition (see Section §2.1.9.2) and selective laser sintering which is now discussed.

2.1.8.6 Selective Laser Sintering (SLS)

The SLS process is very similar to SLA except that, instead of a photopolymer material, SLS solidifies thermoplastic powder layer by layer to produce a 3D part. After completion of one layer, the powder is moved from a feed cylinder (adjacent to the part) to the top of the current layer, which rests upon the solidified layers beneath it and finally on a part platform (which is lowered after completion of each layer). SLS can be used with metal spheres coated with polymers which can be subsequently sintered together to produce near full density metal-polymer composites with the

[2]LENS and laser engineered net shaping are registered trademarks of Sandia national labs–Optomec is commercializing this technology.

possibility for very high (95%) metal volume fractions. When using thermoplastic powders the resulting part is usually highly porous and hence can be infiltrated with other materials (e.g., a metal using the CVD process, discussed in §2.1.9.1) yielding an alternate way to make composite parts via SLS. No support structure is needed as in SLA. Microstructures with characteristic dimensions on the order of 500 μm have been developed, but the process is not a feasible MEMS production technique [116].

2.1.8.7 3D and Waxjet Printing

The 3D printing and waxjet printing processes are very similar and hence are grouped together here. 3D printing uses modified technology based upon that of a conventional inkjet printer to print 2D planar surfaces of wax onto a movable base platform. Moving the platform away from the inkjet head allows the creation of the next cross section and (eventually) the final 3D part. The resolution of commercial systems is roughly 300 dots per inch and the main limitation is that the materials available are essentially worthless in terms of mechanical properties, but, for aesthetic purposes, waxjet printing can be appealing. Another benefit of the process it that the parts produced can be recycled. The 3D printing process deposits a powder material (polymeric or metallic) upon a movable base and brings a jet head over this layer, which deposits adhesive in selected areas to produce a 2D cross section. The technique is the fastest of all the rapid prototyping approaches, requires no support structure as some of the other processes do, and material cost is very low (comparatively). Similar to waxjet printing, the parts are of very low mechanical caliber, but can be used in aesthetic applications, for example.

2.1.9 Deposition Processes

2.1.9.1 Chemical Vapor Deposition (CVD)

Chemical vapor deposition is usually used to coat surfaces with metals or ceramics. To accomplish this, the parts to be coated are placed in a chamber and the temperature is elevated (500-1500 °C) and a reagent gas is flowed through the chamber. The high temperature environment induces chemical reactions at the reagent-part surface interface. There are both hot walled (entire chamber is heated) and cold walled (only the parts are heated, by conduction heating for example) chambers and both can deposit a slew of different metals (e.g., Fe, Mo, Ni, Co, Ag, Au, Si) and ceramics (e.g., Al_2O_3, Si_3N_4, SiC, TiB_2, $MoSi_2$, MoS_2, C). CVD is used in numerous applications, micro and otherwise, including fiber growth, superconducting and metallic film generation, and production of submicron thickness SiC microcantilevers, to name some [130, 113, 228, 232]. The general reaction that takes place at the part surface is that of a metal halide (e.g., $SiCl_4$) with a source or fuel constituent (e.g., H_2O) to produce the coating (e.g., SiO_2) and waste product (e.g., HCl). A catalyst reagent (usually hydrogen) is used on most occasions. To obtain acceptable coatings, considerable experience with the process (or access to a knowledge base) is usually required. A variant of the technique, chemical vapor infiltration (CVI), is used to coat the internal structure of porous materials by placing the porous object in a CVD chamber and allowing the reagent gasses to diffuse into it [131].

2.1.9.2 Laser Chemical Vapor Deposition (LCVD)

LCVD selectively heats a region of space that is occupied by a reagent gas (or gasses). The heat causes the gasses to transform to a solid state that is deposited on an adjacent surface. The laser allows for selective heating and growing of three dimensional structures (e.g., wires or coils). LCVD could be considered a rapid prototyping technique as well as a deposition technique. Many different materials (usually metals

or ceramics) can be deposited such as B, C, SiC, Si, TiC, and W. By changing the reactant gasses during the process, functionally graded and composite parts can be created. Carbon fibers and nanotubes have been grown with LCVD, as well as microsprings, microsolenoids, and microcoils [256, 257, 162].

2.1.10 LIGA

The LIGA process name stems from its German roots as an acronym for "*Li*thografie" and "*Ga*lvanik", meaning lithography and electroplating, respectively.[3] The first stage of LIGA involves a lithography-based pattern replication (see §2.1.1) upon a substrate (usually using synchrotron radiation) to produce structures with aspect ratios up to roughly 100 and surface roughnesses down to 50 nm R_a [186, 48]. Once the structure is defined, electroplating and subsequent etching of the original substrate leaves behind a metal part (the type of metal being defined by what is electroplated) with the inverse of the etched structure impressed upon one surface, which can be used in micromolding or hot embossing (discussed in §2.1.11.1 and §2.1.11.2, respectively).

2.1.11 Plastic Microfabrication Techniques

This subsection details some of the more common fabrication techniques that are used to produce plastic parts and specifically, parts that require a rigid mold in their production.

2.1.11.1 Micromolding

Micromolding is a subset of the injection molding process, where a polymer melt is forced into a cavity, allowed to cool, and removed hence a part that has the same general shape as the cavity. The name micromolding implies that the parts produced

[3]The term LIGA has been redefined in some circles to include the term *A*bformung, which means molding– this obviously came about with the use of LIGA to produce molds for micromolding and hot embossing, both of which are discussed in §2.1.11.

have some type of parameter on the micron scale, but the term has taken on a relatively liberal meaning.[4] For example, a component that has characteristic length scales on the order of millimeters may have surface form requirements (e.g., radius of curvature of a lens face) on the order of nanometers– this part would still be considered to be micromolded component. Micromolding has been used to create a slew of different parts– microfluidic devices [38, 222], micropumps [62], micro-optic components [174, 165], microchannel fluidics for biological applications [163], and more recently, microcantilever sensors and scanning probe microscopy probes, as discussed in this work [170, 169].

2.1.11.2 Hot Embossing

Hot embossing involves pressing a "hard" structured surface against a "soft" polymeric surface under elevated temperature. After sufficient holding and cooling times, the hard surface is removed leaving its impression upon the polymeric substrate. The technique has been used to produce microvalves [90, 91, 73], microsensors [155], diffraction gratings [122], and optical devices [96]. Hot embossing can produce features as small as 25 nm, which approaches the radius of gyration of the polymer molecules themselves [46].

2.1.11.3 Reaction Injection Molding

Reaction injection molding is similar to injection molding in that it involves a cavity which is filled with material to produce a part. However, instead of injecting a single thermopolymer, two components are injected into the cavity and allowed to cure to form a thermoset. Upon setting, the part is ejected and ready for postprocessing and use. Reaction injection molding has seen a decline in usage (in favor of the injection molding process) but has been used (in conjunction with LIGA molds) for

[4]Others have adopted the following classification: if the part volume is less than 1×10^{-6} m^3, the production is dubbed micromolding– note that the volume of a cube with a 10 mm edge length is $1 \times 10^{-6}\text{m}^3 = 1\mu(m^3)$ and *not* considered to be micromolding by many.

microfabrication [65] and to produce high aspect ratio microstructures [95].

2.2 Previous Work in Microcantilever Fabrication

The vast majority of microcantilevers in use are made using the techniques of integrated circuit manufacturing (i.e., all in use except those of this work). This section details the production schemes for producing silicon-type microcantilevers (i.e., SiN, Si, etc.) and polymeric microcantilevers (i.e., photo- and fluoropolymers) as both have only been made with IC techniques. This section closes with some brief coverage of thermoplastic microcantilever production schemes, but leaves the bulk of the discussion on this topic until the later chapters, as this was the main manufacturing goal of this work.

2.2.1 IC-based Production Schemes

Silicon-type microcantilevers are ubiquitous in AFM and microsensing circles, and are commercially available at costs of $5 to $100, or even more, depending upon application [5, 7]. The most common materials used are silicon, silicon-nitride, gallium-arsenide, and occaisionally diamond [198]. The techniques to fabricate these cantilevers begins with masking off a region of a silicon wafer– this is done by first spin-coating a photoresist (usually a photosensitive polymer) on the surface of a wafer, and then bombarding the surface with photons that have been selectively filtered by a mask, as shown in Step 1 of Figure 3. Once cured, the photosensitive material (which was exposed to light) will be fixed to the surface while the uncured resist will be removed. Now, an etchant (which can only erode substrate material and not cured photoresist) is applied to the surface hence removing some of the substrate material as shown in Steps 2 and 3 of Figure 3. The wafer can be flipped over, shielded with an inert filler (i.e., a material that will not be eroded by the removal agent used in the next step– this could be a photopolymer), and subject to another material removal

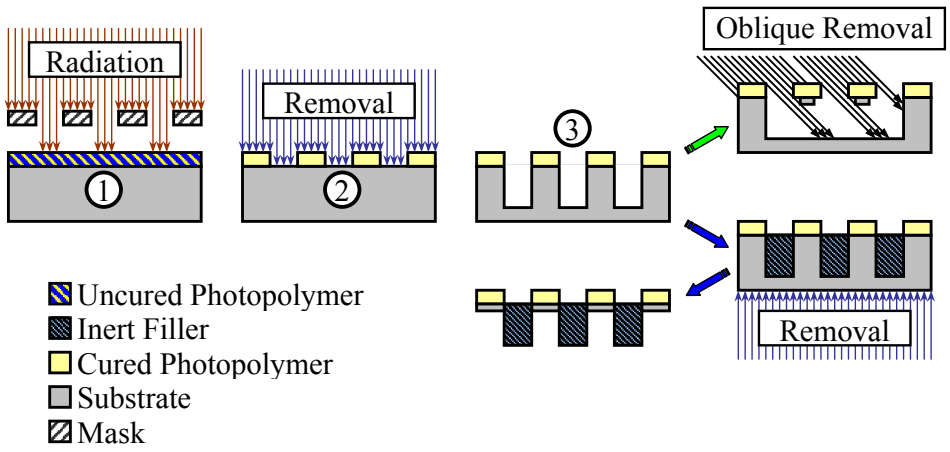

Figure 3: Microcantilever production scheme, similar to the work of Lee *et al.* [136].

step to define the microcantilevers as shown by the blue arrow sequence after Step 3 in Figure 3. Alternatively, once could use an oblique removal technique to produce the cantielevers as shown in the green arrow sequence after Step 3 in Figure 3 [136]. The final stage involves removal of the cured photopolymer and, if present, the inert filler. This is an older approach to production and newer techniques employ multi-layer (e.g., SiO_2-Si-SiO_2 composite sandwiched) substrates and various techniques to produce asperity-like geometries at the end of the cantilevers for probe microscopy procedures (discussed in §2.3.2.1)– see the work of Albrecht *et al.* for an overview of the techniques [14]. More recently, Genolet and coworkers have produced scanning probe microcantilevers from a photopolymer (SU-8). Their approach was to etch a mold in a piece of silicon, fill the mold with SU-8, cure the SU-8, and attach a base part for mounting in an AFM. The resulting parts proved to be feasible for obtaining images of DNA and a Langmuir-Blodgett film with coexisting hydrocarbon and fluorocarbon molecular domains– multiple cantilever parts also were made [85, 86]. More recently, Wang *et al.* also created microcantilevers (SPM probes) using a photopolymer (polyimide) with elastomeric tips [258] using nearly the same technique

as Genolet *et al.* Thaysen *et al.* [240] made photopolymer-based piezoresistive mechanical sensors also employing IC techniques. Lee *et al.* produced microcantilever arrays from fluoropolymers by using photolithograpy to produce a pattern on the polymeric substrate and then selectively remove material using normal and oblique ion beam etching (as in Figure 3) [136]. While these works are important as they have produced polymeric microcantilevers, their reliance on IC fabrication techniques is seen as limiting in the view of the author as they are expensive, limited in feasible materials, and very cost-sensitive to design modification.

2.2.2 Solvent Casting and Injection Molding

In an effort to remedy the shortcomings of the IC-based microcantilever production approaches, this work developed two techniques to produce thermoplastic microcantilevers that do not rely on IC fabrication methods. Chapter 4 will detail the methods and experimental setup in detail but a brief overview is given here.

In solvent casting, a polymer is dissolved in a solvent and the resulting solution is cast upon a flat, glass (usually) substrate [171, 172]. The film is gold coated (so that sufficient laser light is reflected in an AFM employing the optical lever) and strips are cut with custom tooling to the desired microcantilever widths. These strips are fixed to polymer bases and then are ready for use in the AFM. Using this technique, only "diving board" type cantilevers (i.e., beams without SPM tips), although adding tips is possible.

The injection molding approach forces a polymer melt into a cavity, comprising two moveable halves which, when closed, have the desired microcantilever and support structure shape. The melt is allowed to cool, the mold opened, and the microcantilever part removed. Single and multiple beam parts were made with this approach [170], as were microcantilevers with SPM tips [169], which proved to be feasible SPM probes *directly* after being removed from the injection molding machine (i.e., no gold coating,

AFM machine, or part modification was necessary).

2.3 Microcantilever Systems Overview

With the microfabrication techniques introduced and the previous work on the way these techniques were used to make microcantilevers covered, a logical question is: what use are microcantilevers once they are made? This section seeks to answer this question by detailing the applications and operation of microcantilever sensing systems. The various motion detection schemes are discussed first, followed by the previous works showing the wide range applications for which microcantilevers are feasible. Once the applications are explained, the different techniques used to characterize microcantilevers mechanically are covered, as the characterization procedures yield parameters which are requisite knowledge to make sense of the data gathered in sensing applications.

2.3.1 Microcantilever Motion Detection Schemes

In practice, every microcantilever sensing system either measures the deflection of the beam (to obtain surface stress changes or to map out surface topographies, for example) or resonance frequency information (usually shifts of resonance frequency[5]) of one or more resonance modes (to measure microcantilever mass or stiffness changes, for example).

Figure 4 shows how a deflection event is tracked. Some event will cause a microcantilever deflection (e.g., surface stress development or beam tip-surface interaction) which is sensed as a voltage change (the voltage is used here because this work exclusively employs the optical lever technique of §2.3.1.2, which reads a voltage). This voltage is translated into a deflection via a calibration scheme (discussed in a footnote of §2.3.1.2) and the forces acting on the beam can be calculated (via knowledge of

[5]Amplitude and phase information also may be monitored, although this is not common.

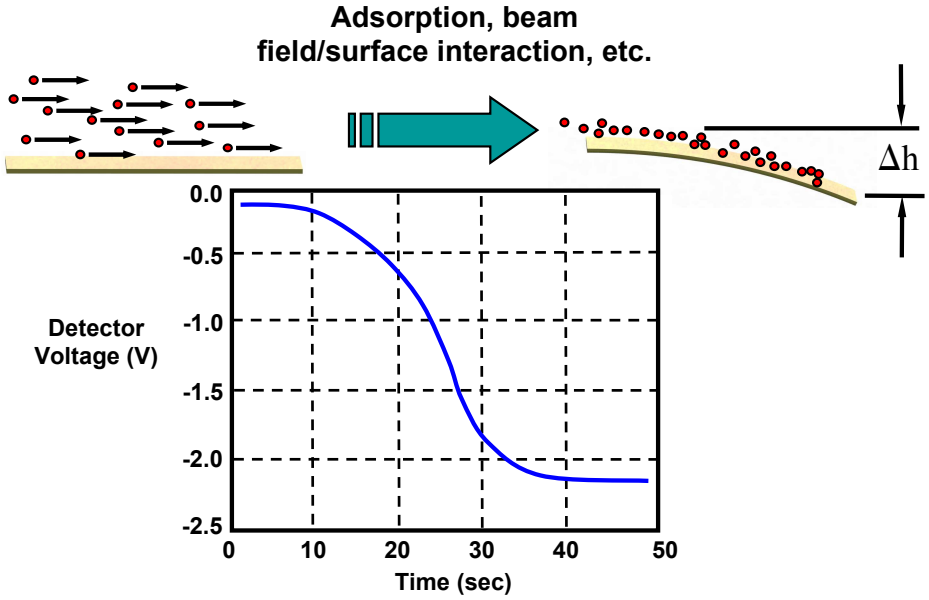

Figure 4: Schematic of the induced deflection (Δh) of a microcantilever.

the beam stiffness).

Figure 5 shows how the resonance behavior is tracked. An event (adsorption in this case as that is the main concern of this work) causes a resonance shift (and possible deflection) of the microcantilever, which is measured and allows for calculation of certain parameters (e.g., surface stress as developed for this work or mass loading). This subsection details the various techniques that have proven feasible to detect deflection and resonance behavior of microcantilevers.

2.3.1.1 Tunneling

One of the earliest devices to employ microcantilevers as sensors was the scanning tunneling microscope (STM) of Binnig and Rohrer [27, 28, 29][6]. The STM moves an asperity-like probe tip translationally (i.e., in the plane normal to where the tip

[6]Gerd Binnig and Heinrich Rohrer shared in the 1986 Nobel prize in physics for this development.

is "pointing") over a flat surface at atomic distance causing tip-surface electron tunneling if the distance is below a threshold value. As the STM tip is scanned over the surface at a distance close enough to induce tunneling (for a given applied bias voltage), the tip is raised or lowered to keep the tunneling current constant allowing the mapping of the surface topography. Unfortunately, the tunneling process is translationally slow and very susceptible to environmental interference, even under vacuum conditions. The atomic force microscope (AFM) of Binnig, Gerber, and Quate [26] was developed to, in part, remedy these shortcomings and to allow imaging on non-conductive samples by using a microcantilever with a "blunt" tip having a radius of curvature of roughly 10-100 nm (blunt when compared to the STM probe tip with a single- to few-atom asperity tip) as a probe.[7] The "blunt"-tipped cantilever is scanned over a surface in the plane normal to the tip[8] so the beam is deflected by the peaks and valleys present in the surface being scanned. To detect beam motion, an STM probe tip is positioned close to the back side of the AFM ("blunt"-tipped) microcantilever and tunneling behavior is monitored. The AFM method in this original form suffers from a low dynamic range and is threatened by the excessive thermal drift. Also, the STM tip exerts forces (electrostatic and Van der Waals) upon the other microcantilever, which can cause errors in the measured parameters. Due to the shortcomings of the tunneling approach, other techniques were developed whereby the probe deflection and resonance can be measured, but without monitoring electron tunneling. It should be noted that the term AFM refers to the STM-based microcantilever deflection scheme of Binnig, Gerber, and Quate, but it has taken on a much broader meaning which includes use of a microcantilever as a measuring

[7] With no restrictions on the maximum radius of curvature of the tip, the AFM also permitted use of a more mechanically robust tip.

[8] In this mode, the beam is scanned in a ⎍⎍⎍ pattern with the data logged during the long, vertical strokes which are scanned in the length direction of the beam while the small, horizontal motions are scanned in the width direction of the beam– this scheme causes any tip-surface interaction to produce a deflection of the beam with no rotation.

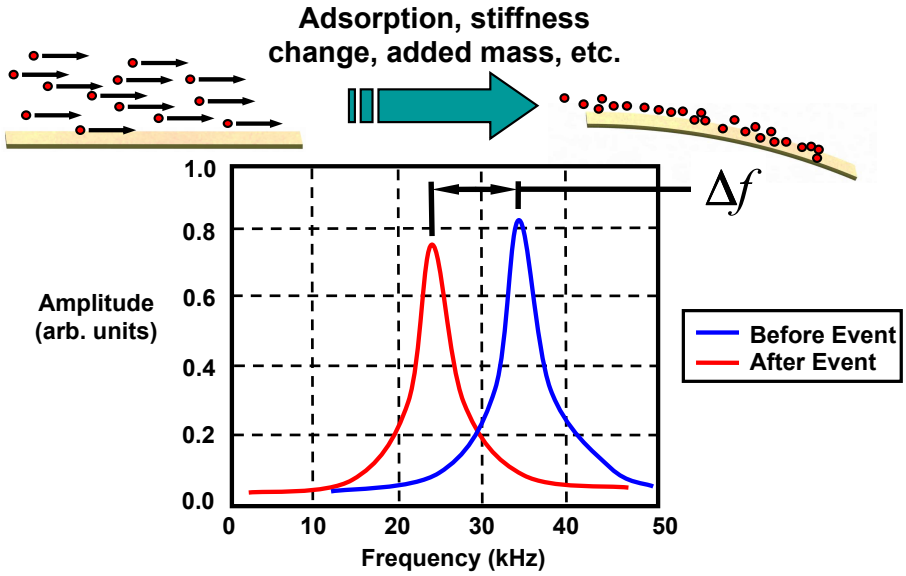

Figure 5: Schematic of the induced resonance shift (Δf) of a microcantilever.

probe employing tunneling or any of the other deflection and resonance techniques now discussed.

2.3.1.2 Optical Lever

The so-called optical lever is a technique used to measure the deflection and resonance of a microcantilever employing a laser with associated optics [e.g., mirror(s)] and a position-sensitive photodiode (PSD) [156]. The operation is depicted in Figure 6. The laser light is aimed at the top of the microcantilever so that the reflected laser light is incident upon the photodiode. Photodiodes used in the optical lever system can be of the two or four quadrant variety, but the operational principles are the same for both. The amount of laser energy incident upon any quadrant induces a voltage signal that is collected for that quadrant alone. Collection of the voltage readings from all of the photodiodes, along with knowledge of the geometry of the experimental setup, allow for the microcantilever slope and subsequently displacement to be determined. One should note that the deflection is initially in units of *volts*, not distance and

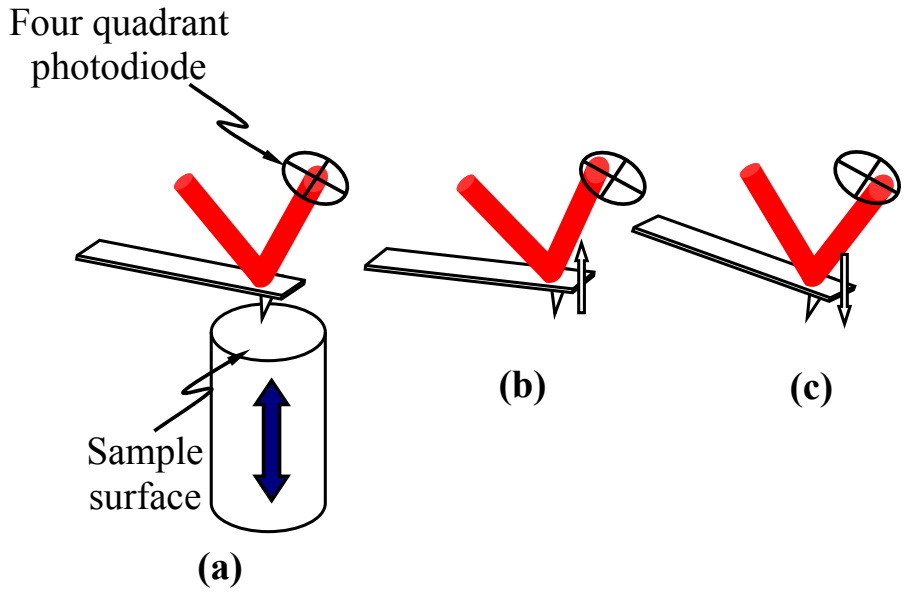

Figure 6: Optical lever schematic (the blue arrow indicates the direction of motion caused by the peizoelectrics) (a) reference position, (b) beam deflection up, and (c) down.

hence, to determine distance, one must perform a calibration procedure.[9] Atomic-scale resolution is possible with the optical lever technique, although it can be limited in the tenable range of deflections when compared to other approaches. Nonetheless, the optical lever is the most widely used of all microcantilever sensing methods.

2.3.1.3 Piezoresistive and Piezoelectric

Another method to determine beam deflection is to employ piezoresistive elements that are manufactured on the beam's surfaces or in its interior. Upon straining of the microcantilever, the resistance in the piezoresistive circuit (depicted in Figure 7)

[9]To obtain the actual beam deflection, the piezoelectric stacks in the AFM are used to determine the voltage sensitivity, C, of the beam in V/m (i.e., the voltage change on the photodiode output versus the deflection of the piezo stacks) which is different for each cantilever and must be determined before the actual experiment that uses the microcantilever can be conducted. Dividing the photodiode output voltage during an experiment by C gives the beam deflection during the experiment.

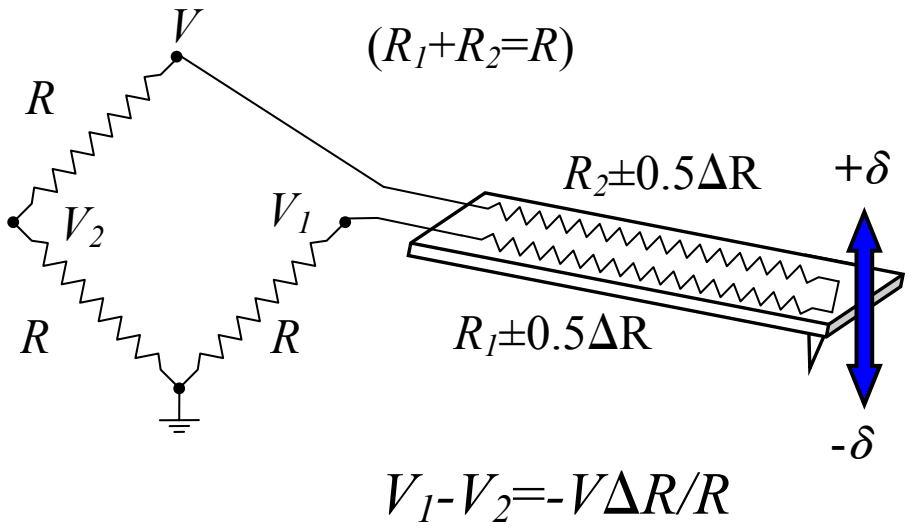

Figure 7: Schematic of piezoresistive-based microcantilever deflection measurement.

changes due to shape effects and piezoresistive effects. Knowledge of the input voltage, output voltage, and resistance in the undeformed circuit allows for the strain to be calculated in the microcantilever, and finally the beam end deflection. After a calibration procedure, the output voltage across the bridge becomes an accurate indicator of beam end deflection– the minimum detectable deflections are on the order of 0.01 nm [245]. The piezoelectric measurement scheme is very similar to the piezoresistive, except that the beam strain generates an electric charge, whose measurement allows for beam deflection calculation– the minimum detectable deflections are commensurate with the piezoresistive approach. A benefit of the piezo-based approaches is their ability to have a microcantilever be completely invisible to any sensing and electronic equipment except for the lead wires; low (nanowatt) power consumption is also possible with piezo-based array systems wired in series [9].

2.3.1.4 Interferometry-based Detection

In this approach a coherent light source is emitted and split, with one half of the signal directed to the top surface of a microcantilever, and the other half sent to a photodiode. The portion of the light sent to the microcantilever surface reflects off

that surface onto the same photodiode where the sister wave arrives. Wave interference patterns are formed and beam end deflections can be determined with sub-Å resolution [71]– this is an application of heterodyne interferometry. Logically enough, homodyne interferometry can be used as well by reflecting orthogonally polarized laser light on the beam end and the base, with the relative orientation phase difference giving means for deflection measurement with resolution of approximately 0.01 Å [223].

2.3.1.5 Capacitive Detection

Capacitive detection schemes measure the capacitance (and change) of a parallel plate capacitor formed by employing for one plate the back of a microcantilever (or a protrusion or surface coating) and for the other plate a reference metallic plate that is positioned upon an adjustable stage so that it can be brought in to close proximity of the microcantilever in a controlled fashion [88]. Sensors with integrated microcantilevers-plate capacitors have been developed to eliminate the need for the second capacitor plate to have its own positioning stage, and sub-Å resolution is possible [193].

2.3.1.6 Diffraction Grating-based Detection

Although not widely used, the diffraction grating-based detection scheme is quite clever. A microcantilever is produced in the form of interdigitated fingers, and alternate fingers are displaced relative to fixed fingers when the beam end is displaced, forming a diffraction grating which is sensitive to the incident laser light (the laser is aimed at the back of the beam as in the optical lever technique, see Figure 6). Measurement of the diffraction modes allows for the beam end deflection to be determined [153]. Further analysis of this procedure showed that it is less susceptible to laser pointing noise (random fluctuations of laser beam direction and shape) and thermally induced mechanical vibrations when compared to the optical lever [268].

2.3.2 Microcantilever Applications

Now that the methods to determe microcantilever deflection and resonance behavior have been discussed, this subsection seeks to show what other researchers have done with these capabilities in a broad spectrum of scientific fields.

2.3.2.1 Surface/Force Microscopy

As mentioned in §2.3.1.1 the first applications of microcantilevers were to map out surface topographies using the STM and AFM with sub-Å resolution. These are so-called contact techniques, where the probe tip was dragged over the surface hence producing the microcantilever deflection. This microscopy approach is not feasible for softer surfaces such as biological cells, as the microcantilever probe tip will damage the entity to be imaged. Therefore, tapping mode microscopy was developed, which holds the probe tip away from the surface and actuates it, often piezoelectrically and usually at the fundamental resonance frequency of the microcantilever, and then monitors changes in the resonance frequency that occur due to the van der Walls-type attraction that occur as the probe tip is brought closer to the entity being imaged or by actual tip-entity contact. The tapping mode has been successfully demonstrated in both air and liquid environments [214]. Lateral force microscopy is similar to the contact mode AFM approach except that the motion of the beam is now in the direction of the beam width, so that tip-surface interactions can cause the microcantilever to deflect in the thickness direction and to exhibit torsional deformation, which can be monitored and used to map out surface topography, for example [52].

The flexibility to choose between contact mode, tapping mode, and near field mode allows microcantilever microscopy to be applied to a wide range of materials. Multiplexed microscopy is feasible in a rapid, automated, and parallel fashion using multi-cantilever arrays [182]. Carbon nanotubes have been used as probe tips due to their asperity-like structure and unique properties [139]. It should be noted here

that the term scanning probe microscopy encompasses all the techniques covered in §2.3.1.1 as well as all those covered in this subsection.

2.3.2.2 Thermal/Photothermal

The microcanatilever has proven useful in thermal and photothermal imaging as well. Infrared detection systems in which the microcantilever deflection is a function of the light intensity incident upon the beam have been produced [197]. The beam deflection is due to either a temperature gradient through the thickness of the beam or due to a "bimetallic" effect if the microcantilever is composite in nature (the beam materials need not be metallic though). The bimetallic effect has also been used to detect enthalpy-induced temperature shifts (i.e., phase changes) and to obtain photothermal heating as a function of frequency to provide absorption spectra for certain materials [23, 20].

2.3.2.3 Chemistry/Biology

The microcantilever as applied to the chemistry and biology fields involves the sensing of bonding or conformational change events that occur on one (or both) sides of a microcantilever. Bonding events on both sides will increase the mass and hence change the resonance frequencies of a microcantilever but, assuming equal bonding on both sides, will not cause a static deflection. The term bonding is broad and does not necessarily refer to a *bona fide* chemical bonding event. For example, when monitoring a microcantilever resonance frequency when it is oscillating in air with increasing humidity, one will see the resonance frequency drop due to moisture clinging to the beam surface, hence increasing the mass [43]. Another type of bonding involves functionalization of one (or both) of the microcantilever surface(s) with a half of a DNA sequence followed by immersion of the microcantilever in a fluid solution containing the complementary DNA sequence. The surface stresses and lowered amount of conformational states available to the DNA after hybridization will cause a

beam to deflect [207]. Applications of functionalized microcantilevers are remarkably sensitive, and can determine if a single *E. coli* cell has bonded to the beam [107]. Wu *et al.* show that microcantilevers of different geometries can detect prostate-specific antigens (PSA) in concentrations from 0.2 ng/ml to 60 μg/ml, which includes the clinically relevant range [263]. McKendry *et al.* performed similar experiments with DNA but used eight cantilevers, each coated with a different thiolated probe treatment to allow for multiplexed DNA hybridization detection [175]. By judicious functionalization, microcantilevers can be used to sense the presence and concentration of a variety of liquid- or air-borne substances.

2.3.2.4 Rheology

By immersing microcantilevers in tiny-volume (<1 nL) liquid samples and observing resonance (and resonance shift) behavior, viscosity can be determined [12, 196]. These early efforts were only valid for liquid viscosity determination and required *a priori* knowledge of the liquid density. Therefore, the method was therefore refined to apply to determination of gas viscosity as well, negating the need for *a priori* fluid density knowledge [33].

2.3.2.5 Magnetometery

In magnetic force microscopy (MFM) a magnetic tip is mounted to, or manufactured on, a microcantilever which is scanned in a noncontact fashion above a surface. Beam deflection and resonance usually are obtained using piezoelectrics or optical levers. In static mode, the deflection is monitored resulting in a force image while in dynamic mode the resonance behavior monitoring allows for a force gradient image. Rudnitsky *et al.* used MFM to sense the location of magnetic particles that were tethered to a substrate [215], while others have used MFM to examine the magnetic domain structure of thin films under imposed strain and examine electron spin configurations resulting in a claimed sensitivity of two electron spins [231, 216].

2.3.2.6 Data Storage

A relatively new application of tipped-microcantilevers is in the field of data storage. The tip is scanned over a polymeric film and at desired locations it is heated (usually by subjecting it to a bias voltage), pressed in to the polymer film, and removed leaving a small pit impression in the film. In the "write" mode the cantilever makes numerous such pits at certain locations to define the zeros and ones which define a data set [152]. In "read" mode, the pits are scanned over, basically using the cantilever as an AFM [47]. Finally, in "erase" mode, the pits are produced very close to each other, and this results in leaving behind a polymer film surface that is only mildly disturbed from the initial flat state, a surface undisturbed enough so that it can be "rewritten" upon [25]. More recent work has shown that this technique may be capable of storage densities one or even more orders of magnitude larger than the current technology of magnetic-based storage. [254].

2.4 Previous Work in Microcantilever Characterization

The previous section showed the ubiquitous nature of microcantilevers as sensors, however, before being feasible for such applications, the mechanical characteristics of the microcantilevers must be determined and this section describes just that– specifically, the techniques available to determine the stiffness and resonance frequencies (fundamental and higher modes) of microcantilevers are covered qualitatively. In Chapter 3, a subset of the approaches described here are rigorously defined and finally compared to the experimental results in Chapter 5.

2.4.1 Mechanics-based Methods as Applied to Microcantilevers

As conventional engineering mechanics approaches are based solely upon beam geometries and material properties, they are entirely non-empirical and will be discussed

first with the description of the empirical methods following.

2.4.1.1 Conventional Approaches

A common albeit rudimentary approach to estimate the stiffness, k,[10] of a microcantilever under end loading conditions is to employ Euler-Bernoulli (EB) beam theory. This is a standard engineering approach and, if the assumptions of the theory are satisfied, gives reasonable agreement with measured values. One can appeal to another engineering mechanics approach to predict the ith mode resonant frequency (f_i) of a microcantilever, namely the method of assumed modes, which also shows reasonable agreement to measured values. As these two approaches are used extensively in this work, the mathematics are left until Chapter 3.

2.4.1.2 Length Scale Dependence

While the rudimentary theories just discussed (EB beam theory and the method of assumed modes) do match experiment in many situations, both assume the constitutive model has no length scale dependence (e.g., Hooke's Law). This assumption works well for macro-scale structures but it is known that experimentally some structures show increasing resistance to certain deformation modes as length scales decrease, a phenomenon which is neglected by the Hooke's Law-type constitutive formulation. This is a main area of theoretical investigation for this work, and the mathematical details are left until Chapter 3.

2.4.2 AFM-based Static Methods

Attention now turns to AFM-based microcantilever characterization, all of which involve one of the microcantilever measurement techniques discussed in §2.3.1, usually the optical lever. The static methods only determine the microcantilever stiffness (in many microcantilever sensing applications the resonant frequency is unnecessary).

[10]Qualitatively, the stiffness here quantifies the amount of deflection a microcantilever will experience in the thickness direction when subjected to a force in that direction.

One of the first of the static methods employed was in the work of Senden *et al.*, which determined the spring constant by measuring the static deflection of a silicon-nitride microcantilever with an added end mass (tungsten spheres 10-50 μm in diameter) using an AFM [226]. Stiffness values for the cantilevers showed significant variation from both the manufacturer-supplied values and those obtained by other researchers (for cantilevers of the same model and from the same manufacturer). A similar static measurement technique was employed by Li *et al.*, which involved gluing 2 μm diameter polystyrene spheres to microcantilevers and measuring the deflection caused by the interaction between the PS sphere glued to the beam and an identical PS sphere fixed to a mica surface [140]. Uncertainties in the measured attraction forces were on the same order of magnitude as the forces themselves indicating that this method is not of the caliber necessary for accurate microcantilever characterization. Tortonese and Kirk introduced yet another static method which involves pressing the test beam against a reference microcantilever and measuring the deflections of the test beam with the optical lever method [246]. Results were mixed showing an average error of 16% but maximum errors over 100% in some cases.

2.4.3 AFM-based Dynamic Methods

Dynamic methods, oddly enough, measure the dynamic behavior of a microcantilever and use the data to find both beam stiffness and resonance frequencies. The approach of Cleveland *et al.* measures the fundamental resonant frequency both before and after adding mass(es) to the beams in the form of tungsten spheres (roughly 20 μm in diameter) and employ mathematical modeling to derive the beam stiffness [50]. This technique is appealing because it allows for multiple data points to be obtained from the same beam (by adding different masses) and this allowed a determination of stiffness values in one instance to roughly 0.031 ± 0.001 N/m.[11] While the method

[11] In theory, a plot of added mass versus $(2\pi f_1)^{-1}$ has a slope equal to the beam stiffness.

of Cleveland *et al.* is highly accurate, it is very tedious and time consuming to acquire multiple points for a single cantilever. In addition, excessive handling of the beams can cause damage or even destruction. Therefore, a method that requires no invasive (i.e., mass adding) steps would be advantageous because it would eliminate the large time requirements and possibility of beam destruction inherent in the static and dynamic methods.

Partially in an effort to remedy these limitations, methods were developed which involve time-history measurement of beam deflections caused by Brownian motion of the fluid engulfing the microcantilever (e.g., thermal spectra techniques). Fundamental work was done by Hutter and Bechoefer who assumed that a microcantilever vibrating in a fluid could be described adequately by a simple harmonic oscillator (SHO) [105]. An analytic form is fit to the thermal spectra data, yielding the resonance frequency, and statistical mechanics equate the mean value of any harmonic energy term to the thermal energy (i.e., the equipartition theorem), allowing for stiffness determination. The work of Hutter and Bechoefer requires that the actual deflection of the microcantilever be known, which is not simple to determine using an optical lever. Sader's method [219, 217, 220] also fits an analytic form to thermal spectra data (hence obtaining f_1) but it eliminates the need for calculation of the actual cantilever deflection by looking to fluid mechanics principles. As both methods discussed in this paragraph are treated mathematically in Chapter 3 and the experimental details are covered in Chapter 4, no further coverage is provided here. Rather, attention is turned to static techniques, one of which plays a central role in this dissertation.

2.4.4 Non-AFM-based Static Methods

The non-AFM-based static methods involve deflecting the end of a microcantilever and measuring the applied force as a function of displacement. The slope of applied

force versus displacement gives the beam stiffness (resonance frequency information is not tenable). Usually, experimental equipment from the fields of tribology and nanoindentation are applied. One example of this was the work of Holbery *et al.* who employed a nanoindenter in conjunction with a capacitive displacement transducer interfaced to an AFM [100]. The results were promising with a claimed accuracy of less than 10% (based upon manufacturer-supplied data), showing that this technique, while rather complicated and in need of two expensive machines (an AFM and a nanoindenter), is likely a valid means to characterize microcantilevers. Others have employed the nanoindenter technique to measure stiffness of fixed-fixed microbeam structures and showed reasonable agreement with theory [72]. This concludes the discussion on the different microcantilver characterization techniques and attention now turns to computer simulation techniques.

2.5 Previous Work in Computer Simulation

As a goal of this dissertation involves simulating the microcantilever, this section qualitatively details the general approaches at this type of simulation. The different available simulation techniques are described briefly and qualitatively in this section, with a detailed treatment of the techniques employed for this dissertation being left until Chapter 3. The general scheme of this section is to start with small-scale (spatial) simulations (i.e., *ab initio* or first principles techniques), and progress to large-scale (spatial) simulation approaches (i.e., finite differences and finite elements).

2.5.1 Quantum Mechanics: *Ab Initio*

Ideally, one would like to examine the electronic distribution of each atom in the material involved in a simulation, solve the Schrödinger equation for the system, and back out the desired parameters. Unfortunately, this is not possible for polyelectronic systems and the penultimate approach is to use an approximation. *Ab initio* ("first principles" or "from the beginning") methods do just that by using an approximation

to the wave functions to compute the electronic distribution in each molecule. The basic idea is to assume that each electron in the system can be thought of as moving through an electrostatic field due to the nuclei and remaining electrons. By relating the electronic configuration to the system's energy, other parameters such as forces and velocities become tenable. While quantum theory-based *ab initio* techniques yield results that agree with experiment to measurement uncertainty, the scales feasible for modeling with today's computing power is on the order of 100,000 atoms, which is a very small volume of material [202]. *Ab initio* approaches have modeled vacancy ordering in TiC_x, concentration dependence of the electric conductivity of NaSn alloys, and the hydrolysis of methyl chloride [205, 115, 265]. Unfortunately, this size scale of modeling is almost useless (e.g., due to the inability to model the defects and interfacial structure present in real materials), in an engineering sense (although quite valuable to the materials scientist or computational chemist) and other methods have been developed to increase the feasible spatial-scale of computer simulation.

2.5.2 Molecular Scale: Molecular Dynamics

Molecular dynamics (MD) simulations accomplish this spatial-scale increase by replacing the electron wave functions by effective forces, hence reducing the computing time necessary for a simulation as compared to *ab initio* methods. In MD, each atom is treated as a point mass particle located at the center of the atom nucleus. The steps for a MD simulations are to set up an initial configuration (corresponding to the density, geometry, size, and crystal structure of the actual material) for the group of atoms to be simulated, prescribe an initial velocity vector for each atom, choose an interatomic field that gives the forces acting on the atoms as a function of relative position, and apply Newton's law to each atom [i.e., $\mathbf{F} = d(m\mathbf{v})/dt$]. As the force acting on each atom is known (from the interatomic potential), the acceleration, velocity, and position can be calculated at each time step, and iteration allows for time

progression. Proper setup of the initial conditions can be difficult (e.g., polymeric materials) and the time steps for this technique are on the order of femtoseconds (1×10^{-15} seconds) so the computing time for MD simulations can be prohibitively long. Nonetheless, MD has been used to simulate both contact and non-contact atomic force microscopy processes, liquid (water) motion, and vibrational modes of solids, to name a few applications [251, 74, 129, 64].

2.5.3 Macro Scale: Continuum Modeling

Continuum modeling techniques use continuum relations, (e.g., a Hooke's law constitutive model) which inherently do not include molecular-scale events. However, the techniques could, with the proper considerations (e.g., mesh development and element type), simulate molecular scale events, although this is quite rare. The main advantage of these techniques with relation to this work is that they allow simulation of a much larger spatial dimension with acceptable computation times, at the expense of a "less accurate" (theoretically) result than would be given by the molecular-scale methods previously discussed. Nonetheless, results from the continuum-scale methods have been shown to agree very well with experiment in many circumstances.

The first three methods discussed take advantage of the fact that many engineering problems (i.e., elasticity, thermal, and electrostatic problems) can be described by governing equations (usually partial differential equations) that must be satisfied on the interior of a region and boundary conditions that must be satisfied on the boundary of that region. The last method (finite volume method) realizes that certain conservation laws (e.g., mass, momentum, and energy) appear often in engineering problems and formulate approximation techniques using this fact.

2.5.3.1 Finite Difference Method (FD)

Finite differences are rudimentary numerical approaches used to solve partial differential equations (PDEs), which commonly manifest themselves in numerous fields

of science. The usual approach to derive a finite difference operator is to employ a Taylor's series expansion of a function and then truncate the series after a given number of terms. Clever addition and subtraction of multiple Taylor's series allow one to approximate the PDEs by evaluating the function at discrete grid points. The geometric domain of the problem is broken up into a discrete number of these points and the finite difference formulas are applied at each to obtain a set of equations, which are usually solved via matrix algebra. While finite differences can solve problems of arbitrary scale (simply by choosing a finer mesh), this has not been done as the techniques of §2.5.1 and §2.5.2 are superior.

2.5.3.2 Finite Element Method (FEM)

The finite element method has its roots in the energy method approaches to mechanics and is based on a partial differential equation formulation.[12] Most finite element analyses are approximations to partial differential governing equations via piecewise application of the Rayleigh-Ritz method, which assumes a functional form for the primary field of simulation (e.g., the varaible(s) in the governing PDE) abiding by certain rules (e.g., satisfaction of boundary conditions, completeness, linear independence) that minimizes the potential energy of the system via the calculus of variations to formulate a set of matrix equations that are solved to determine the desired parameters. The approach can be generalized and applied to problems outside of structural mechanics (i.e., not using Rayleigh-Ritz methods), so long as there is some minimization (or maximization) functional that exists or some type of goal to be satisfied (e.g., weighted residual methods, Lagrangian multiplier techniques, and penalty function methods) [209].

The Rayleigh-Ritz structural finite element method differs from a conventional

[12]Finite element equations can be set up via a governing PDE or by a weak formulation which, in the context of solid mechanics, is an energy statement– the important idea here is that, regardless of the formulation approach, PDEs are involved.

approach in that, instead of assuming a functional form valid over the entire domain, it breaks the domain up into smaller, *finite elements*, assumes a functional form over each of them, and enforces interelement conditions such as C_0 and higher continuity, for example. Some advantages of the finite element method are that it can handle very complicated geometries (where closed-form solutions are untenable), is amenable to computer calculation, and changing of the boundary conditions requires only minimal recalculation once the matrix equations of the method are set up. The finite element approach was employed first by Courant in terms of linear elastic equilibrium and vibration problems [54], and later used by Clough in his seminal paper on finite element analysis (FEA) as applied to plane stress analysis [51]. With the rise in computing power, the finite element method has become one of the most widely used engineering tools.

2.5.3.3 Boundary Element Method (BEM)

The boundary element method is another technique used to solve partial differential equations with the advantage that the dimension of the solution space is one less than the dimension of the problem domain (e.g., a 3D spatial problem requires solution on a 2D domain). BEM starts with the same weak formulation as a weighted-residual FEA,[13] and then transforms this integral statement of n dimensions to one of $n-1$ dimensions (think of transforming a volume integral to a surface integral). This reduction of dimension can lead to reduced computing times as compared to other methods, but is not useful in highly nonlinear problems. Additionally, the matrix equations formed by the BEM are not sparsely populated as they usually are in other methods (especially FEA).

[13]This "weak" formulation states that: $\int_\Omega f(\mathbf{x})w(\mathbf{x})d\Omega = 0$ where Ω is the domain of interest, $f(\mathbf{x})$ is the governing function, $\mathbf{x}$ is a vector describing the problem variables position, and $w(\mathbf{x})$ is a weight function.

2.5.3.4 Finite Volume Method (FVM)

Similar to FEA, the finite volume method also breaks the domain of simulation into smaller regions (e.g., *finite volumes* with nodes at the center of each volume usually) and enforces some "law" that must be obeyed (e.g., conservation of mass) along with intervolume constraints (e.g., mass balances for a mass-conservative system). However, the FVM employs an integral conservation law whereas FEA and FD start with partial differential equations. This integral-based form lends itself naturally to fluid dynamics problems and this is indeed the field where the FVM enjoys the most usage. While the technique is applied easily to complex geometries, numerically-induced advection can be a problem if intervolume interpolation is not carried out carefully.

2.5.3.5 Comparison of Continuum Modeling Methods

This section simply presents Table 1, showing the advantages and disadvantages of the various continuum modeling methods. It should be noted that the equations approximated here are assumed to be on a geometry precluding the possibility of a closed-form solution (i.e., an approximation scheme is necessary), which is the case for all but very simple geometries.

2.6 Summary

This chapter gave a rather extensive review of microfabrication techniques, the discussion of which funneled in to the methods used to make microcantilever parts. Next, the operational techniques and examples of microcantilever sensing systems were covered. This led into the need for and description of microcantilever characterization (via theory and experiment). Chapter 3 gives mathematical rigor to a subset of the topics covered in this chapter– topics implemented experimentally on microcantilever parts, the results of which are discussed in Chapter 5.

Table 1: Comparison of simulation methods.

METHOD	ADVANTAGES	DISADVANTAGES
FINITE DIFFERENCE METHOD (FM)	• Simple to code by hand- could be a good starting point • Effective on structured grids (i.e., equally spaced nodes)	• Conservation not enforced unless dealt with specifically • Restricted to simple geometries • Sensitive to boundary condition changes • Inherent errors due to truncated terms in Taylor's series
FINITE ELEMENT METHOD (FEM)	• Feasible with complex geometries • Insensitive to boundary condition changes • Ability to automatically, selectively refine mesh	• Numerically induced advection in certain fluid flow problems • Solution is sensitive to mesh density- experience required to construct mesh and interpret results
BOUNDARY ELEMENT METHODS (BEM)	• Discretization of boundary only • Simple and accurate modeling of problems involving infinite and semi-infinite domains • Feasible with complex geometries	• Non-symmetric, fully populated system of equations • Treatment of inhomogeneous and non-linear problems • Practical application relatively recent, not as well known as FEM among users
FINITE VOLUME METHOD (FVM)	• Conservation is implicitly enforced • Feasible with complex geometries	• Certain interpolation approaches may lead to numerical errors • Numerically induced advection in certain fluid flow problems

CHAPTER III

THEORETICAL FRAMEWORK

This chapter opens with many of the available continuum elasticity theories, some of which are used in the mechanical characterization of microcantielevers. This characterization follows, detailing the relevant previous works and the advancements of these works developed for this research. A brief mathematical introduction to optimization is presented, followed by simulation details germane to this work. The theoretical work of this chapter lays the framework for Chapter 4 which details how this theoretical work was investigated experimentally. Chapter 5 then compares the experimental results, obtained using the techniques of Chapter 4, to the theoretical predictions of this chapter.

3.1 Overview of Continuum Theories

Conventional elasticity (e.g., Hooke's law) models have been used widely in the analysis of deformable bodies undergoing small strains. While these theories are the most well known, other constitutive models exist, all of which are self-consistent. The task then is to select a model which is most appropriate for a given problem, and this can entail a comparison of theory to experiment for validation. This section details some of the available constitutive models, and shows that some predict a dependence of resistance to deformation upon the size of the object being deformed. As the microcantilever structures examined in this work are micron scale, it will be seen that a simple constitutive model is insufficient to characterize the stiffness of these structures adequately, and a more advanced constitutive model is derived.

Here it is noted that the continuum theories do not actually account for microstructure (as do, for example, the molecular dynamics simulations of §2.5.2) but attempt to include microstructural effects in an average sense. Nonetheless, as even micron-scale parts consist of a large number of molecules, some of the continuum theories to be discussed have shown good agreement with experiment. The first two theories do not have length-scale dependence while the final five do. Also, the discussion is limited to linear, isotropic, and elastic models.

3.1.1 Uniconstant Elasticity

The so-called uniconstant elastic theory was presented to the Paris Academy by Navier in 1821 [151], with the form of Equation 1 (summation notation is used freely)

$$\sigma_{ij} = 2\mu\epsilon_{ij} + \mu\epsilon_{kk}\delta_{ij} \tag{1}$$

where δ_{ij} is the Kronecker delta,[1] ϵ_{ij} are the components of the infinitesimal strain tensor,[2] σ_{ij} are the components of the Cauchy stress tensor, and μ is the shear modulus. This is a rudimentary model based upon interatomic potentials and highly idealized molecular structure and deformation. In this form, the law receives little usage, but is an important starting point for the classical theory of elasticity. Note that there is no length scale dependence.

3.1.2 Classical Elasticity

An inadequate molecular model led Navier to use the same constant (i.e., μ) in Equation 1, but this deficiency subsequently was corrected by Cauchy in 1823, leading to Equation 2

$$\sigma_{ij} = 2\mu\epsilon_{ij} + \lambda\epsilon_{kk}\delta_{ij} \tag{2}$$

[1]The Kronecker delta, δ_{ij} is defined as equal to 1 when $i = j$ and 0 when $i \neq j$.

[2]$\epsilon_{ij} = 1/2[\partial u_i/\partial x_j + \partial u_j/\partial x_i]$ where u_i and x_i are the ith component of the displacement vector and ith coordinate direction, respectively.

where λ is a Lamé constant and, again, μ is the shear modulus.[3] While Equation 2 holds very well at the macroscale, it was realized long ago that additional parameters are necessary to relate stress and strain at the microscale [247, 181, 124, 178, 179].

3.1.3 Nonlocal Elasticity

The nonlocal theory of elasticity proposes that the stress at a point is due not only to the strain at that point but also due to the strain in a small neighborhood around that point. The constitutive relations now involve an integral form with a kernel function, given as Equation 3

$$\sigma_{ij}(\mathbf{x}) = \int_V \left[\lambda\left(|\mathbf{x}' - \mathbf{x}|\right)\epsilon_{kk}\left(\mathbf{x}'\right)\delta_{ij} + 2\mu\left(|\mathbf{x}' - \mathbf{x}|\right)\epsilon_{ij}\right] dV\left(\mathbf{x}'\right) \tag{3}$$

where $\mathbf{x}$ is the local position and $\mathbf{x}'$ is a position vector from that point defining the volume neighborhood, V [70]. Different integral forms have been formulated, but the important point to notice is that one must define a neighborhood in some fashion by choosing $\mathbf{x}'$ (or some restraint function, which itself is a function of $\mathbf{x}'$) [189].

3.1.4 Void Elasticity

Void elasticity theory incorporates a volume change as a kinematic variable in addition to strain, leading to the model described by Equations 4 through 6

$$\sigma_{ij} = 2\mu\epsilon_{ij} + \lambda\epsilon_{kk}\delta_{ij} + \beta\vartheta\delta_{ij} \tag{4}$$

$$h_k = \alpha\vartheta_k \tag{5}$$

$$g = -\xi\vartheta - \beta\epsilon_{kk} \tag{6}$$

where ϑ is the change in volume fraction of the material which can be thought of as a dilatation of the points of the continuum, h_k are the components of the stress traction vector, g is the equilibriated body force, λ and μ are the Lamé constants and, β, α, and ξ are material constants.

[3] Equation 2 is just a form of Hooke's law, which can be expressed in many forms using only two independent elastic constants– the Lamé form is just one of these.

3.1.5 Microstructure (micromorphic) Elasticity

In microstructure (due to Mindlin [180]) and micromorphic (due to Eringen [70]) elasticity, the general idea is that the points of the continuum are attached with a microstructure of finite size and can deform macroscopically producing the classical elasticity case as well as microstructurally producing a length scale dependence. For the isotropic case, the theories yield 18 independent material constants. The mathematics are unnecessary as the theory is not employed in this form, but it should be noted that micropolar (discussed next), classical, and uniconstant elasticity are special cases.

3.1.6 Micropolar Elasticity

The brothers Cosserat introduced their couple stress theory in 1909, taking into account not only local translational motion of a point in the material body, but also the local rotation of that point [53], yielding the constitutive model described by Equations 7 and 8.

$$\sigma_{ij} = (2\mu + \kappa)\epsilon_{ij} + \lambda\epsilon_{kk}\delta_{ij} + \kappa e_{ijm}(w_m - \phi_m) \tag{7}$$

$$m_{ij} = \alpha\phi_{r,r}\delta_{ij} + \beta\phi_{i,j} + \gamma\phi_{j,i} \tag{8}$$

Here commas indicate partial differentiation with respect to the coordinates (i.e., $\xi_{,i} = \partial\xi/\partial x_i$), m_{ij} is the couple stress (torque per unit area), ϕ is the microrotation at a given position in the deformed body, w is the macrorotation of conventional continuum mechanics[4] $\mathbf{w} = \frac{1}{2}\nabla\times\mathbf{u}$, and e_{ijm} is the Levi-Civita (or alternating) tensor.[5] The remaining undefined parameters (i.e., α, β, γ, and κ) are material constants. The idea of a couple stress is due to Voight [255] but was first rigorously defined by the Cosserats as Equations 7 and 8. By requiring things such as antisymmetry

[4]The macrorotation applies to the *entire* body, like spinning a top, while the microrotation refers to the rotation of a triad of vectors from initial to deformed states at a *single material point.*

[5]e_{ijm} is defined to equal one for a cyclic order of ijm (i.e., 123, 231, and 312), minus one for an acyclic order of ijm (i.e., 132, 321, and 213), and zero otherwise.

of the microrotation tensor (the last term in Equation 7) and stress moment tensor (m_{ij}), Eringen and Suhubi obtained the micropolar elasticity theory whose governing equations are the same as Equations 7 and 8, except that 2μ and $\kappa e_{ijm}(w_m - \phi_m)$ are replaced by μ and $\mu\epsilon_{ji}$ in Equation 7 [84]. A cantilevered plate bending stiffness is derived in this work using the micropolar theory and is compared to an analogous expression derived by other researchers using a strain gradient approach, which is discussed next.

3.1.7 Strain Gradient Theory

Strain gradient theory, due to Fleck and Hutchinson (and based on Mindlin's work [181, 178, 179]) is introduced here as other researchers have derived a length-scale dependent bending stiffness for plates using this theory, and this work derives the same result using micropolar theory as a basis. Strain gradient theory is very similar to the couple stress theories in that it uses the second order deformation gradients (which lead to the $\phi_{s,r}$ of Equation 8) but decomposes these gradients into two independent parts, namely the stretch gradient tensor and the rotation gradient tensor [79, 80]. Unfortunately, one was stuck with only two equilibrium equations at this point (i.e., conservation of momentum and moment of momentum) and higher order equilibrium (e.g., moment of moment of momentum) was ignored. Yang *et al.* introduced the concept of a representative volume element, which allowed imposition of a higher order equilibrium condition [266]. This additional equilibrium condition is discussed next in order to introduce a length scale-dependent bending stiffness in §3.3.1.2.

3.1.7.1 Higher Order Equilibrium Constraint

In conventional mechanics approaches, a material body is treated as a volume consisting of an infinite number of material particles. The two conventional equilibrium equations using couple stress theory are obtained by equating the forces and moments of forces acting on a body equal to zero, as a direct consequence of Newton's 2$^{\text{nd}}$ Law.

These two balances are given as Equations 9 and 10

$$\int_{\partial V} \mathbf{t} dS + \int_V \mathbf{f} dV = \mathbf{0} \Rightarrow \int_{\partial V} \sigma_{ji} n_j dS + \int_V f_i dV = \int_v (\sigma_{ji,j} + f_i) dV = 0 \Rightarrow \sigma_{ji,j} + f_i = 0 \tag{9}$$

$$\int_{\partial V} (\mathbf{x} \times \mathbf{t} + \mathbf{m} \cdot \mathbf{n}) dS + \int_V (\mathbf{x} \times \mathbf{f} + \mathbf{l}) dV = \mathbf{0} \Rightarrow$$

$$\int_{\partial V} (e_{ijk} x_j \sigma_{ks} + m_{is}) n_s dS + \int_V (e_{ijk} x_j f_k + l_i) dV = 0 \Rightarrow m_{ij,j} + l_i - e_{ijk} \sigma_{jk} = 0 \tag{10}$$

where $\mathbf{f}$ is a body force vector, $\mathbf{l}$ is a body couple, $\mathbf{n}$ is a unit normal, $\mathbf{x}$ is a position vector, $\mathbf{t} = \sigma^T \cdot \mathbf{n}$ is the traction vector, V is the volume of integration, ∂V is the surface of integration, and $\mathbf{0}$ is a zero vector of proper dimension. Note that Equation 10 does not imply that $\sigma_{ij} = \sigma_{ji}$ as it does in conventional elasticity, and Equation 9 is used in to progress to the final form of Equation 10.

An additional equilibrium condition has been proposed, and it is, somewhat intuitively, that the moment of moments of momentum be equal to zero, given as Equation 11 [133]

$$\int_{\partial V} \mathbf{x} \times (\mathbf{x} \times \mathbf{t} + \mathbf{m} \cdot \mathbf{n}) dS + \int_V \mathbf{x} \times (\mathbf{x} \times \mathbf{f} + \mathbf{l}) dV = \mathbf{0} \Rightarrow$$

$$\int_{\partial V} (\mathbf{x} \times \mathbf{m} \cdot \mathbf{n}) dS + \int_V \mathbf{x} \times (\mathbf{l} - \mathbf{e}{:}\sigma) dV = \mathbf{0} \Rightarrow$$

$$\int_V [\mathbf{x} \times (\mathbf{l} - \mathbf{e}{:}\sigma + \nabla \cdot \mathbf{m}) - \mathbf{e}{:}\mathbf{m}] dV = \mathbf{0} \Rightarrow e_{ijk} m_{jk} = 0 \Rightarrow m_{ij} = m_{ji} \tag{11}$$

where $\mathbf{e}{:}\sigma = e_{ijk} \sigma_{ij} \hat{\mathbf{e}}_k$ where $\hat{\mathbf{e}}_k$ is a unit vector in the kth direction, and similarly for $\mathbf{e}{:}\mathbf{m}$. The higher order equilibrium constraint implies that the couple stress tensor (i.e., $\mathbf{m}$) is symmetric but the Cauchy stress (i.e., σ) is not. However, one sees that if the couple stresses and body couples are zero in Equation 10, this implies that $e_{ijk} \sigma_{jk} = 0$ or that the Cauchy stress is symmetric, as in isotropic classical elasticity. It should be noted that Equations 9 and 10 can be manipulated to give the same form of the original couple stress theory (with the notation of [124]), but the moment of the moment balance (i.e., Equation 11) is not a part of the original theory [266].

3.2 Why not just Hooke's Law?

The source of material behavior is due to the electronic interactions which are neglected by the continuum theories discussed here. The uniconstant theory (see §3.1) was developed assuming a "perfect" grid of atoms that deformed in a"perfect" manner, which is obviously untrue (e.g., the flaws present in real materials). It has been proposed that the more advanced continuum theories (i.e., those with length scale dependence of §3.1) account for microstructural behavior (such as propagation of interatomic forces past a single atomic spacing) better than the uniconstant and classical elasticity theories, hence the better agreement with experimental data at smaller length scales (where the length scale influences become more significant) [127]. As the experimental evidence of previous works (and this work as discussed in Chapter 5) suggests that smaller structures with certain microstructures are stiffer than larger ones, then the microcantilever sensor experimental evidence, if rooted in the length scale-free formulations, could be incorrect. Employing the elasticity theories of the previous section, along with other techniques of engineering mechanics, allow equations to be developed which predict microcantilever behavior and how length scales will effect such behavior (e.g., stiffness and resonance frequencies), which is now discussed after a brief review of microcantilever experimental modes.

3.3 Microcantilever Experimental Modes

As briefly covered in §2.3.1, microcantilever sensor systems can be operated in two modes– one which measures static deflection and another which measures the resonance behavior of the beam. This section details the previous theoretical and experimental techniques used in both areas, coverage which is necessary as the new results of this dissertation are closely related. The section opens with the static-relevant behavior (e.g., stiffness and surface stress effects on bending) and then covers the

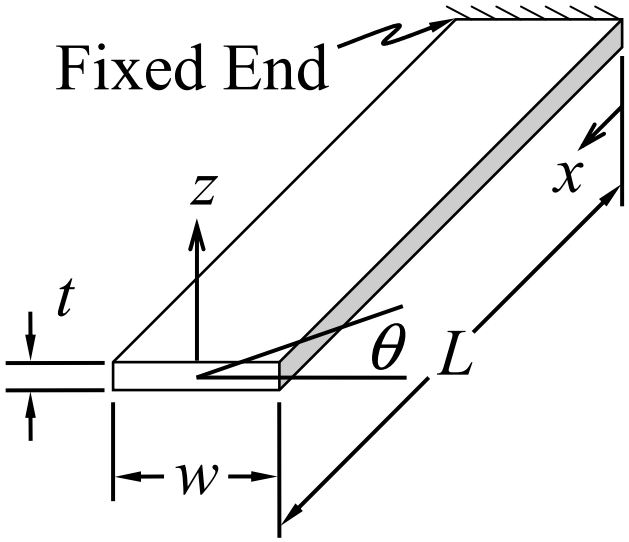

Figure 8: Microcantilever geometry and nomenclature, z denotes the deflection in the thickness direction as a function of position along the beam length and time [i.e., $z(x,T)$] and does not indicate the origin of the coordinate system in this figure.

dynamic-relevant modeling (e.g., mass and surface stress effects on resonance frequency).

3.3.1 Theoretical Determination of Microcantilever Stiffness

The microcantilever stiffness is a parameter that predicts how much the end of a microcantilever will deflect when subjected to a unit load applied at the end and mid-width of the beam, in the direction of the beam thickness. The discussion proceeds from the elementary (e.g., beam theory) to the more complex (e.g., couple stress and plate theory) to cover the existing work and ultimately derive a new stiffness parameter. Parallels are drawn between the elementary and new theories, so inclusion of the rudimentary theories makes the discussion much more accessible. Figure 8 shows a microcantilever beam with the nomenclature that will be used subsequently.

3.3.1.1 Euler-Bernoulli Beam Theory-based Stiffness

The assumptions inherent in Euler-Bernoulli (a.k.a. classical or EB) beam theory based upon the work of Da Vinci, Galileo, Bernoulli, etc.– are small deflections (so Hooke's Law can be applied), small slopes (to allow for curvature approximation) and that normals (lines $\perp$ to the undeformed beam's neutral midplane, which is $\parallel$ to the top and bottom surface of the undeformed beam) remain straight, unstretched, and normal to the neutral plane after deformation (to neglect shear effects), as shown in the deformed element in Figure 9. Under these assumptions (the validity of which are verified in §3.3.1.6), an expression relating the transverse beam deflection to the beam geometry, material, and end loading is desired. To obtain this, one first starts with a force and moment balance of a microcantilever beam element (as shown in Figure 9) to arrive at Equations 12 and 13

$$\Sigma F_y = 0 : V - f(x_0)\Delta x - (V + \Delta V) = 0 \tag{12}$$

$$\Sigma M_B(+\circlearrowleft) = 0 : -V\delta x - M + (M + \Delta M) + (f_0 \Delta x)\frac{\Delta x}{2} \tag{13}$$

where $x_0 \in [x, x + \Delta x]$. Dividing both of these equations by Δx and taking the limit as $\Delta x \to 0$ gives Equations 14 and 15, which lead to Equation 16.

$$\frac{dV}{dx} = -f(x) \tag{14}$$

$$\frac{dM}{dx} = V \tag{15}$$

$$\frac{d^2M}{dx^2} = -f(x) \tag{16}$$

Now we look to kinematics and see that the axial strain is given by Equation 17

$$\epsilon_x = \frac{A'B' - AB}{AB} = \frac{(\kappa - z)d\theta}{\kappa d\theta} - 1 = -\frac{z}{\kappa} = -z\frac{d^2u_z/dx^2}{\left[1 + (du_z/dx)^2\right]^{3/2}} \approx -z\frac{d^2u_z}{dx^2} \tag{17}$$

where u_z is the transverse beam displacement and $d\theta$ is the angle subtended by the lines $A'C'$ and $B'D'$ in Figure 9. We can now recall that $\sigma_x = E\epsilon_x$ and use this along

with an equilibrium of axial moments to obtain Equation 18, which combined with Equation 16 gives the desired result, Equation 19.

$$M = -\int_A \sigma_x z dA = E\frac{d^2u_z}{dx^2}\int_A z^2 dA = EI\frac{d^2u_z}{dx^2} \tag{18}$$

$$EI\frac{d^4u_z}{dx^4} = -f(x) = 0 \tag{19}$$

Here $f(x) = 0$ because we are considering a point load at the end of the beam only. Equation 19 implies that the transverse beam deflection will take the form of a cubic polynomial. We know that the slope and deflection are zero at $x = 0$ so the constant term and the coefficient of the first order term in the polynomial are zero. We also know that the moment acting on the beam at $x = L$ is zero (i.e., $d^2u_z/dx^2 = 0$ at $x = L$), so the coefficient of the second order term is zero, leaving the final boundary condition, specifically $EId^3u_z/dx^3 = P$ at $x = L$ yielding Equation 20.

$$u_z(x) = \frac{PL}{EI}\left(\frac{x^2}{2} - \frac{x^3}{6L}\right) \tag{20}$$

Finally, we arrive at the stiffness equation by solving Equation 20 for P and the differentiating with respect to u_z and evaluating the result at $x = L$, giving the final form of the stiffness expression, Equation 21 (recall that $k = dP/dx$ in this scenario)

$$k = \frac{3EI}{\varphi L^3} \tag{21}$$

where E is the beam material elastic modulus, L is the beam length, I is the second moment of the beam cross sectional area (which is $wt^3/12$ for a rectangular beam where w and t are the width and thickness, respectively), and φ accounts for the stress state ($\varphi = 1$ for plane stress and $\varphi = 1 - \nu^2$ for plane strain[6]).[7]

[6]From Hooke's Law $\epsilon_x = E^{-1}(\sigma_x - \nu\sigma_y)$, but from the plane strain assumption $\epsilon_y = 0 = E^{-1}(\sigma_y - \nu\sigma_x) \Rightarrow \sigma_y = \nu\sigma_x \Rightarrow \epsilon_x = E^{-1}(\sigma_x - \nu\sigma_y) = E^{-1}(\sigma_x - \nu^2\sigma_x) \Rightarrow E\epsilon_x(1-\nu^2)^{-1} = \sigma_x$, which, when substituted into Equation 18 makes the use of φ obvious– in this work the geometries of the microcantilevers are those of "plates", or one which would imply a plane strain situation so one should use $\varphi = (1 - \nu^2)$.

[7]A plane stress situation as relevant to this work would be when a structure has a width that is much less than both its length and thickness whereas a plane strain situation is when the thickness is much less than both the width and length– in this work the term "beam" is used interchangeably with microcantilever, and should not be confused to imply a plane stress situation as is sometimes the convention in engineering; the term plate is used exclusively to imply a plane strain situation.

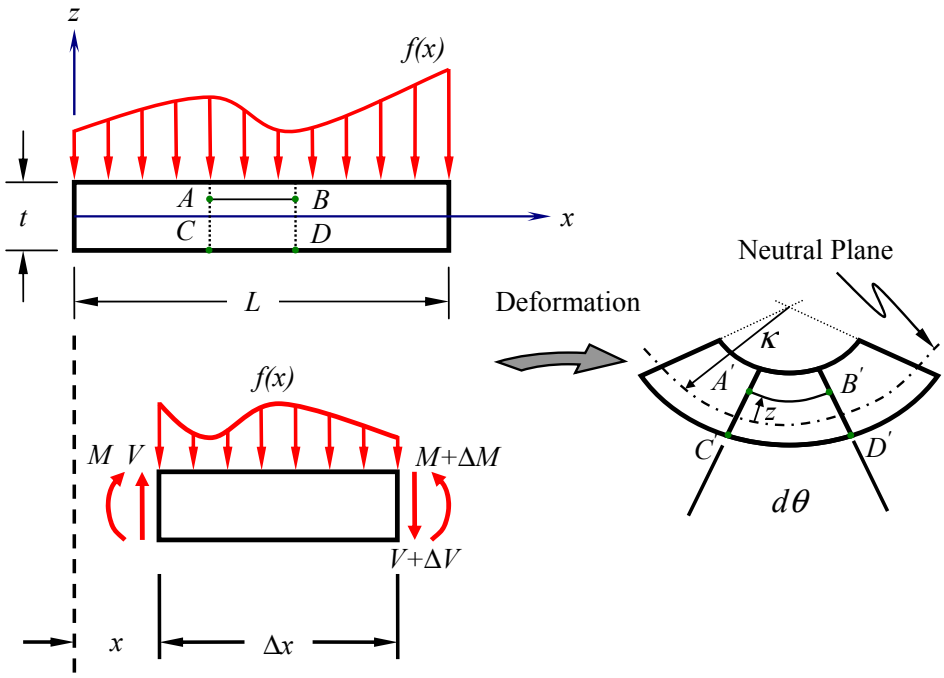

Figure 9: Definition of beam forces and moments, along with beam deformation and geometry – this figure is a plane, parallel to the plane formed by the x and z directions in Figure 8, placed at the mid-width of the beam.

3.3.1.2 Length Scale-Dependent Bending Stiffness– Existing Approach

While the approach of the previous subsection employed classical elasticity, another approach has yielded fruitful results. The additional equilibrium constraint discussed in §3.1.7.1 (i.e., Equation 11) allows for the derivation of four new forms of constitutive equations to describe a strain gradient type material, given as Equations 22 through 25 as shown by the work of Lam *et al.* [133]

$$\sigma_{ij} = \mathcal{K}\epsilon_{kk}\delta_{ij} + 2\mu\epsilon'_{ij} \tag{22}$$

$$p_i = 2\mu l_0^2 \epsilon_{mm,i} \tag{23}$$

$$\tau_{ijk}^{(1)} = 2\mu l_1^2 \eta_{ijk}^{(1)} \tag{24}$$

$$m_{ij}^{s} = 2\mu l_2^2 \chi_{ij}^{s} \tag{25}$$

where $\mathcal{K}$ is the bulk modulus,[8] ϵ'_{ij} is the deviatoric strain,[9] $\eta_{ijk}^{(1)}$ is the so-called deviatoric stretch gradient tensor,[10] χ_{ij}^{s} is the symmetric rotation gradient tensor,[11] and l_0, l_1, and l_2 are the new material length scale parameters.

A cantilevered plate stiffness expression is desired using this more advanced theory (as opposed to classical elasticity), and Lam *et al.* solved this problem using a power series expansion of the beam deflection coupled with the equilibrium relations (i.e., Equations 9, 10, and 11) and the boundary conditions (i.e., zero displacement and slope at the fixed end of the beam, zero moment and force P at the free end) to approximate the end deflection $[u_z(L)]$ due to the end force as shown in Equation 26

$$u_z(L) \approx \frac{4PL^3}{D'wt^3},\ D' = \frac{E}{\varphi}\left[1 + \left(\frac{b_h}{t}\right)^2\right] \tag{26}$$

[8] The bulk elastic properties of a material determine how much it will compress under a given amount of external pressure: $\mathcal{K} = -V(dP/dV) = E/3(1-2\nu)$.

[9] $\epsilon'_{ij} = \epsilon_{ij} - \frac{1}{3}\epsilon_{kk}\delta_{ij}$

[10] $\eta_{ijk}^{(1)} = \frac{1}{3}(\epsilon_{ij,k} + \epsilon_{jk,i} + \epsilon_{ki,j}) - \frac{1}{15}[\delta_{ij}(\epsilon_{mm,k} + 2\epsilon_{mk,m}) + \delta_{jk}(\epsilon_{mm,i} + 2\epsilon_{mi,m}) + \delta_{ki}(\epsilon_{mm,j} + 2\epsilon_{mj,m})]$

[11] $\chi_{ij}^{s} = \frac{1}{2}(e_{imn}\epsilon_{nj,m} + e_{jmn}\epsilon_{ni,m})$

where b_h is a material length scale parameter which is a *material property* of the microcantilever material. This approach gives a length dependent stiffness, Equation 27

$$\hat{k} \approx \frac{Ewt^3}{\varphi 4L^3}\left[1+\left(\frac{b_h}{t}\right)^2\right] = \frac{3EI}{\varphi L^3}\left[1+\left(\frac{b_h}{t}\right)^2\right] \tag{27}$$

where I is the second moment of the cross sectional area of the plate (i.e., the rectangular microcantilever).[12] The bracketed term shows that the stiffness increases as the plate thickness approaches b_h, which is on the order of tens of nanometers to microns for many materials. The conventional neglect of length-scale dependence is obvious now– for macro-scale structures $b_h \ll t$ so the bracketed term in Equation 27 approaches unity. The length scale effects are particularly important for any microcantilever application which uses the classical formula for stiffness calculation (i.e., $k = 3EI/L^3$) as the forces calculated could be inaccurate (recall that force equals deflection multiplied by stiffness). This work derived a length scale dependent stiffness, but used micropolar theory as a basis instead of strain gradient theory (which was used to obtain Equation 27).

3.3.1.3 Length Scale-Dependent Bending Stiffness– New Approach

The length-scale dependent stiffness of this work is derived in a much simpler fashion than Equation 27 [167]. The plate theory, micropolar-based approach of Gauthier yields a moment-curvature relation given as Equation 28 [84]

$$\frac{\hat{M}}{D+\gamma t} = \frac{\partial^2 u_z}{\partial x^2} \tag{28}$$

where $D = Et^3/12(1-\nu^2)$ and $\hat{M}$ is the moment per unit width ($= M/w$) and γ is a material constant from micropolar elasticity (§3.1.6). Gauthier then developed a model for a plate bent solely by a moment at the end, which, while close, is not the desired result for this dissertation, that of a stiffness due to end-loading. Note

[12] $I \equiv \int_A r^2 dA$ where the cross section of the microcantilever is area of integration and r is generic lever arm from the centroid of the area (for linear elastic, isotropic beam bending).

the similarities between Equation 28 and Equation 18– the numerator in each (i.e., $D+\gamma t$ and EI) relates the amount of change in the curvature (i.e., $u_{z,xx}$) that a unit change in the moment (M) will cause, except that Equation 28 is for a plate and has a length-scale dependence due to the more advanced constitutive model chosen (e.g., micropolar elasticity as compared to Hooke's Law of classical elasticity).

The deflection as a function of position along the plate length for a cantilevered plate (subject to end-load P) is determined by assuming that the curvature is small (an assumption justified in §3.3.1.6), substituting $M = P(L-x)$ into Equation 28,[13] and integrating twice to yield Equation 29.

$$u_z(x) = \frac{1}{w(D+\gamma t)}\left(\frac{PLx^2}{2} - \frac{Px^3}{6} + C_1 x + C_2\right) \tag{29}$$

Here the boundary conditions of the cantilevered plate [i.e., $w(0) = w_x(0) = 0$] imply that $C_1 = C_2 = 0$. The quantity of $D+\gamma t$ can be rewritten as $D[1+\hat{b}_h^2 h^{-2}]$.[14] This yields the deflection function of the beam, given as Equation 30.

$$u_z(x) = \frac{P}{wD[1+\hat{b}_h^2 h^{-2}]}\left(\frac{Lx^2}{2} - \frac{x^3}{6}\right) \tag{30}$$

Now the stiffness is determined by solving Equation 30 for P, differentiating with respect to u_z, and evaluating at $x = L$, yielding Equation 31.

$$\tilde{k} = \frac{3wD}{L^3}\left[1+\left(\frac{\hat{b}_h}{t}\right)^2\right] = \frac{Ewt^3}{4L^3(1-\nu^2)}\left[1+\left(\frac{\hat{b}_h}{t}\right)^2\right] \tag{31}$$

Equation 31 is identical to the Equation 26 with $\varphi = 1-\nu^2$, which makes sense as the plate situation is one of plane strain. This derivation is much cleaner than that of Equation 26, which employed a complicated power series expansion of the deflection in terms of the beam thickness. This is not meant to imply that this approach yields an exact solution (indeed there are assumptions listed in the derivation), but

[13] For an end-loaded beam, the moment will vary linearly from PL at $x = 0$ to zero at $x = L$, hence $M = P(L-x)$.

[14] $\hat{b}_h^2 = 12(1-\nu^2)\gamma/E$

it is reassuring that two approaches based on different, albeit related, assumptions (i.e., the strain gradient theory used by Lam *et al.* and the couple stress approach used here) yield nearly identical results. Additionally, a new derivation for a plane stress situation was developed for this work and amounts to setting $(1-\nu^2)=1$ in Equation 31 as expected, however, this *should not* be used for microcantilevers as they are deserved of a plane strain situation. The plane strain situation is a result of the large width of the microcantilever (in comparison to the thickness) restricting the deformation of the material in the width direction; as this extra material is present it is assumed that the strain in the width direction is zero (i.e., a plane strain situation). This point is admittedly overemphasized but only because of the common use of $\varphi=1$ in the microcantilever literature.

3.3.1.4 Length Scale-Dependent Bending Stiffness– Experimental Implications

To experimentally determine the presence (if any) of a length scale dependence, the general idea was to use the nanoindenter (discussed in §4.2.2) to obtain force-deflection data for microcantilevers with a constant stiffness, but with decreasing thicknesses. This rationale is attained from Equation 31, with which one can derive a useful relationship between the transverse force applied to end of a cantilever (F) and the cantilever deflection (δ), given as Equation 32.

$$\underbrace{\tilde{k}=\frac{Ewt^3}{4L^3(1-\nu^2)}\left[1+\left(\frac{\hat{b}_h}{t}\right)^2\right]}_{\text{Equation 31}} \Rightarrow F=\tilde{k}\delta=\delta\ \underbrace{\frac{Ewt^3}{4L^3(1-\nu^2)}}_{k\text{ from Equation 21}}\left[1+\left(\frac{\hat{b}_h}{t}\right)^2\right] \Rightarrow$$

$$F=\delta k\left[1+\left(\frac{\hat{b}_h}{t}\right)^2\right] \tag{32}$$

Recall that k from Equation 21 is the stiffness of a cantilever *without* length scale effcts. Equation 32 shows that if plots are generated for F versus δ from the nanoindenter data, the slope should be equal to $k[1+\hat{b}_h^2 t^{-2}]$. Therefore, if F versus δ plots are generated for multiple beams having *the same* length scale independent stiffness

(k) but *different* thicknesses (t), then regression analysis of the different $F - \delta$ data sets will allow multiple estimations of $\hat{b}_h$. Since k and $\hat{b}_h$ (a material property) are constant, one would expect the slopes of these such plots to increase as the beam thickness decreases. However, if $\hat{b}_h$ is much less than the minimum possible thickness, then the length scale effect may not be observable. It should be noted that the material properties are assumed constant and known, and these assumptions are dealt with in Chapter 5.

3.3.1.5 Length Scale-Dependent Bending Stiffness– Observability?

After all this derivation and discussion of the length scale dependent stiffness, two logical questions arise, (i) how significant is the effect of $\hat{b}_h$ for microcantilevers and, more importantly, (ii) is the length scale effect actually validated by experiment? The answer to (ii) is yes, as will be detailed in Chapter 5. To answer (i) and gauge the theoretical influence of the length scale upon a "generic" microcantilever, representative values were taken to give an equal length scale independent stiffness ($k = 0.6$ N/m) for four different beam geometries, each having a different thickness and plots of force versus deflection were generated, as shown in Figure 10. It is obvious from this figure that if $\hat{b}_h$ for a microcantilever material is on the order of the microcantilever thickness, then the length scale effect could be quite influential. $\hat{b}_h$ for metals (i.e., steel and aluminum) has been shown to be on the order of 10 μm (for a plate with a 50 μm thickness) as has $\hat{b}_h$ for a dense polystyrene foam (plate thickness 1 mm), so the length scale effect could be relevant for polymeric and silicon microcantilevers as well as their thicknesses are often on the order of 1 μm [67, 132].

3.3.1.6 Validation of Assumptions Employed

The theories of §3.3.1.2 through §3.3.1.4 employ some assumptions, which are now justified. The first is the neglect of any shear deformation (e.g., Timoshenko-type theories), but, as pointed out by other authors, the shear deformation effects are less

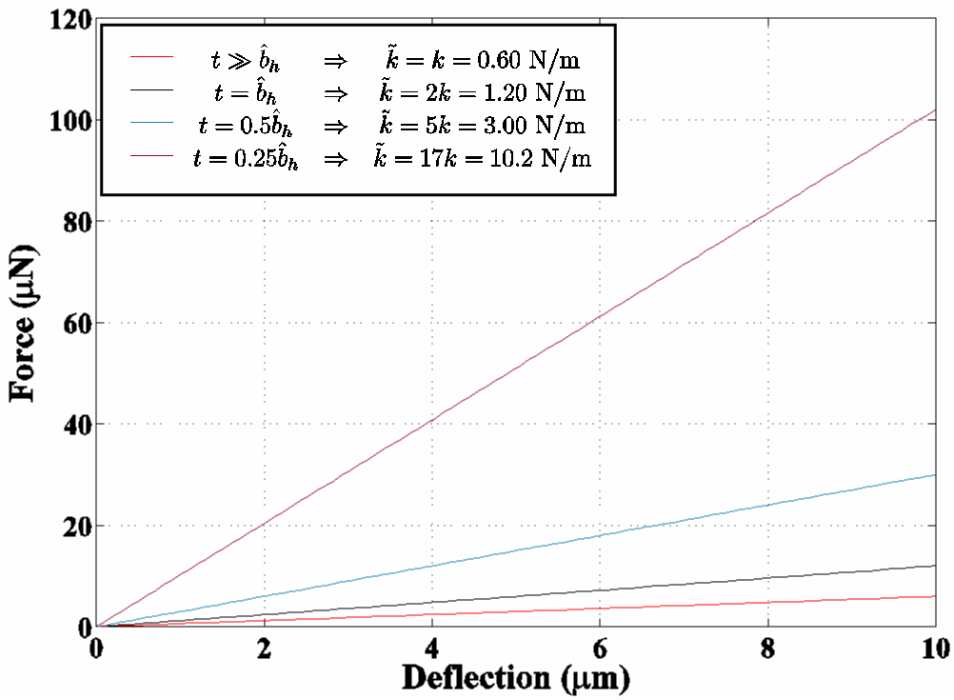

Figure 10: Size effect upon beam stiffness.

than 1% of the normal deformation effects for beams plates with aspect ratios (i.e., L/t) over 20 [10]. As a rough estimate of the shear stress influence on deflection, one can look at the ratio of maximum normal stress ($= FLt/2I$) to maximum shear stress ($= Ft^2/8I$) for an end-loaded, rectangular beam and find $\tau_{max}/\sigma_{max} = t/4L$; for the geometries considered in this work $t/L \lesssim 20 \Rightarrow \tau_{max}/\sigma_{max} \lesssim 1\%$.

A second assumption of is $(du_z/dx) \ll 1$ (used in the curvature relation of Equation 17 and in the derivation leading up to Equation 28) and the deflections experienced by the microcantilevers in use are on the order of the the beam thickness at worst, and assuming L, w, t, and E of 500, 100, 10 μm and 3 GPa, respectively, with an end deflection of 5 μm, gives $du_z/dx = 0.015 \Rightarrow [1 + (du_z/dx)^2]^{3/2} = 1.00034$, which justifies the curvature assumption.

Another assumption is that of small strain, which allows employment of the infinitesimal strain tensor in the constitutive model. In actuality, the strain is given as $\epsilon_{ij} =$

$\frac{1}{2}(u_{i,j}+u_{j,i}-u_{m,i}u_{m,j})$, so the axial strain (the component used in the germane derivations) experienced by a plate or beam is $\epsilon_{11} = u_{1,1} - \frac{1}{2}(u_{1,1}u_{1,1} + u_{2,1}u_{2,1} + u_{3,1}u_{3,1})$. The plane strain assumption states that $\epsilon_{22} = u_{2,2} = 0 \ \forall x \Rightarrow u_2 = f(y,z) + C \Rightarrow u_{2,1} = 0 \Rightarrow u_{2,1}u_{2,1} = 0$ (C is a constant). The small influence of the linear shear strain term $u_{3,1}$ (discussed two paragraphs prior) indicates that the $u_{3,1}u_{3,1}$ term is certainly negligible. From Equations 17 and 19 it is seen that the maximum axial strain will be $\epsilon_x = \epsilon_{11} = tM/EI$. If a generic values of L, w, t, P, and E of 500, 100, 10 μm, 3 GPa, and 10 μN are used the maximum axial strain is 0.002 m/m; therefore, inclusion of the remaining second order term produces a change in the finite axial strain [i.e., $\epsilon_{11} = u_{1,1} - \frac{1}{2}(u_{1,1}u_{1,1})$] of 0.2%. This is considered negligible and hence ϵ_{11} is acceptably close to $u_{1,1}$.

The fourth assumption is that the beam mass will not severely influence the static beam deflections. If a generic microcantilever geometry (L, w, t, ρ_b, and E of 500, 100, 10 μm, 1000 kg/m^3, and 3 GPa, respectively) is assumed, the total force due to the mass is 5 nanoNewtons, which, if applied at the end of the microcantilever (a worst-case scenario) will deflect the beam less than 8 nm, which is roughly 0.5% of the deflections seen in practice and in the nanoindentation characterization techniques of this work, showing that the weight influence is negligible. With the stiffness and length scale dependent stiffness discussed and the assumptions validated, attention now turns to the effect that a surface stress will have on beam deflection; the length scale dependent values will come into play here as well.

3.3.2 Theoretical Determination of Surface Stress Effects on Deflection

In the practical use of microcantilevers as sensors in the context of this work, the measurement of the beam deflection allows for determination of a surface stress difference between the top and bottom of the microcantilever (as discussed in §2.3.2.3). This approach will be used to evaluate an expression derived for this work which

predicts the resonance shift due to surface stresses. The deflection due to adsorption-induced surface stresses can be approximated by Equation 33 (also known as Stoney's equation) [233]

$$\frac{1}{R} = 6\frac{1-\nu}{Et^2}(\Delta\sigma_1 - \Delta\sigma_2) \tag{33}$$

where R is the beam radius of curvature ($R^{-1} = 2\Delta z/L^2$ where Δz is the beam tip deflection), ν is Poisson's ratio, E is the elastic modulus of the beam material, t is the beam thickness, and $\Delta\sigma_1$ and $\Delta\sigma_2$ are surface stresses acting on the beam top and bottom, respectively. Stoney's equation is an exact solution for a plate bending which is unrestrained at all edges, and hence a more accurate equation is necessary for the cantilevered situation of this work. To examine the stress-induced bending of microcantilevers analytically, we must look to refinements of Stoney's equation (i.e., inclusion of the cantilevered boundary condition and strain gradient effects) and this is done by first employing plate theory, which is now discussed.

3.3.2.1 Governing Equation

The goal of this subsection is to lay the groundwork for a displacement-based governing equation for the bending of a thin plate and to obtain an approximate solution for the cantilever boundary conditions. In thin plate theory and for isotropic, homogeneous plates where the influence of in-plane deflection on out-of-plane deflection (which is taken to be small) is assumed negligible, the in-plane stress and strain fields are described by Equations 34 and 35 while a representative geometric description is shown in Figure 11

$$\sigma_{11} = \frac{E}{1-\nu^2}\left(\epsilon_{11} + \nu\epsilon_{22}\right) + \sigma_s, \sigma_{22} = \frac{E}{1-\nu^2}\left(\epsilon_{22} + \nu\epsilon_{11}\right) + \sigma_s, \sigma_{12} = \frac{E}{2\left(1+\nu\right)}\epsilon_{12} \tag{34}$$

$$\epsilon_{ii} = u_{i,i} - x_3 u_{3,ii} \text{ (for } i = 1,2), \epsilon_{12} = u_{1,2} + u_{2,1} - 2x_3 u_{3,12} \tag{35}$$

where $\sigma_s = \sigma_s^+\delta\left(z - \frac{t}{2}\right) + \sigma_s^-\delta\left(z - \frac{t}{2}\right)$, $\delta\left(\bullet\right)$, is the Dirac delta, u_i is the midplane displacement in the ith coordinate direction, x_i, ν is the Poisson's ratio of the material, $u_{i,j} = \partial u_i/\partial x_j$, and $u_{i,jk} = \partial^2 u_i/\partial x_j \partial x_k$.

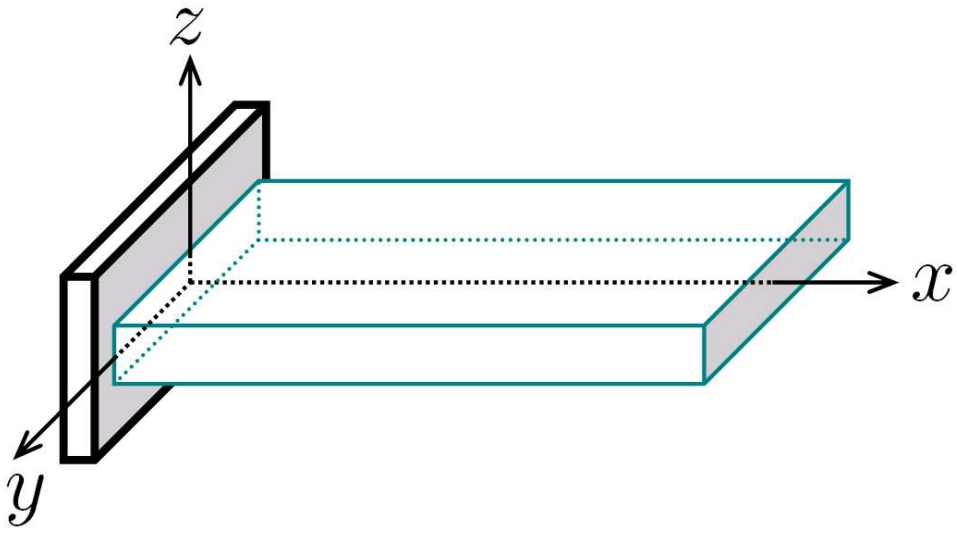

Figure 11: Plate geometry where $x \in [0, L]$, $y \in [-w/2, w/2]$, and $z \in [-t/2, t/2]$.

Basic mechanics approaches yield the moments (per unit length) acting on the beam edges as Equations 36 to 38, Figure 12 gives a graphical description of the forces and moments acting on generic portion of the beam where the Q_i are shear forces in the ith coordinate direction. Note that by imposing equilibrium in the z direction, these shear forces cancel out.

$$M_{11} = \int_{-t/2}^{t/2} \sigma_{11} x_3 dx_3 = -D\left(u_{3,11} + \nu u_{3,22}\right) + \Delta\sigma_s \frac{t}{2} \tag{36}$$

$$M_{11} = \int_{-t/2}^{t/2} \sigma_{22} x_3 dx_3 = -D\left(u_{3,22} + \nu u_{3,11}\right) + \Delta\sigma_s \frac{t}{2} \tag{37}$$

$$M_{12} = M_{21} = \int_{-t/2}^{t/2} \sigma_{12} x_3 dx_3 = -D\left(1 - \nu\right) u_{3,12} \tag{38}$$

where $D = Et^3\left[12\left(1 - \nu^2\right)\right]^{-1}$ as in §3.3.1.3. Substitution of the moment equations into equilibrium equations gives Equation 39, the governing equations for plate bending under the aforementioned assumptions.

$$\begin{gathered} \underbrace{M_{11,11} + 2M_{12,12} + M_{22,22} = -P\left(x, y\right)}_{z-\text{direction equilibrium}} \Rightarrow \\ -D\left(u_{3,1111} + 2u_{3,1122} + u_{3,2222}\right) = -P\left(x, y\right) \Rightarrow \\ \nabla^4 u_3 = P\left(x, y\right) D^{-1} = 0 \end{gathered} \tag{39}$$

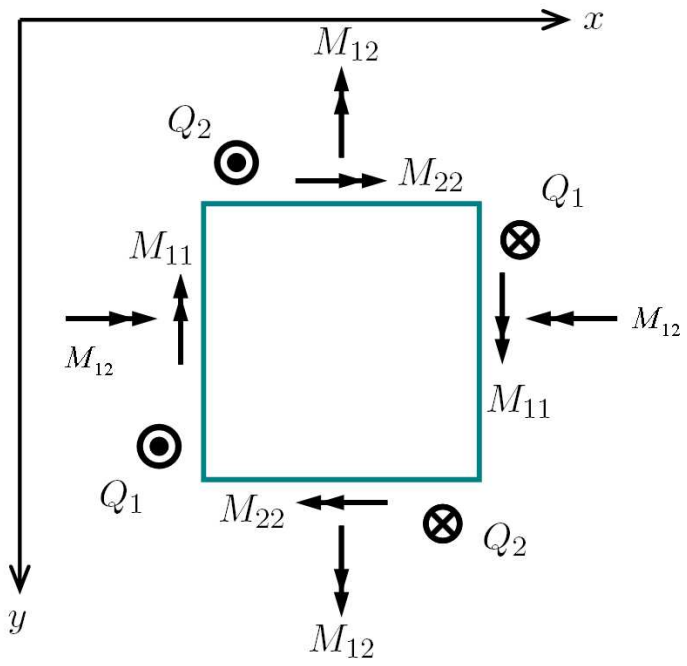

Figure 12: Graphical description of forces and moments acting on a generic plate element.

$P(x, y)$ is the transverse pressure load (normal to the surfaces defined by $2z = \pm t$, units of force per area), which is zero in our case as we only consider in-plane surface stresses, hence the final form of Equation 39.

3.3.2.2 Approximate Governing Equation Solution

To obtain an approximate solution for a cantilevered plate governed by Equation 39 (exact solutions only exist for rudimentary boundary conditions, which do not encompass the cantilevered plates considered here), the boundary conditions for the clamped face are given by Equation 40.

$$u_3|_{(x=0,y)} = u_{3,1}|_{(x=0,y)} = 0 \tag{40}$$

These boundary conditions simply state the z deflection and slope of the beam are both zero at the fixed edge. At the remaining three unclamped faces of the beam ($x = L$ and $2y = \pm w$), the normal component of any moment must be zero (because

these are free surfaces) as must all shear forces (as there are none applied), so the boundary conditions follow from the moment expressions (Equations 36 to 38) and are given as Equation 41 [218]

$$\left[\frac{\partial^2 u_3}{\partial n^2} + \nu\frac{\partial^2 u_3}{\partial s^2}\right]\Bigg|_{\text{Free Edge}} = \frac{\Delta\sigma_s t}{2D}, \left[\frac{\partial^3 u_3}{\partial n^3} + (2-\nu)\frac{\partial^3 u_3}{\partial s^2 \partial n}\right]\Bigg|_{\text{Free Edge}} = 0 \qquad (41)$$

where (n, s) is a local right-handed coordinate system at that specific edge (normal and tangential directions, respectively). As pointed out by Sader [218], this formulation shows that application of differential surface stress is equivalent to the application of a moment with magnitude $\Delta\sigma_s t/2D$ to each of the three unclamped surfaces ($x = L$ and $2y = \pm w$), so the deflection of the cantilever can be obtained using Equations 39 through 41. Stoney's Equation (Equation 33) is the solution of Equation 39 for a free plate (i.e., a plate with no displacement or first displacement derivative restrictions on all surfaces except those where $2z = \pm t$). An alternative form of Stoney's Equation is given as Equation 42

$$u_{3(free)} \equiv w_{free} = \Omega\left(x_1^2 + x_2^2\right) \equiv \Omega\left(x^2 + y^2\right) \qquad (42)$$

where $\Omega = \Delta\sigma_s t/4D\left(1+\nu\right)$. Obviously, at $x = 0$ this solution violates the displacement boundary condition of the cantilevered plate. To remedy this (following the work of Sader) the solution of Equation 39 using the boundary conditions of Equations 40 and 41 is split into two problems; the first problem (free problem) is just that of the unrestrained plate with the solution given by Equation 42 and the second (correction problem) is a plate subject to the boundary conditions of Equation 43.

$$u_{3(corr)}\left(0, y\right) \equiv w_{corr}\left(0, y\right) = -\Omega y^2, \frac{\partial w_{corr}}{\partial x}\Bigg|_{(x=0)} = 0 \qquad (43)$$

Finally, the cantilevered plate problem (w_{cant}) is defined in the composite form of Equation 44.

$$w_{cant} = w_{corr} + w_{free} \qquad (44)$$

By defining the cantilever problem as the sum of the free and correction problems, one sees that this composite function will satisfy the boundary conditions of Equations 40 and 41, and the governing biharmonic equation (Equation 39). With the solution to the free problem known, an asymptotic solution ($w < L$, which is justified for our situation where $L \approx 5w - 10w$) to the correction problem was developed by expanding w_{corr} in a power series in y and retaining the first two nonzero terms giving the approximation shown in Equation 45, remembering that the deflection will be symmetric about the x axis (see Figure 11).

$$w_{corr} \approx f(x) + y^2 g(x) \tag{45}$$

Equating the total energy of the system to the strain energy (as the only energy source is due to the imposed displacement boundary condition of the clamped edge of the correction problem) and using Reissner's principle[15] allows for the determination of the functions $f(x)$ and $g(x)$ in Equation 45, and for a final form of Equation 44 given as Equation 46 [218]

$$\begin{aligned} w_{cant}(X,Y) = \Omega L^2 \Big\{ & X^2 + 2\nu X \left[\tau_1^{-1} + \tau_2^{-2}\right](wL^{-1}) \\ & - \left[12^{-1} + 2\nu\left(\tau_1^{-2} + \tau_1^{-2} + \tau_1^{-1}\tau_2^{-1}\right)\right] \\ & - \textstyle\sum_{i=1}^{2} d_i \left(12^{-1} + 2\nu\tau_i^{-2}\right) \exp\left(-\tau_i X L w^{-1}\right)(wL)^{-2} \\ & + Y^2 \left[1 - \textstyle\sum_{i=1}^{2} d_i \exp\left(-\tau_i X L w^{-1}\right)\right] \Big\} \end{aligned} \tag{46}$$

where $X = xL^{-1}$, $Y = yL^{-1}$, $d_i = \tau_{3-i}\left(\tau_{3-i} - \tau_i\right)^{-1}$, and the material property dependent $\tau_i = 2\sqrt{3}\left[5(1-\nu) + (-1)^i \sqrt{10(1-\nu)(2-3\nu)}\right]$. Equation 46 satisfies the boundary conditions of the cantilevered plate at $x = 0$ and returns Stoney's Equation (Equation 33) as $L/w \to \infty$, as desired. As Equation 46 is an improvement

[15]Reissner's principle is a stationary principle where the functional formed is as follows: $I_R = \iiint_V [\sigma_{ij}\epsilon_{ij} - U_0^*(\sigma_{ij})]dV - \iiint_V \rho b_i u_i dV - \iint_S t_i u_i dA$. Setting the first variation of I_R=0 (i.e., $\delta I_R = 0$) returns a constitutive model ($\epsilon_{ij} = \partial U^*/\partial\sigma_{ij}$), static equilibrium conditions ($\sigma_{ji,j} + \rho b_i = 0$) and boundary conditions – this is a compact manner to obtain all of these relations and is considered superior to virtual work principles as it gives a good approximation to *both* displacements and stresses.

over Equation 33, it should be used in all situations to determine the surface stress difference necessary to cause a given deflection on a given point of the surface of a cantilevered plate that satisfies the plate assumptions discussed in this subsection. Experimentally, Equation 46 becomes useful in the following situation: if microcantilever resonance frequency data *and* beam deflection are monitored during the same adsorption event, then Equation 46 can be used to predict the surface stresses, and a new expression developed for this work that predicts the surface stress as a function of resonance frequency (discussed in §3.3.3.6) can be validated or rejected.

3.3.3 Theoretical Determination of Microcantilever Resonant Frequency(ies)

When an analyte is adsorbed onto the surface(s) of a microcantilever, there can be many sources of resonance frequency change; the adsorbed mass will change the effective mass of the microcantilever and hence lower the resonance frequency, the adsorbed mass can form a layer on one or both sides of the microcantilever hence forming a composite structure with an increased resistance to deflection (due to the increased second moment of the cross sectional area), and the adsorbed mass can have conformational states associated with it and hence entropic effects whose influence on resonance via the developed surface stresses can become relevant. The equations for all of these cases are now presented. Mathematical treatment of the resonance determination of an unladen beam is given first, as the results from this rudimentary case are drawn upon for treatment of the analyte adsorption effects. However, the mathematics are prefaced with a description of the beam quality factor, as it is an important experimental parameter relevant to any discussion involving resonance frequency behavior.

3.3.3.1 Beam Quality Factor (Q)

The quality factor of a microcantilever quantitatively characterizes the shape of the frequency response curve (e.g., displacement amplitude versus frequency) near a resonance mode of the cantilever. Accordingly, each resonance mode has its own quality factor. Mathematically, the ith mode quality factor Q_i is defined as the ratio of the resonance frequency the ith mode, f_i, to the full width of the resonance peak evaluated at the half maximum (FWHM) of the peak. Figure 13 shows some generic frequency response curves along with their Q factors and f_1 values. It is apparent from Figure 13 that the two curves with equal resonance frequencies (50 kHz) have markedly different shapes, as characterized by their different quality factor. The curve with $f_1 = 50$ kHz and a Q of 100, has a sharper peak than the curve with $f_1 = 75$ kHz and Q of 100. This is inherent in the definition of $Q_i \equiv f_i/\text{FWHM}$; as the resonance frequency increases for a given Q, the FWHM increases. The Q factor depends upon the cantilever geometry and the fluid which engulfs the cantilever (if any). Increased damping effects lead to a lower Q value while a higher Q is desired as it lowers the minimum detectable resonance shift (i.e., it increases the frequency resolution). For a Q factor of 10, the minimum detectable resonance frequency shift is roughly 25 Hz, while a Q of 100 allows for a frequency resolution below 10 Hz.

3.3.3.2 Unladen Beam

To derive an equation for the resonant frequencies of a microcantilever analytically, the equations of motion are formulated, which must be satisfied to appease Newton's 2$^{\text{nd}}$ law (e.g., force equals time rate of change of momentum). This has been done previously for a cantilevered beam (using Euler-Bernoulli beam theory discussed in §3.3.1.1) with the resulting equation of motion given as Equation 47 (it should be noted that damping effects are ignored here but the approach is still accurate for

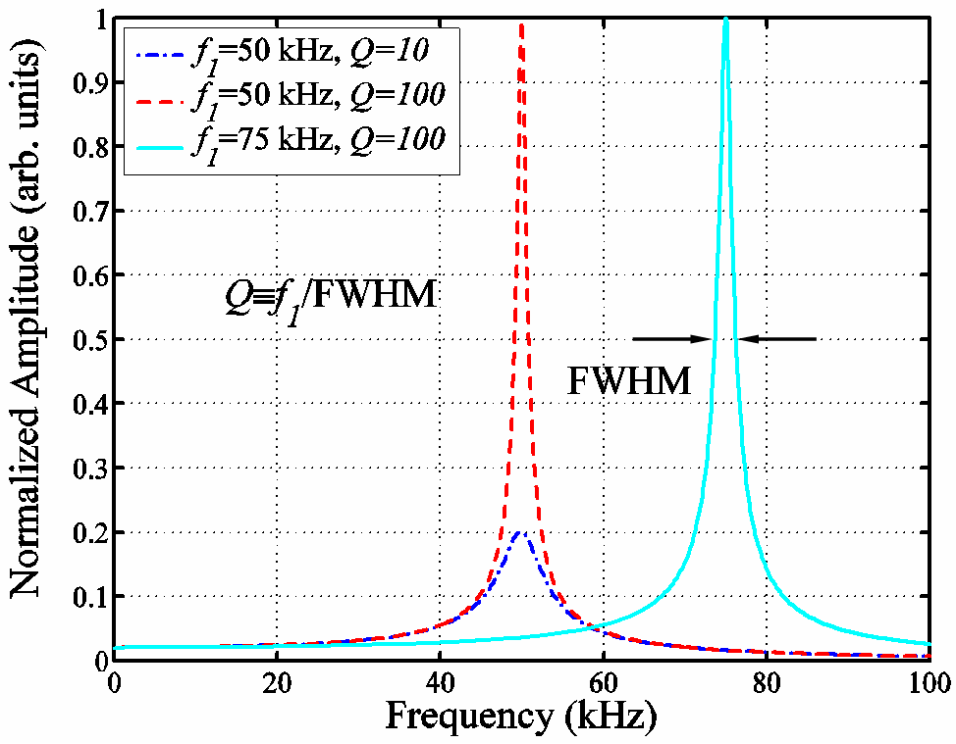

Figure 13: Generic frequency response curves.

certain situations, namely a cantilever vibrating in air as discussed in §3.3.3.7)

$$\frac{\partial^2}{\partial x^2}\left(EI\frac{\partial^2 z(x,T)}{\partial x^2}\right) = -\rho_b A\frac{\partial^2 z(x,T)}{\partial T^2} \tag{47}$$

where ρ_b is the beam material density, $z(x,T)$ is the transverse deflection of the beam as a function of the coordinate in the length direction of the beam (x) and time (T), and the quantity EI will henceforth be assumed constant. By assuming harmonic motion, the deflection can be separated into an infinite series of products of time-independent $[X_i(x)]$ and time-dependent expressions, as shown in Equation 48

$$z = \sum_{i=1}^{\infty} X_i(x)(K_i \cos\omega_i T + L_i \sin\omega_i T) \tag{48}$$

where $\omega_i = 2\pi f_i$ is the angular frequency of vibration of the ith mode and the K_i and L_i are constants. Substitution of Equation 48 into Equation 47 yields Equation 49

$$\frac{d^4 X_i}{dx^4} - s_i^4 X_i = 0 \tag{49}$$

where $s_i^4 = \omega_i^2/a^2$ and $a^2 = EI/\rho_b wt$. The general solution of Equation 49 can be written as Equation 50

$$X_i = A_i \sin s_i x + B_i \cos s_i x + C_i \sinh s_i x + D_i \cosh s_i x \tag{50}$$

where the A_i, B_i, C_i, and D_i are constants determined from the boundary conditions. For the case of the cantilevered beam free from forces, the slope and displacement at the base of the beam must be zero given any time (i.e., $z(x,T)|_{0,T} = \partial z(x,T)/\partial x|_{0,T} = 0$), which implies $A_i = -C_i$ and $B_i = -D_i$. Additionally, at the end of the beam (i.e., at $x = L$) the moment and force acting on the beam are zero given any time (i.e.,$\partial^2 z(x,T)/\partial x^2|_{L,T} = \partial^3 z(x,T)/\partial x^3|_{L,T} = 0$). These last two conditions allow for a matrix form to be used as given by Equation 51

$$\begin{bmatrix} -\sin s_i L - \sinh s_i L & -\cos s_i L - \cosh s_i L \\ -\cos s_i L - \cosh s_i L & \sin s_i L - \sinh s_i L \end{bmatrix} \mathbf{C} = \mathbf{MC} = \mathbf{0} \tag{51}$$

where $\mathbf{C} = [A_i, B_i]^T$ and $\mathbf{0} = [0,0]^T$. The determinant of the bracketed matrix must vanish for Equation 51 to have a nontrivial solution (i.e., $|\mathbf{M}| = 0$), which yields Equation 52

$$(\sin s_i L + \sinh s_i L)(-\sin s_i L - \sinh s_i L) - (\cos s_i L \cosh s_i L)(-\sin s_i L - \sinh s_i L) \Rightarrow$$

$$-\sin^2 s_i L + \sinh^2 s_i L - \cos^2 s_i L + 2\cos s_i L \cosh s_i L - \cosh^2 s_i L \Rightarrow$$

$$-(\sin^2 s_i L + \cos^2 s_i L) + (\sinh^2 s_i L - \cosh^2 s_i L) - 2\cosh s_i L \cos s_i L \Rightarrow$$

$$\cosh \alpha_i \cos \alpha_i + 1 = 0 \tag{52}$$

where $\alpha_i = s_i L$. By solving $s_i^4 = \alpha_i^4/L^4 = \omega_i^2/a^2 = (2\pi f_i)^2/a^2$ for f_i and numerically calculating the α_i from Equation 52, the predicted ith mode resonance of the beam is given by Equation 53.

$$f_i = \frac{1}{2\pi}\left(\frac{\alpha_i}{L}\right)^2 \sqrt{\frac{EI}{\rho_b wt}} \tag{53}$$

Finally, substitution of the formula for I of a rectangular cross section ($I = wt^3/12$) into Equation 53 gives Equation 54 to predict the resonance frequencies for a rectangular cantilever.

$$f_i = \frac{t}{4\pi}\left(\frac{\alpha_i}{L}\right)^2\sqrt{\frac{E}{3\rho_b}} \Rightarrow f_i = \frac{\alpha_i^2}{2\pi\sqrt{3}}\sqrt{\frac{k}{M_b}} \tag{54}$$

An assumption here is that the rotational inertia effects are negligible (in the derivation of Equation 47), but, as pointed out by Timoshenko, these effects are roughly one third of the shear effects, which were shown to be negligible in §3.3.1.1 [244]. Additionally, viscous damping due to the fluid engulfing the microcantilever is neglected, but is shown to be negligible in certain cases in §3.3.3.7.

One important point here is that the elastic modulus terms are assumed constant, when in reality (and particulary for polymeric cantilevers), the modulus is a function of frequency as well [e.g., $E = E(\omega)$]. To model this, one can take the Fourier transform[16] of Equation 47 with the result shown in Equation 55

$$\frac{d^4\hat{X}_i}{dx^4} - \hat{s}_i^4\hat{X}_i = 0 \tag{55}$$

where $\hat{X} = \hat{X}(x,\omega)$ is the Fourier transform of $X = X(x,t)$ and $\hat{s}_i^4 = \omega_i^2/a(\omega)^2$ and $a(\omega)^2 = \Re\{E\}[1 + j\eta(\omega)]I/\rho_b wt$, where $\eta(\omega)$ is an arbitrary function of frequency, sometimes referred to as the structural damping ($j = \sqrt{-1}$ and $\Re\{E\}$ is the real portion of the elastic modulus) [164, 262]. The resulting solution (for a cantilevered, rectangular cross-sectioned beam) of Equation 55 is the same as Equation 54, except E is replaced by $E[1 + \eta(\omega)]$ {or k by $k[1 + \eta(\omega)]$ in the second form of Equation 54}, showing that the modal frequencies are now a function of frequency

[16]The Fourier transform and inverse transform (i.e., a Fourier transform pair) are defined as $\hat{G}(x_1, x_2, \ldots, x_n, \omega) = \sqrt{\frac{|b|}{(2\pi)^{1+a}}}\int_{-\infty}^{\infty} G(x_1, x_2, \ldots, x_n, t)e^{ib\omega t}\mathrm{d}t$ and $G(x_1, x_2, \ldots, x_n, t) = \sqrt{\frac{|b|}{(2\pi)^{1+a}}}\int_{-\infty}^{\infty}\hat{G}(x_1, x_2, \ldots, x_n, \omega)e^{-ib\omega t}\mathrm{d}\omega$. a and b are usually chosen as zero and one, respectively, to introduce symmetry. For this work, the transform is useful for casting a time-dependent phenomena (e.g., microcantilever tip deflection amplitude as a function of time) into a frequency-dependent form (e.g., microcantilever tip deflection amplitude as a function of frequency to observe resonance frequencies).

themselves (via the elastic modulus). The elastic modulus of viscoelastic materials increases (monotonically in theory) with frequency [77], and the ramifications of this behavior (i.e., a higher modulus at higher frequencies) will be evidenced in Chapter 5 when the predicted resonant frequency (which occurs at high frequency) obtained via Equation 54 is lower than the observed resonant frequency when the elastic modulus value used is the manufacturer-provided value, which is obtained via tensile tests which are low frequency.

A "shortcut" approach to determine the first resonant frequency is to model the microcantilever as a spring-mass system (i.e., a simple harmonic oscillator or SHO) and then find an effective mass (m_{eff}) that will match the resonant frequency of the SHO model to that of a vibrating beam, a value calculated from Equation 53 (or Equation 54 for a rectangular cantilever). This technique is called the SHO–matching model and avoids employing the somewhat complicated beam vibration equations (especially the numerical solution of Equation 52) and is presented here because it is so widely used in practice.

The first step in the SHO–matching model is to set up the equations of motion for the system, given as Equation 56 (scaled dynamic force plus scaled viscous drag force plus scaled deflection force equals zero) [177].

$$\frac{d^2x}{dt^2} + \frac{b}{m_{\text{eff}}}\frac{dx}{dt} + \frac{k}{m_{\text{eff}}}x = 0 \tag{56}$$

The solution to this has the form of Equation 57

$$x = Ae^{-\gamma t}\cos(w_d t + \phi) \tag{57}$$

where $\gamma = b/2m_{\text{eff}}$ and ω_d is the damped frequency (b is a damping coefficient). A common approach, when the beams are vibrating in air, is to neglect the damping effects (i.e., set $b = 0$) which results in the expression of Equation 58, for the resonant frequency, f_1.

$$f_1 = \frac{1}{2\pi}\sqrt{\frac{k}{m_{\text{eff}}}} \tag{58}$$

We now want a relationship between the actual beam mass, M_b (i.e., $Lwt\rho_b$ where ρ_b is the beam density) and m_{eff}. To find this we set the right-hand side of Equation 58 equal to the RHS of Equation 54 (for $i = 1$, corresponding to the first mode), yielding the SHO–matching model prediction of $m_{\text{eff}} = 3M_b/\alpha_1^4 \approx 0.2427M_b$. This factor is used widely in the literature (although hardly ever explained or referenced properly) and was presented here to show its origins. Note that this approach can be used for higher modes as well (e.g., for the third mode $m_{\text{eff}} = 3M_b/\alpha_3^4$).

Equations 21 and 54 give two geometric means to calculate the stiffness and resonant frequency without strain gradient effects while Equations 31 and 54 (using the strain gradient-inclusive stiffness, $\tilde{k}$) are analogous forms which include these effects- these techniques are dubbed geometric methods because they involve only beam geometries and material properties.[17] The experimental methods present advantages over the geometric methods mainly in that they do not require measurement of beam thickness (an error-prone process, which can introduce significant error in the beam stiffness calculation), but rather involve using different experimental parameters to back out beam stiffness and resonant frequency. With the resonance behavior of an unladen cantilever dealt with, attention now turns to the effects that the adsorption of species (or change in conformation or state of a species already attached to a microcantilever) can have on the microcantilever resonance.

3.3.3.3 Mass Change Effects

The mass change-induced resonant frequency shifts are the simplest and hence are dealt with first. By examining the method of assumed modes's final equation (i.e., Equation 54), one sees that the mass of the system (i.e., the denominator in the square root term) upon adsorption will be the beam mass, M_b plus the adsorbed mass, ΔM.

[17]The geometric methods traditionally only encompass the non-strain gradient equations, but the nomenclature is adopted here as well, even though Equations 31 and 54 (including strain gradient effects) are new to the literature.

Therefore, the new resonance frequencies, f_i^{+m}, are given as Equation 59.

$$f_i^{+m} = \frac{\alpha_i^2}{2\pi\sqrt{3}}\sqrt{\frac{k}{M_b + \Delta M}} \tag{59}$$

3.3.3.4 Stiffness Change Effects

In addition to changing the effective mass of a system, the adsorbed substance effectively increases the second moment of the microcantilever cross sectional area (I), making the beam stiffer (recall that a basic expression for stiffness is $k = 3EI/L^3$). To examine this change one can employ beam theory and deduce that the flexural rigidity of the composite system will be $E_{csys}I_{csys} = E_bI_b + E_{ads}I_{ads}$ where the subscripts *csys*, *b*, and *ads* stand for composite system, beam, and adsorbed species, respectively. The resulting equation for the new resonant frequencies due solely to stiffening, f_i^{+k} is given as Equation 60.

$$f_i^{+k} = \frac{\alpha_i^2}{2\pi\sqrt{3}}\sqrt{\frac{3E_{csys}I_{csys}}{L^3M_b}} = \frac{\alpha_i^2}{2\pi\sqrt{3}}\sqrt{\frac{3E_bI_b + 3E_{ads}I_{ads}}{L^3M_b}} = \frac{\alpha_i^2}{2\pi\sqrt{3}}\sqrt{\frac{k}{M_b} + \frac{3E_{ads}I_{ads}}{L^3M_b}} \tag{60}$$

Similar to Equation 59, one can include the effects of increased stiffening and added mass, to give the new resonant frequencies after the adsorption event, $f_i^{+m,+k}$, as Equation 61

$$f_i^{+m,+k} = \frac{\alpha_i^2}{2\pi\sqrt{3}}\sqrt{\frac{3E_{csys}I_{csys}}{L^3(M_b + \Delta M)}} = \frac{\alpha_i^2}{2\pi\sqrt{3}}\sqrt{\frac{k}{M_b + \Delta M} + \frac{3E_{ads}I_{ads}}{L^3(M_b + \Delta M)}} \tag{61}$$

where $I_b = wt_s^3/12 + wt_b[y_{cm} - (t_b/2)]^2$, $I_{ads} = wt_{ads}^3/12 + wt_{ads}[(t_{ads}/2) - t_b - y_{cm}]^2$ (via the parallel axis theorem) and the new centroid of the cross section is given as $y_{cm} = [E_bt_b^2 + E_{ads}(2t_{ads}t_b + t_{ads}^2)]/(2E_{ads}t_{ads} + 2E_bt_b)$ where t_{ads} is the thickness of the adsorbed layer and t_b is the beam thickness [118].

3.3.3.5 Surface Stress Change Effects- Existing Approach

As mentioned in §3.3.3, a difference in surface stress between the top and bottom of a microcantilever will induce a beam deflection. Experimentally, this surface stress-induced deflection has been shown to alter the resonance frequencies of the micro-cantilver. The literature has seen rudimentary approaches to this problem as well as more advanced theories, but the problem is relatively unexplored. Chen *et al.* modeled a microcantilever as a taut string and assumed that the changes in stiffness and mass due to an adsorption or conformation change event are small compared to the stiffness and beam mass, respectively [44]. This yielded Equation 62 to predict resonance frequency changes (first mode) due to a change in stiffness (due to surface stresses) and mass (due to adsorption).

$$f_1^{+m,+k} = f_1 \left[1 + \frac{1}{2} \left(\frac{\delta k}{k} - \frac{\delta m_{\text{eff}}}{m_{\text{eff}}} \right) \right] \tag{62}$$

Equation 62 assumes that $\delta k \ll k$ and $\delta m_{\text{eff}} \ll m_{\text{eff}}$, but recent experimental data of Lee *et al.* show that the change in stiffness due to surface stresses is not small, and their measured values were two orders of magnitude higher than predicted by the existing theory [135]. Other work by Thundat *et al.* also showed a large discrepancy between theory and experiment (theory underestimating by roughly one order of magnitude [45]) indicating that the existing model of Equation 62 is insufficient in certain cases.

3.3.3.6 Surface Stress Change Effects- New Approach

Due to the lack of appropriate modeling in the literature, this work modeled the microcantilever system using the method of assumed modes and derived an equation relating the fundamental resonant frequency to the applied surface stresses [168]. The model assumed that the effect of the surface stress is linear elastic in nature and can be applied equivalently as a force (F) and moment (M) acting at the end of the beam, as shown in Figure 14. It is realized that the resonance frequency will

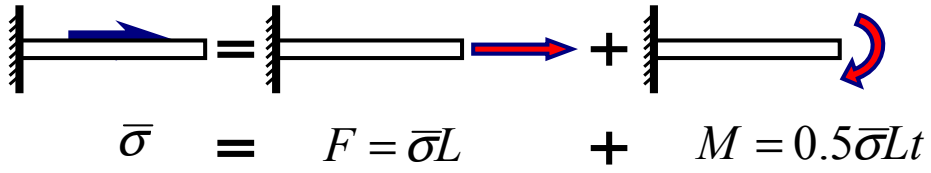

Figure 14: Decomposition of a surface stress into an equivalent force (F) and moment (M).

not be changed by the applied moment, because it puts one half of the beam into tension (with a tendency to increase the resonant frequency) and the other side into compression (with a tendency to decrease the resonant frequency)– the effects cancel. Therefore, only the force need be considered and Equation 47 is still the governing equation, except that a force term must now be added to the equilibrium statement, giving Equation 63 (the notation here is the same as in §3.3.3.2 where x is the position along the beam length and T denotes time; T is used instead of the more conventional t to avoid confusion of time with beam thickness, which was previously defined as t).

$$\frac{\partial^2}{\partial x^2}\left[EI\frac{\partial^2 z\,(x,T)}{\partial x^2}\right] + \rho_b A\frac{\partial^2 z\,(x,T)}{\partial T^2} - F\frac{\partial^2 z\,(x,T)}{\partial x^2} = 0 \tag{63}$$

By assuming resonant behavior and employing the method of assumed modes as in §3.3.3.2 (i.e., Equation 48) and assuming that the product EI is constant, Equation 63 becomes Equation 64

$$EI\frac{\partial^4 X_i}{\partial x^4} - \hat{\psi}\frac{\partial^2 X_i}{\partial t^2} - s^4\frac{\partial^2 X_i}{\partial x^2} = 0 \tag{64}$$

where $\hat{\psi} = F/EI$ and $s_i^4 = \rho_b wt\omega_i^2/EI$. Now the general solution of Equation 64 is given by Equation 65 [146].

$$X_i(x) = A_i \cosh p_i x + B_i \sinh p_i x + C_i \cos q_i x + D_i \sin q_i x \tag{65}$$

$$p_i = \left[\frac{\sqrt{\hat{\psi}^2 + 4s_i^4} + \hat{\psi}}{2}\right]^{\frac{1}{2}} \quad \text{and} \quad q_i = \left[\frac{\sqrt{\hat{\psi}^2 + 4s_i^4} - \hat{\psi}}{2}\right]^{\frac{1}{2}}$$

Note the similarities between Equation 50 of §3.3.3.2 and Equation 65– the two approaches (i.e., that of §3.3.3.2 and the current section) are identical except that the governing equations (i.e., Equations 47 and 64) are different, as is one of the four boundary conditions.

The first two boundary conditions are unchanged from the freely vibrating cantilever problem (i.e., zero displacement and slope at $x = 0$), and are repeated as Equations 66 and 67. Conversely, a force and moment are now acting at the end of the beam (i.e., at $x = L$), which are mathematically described as Equations 68 and 69

$$z(0,T) = 0 \tag{66}$$

$$\frac{\partial z(0,T)}{\partial x} = 0 \tag{67}$$

$$\frac{\partial^3 z(L,T)}{\partial x^3} - \hat{\psi}\frac{\partial z(L,t)}{\partial x} = 0 \tag{68}$$

$$\frac{\partial^2 z(L,T)}{\partial x^2} = \frac{M}{EI} = 0 \tag{69}$$

where the final conclusion of Equation 69 follows from the argument that the moment is ineffectual in this case. The first two boundary conditions (i.e., Equations 66 and 67) give $A_i + C_i = 0 \Rightarrow A_i = -C_i$ and $B_i + D_i = 0 \Rightarrow B_i = -D_i$, respectively. These new relations allow Equation 65 to be rewritten as Equation 70.

$$X_i(x) = A_i(\cosh p_i x - \cos q_i x) + B_i(\sinh p_i x - \sin q_i x) \tag{70}$$

Now, applying the boundary conditions of Equations 68 and 69 to Equation 70, gives Equation 71

$$\begin{bmatrix} (p^3\hat{s}_p - q^3 s_q - \psi p\hat{s}_p - \psi q s_q) & (p^3\hat{c}_p + q^3 c_q - \psi p\hat{c}_p + \psi q c_q) \\ q^2 c_q + p^2\hat{c}_p & q^2 s_q + p^2\hat{s}_p \end{bmatrix} \begin{Bmatrix} A_i \\ B_i \end{Bmatrix} = \begin{bmatrix} 0 \\ 0 \end{bmatrix} \tag{71}$$

where $\hat{s}_p = \sinh p_i l$, $\hat{s}_q = \sinh q_i L$, $s_p = \sin p_i L$, $s_q = \sin q_i L$, $\hat{c}_p = \cosh p_i L$, $\hat{c}_q = \cosh q_i L$, $c_p = \cos q_i L$, and $c_q = \cos q_i L$. Equation 71 will have a solution only when

the determinant of the matrix (i.e., the bracketed term) is zero, which, after lengthy algebra, gives the frequency relation of Equation 72.

$$\left[\left(\frac{p_i}{q_i}\right)^2 + \left(\frac{q_i}{p_i}\right)^2\right]\cosh p_i \cos q_i + \left[\left(\frac{p_i}{q_i}\right)^2 - \left(\frac{q_i}{p_i}\right)^2\right]\sinh p_i \sin q_i + 2 = 0 \tag{72}$$

Solving Equation 72 first entails use of the conditions imposed by Equation 71, and these details are presented in Appendix A. Equation 73 is used to predict the final resonant frequency from the addition of a surface stress where $\alpha_1^{\Delta\sigma}$ is determined from Equation 74 (recall that $\bar{\sigma}$ is the surface stress and $\hat{\sigma} = \bar{\sigma}L^3/EI$ is the dimensionless surface stress).

$$f_i^{+\Delta\sigma} = \frac{(\alpha_i^{\Delta\sigma})^2}{2\pi\sqrt{3}}\sqrt{\frac{k}{M_b}} \tag{73}$$

$$\alpha_i^{\Delta\sigma} = \alpha_i\left[1 + \frac{4\bar{\sigma}EI}{L^3\pi^2}\right]^{\frac{1}{4}} = \alpha_i\left[1 + \frac{4\hat{\sigma}}{\pi^2}\right]^{\frac{1}{4}} \tag{74}$$

While the force decomposition of Figure 14 allowed for a clean, closed form equation to predict the influence of surface stresses upon resonance behavior, it is still an approximation to the actual force distribution. However, it reveals a relation to the buckling analysis of an axially end-loaded column. Therefore, the buckling of a column under a uniform axial load was examined [155], and Equation 75 was obtained, which relates the resonance frequency dependence upon a uniformly applied axial load (e.g., a surface stress without the moment-inducing element), where $\underline{\alpha}_i^{\Delta\sigma}$ is obtained from Equation 76.

$$f_i^{+\Delta\sigma} = \frac{(\underline{\alpha}_i^{\Delta\sigma})^2}{2\pi\sqrt{3}}\sqrt{\frac{k}{M_b}} \tag{75}$$

$$\underline{\alpha}_i^{\Delta\sigma} = \alpha_i\left[1 + \frac{2\bar{\sigma}EI}{L^3\pi^2}\right]^{\frac{1}{4}} = \alpha_i\left[1 + \frac{2\hat{\sigma}}{\pi^2}\right]^{\frac{1}{4}} \tag{76}$$

The reader should note that setting $\bar{\sigma} = 0$ ($\Rightarrow \hat{\sigma} = 0$) in Equations 74 and 76 returns the frequency prediction equation for a cantilevered beam. A tensile surface

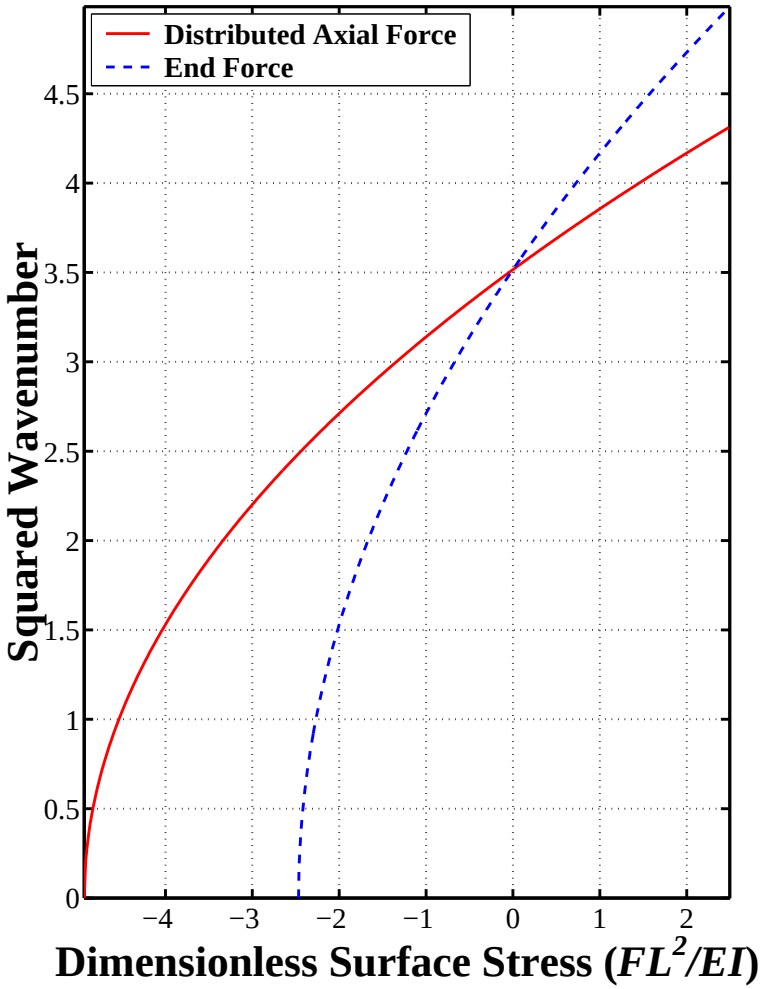

Figure 15: Dashed line showing the end force model first squared wavenumber, $(\alpha_1^{\Delta\sigma})^2$, versus dimensionless surface stress from Equation 74 and solid line showing the uniformly distributed axial force model first squared wavenumber, $(\underline{\alpha}_1^{\Delta\sigma})^2$, versus dimensionless surface stress from Equation 76.

stress, which tends to compress the beam (i.e., $\hat{\sigma} < 0$) will reduce the resonant frequencies of a microcantilever and vice-versa for compressive surface stresses.[18] Figure 15 shows plots of the squared first wavenumber for the end load model [i.e., $(\alpha_1^{\Delta\sigma})^2$] and the axial force model [i.e., $(\underline{\alpha}_1^{\Delta\sigma})^2$] versus normalized surface stress (FL^2/EI), where the plots where obtained from Equations 74 and 76, respectively.[19]

The first mode resonant frequency will decrease when the applied surface stress tends to compress the beam, and at the buckling load for the given loading (e.g., end-load or axially distributed load) the mode of deformation shifts from axial to buckling and the resonance frequencies for all modes go to zero. For an end loaded cantilever beam in the first buckling mode, $F_{euler} = EI\pi^2/4L^2$. So, if $\bar{\sigma} = -\pi^2/4 \approx -2.467$, then $\alpha_1^{\Delta\sigma}$ should be zero, and this is shown by Equation 74 and Figure 15. Similar arguments can be made for the axially distributed force of Equation 76 so that $\underline{\alpha}_1^{\Delta\sigma}$ evaluated at $\hat{\sigma} = -\pi^2/2$ should be zero, and this is seen in Equation 76 and Figure 15.

The magnitudes of compressive surface stresses seen in experiment (i.e., stresses tending to decrease the resonance frequencies, so $\hat{\sigma} > 0$ in Figure 15) are in the range of 0.01 to 10 N/m [185, 206], which correspond to dimensionless surface stresses ($\hat{\sigma}$) of roughly 1. Compressive surface stresses (i.e., stresses tending to increase the resonance frequencies, $\hat{\sigma} < 0$ in Figure 15) have seen very little attention but recent work shows that they are on the order of 0.001-0.01 N/m, although the literature has not seen a proper theoretical characterization of the phenomena, except to state that it is due to compressive stresses [135].

By including the effects of an increased stiffness and added mass, Equations 77 through 79 account for a resonance change due to the effects of mass plus surface

[18]The sign convention of tensile surface stresses being less than zero and compressive surface stresses being larger than zero may seem contrary to popular engineering nomenclature, but it is adopted here (and many times in the literature) because a tensile/compressive surface stress will induce a compressive/tensile stress in the *microcantilever itself.*

[19]The behavior for the ith mode wavenumbers ($i > 1$) are of the same form of Figure 15, except the ordinate values are multiplied by the scalar $(\alpha_i/\alpha_1)^2$.

stress, ($f_i^{+m,+\Delta\sigma}$), stiffness plus surface stress ($f_i^{+k,+\Delta\sigma}$), and finally mass, stiffness, and surface stress ($f_i^{+m,+k,+\Delta\sigma}$), respectively.

$$f_i^{+m,+\Delta\sigma} = \frac{(\alpha_i^{\Delta\sigma})^2}{2\pi\sqrt{3}}\sqrt{\frac{k}{M_b + \Delta M}} \tag{77}$$

$$f_i^{+k,+\Delta\sigma} = \frac{(\alpha_i^{\Delta\sigma})^2}{2\pi\sqrt{3}}\sqrt{\frac{k}{M_b} + \frac{3E_{ads}I_{ads}}{L^3 M_b}} \tag{78}$$

$$f_i^{+m,+k,+\Delta\sigma} = \frac{(\alpha_i^{\Delta\sigma})^2}{2\pi\sqrt{3}}\sqrt{\frac{k}{M_b + \Delta M} + \frac{3E_{ads}I_{ads}}{L^3(M_b + \Delta M)}} \tag{79}$$

Analogously, to include the effects of surface stresses modeled with the axially-loaded beam, one could use $\underline{\alpha}_i^{\Delta\sigma}$ of Equation 76 in Equations 77 through 79. The reader should note, however, that the effects may be coupled (e.g., a tensile surface stress and a mass loading will both act to reduce the ith mode resonance frequency).

Currently, the exact cause of the surface stress difference is undergoing scrutiny by many groups. An earlier school of thought proposed a free energy difference between the surfaces as in the work of Wu *et al.* and Chakraborty *et al.* [263, 41]. These arguments of reduced conformational states of the adsorbed molecules with increasing adsorption is backed by experimental evidence which is mainly limited to long-chain molecules (e.g., DNA and polymers) and hence could be insufficient for shorter chain molecules. Two other explanations are due to Hagan *et al.*, who propose that the deflection may be due to hydration forces in certain cases [94], and Liu *et al.* who claim that the deflection may be due to the flexoelectric effect, which states that the change in electric potential across the adsorbed layer will change the curvature of the microcantilever [144]. These works do not give a general scheme for the effect of surface stress, as is developed here. However, the root cause of surface stress generation is not considered for this work under given adsorption situations, only the effects of the surface stress upon resonance.

3.3.3.7 Damping Effects

The no-damping assumption leading to Equations 54 and 58 (and the subsequent equations derived from these) is only used when the beam is operated in a medium which will not severely effect its motion. This can be estimated by Equation 80, which relates the ith mode resonant frequency of a beam with density ρ_b oscillating in a vacuum, f_i^v, to the frequency when oscillating in, and hence damped by, a fluid of density ρ, f_i^D for a Reynolds number[20] much greater than 1 (i.e., inertia-resistance dominated, so the resistance is roughly proportional to the acceleration of the cantilever [142]).

$$\frac{f_i^v}{f_i^D} = \left(1 + \frac{\pi \rho w}{4 \rho_b t}\right)^{-\frac{1}{2}} \tag{80}$$

Figure 16 shows a plot of percent frequency error due to damping effects error [i.e., $100(f_i^D - f_I^v)/f_i^v$] as a function of beam width and thickness when the beam is oscillating in air. All of beams produced for this work will exhibit an error of less than 3%, the vast majority are under 2%, and roughly half are below 1%. It should be noted that while the damping effects in air have only a minute effect on the resonance frequency, the effect on the beam quality factor (Q) can be quite dramatic, with Q jumping from the order of 10-100 in air to the order of 1000-10,000 in vacuum [14]. For flows where the Reynolds number is much less than 1 (i.e., damping mainly due to the viscosity of the fluid engulfing the beam), an expression for f_i^v/f_i^D is given as Equation 81 [220].

$$\frac{f_i^v}{f_i^D} = \left(1 - \frac{1}{4Q_i^2}\right)^{-\frac{1}{2}} \tag{81}$$

This form for an error estimate was chosen because the ith mode quality factor, Q_i, is commonly measured and is nearly always greater than 10 (when a beam is measured in air). This indicates that the error will be less than 0.5%, making the no-damping

[20]The reader will recall that the Reynolds number is a commmonly-employed dimensionless parameter which is a ratio of the inertial forces in a fluid flow to the viscous forces – among other things, the Reynolds number will dictate when a fluid flow will progress from laminar to turbulent.

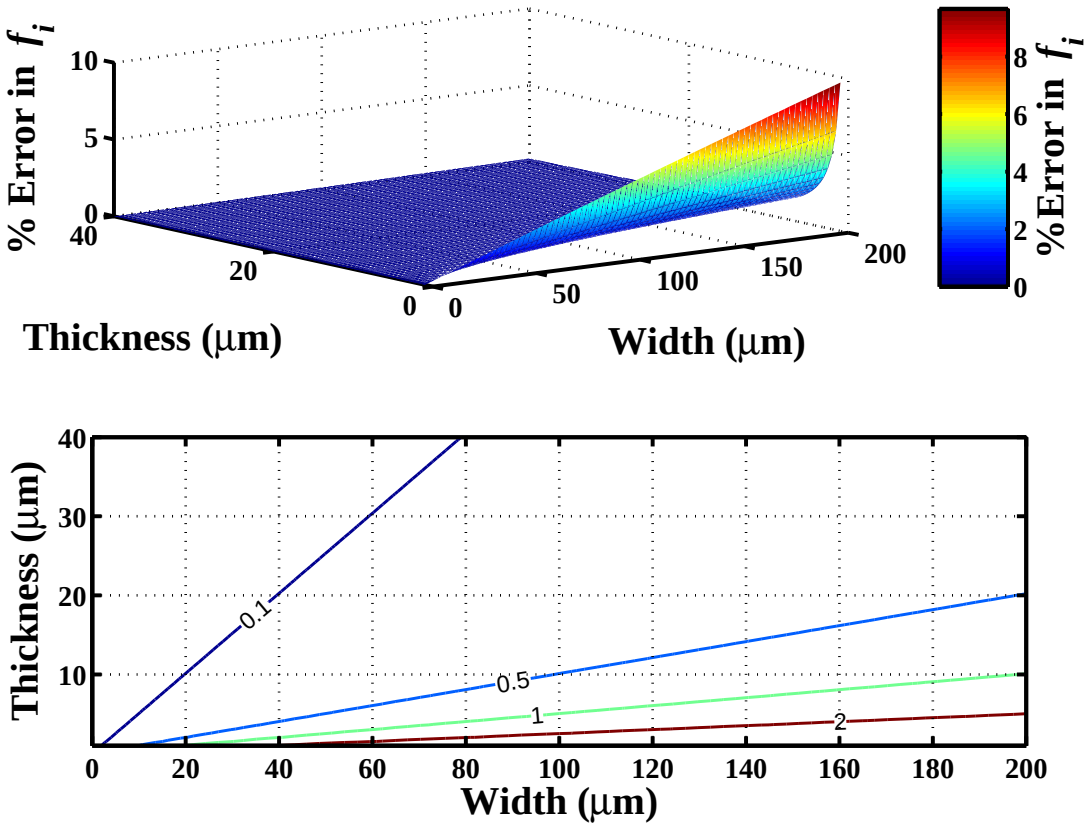

Figure 16: Surface (top) and contour (bottom) plot of percent error in f_i for a microcantilever oscillating in air versus oscillating in vacuum as a function of beam width and thickness, for Reynolds numbers much larger than one (numbers in the contour lines of the bottom plot denote percent error in stiffness).

assumption acceptable in air. Indeed, previous work has shown the resonance due to air damping will reduce by roughly 2% [220].

The reader will realize that, in addition to damping effects, the non-ideal boundary conditions at the base of the microcantilever will influence its resonance behavior. While this is true to some extent, for the microcantilever part geometries of this work the effects are shown to be negligible in Appendix B.

3.3.4 Theoretical Determination of Microcantilever Geometry– New Approach

With the free resonance of a microcantilever discussed in §3.3.3.2, coverage of the torsional resonance frequency allows for the determination of microcantilever geometry solely by observation of resonance phenomena [173]. This approach to geometry and hence bending stiffness, torsional stiffness, and mass determination (assuming certain material properties are known) is new to the literature and is useful because it requires no invasive (and potentially destructive) procedures as in the method of Cleveland *et al.* [50] and Holbery *et al.* [100], no deflection calibration as in the method of Hutter and Bechhoefer [105], no curve fitting as in Sader's Method [219] and the method of Hutter and Bechhoefer [105], no beam geometry measurement as needed for Sader's method and to employ EB beam theory, and no reference microcantilever knowledge as in the method of Tortonese and Kirk [246]. The sole requirements of this new method are *estimates* of the beam geometry, and knowledge of the beam elastic modulus, density, and Poisson's ratio, all of which are nearly always available from the manufacturer [7, 5]. With these pieces of information, one may use the measured frequency of a lateral, bending, and torsional resonance mode to determine the beam geometry (to high accuracy). The untreated mathematical details of this technique are now covered.

A similar approach as that used to obtain Equation 53 is employed to obtain the sth mode torsional resonance frequency of a cantilevered beam, f_s^t. The equations of

free motion are given as Equation 82

$$\left(\frac{G\xi}{\rho_b I_\mathrm{p}}\right)\frac{\partial^2\theta}{\partial x^2} = \frac{\partial^2\theta}{\partial T^2} \tag{82}$$

where $\theta(x,T)$, ρ_b, and I_p are the twist angle (see Figure 8) as a function of position along the beam length (x) and time (T), density, and polar moment of the cross sectional area of the cantilever, respectively, and ξ is a function of the cross section to be discussed subsequently. Assuming harmonic motion allows for the twist to be expressed as Equation 83

$$\theta = \sum_{s=1}^{\infty}\Theta_s(x)(F_s\cos\varpi_s T + G_s\sin\varpi_s T) \tag{83}$$

where $\varpi_i = 2\pi f_s^t$ is the torsional angular frequency of vibration of the sth torsional mode, the Θ_s are the modeshapes, and the F_s and G_s are constants. Substituting Equation 83 into Equation 82 yields Equation 84

$$\frac{\partial^2\Theta_s}{\partial x^2} + q_s^2\Theta_s = 0 \tag{84}$$

where $q_s^2 = \varpi^2\rho_b I_\mathrm{p}/G\xi$. The general solution to Equation 84 is $\Theta_s = A_s\sin q_s x + B_i\cos q_s x$ where A_s and B_s are constants. The first boundary condition of no twist at the base of the cantilever $[\theta(0,T)=0]$ implies that the $B_s = 0$. The second boundary condition of no torque acting on the end of the cantilever gives Equation 85.

$$\left.\frac{\partial\theta}{\partial x}\right|_{x=L} = 0 \Rightarrow \cos q_s L = 0 \Rightarrow$$

$$q_s = \frac{(2s-1)\pi}{2L} \text{ for } s = 1,2,3,\ldots \tag{85}$$

Using Equation 85 along with the expression $q_s^2 = \varpi^2\rho_b I_\mathrm{p}/G\xi$, yields Equation 86, which gives the sth mode torsional resonance frequencies for a cantilever beam.

$$f_s^t = \frac{(2s-1)}{4L}\sqrt{\frac{G\xi}{\rho_b I_\mathrm{p}}} \tag{86}$$

For reference, Figure 17(a) through (c) shows the first bending, lateral, and torsional modeshape.

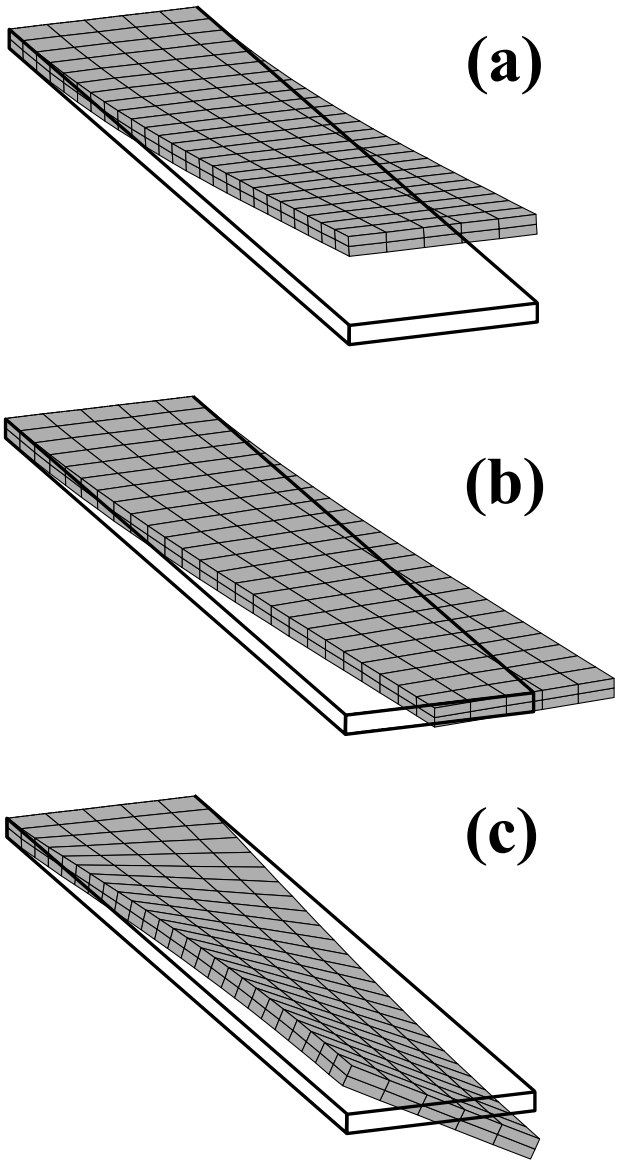

Figure 17: First bending (a), lateral (b), and torsional (c) modeshapes, the heavy solid lines denote the undeformed cantilever.

3.3.4.1 Experimental Implications

Some new notation is introduced here to describe the ith bending mode f_i^b [Figure 17(a)], and the jth lateral mode f_j^l [Figure 17(b)]. Equation 54 gives f_i^b, and substitution of w for t in Equation 54 gives Equation 87 to calculate the f_j^l, as the microcantilever is now deflecting in the width direction[21].

$$f_i^l = \frac{w}{4\pi}\left(\frac{\alpha_i}{L}\right)^2\sqrt{\frac{E}{3\rho_b}} \tag{87}$$

The α_i^b and α_j^l are known from Equation 52. Assuming that the microcantilever material properties are known [e.g., ρ_b, E, and ν (or equivalently, G)], and that a bending, lateral, and torsional frequency can be measured, Equations 54, 86, and 87 comprise three equations in three unknowns (e.g., L, w, and t). Therefore, it could be possible to determine the beam geometry (i.e., L, w, and t) if, for example, f_1^b, f_1^l, and f_1^t can be measured, so long as the ξ of Equation 86 can be manipulated properly. With certain reasonable assumptions, this is possible as is now shown.

The ξ of Equation 86 is defined in Equation 88 [243].

$$\xi = \frac{1}{3}t^4\left(\frac{w}{t} - \frac{192}{\pi^5}\sum_{n=1}^{\infty}\frac{1}{n^5}\tanh\frac{n\pi w}{2t}\right) \tag{88}$$

To avoid the use of numerical procedures, it is realized that the hyperbolic tangent function in Equation 88 converges rapidly to unity when the argument grows. Assuming a small width-to-thickness ratio of 5 (i.e., a conservative approach), the value of the hyperbolic tangent term for $n = 1$ differs from unity only in the fifth decimal place, for $n = 2$ in the twelfth decimal point, and is equal to unity to working precision for $n \geq 3$. Therefore, it is acceptable to approximate the hyperbolic tangent term as unity for each n, and the summation can be rewritten as Equation 89

$$\sum_{n=1}^{\infty}\frac{1}{n^5}\tanh\frac{n\pi w}{2t} \approx \sum_{n=1}^{\infty}\frac{1}{n^\beta} \tag{89}$$

[21]Shear effects will become more dominant in the lateral mode, and will be on the order of 5-10% [244]

where $\beta = 5$. For $\beta > 1$ Equation 89 is a rapidly convergent series [109]; the value is approximately 1.040 for $n = 1 \times 10^6$. Equation 88 can now be recast as Equation 90.

$$\xi = \frac{1}{3}t^4 \left(\frac{w}{t} - \frac{192}{\pi^5} \sum_{n=1}^{\infty} \frac{1}{n^5} \right) \tag{90}$$

It is now desired to obtain an expression for the quantity $\sqrt{\xi / I_{\mathrm{p}}}$ *solely* in terms of the empirical parameters f_i^l and f_j^b. This result, when substituted into Equation 86, will allow for a completely empirical determination of L, and subsequent determination of w and t, and other desired beam parameters (e.g., stiffness, $k = Ewt^3/4L^3$ and mass, $m = Lwt\rho_b$).

Examination of Equations 54 and 87 shows that the quantity w/t in Equation 90 is equal to $f_j^l(\alpha_i^b)^2 / f_i^b(\alpha_j^l)^2 \equiv \Psi$. Coupled with Equation 90, ξ can be expressed as Equation 91

$$\xi = \frac{1}{3}t^4 \Lambda \tag{91}$$

where Λ, which is entirely empirical, is defined by Equation 92.

$$\Lambda = \left(\Psi - \frac{192}{\pi^5} \sum_{n=1}^{\infty} \frac{1}{n^5} \right) \tag{92}$$

The definition of I_{p} for a rectangular cantilever is given as Equation 93 [242].

$$I_{\mathrm{p}} = \frac{1}{12} \left(tw^3 + wt^3 \right) \tag{93}$$

Combining Equations 91 and 93 yields Equation 94.

$$\sqrt{\frac{I_{\mathrm{p}}}{\xi}} = \left[\frac{1}{4\Lambda} \left(\frac{tw^3 + wt^3}{t^4} \right) \right]^{\frac{1}{2}} \Rightarrow$$

$$\sqrt{\frac{\xi}{I_{\mathrm{p}}}} = \left[\frac{1}{4\Lambda} \left(\Psi^3 + \Psi \right) \right]^{-\frac{1}{2}} \tag{94}$$

Substitution of Equation 94 into Equation 86 and solving the result for L, yields Equation 95

$$L_{ijs} = \frac{(2s-1)}{2f_s^t} \sqrt{\frac{G\Lambda}{\rho_b}} \left(\Psi^3 + \Psi \right)^{-\frac{1}{2}} \tag{95}$$

where the s index (denoting the torsional mode number) is used because the the torsional mode need not be the same as the lateral and bending modes (denoted by i and j, respectively).

Equation 95 is *entirely* empirical, and substitution of the L value obtained from it into Equations 54 and 87 allow for an *entirely* empirical determination of the microcantilever geometry solely by measuring resonance behavior. Additionally, one could measure the resonant frequencies (of either the bending, lateral, or torsional modes or any combination thereof) for different values of i, j, and s in Equation 95 (i.e., L_{111}, L_{121}, L_{112}, etc.) to get multiple estimates of L (and subsequently w and t), although experimental limitations (e.g., Nyquist frequency) may only allow the lower modes to be measured. The approach of this subsection is capable of determining the beam geometry (and hence stiffness and mass), and is new to the literature. The following subsection details the other experimental approaches that were used to characterize the microcantilevers of this work.

3.3.5 Experimental Determination of Stiffness and Resonant Frequency

The techniques in this subsection are mainly empirical, and as such they, in theory, do include the length scale effects of some of the continuum models in §3.1, although these effects are not dealt with specifically in the formulation of the methods. Rather, the formulation employ energy arguments which implicitly include strain gradient-type effects due to the empirical nature of the techniques.

3.3.5.1 The Equipartition Method (a.k.a. Sensitivity Method or Method of Hutter and Bechoefer)

One of the techniques used to determine stiffness and resonant frequency in this work is that of Hutter and Bechoefer, who assumed that a microcantilever vibrating in a fluid could be adequately described by a simple harmonic oscillator, and hence

modeled the thermally-induced beam displacement as shown in Equation 96 [105]

$$A(f) = A_{DC} f_1^2 \left[(f_1^2 - f^2)^2 + \frac{f_1^2 f^2}{Q^2} \right]^{-\frac{1}{2}} \tag{96}$$

where $A(f)$ is the amplitude as a function of frequency, A_{DC} is the DC amplitude, f_1 is the first resonant frequency, and Q is the beam quality. Hutter and Bechoefer then employed statistical mechanics and equated the mean value of any harmonic energy term to the thermal energy (i.e., the equipartition theorem) as described by Equation 97

$$\frac{1}{2} K_B T = \frac{1}{2} k \langle A^2 \rangle \tag{97}$$

where K_B is the Boltzmann constant, T is the absolute temperature, k is the effective beam stiffness, and $\langle A^2 \rangle$ is the mean-square amplitude of the cantilever thermal motion. Therefore, if one can calculate $\langle A^2 \rangle$, then the beam stiffness may be determined directly. To find $\langle A^2 \rangle$, the thermal spectra data is fit to an analytical equation, such as Equation 96. This work used a more advanced fit form, which included terms for a white noise floor, and $1/f$ noise of the form shown in Equation 98

$$A(f) = C_0 + \frac{C_1}{f^{C_2}} + A_{DC} f_1^2 \left[(f_1^2 - f^2)^2 + \frac{f_1^2 f^2}{Q^2} \right]^{-\frac{1}{2}} \tag{98}$$

where the fit quantities (determined via a nonlinear least squares optimization algorithm) are: C_0, C_1, C_2, A_{DC}, f_1, and Q. One shortcoming of techniques requiring $\langle A^2 \rangle$ is that to determine $\langle A^2 \rangle$ one must measure the sensitivity, c, of the specific AFM-microcantilever configuration (i.e., the amount of voltage change measured by the AFM needed to produce a unit microcantilever deflection). To determine c, the microcantilever is brought into contact with a rigid, flat surface (e.g., mica), the piezoelectrics in the AFM are used to oscillate the entire microcantilever holding mechanism with a given amplitude, and the time-history voltage data acquired by the PSD is logged. A curve of voltage versus deflection is plotted, and the slope of this curve in the region corresponding to rigid surface-microcantilever contact yields the sensitivity; this is a tedious, time consuming process.

It should be noted here that the equipartition theorem in the form of Equation 97 is an approximation assuming that the microcantilever is a harmonic oscillator, the mean total energy of which is equal to K_BT– this is only valid if $K_BT \gg \hbar(2\pi f_i)\forall i$ [60, 99]. Phenomenologically, this limit implies that the approximation is valid as long as the thermal energy supplied to the oscillator (i.e., $K_BT/2$) is sufficient for the oscillator to explore many individual possible quantum states (i.e., resonance modes) – if the modes resonate so high that the energy supplied for the modes ($K_BT/2$) only allows the oscillator to explore a few modes, then the approach is invalid. Experimentally, the limit shows that the method of Hutter and Bechoefer can be used up to resonant frequencies of roughly 10 GHz, which is approximately five orders of magnitude higher than those encountered in this work, making Equation 97 valid.

The correction factor of Butt and Jaschke was used to correct the mean squared amplitude value for a cantilevered beam measured with an optical lever [39]. Their work shows that the apparent mean-squared deflection (i.e., that seen by the photodiode) is four-thirds of the actual mean-squared deflection experienced by the cantilever. This is because, when using the optical lever, the beam end slope information is acquired (from the photodiode output) to determine deflection (via the first derivative of Equation 20), and the deflection is assumed to come *only* from the first mode, when, in reality, *each* mode (there are an infinite number of them) contributes to the slope and hence the displacement. Butt and Jaschke showed the "4/3" factor transforms the mean squared amplitude from the single mode assumption to the correct, infinite mode situation.

3.3.5.2 Sader's Method

Sader's method, which does not require sensitivity calculation, also was employed in this work [219, 217, 220]. The derivation of this technique starts with the dynamic

governing equation for a beam and, through the use of Fourier transforms, casts the equation into the frequency domain. Extensive mathematics provide exact answers for bars of circular cross-section and, through use of a correction factor, give an approximation good to less than 0.1% for a wide range of Reynolds numbers ($Re \in [10^{-6}, 10^{4}]$). For rectangular beams, the final equation for calculating beam stiffness is reproduced as Equation 99

$$k = 0.1906\rho_f w^2 L Q \Gamma_i(\omega_1)\omega_1^2 \tag{99}$$

where ρ_f is the density of the fluid that the beam is in, ω_1 is the characteristic radial vibration equal to $2\pi f_1$, and Γ_i is the imaginary component of the hydrodynamic function defined in Equation 100. The values for f_1 and Q are obtained by fitting an analytic form, such as Equation 98 to thermal spectra data

$$\Gamma(\omega) = \left[1 + \frac{4iK_1\left(-i\sqrt{iRe}\right)}{\left(-i\sqrt{iRe}\right)K_0\left(\sqrt{iRe}\right)}\right]\Omega(\omega) \tag{100}$$

where K_0 and K_1 are modified Bessel functions of the third kind,[22] Re is the Reynolds number equal to $\rho_f \omega w^2/4\eta$, where η is the dynamic viscosity of the fluid in which the beam vibrates. The lengthy expression for $\Omega(\omega)$ is given in Equation 101 with plots

[22]Bessel functions of the third kind and order ν, $K_\nu(z)$ $(z \in \mathbb{C})$ are solutions to the so-called modified Bessel differential equation: $z^2y'' + zy' - \left(z^2 - \nu^2\right)y = 0$.

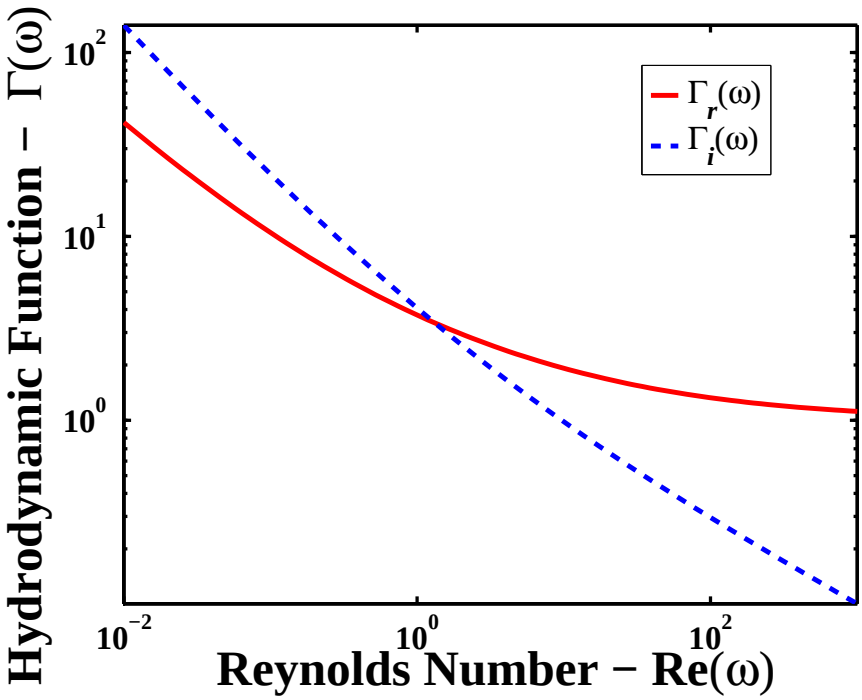

Figure 18: Hydrodynamic function values.

of the real and imaginary components given for reference in Figure 18.

$$\Omega(\omega) = \Omega_r(\omega) + i\Omega_i(\omega)$$

where

$$\Omega_r(\omega) = (0.91234 - 0.48274\tau + 0.46842\tau^2 - 0.12886\tau^3 + 0.044055\tau^4$$
$$-0.0035117\tau^5 + 0.00069085\tau^6)(1 - 0.56964\tau + 0.48690\tau^2 - 0.13444\tau^3$$
$$+0.045155\tau^4 - 0.0035862\tau^5 + 0.00069085\tau^6)^{-1}$$

and (101)

$$\Omega_i(\omega) = (-0.024134 - 0.029256\tau + 0.016294\tau^2 - 0.00010961\tau^3$$
$$+0.000064577\tau^4 - 0.000044510\tau^5)(1 - 0.59702\tau + 0.55182\tau^2 - 0.18357\tau^3$$
$$+0.079156\tau^4 - 0.014369\tau^5 + 0.0028361\tau^6)^{-1}$$

and

$$\tau = \log_{10} Re$$

The works of Sader *et al.* also showed that in the limit of small dissipative effects (i.e., beam motion in a vacuum) and with $Q \gtrsim \mathcal{O}(10)$, as it is for this research,

that the model reduces to the SHO system, which is reassuring. Additionally, recent work has shown that Sader's method is still applicable to microcantilevers with end masses attached, so long as the end mass is less than the equivalent mass of a sphere with diameter equal to half the cantilever width and made from the same material as the cantilever– this will come into play when Sader's method is used to characterize injection molded SPM probes, as discussed in Chapter 5 [92]. In closing, it should be noted that Sader's method is fundamentally an energy-based method, as it employs the equipartition theorem of §3.3.5.1. This concludes the discussion of beam stiffness and resonant frequency determination techniques for this chapter.

3.4 Summary

This chapter opened with coverage of elasticity theories (§3.1), a subset of which were used to present existing and derive new length scale dependent bending stiffnesses for microcantilevers along with new resonance and surface stress relations involving length dependencies (§3.3). The operational modes of microcantilevers were discussed along with existing and new theories of analytically characterizing the stiffness and resonance behavior of microcantilevers. Chapter 4 discusses the experimental procedures and equipment used to examine the validity of the new theories presented in this chapter (e.g., the length-scale dependent stiffness of §3.3.1.3, the surface stress effects on resonance frequency of §3.3.3.6, and the resonance-based geometrical characterization technique of §3.3.4), and to discuss the software intricacies involved with the finite element analyses. Chapter 5 presents the simulation and experimental results (obtained using the methods of Chapter 4) and compares them to the theories of this chapter.

CHAPTER IV

EXPERIMENTAL METHODS

This chapter details the experimental apparatus and procedures used to produce the polymeric microcantilevers, along with some of the associated microcantilever characterization approaches. The chapter opens with a description of the manufacturing equipment and techniques used to make polymeric microcantilevers by solvent casting (§5.1.1) and followed by injection molding (§4.1.2). Next, the characterization equipment and procedures are described (§4.2) and the chapter closes with the details of the finite element analyses used for this work (§4.3).

4.1 Manufacturing Details

This section describes the successful manufacturing schemes used for this work, along with the associated equipment, fabrication, and design processes employed.

4.1.1 Solvent Casting

The solvent casting approach consists of producing a polymer film upon a glass base, cutting the film using custom tooling, and mounting of cut strips of film to base parts for subsequent characterization in an atomic force microscope [172].

4.1.1.1 Experimental Methods

To make the polymer film, polystyrene pellets (Chevron GPPS 3600, Chevron Phillips Chemical Co., Woodlands, TX) were dissolved in xylene (at room temperature for approximately one hour) to make a 1:15 PS-xylene solution that was deposited onto glass microscope slides with a syringe and allowed to dry (≈15 min for a 15:1 solution)

producing a polystyrene film. Film thickness can be controlled by varying the xylene-PS mixture ratio; submicron films are possible. The films then were coated with roughly 25 nm of gold using an electron beam evaporator (CVC Products Electron Beam Evaporator, CVC Products Inc., Rochester, NY) at a rate of 0.5 Å per second.

To produce the microcantilever parts, the films were cut with a razor blade mounted in a machining center (Benchman VMC-4000, Light Machines Division, Intelitek, Inc., Manchester NH, positional accuracy of ± 2 μm). First, cuts were made in the x-axis direction, as shown in Figure 19(a), with a y-axis direction spacing equal to the desired beam width. This produces strips of polymer film that will become the microcantilevers. Next, cuts were made in the y-axis direction (with an x-axis direction spacing that determines the final beam length) and PS base parts were glued to the films at specific locations as shown in Figure 19(b). The surfaces of the base parts that come into contact with beams were lightly coated with xylene and then pressed upon the polymer film, which effectively joins the base parts and beams. To remove the base parts with the beams attached to them, the entire assembly (glass base, PS film, and PS base parts) was placed in water for roughly one hour; the hydrophylicity of the glass caused water to seep in between the glass base and the polymer film, hence freeing the beams from the glass base. This produced a base with a microcantilever attached to it, as shown in Figure 19(c). Using this solvent casting technique, beams with micron thicknesses and widths down to 25 microns were produced. The technique can produce beams with lengths of up to 25 mm, but for AFM-type applications, the beams were made with lengths of roughly 500 microns.

4.1.2 Injection Molding (IM)

Injection molding (or micromolding as applied to this work) presents itself as an economical and reliable way to mass-produce a variety of parts. Traditionally, products ranging from disposable cups and silverware to cellular phone cases and toothbrushes

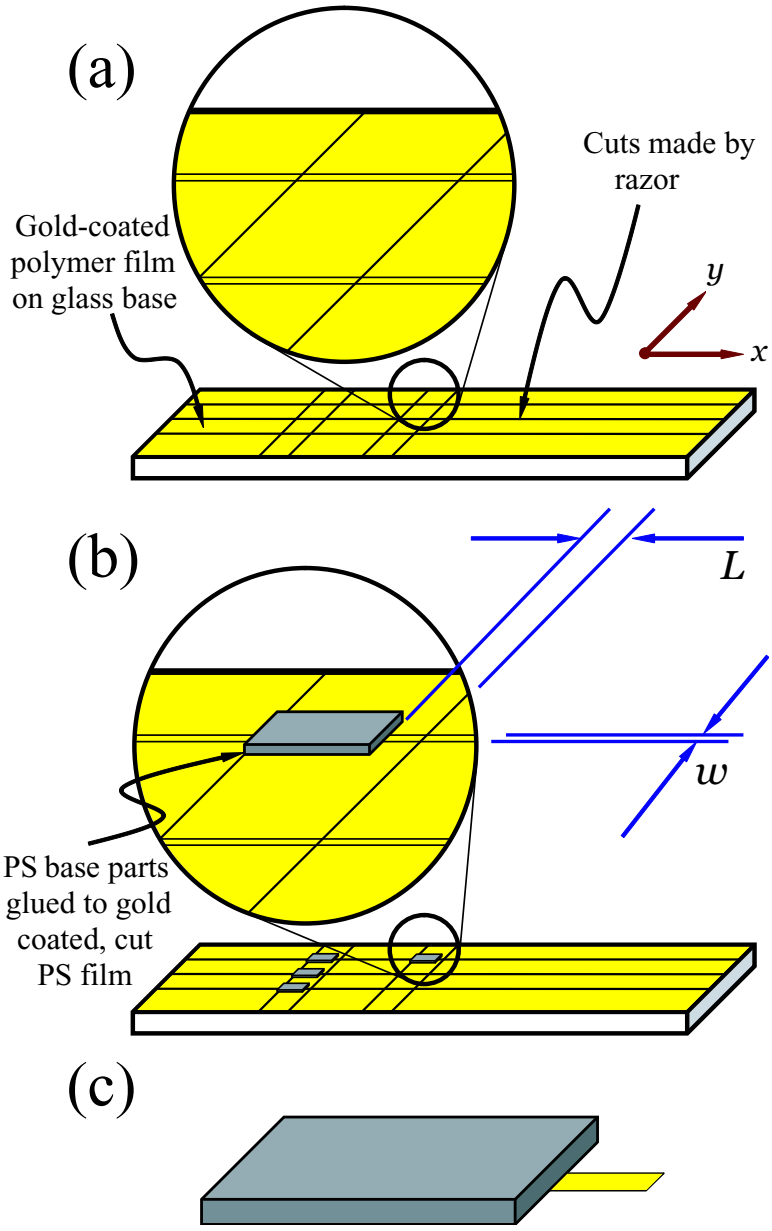

Figure 19: (a) The polymer film cutting geometry scheme; (b) The method of attaching the beams to base parts for subsequent measurement in an AFM; (c) The final microcantilever parts (as in the previous chapter, L, w, and t are the length, width, and thickness of the microcantilever, respectively).

are injection molded. This subsection details the injection molding process and then covers the equipment and fabrication techniques used to employ IM for this work [170].

4.1.2.1 Injection Molding Process

While the micromolding process was covered briefly in §2.1.11.1, a more thorough description is given here as the technique is the primary manufacturing approach of this work. The most important components involved in the injection molding process of this work are the the mold halves (see Figure 20), either or both of which contain the cavity with the desired shape of the part. Part production begins with the injection stage in which the two mold halves are forced together to mate at the "parting plane" and the polymer melt is delivered by other components of the injection molding machine (see Figure 20). During the holding stage, the polymer is allowed to cool, while pressure is still applied to the melt to minimize thermal shrinkage (see Figure 20). The cooling stage removes heat from the part (as in the water cooling of this work) and the part ejection stage consists of opening the mold halves, removing the part, and reheating the mold for the next cycle. Figure 20 is a depiction of the micromolding cycle, which is different than the cycle of a conventional scale injection molding machine mainly in that, in micromolding, the molds must be heated above the glass transition temperature of the polymer prior to melt injection to ensure that the melt does not freeze prematurely (e.g., a short shot).

4.1.2.2 Mold Design and Production

In conventional injection molding, the general approach is to produce the mold and associated support components in as rigid a fashion as possible, in an attempt to ensure acceptable alignment and mating of the relevant portions of the molding apparatus. Proper specification and rigorous attainment of the manufacturing tolerances (e.g., parallelism, surface roughness, cylindricity, and concentricity) is necessary for the molding system to satisfy these criteria. In micron-scale IM (dubbed micromolding

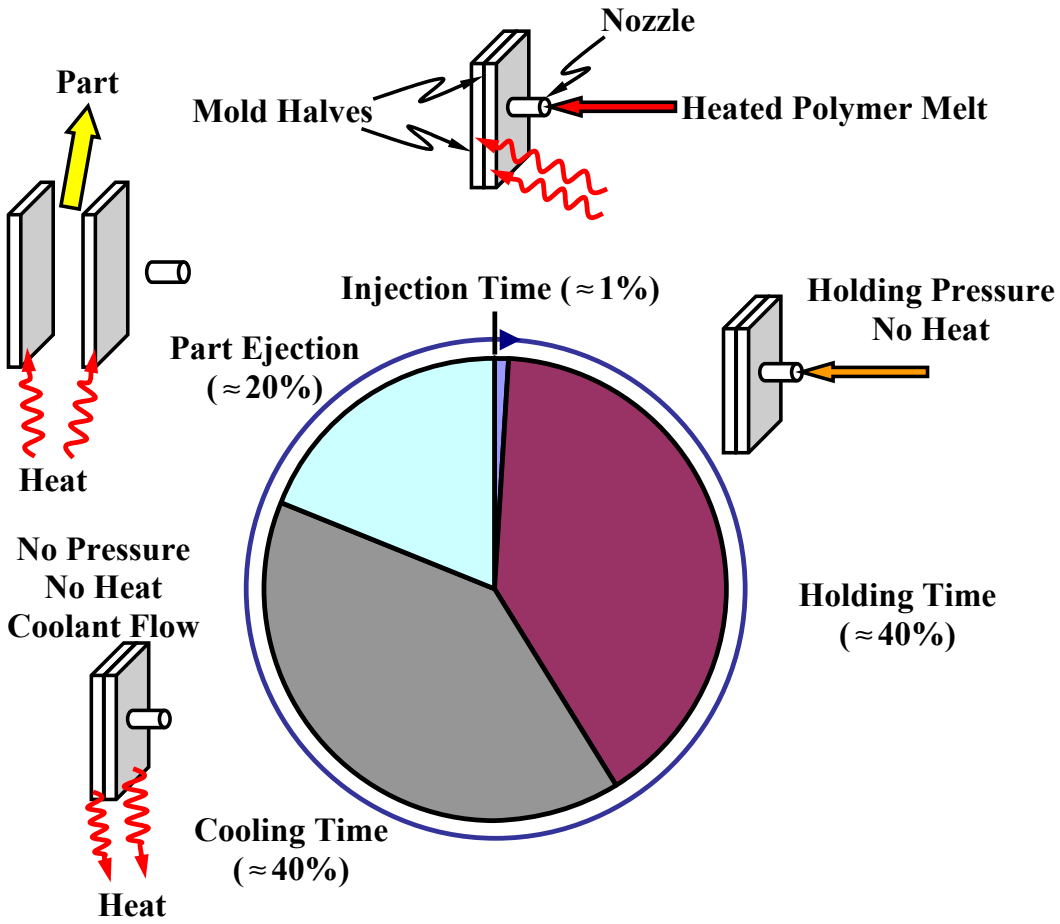

Figure 20: Schematic of the main stages of the micromolding process, associated equipment, and percentage of total cycle time spent at each stage (cycle time is roughly one minute for a single part).

in some circles), the magnitude of these tolerances diminishes significantly. Production of a rigid mold component setup for true micromolding is problematic as the compliance and stack-up error of the individual components will likely violate the tolerance requirements necessary at the parting plane. For example, a maximum error of parallelism at the parting plane of a molding system (which would usually consist of at least four components) of one ten-thousandth an inch (equal to roughly 2.54 μm) would be extremely difficult to satisfy, but is usually considered very precise for a conventional-scale mold. In the micromolding considered in this work, a parallelism error of 2.54 μm would be catastrophic; the error is nearly as large as the thickness of the microcantilevers themselves. With this magnitude of error, the plastic would flow in regions other than the mold cavity (i.e., flash) rendering the parts useless.

To overcome the need for such high-precision machining of all parts of the molding system, one half of the mold is supported by a spring-loaded floating support structure and mates with the other half of the mold which is rigidly mounted [166]. Figure 21 shows an exploded view of the mold setup while Figure 22 shows a collapsed view. The spring-loaded half of the mold can translate in the direction normal to the parting plane (the plane where the two halves of the mold meet) and rotate about any two orthogonal axes in the parting plane, hence allowing for accurate surface alignment of the two mold halves. This design ensures sufficient parallelism with stringent flatness and surface tolerances on *only two* surfaces (i.e., the two surfaces which meet at the parting plane), which is a significant improvement over existing designs.[1]

The mold cavities which form the microcantilever parts are confined to the top and bottom insert shown in Figure 21. Machining of the mold cavity was performed in two

[1]Flatness, as defined by Federal Specification GGG-P-463c is: All points on the surface lie between two parallel planes, separated by 'X' distance, where 'X' is the overall flatness tolerance. This is a unilateral tolerance, not a plus/minus tolerance. The parallelism is numerically defined as the difference in slopes (or normals) between two planar surfaces.

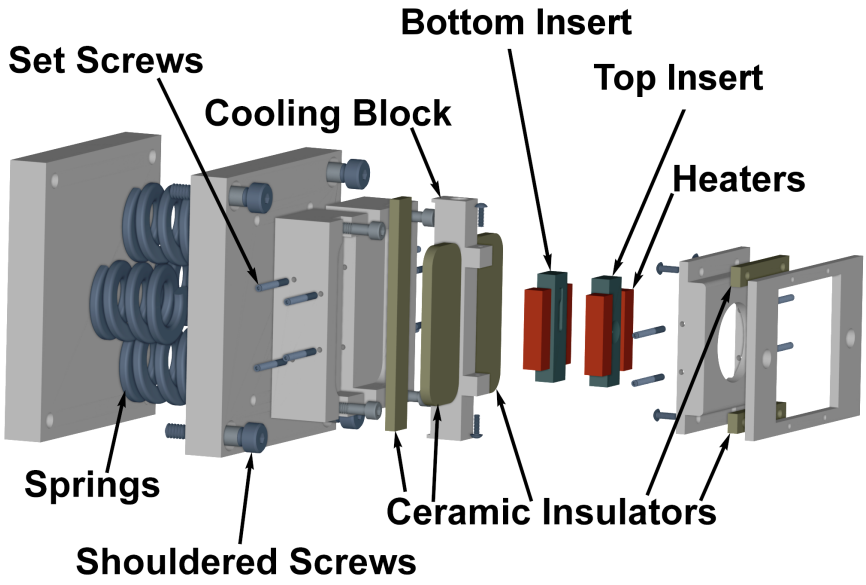

Figure 21: Exploded view of injection mold setup.

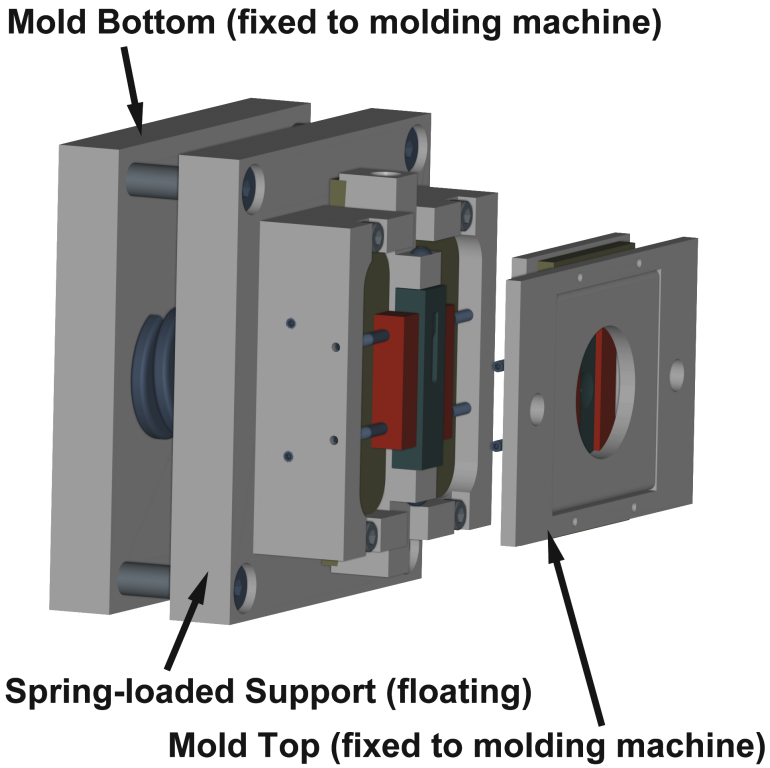

Figure 22: Collapsed view of injection mold setup.

steps. In the first, a CAD model was generated (Pro Engineer Wildfire, Parametric Technology Corp., Needham, MA) and imported into a numerical control code generation program (SurfCAM 2001, Surfware, Inc., Westlake Village, CA), the output of which was passed to a machining center (Benchman VMC-3000, Light Machines Corp., Manchester, NH) to machine the part cavity that comprised the base part, generically shown in the bottom portion of Figure 23. The cavities that define microcantilever dimensions (generically shown in the bottom portion of Figure 23) were cut into the same steel block using a custom-made piezoelectric positioning stage-spindle setup (Stage/Positioning setup: FiberMax 6-axis Nano-Positioner, U500 Motion Controller, DR300 Amplifiers $\times 2$, all from Aerotech, Inc. Pittsburgh, PA. Spindle/drive setup: SLF Fraureuth FS33-60/0.15.1 0-60 kRPM spindle, HPT Precision Spindles & Drives, Inc., Newport Beach, CA, with a Hofer AC/DC 0302 Frequency Converter, Hofer Precision Tool Imports Co., Port Washington, NY).[2] The base part cavity was machined in 10 μm steps in the direction normal to the parting plane (plunge feed rate of 0.1 mm/min) at a linear feed rate of 1 mm/min in the parting plane directions using a four flute, 0.8 mm diameter, center-cutting cobalt end mill operated at 5,000 RPM. The channels for the microcantilevers were cut with two flute, center-cutting end mills (50, 75, and 100 μm diameter, depending on desired channel width, all at 50,000 RPM) using a linear feed of 1 mm/min in the parting plane directions and a single step down in the beam thickness direction (with a step distance equal to the desired microcantilever thickness). The plunge motion for these cuts was performed over the previously cut base part cavity, so that no material was removed on the plunge. Multiple passes in the beam length direction produced the various cavity

[2]Daniel Cox, a graduate student of Dr. Steven Y. Liang in the George W. Woodruff School of Mechanical Engineering at the Georgia Institute of Technology, was the impetus behind the design, construction, and successful operation of this micromachining setup and generously donated advice and training.

widths. Figure 24 shows an actual mold cavity for producing three-beam microcantilever parts.

To ensure acceptable tolerances, the mating surfaces of the top and bottom mold inserts must be very flat and smooth. To accomplish this, commercially available gage blocks were used (0.25 inch rectangular Federal Grade II Gage Blocks, Swiss Precision Instruments, Garden Grove, CA). These parts have an average surface roughness of approximately 1 nm [as determined by white light interferometry (Zygo NewView 3000, Zygo Corp. Middlefield, CT.)] and, more importantly, a flatness error less than roughly 51 nm, a value that is certified and NIST-traceable. NIST stands for the National Institute of Standards and Technology, which is a certification and measurement bureau that, among other functions, provides metrological verification, testing, and standards. Gage blocks come with either a "Certificate of Standards", by which the manufacturer ensures that the parts are within specified tolerances when shipped, or a NIST-traceable "Certificate of Calibration" (as the blocks for this work did), which provides exact readings for each gage block along with information such as the NIST test number used in the measurement of the gage blocks and the serial number and grade of each gage block– the flatness and parallelism error is determined via optical flats [61].

4.1.2.3 Workpiece Alignment

To align the workpiece to the tool spindle properly (i.e., to ensure that the spindle axis is as close to perpendicular to the gage block surface as possible) a 500 μm diameter ball end mill was used. Two plunge cuts[3] were made at locations "1" and "2" (approximately 1 inch apart, as shown in Figure 25) to equal machine depth read outs, with optical micrographs of the resulting cuts labeled "A" and "B" in Figure 25. If the was workpiece perfectly normal to the spindle and perfectly flat, these two holes

[3]A plunge cut is a cut caused by motion in the machine axis that should be normal to the workpiece surface in this case.

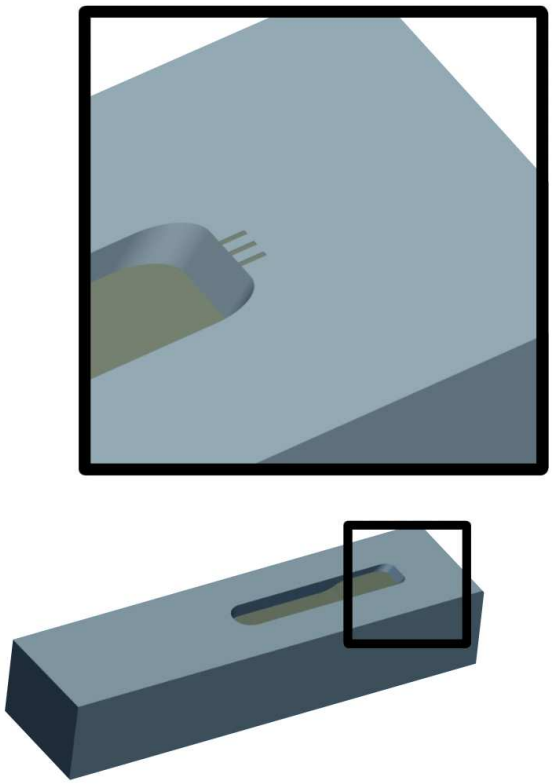

Figure 23: CAD drawing detailing the two machining stages.

would have roughly the same diameter at the workpiece surface. As the marks were not of the same diameter, the geometry of the end mill and the diameter of the cuts allowed for the slope of the block to be calculated. To compensate for the slope, shim stock was placed under the workpiece at its low side, and new plunge cuts were made at at locations "3" and "4" (approximately 1.25 inches apart, as shown in Figure 25) to equal machine depth read outs, with optical micrographs of the resulting cuts labeled "C" and "D" in Figure 25. The diameter scales for the first two cuts (i.e., the red double-headed arrow in Figure 25) is the same as is the diameter scale for the second two cuts, indicating that the alignment procedure was relatively successful. The analogous procedure could only be performed along one direction (since shims could not be used to elevate two sides of the gage block without instability) so the length direction flatness was chosen as the most important. A flat length axis will

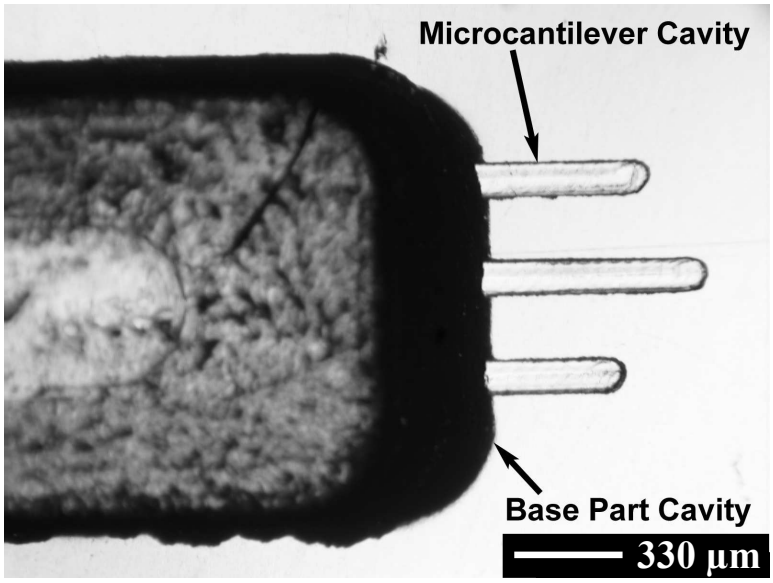

Figure 24: Picture of a mold showing three microcantilever cavities (depth into page ≈ 10 μm).

still leave prismatic beams (so the theories of this work can still be used) but can lead to beam-to-beam thickness variation as the flatness error in the width direction could be large. Nonetheless, width-direction thickness variation will still yield prismatic beams.

4.1.2.4 Mold Heating/Cooling Considerations

In conventional injection molding, the mold itself is usually left at or somewhat above room temperature while the polymer melt is injected at temperatures above its glass transition temperature (e.g., 100 °C for polystyrene). This is unacceptable in micromolding as the flow geometries are so much smaller that *short shots*, or incomplete mold filling, can result. In this work, the mold inserts were heated because the incoming polymer melt would freeze before complete microcantilever channel filling. To accomplish this, two rectangular cross-sectioned heaters (120 V Sunrod Heaters, Sun Electric Heater Company, Danvers, MA) shown in Figures 21 and 22 were used, with the top two heaters wired in series, and likewise for the bottom. The top and bottom

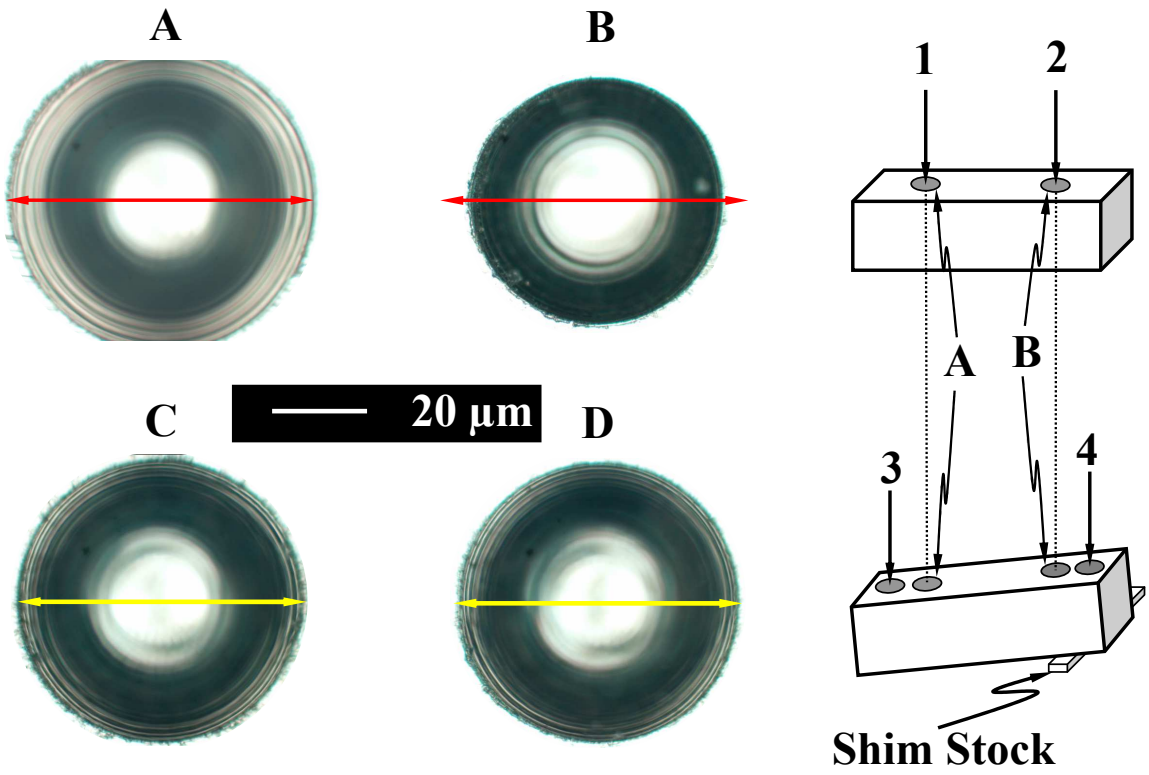

Figure 25: Micromachining table/mounting slope correction procedure (the 20 μm scale applies only to the optical micrographs).

groups were operated by one controller unit each (Eurotherm 2216e General Purpose PID controller, Eurotherm USA, Leesburg, VA). The controllers take a J-type thermocouple as an input, and these thermocouples were internal to the heater blocks shown in Figures 21 and 22.

Heating the mold inserts to T_g posed two post-filling problems, namely extended cooling times and insufficiently rapid cooling, which led to warpage. Therefore, a cooling system was employed to remove heat from the bottom mold by running water through the "Cooling Block" shown in Figures 21 and 22 at flowrates ranging from roughly 0.04 to roughly 0.4 liters per minute. With the highest cooling flowrate (roughly 2 liters per minute) the inserts, which are still forced together during this cooling stage as shown in Figure 20 so the top insert is cooled as well, could be brought from roughly 150 °C to roughly 80 °C in approximately 20 seconds. The total cycle time for one part ranged from roughly 30-60 seconds, and this value was determined by the required maximum mold temperature.

4.1.2.5 Injection Molding Machine

The molding components just discussed were fixed in a machine to process and deliver the polymer melt to the cavities, along with providing a support structure, clamping force for the mold inserts, etc. Due to the small scale of the parts to be produced, a traditional size injection molding machine would possibly not have sufficient filling pressure and would be too large and bulky for convenient mold component positioning and manipulation and for general use. This led to employment of the Sesame .080 Nanomolder (Murray Engineering, Buffalo Grove, IL), a machine geared toward production of small volume parts. Figure 26 is a picture of the machine, with germane components labeled.

The Sesame machine is highly flexible in the selection of process parameters and machine adjustment. Table 2 shows some of the pertinent adjustable variables, their

ranges, and the values for some of the constant parameters used. A touch screen interface allows the user to interact with the software to tailor the machine variables for a specific part. Programs may be created and saved for future production of these parts. The machine is equipped with two temperature controllers to manipulate the nozzle and mold block temperatures. While the touch screen is the main user interface, the machine connects to a personal computer that controls the higher-level machine controls and operation. The Nanomolder possesses manual, semi-automatic, and fully automatic modes.

To produce parts, the hopper motor first loads plastic pellets into the pellet feeder, shown in Figure 27. A pneumatic, *plasticizing cylinder* forces the plasticizing plunger downward into the plasticizing cylinder, melting pellets under pressure in the *heated central block*. The polymer melt applies a force upon the 1.58 mm diameter *injection pin*, pushing the pin and *linear motor sled* backwards until reaching a distance commensurate with the predetermined shot size. Next, closing a high pressure valve restricts polymer flow into the plasticizing cylinder during injection, and activates pneumatic cylinders clamping the mold top and bottom together. The *nozzle sled* is moved forward forcing the *nozzle* against the back of the mold top insert. Then, the linear motor sled moves forward, forcing melt through the injection nozzle and top insert into the mold cavity via the syringe-like action of the *injection pin*. Finally, separate pneumatic cylinders raise the plasticizing plunger, and open the mold. At this stage the machine is ready to repeat the process and produce another part.

4.1.2.6 Shot Size Control Considerations

Early in the project, it was relatively certain that the Sesame molding machine just discussed would be used. This machine is at the forefront of commercially-available machines in terms of shot-size control with a value of roughly $\pm$ 0.01 mm^3, which can

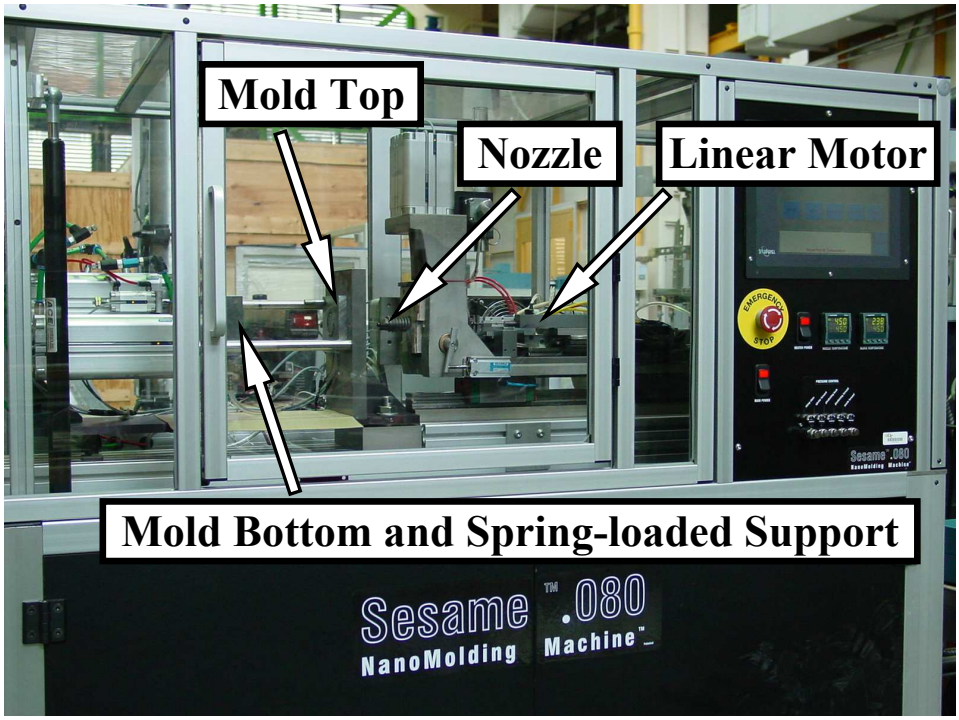

Figure 26: Front view of the Nanomolding machine– dimensions are roughly 2×1×1 meters.

be considered the minimum attainable value barring any serious machine redesign.[4] Two schools of though emerge here, the first proposes to control the metering of the polymer melt into the cavity with such precision that the cavity will be filled "completely" but without any undue pressure (i.e., fill a 1 mm^3 cavity with 1 mm^3 of melt, plus any extra melt to account for thermal shrinkage). The other approach is to make the molding setup robust enough that it could endure excessive pressure encountered when attempting to force "large" melt volume (i.e., more than the cavity volume plus any thermal effects) into the cavity (i.e., trying to push 20 mm^3 of melt into a 1 mm^3 part cavity). Many groups have adopted the prior approach with success, but for this project the last portion of the mold to fill (the microcantilever cavities themselves) is not only the smallest in volume but is also the region of the mold most

[4]This is calculated by taking the area of the injection pin (1.5 mm diameter) and multiplying by the positional resolution of the injection sled in the axial direction of injection pin (± 5 μm).

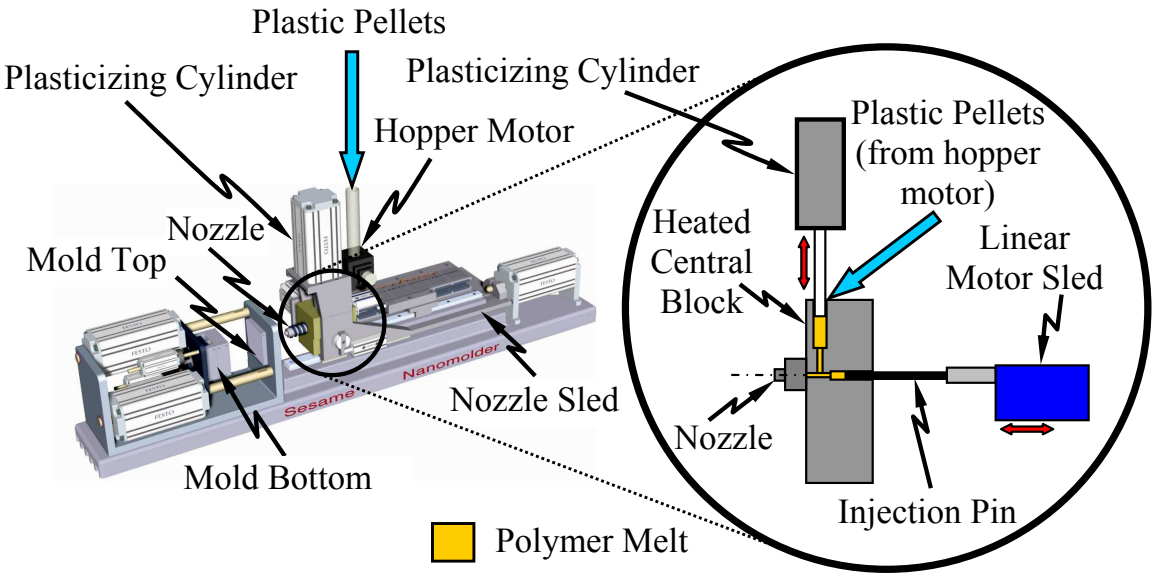

Figure 27: Schematic of the main stages of the micromolding process and associated equipment.

susceptible to flash. To attempt a shot-size control approach, one could realize that the volume of an *entire* microcantilever is roughly 0.005 mm^3, which is less than the shot-size control of the Sesame machine of ± 0.01 mm^3; therefore the the robust mold design approach was taken, which is a very uncommon one in micromolding as it requires much more stringent tolerances on the mold system. One direct effect of this is to remove the dependency of the final part parameters upon requested shot size, as only roughly 50% of the requested shot size actually enters the mold cavity.

4.1.2.7 Material Selection

As mentioned throughout this dissertation, one of the shortcomings of IC-based fabrication is the limited feasible materials available and hence material property ranges of the microcantilevers. To show that the injection molding process has overcome this hurdle, microcantilevers were made of numerous polymeric materials. Two groups of materials were chosen, the first of which is shown in Table 3. This first group

Table 2: Definition and setting of the main injection molding machine parameters.

VARIABLE	DESCRIPTION	RANGE	VALUE USED
MOLD COOL TIME	Time from end of holding pressure application to mold open.	0-60 seconds	Varied
EJECTOR FORWARD DELAY	Time from mold fully open until ejectors are actuated.	0-∞ seconds	Not used
SHOT SIZE POSITION	Distance sled travels back as plastic is loaded (i.e., shot size).	0-40 mm	35 mm
MAXIMUM INJECTION PRESSURE	Maximum allowed pressure during injection of the melt.	10-255 MPa	Varied
SWITCH TO HOLDING PRESSURE	Distance before full excursion that the injection sled will change from velocity control to pressure control.	0-40 mm	40 mm
HOLDING PRESSURE 1	Holding pressure during the first portion of total holding time. Two set points are input here, the first is the pressure and the second is the length of holding time at that pressure.	Set Point 1: 0-255 MPa Set Point 2: 0-20 seconds	Set Point 1: Varied Set Point 2: Varied seconds
HOLDING PRESSURE 2	Holding pressure during the second portion of total holding time. Two set points are input here, the first is the pressure and the second is the length of holding time at that pressure.	Set Point 1: 0-255 MPa Set Point 2: 0-20 seconds	Set Point 1: Varied Set Point 2: Varied
CLAMPING FORCE	Force exerted upon mold to contain injected melt.	0-8.05 kN	8.05 kN
EJECTOR FORCE	Force exerted on ejection plate setup.	0-222.4 N	Not used
NOZZLE FORCE	Force applied on mold top by nozzle assembly during injection.	1.12 kN	1.12 kN

of plastics was chosen to show that injection molding can produce microcantilevers from amorphous polymers, crystalline polymers (roughly 80% by weight [102]), liquid-crystal polymers, and nanoclay-polymer composites with a large variety of flow indices (i.e., material variety).[5]

The second group of materials comprised a neat (i.e., unfilled) PMMA and PMMA-carbon nanofiber (CNF) composites, shown along with their elastic moduli in Table 4.[6] Two different types of CNFs, PR-21-PS and PR- 24-PS of Pyrograf-III™, were used as fillers (Applied Sciences Inc., Cedarville, OH). All CNFs are pyrolytically stripped and polyaromatic hydrocarbons are removed from their surface. The PR-21-PS fiber is a larger diameter than the PR-24-PS ($\approx$ 200 nm versus $\approx$ 100 nm [101]). This second group of materials (i.e., those listed in Table 4) was chosen to show that, given a fixed microcantilever geometry, the beam behavior can be tailored via manipulation of filler percent *for a given polymer*. This tailoring is relevant in situations where a particular beam geometry (from experimental apparatus considerations) and polymer are desired (from chemical bonding considerations), but the unfilled polymer has an elastic modulus too low to provide the correct stiffness for that particular application; boosting the elastic modulus via fillers can raise the stiffness, thereby making the composite beams feasible for use where beams made from neat material would be infeasible. This concludes the discussion of the different materials employed and the logic behind their selection. Attention now turns to the selection of the mold cavity geometry, which is the final destination for the different materials just discussed.

[5]The melt flow index (or melt index) is the number of grams of a fluid (usually a thermoplastic melt) which can be forced through an extrusion rheometer orifice with a specific diameter, under a specified force, in a given amount of time and temperature.

[6]These elastic moduli were experimentally determined via tensile testing of fiber spun specimens of roughly 60 μm diameter.

Table 3: Material group number one descriptions and germane property values.

	Chevron GPPS 3600	Basell/ Montell ProFax 6323	Ticona Vectra A130	Honeywell Aegis XA-2908
Material Description	Atactic, amporphous polystyrene (PS)	Crystalline (≈ 80 wt.%) polypropylene (PP)	Glass fiber filled (30 wt.%), liquid crystal polymer (LCP)	Nanoclay and Nylon 6 composite (NN6)
Density (kg/m^3)	1,040	900	1,400	1,130
Elastic Modulus (GPa)	3.0	1.45	9.1	2.83
Melt Flow Index (grams per 10 minutes)	13.0	12	≈100	4.0

Table 4: Material group number two descriptions and elastic modulus values [270]– the composite materials all use the same PMMA as the matrix material (Cryo Inc., with a MFI 1.8 g/10 min and a density of 1,190 kg/m^3).

Sample	Percent Filler (wt. %)	Elastic Modulus (GPa)
PMMA Control	0	4.7±1.5
PMMA/PR-21-PS	5	8.0±1.2
PMMA/PR-21-PS	10	7.7±1.0
PMMA/PR-24-PS	5	7.5±1.3
PMMA/PR-24-PS	10	7.6±0.9

4.1.2.8 Mold Geometry Selection

The mold geometries were selected in two phases. The first phase was a feasibility study, and hence molds were created with varying designs and number of cantilevers per part (roughly 20 different molds were produced for both an AFM and for the Scentris system of §4.2.3, with the number of microcantilevers per part ranging from one to five). The results presented for these molds in Chapter 5 provide no repeatability analysis but rather attempt to show the range in beam geometries that is possible; some of these molds are used to explore the length scale dependent stiffness of §3.3.1.3. After use of these initial molds showed feasible parts, two molds were created, each with the proper pitch of 250 μm for use with the Scentris system (discussed in §4.2.3). The two molds were chosen such that one would test the minimum thickness parts that could be made, and one for use in resonance- or deflection-based sensing with a first-mode resonance frequency of roughly 20-25 kHz and a stiffness of roughly 1 N/m. The minimum thickness part mold is not incredibly useful from a sensor standpoint, rather it was produced to test the limits of the injection molding process. The "useful" mold (i.e., that designed for the deflection and resonance sensing) was used for the repeatability analysis and to produce parts from the various materials (discussed in §4.1.2.7). This concludes the discussion of the injection molding process, equipment, and mold design methodology. Characterization of the microcantilever parts is now discussed.

4.2 Characterization Details

This section details the characterization of the microcantilever parts, which was accomplished using three different pieces of equipment.

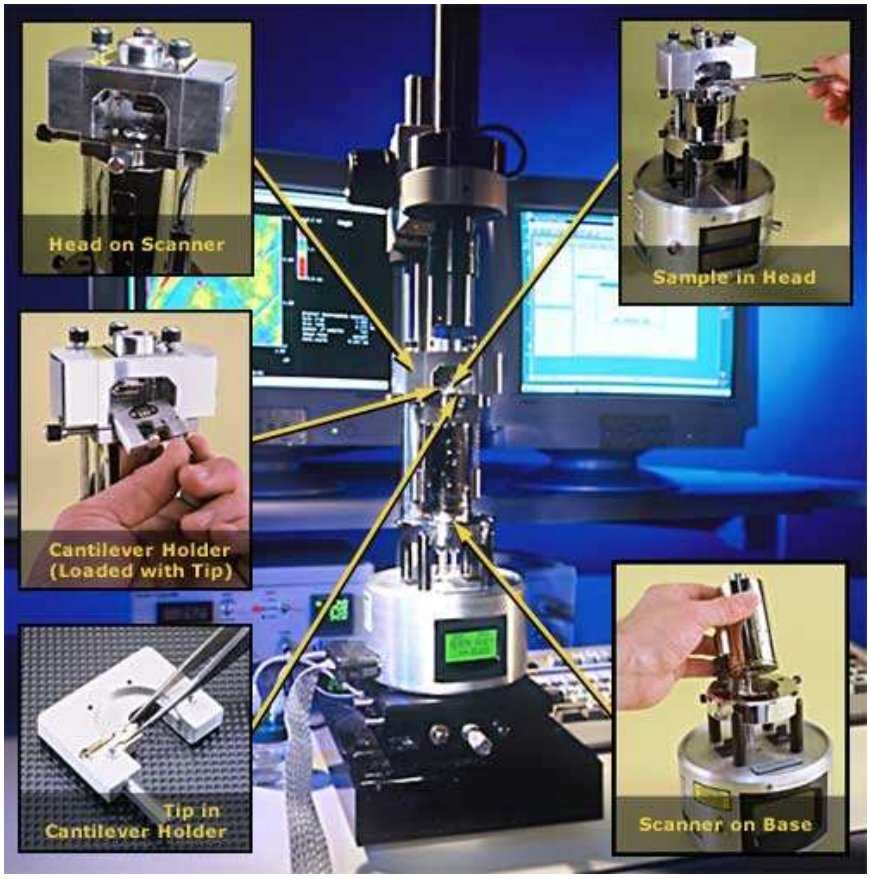

Figure 28: AFM and associated components [6].

4.2.1 Experimental Approach One: Atomic Force Microscope

An AFM (Nanoscope IIIa scanning probe microscope, Veeco Instruments Inc., Metrology Division, Santa Barbara, CA) was used for both stiffness and resonance frequency determination for polymeric and silicon microcantilevers. The machine uses the optical lever (§2.3.1.2) in conjunction with a four quadrant photodiode and either a data card (NI 6120 Card, National Instruments, Austin, TX; maximum sampling rate of 800 kHz) or an access module (SRS 785 Dynamic Signal Analyzer Stanford Research Systems, Sunnyvale, CA; maximum sampling rate of roughly 210 kHz) to determine beam deflection as a function of time; the AFM and associated components are shown in Figure 28.

To calibrate the beam deflection as recorded by the AFM photodiode, a sample

surface with pyramidal peaks is brought in and out of contact with the microcantilever by piezoelectric actuation components present in the AFM scanner, deflecting the end of the microcantilever in the thickness direction of the beam [141]. The spacing of the pyramidal peaks is large enough that a single peak can be used to deflect a microcantilever with the pyramid-beam contact occurring at the mid-width of the free end of the beam (or as close as possible to this position). The sample surface motion is assumed to be known "exactly," and as the beam deflects the laser to moves on the photodiode creating a voltage change, which is logged. By knowing the voltage change and the distance moved by the end of the beam, one can easily calculate a scalar constant called the sensitivity, C, which will simply be the voltage divided by the deflection (so the units of C are volts/distance); at such small deflections the voltage-displacement relationship is nearly linear. One may monitor the voltage output of the photodiode during an experiment, and divide that voltage by C to subsequently determine the deflection of the microcantilever during the experiment. The AFM was primarily used with Sader's method and the method of Hutter and Bechhoefer, which are now discussed.

4.2.1.1 Sader's Method: Experimental Details

Sader's method (discussed in §3.3.5.2) was one of the three methods employed to experimentally (using the optical lever of §2.3.1.2) determine the microcantilever stiffness and, inherently, the resonant frequency. The reader will recall that the microcantilever length and width are the two required geometric parameters for this technique, and these were both acquired using a while light interferometer. To obtain the thermal spectra data, the beams were mounted into an AFM (§4.2.1). To characterize the beams, Equation 98 was fit to the fast Fourier-transformed data using a nonlinear least squares algorithm in the MATLAB package (The Mathworks Inc., Natick, MA). This yielded the beam quality factor and fundamental resonant

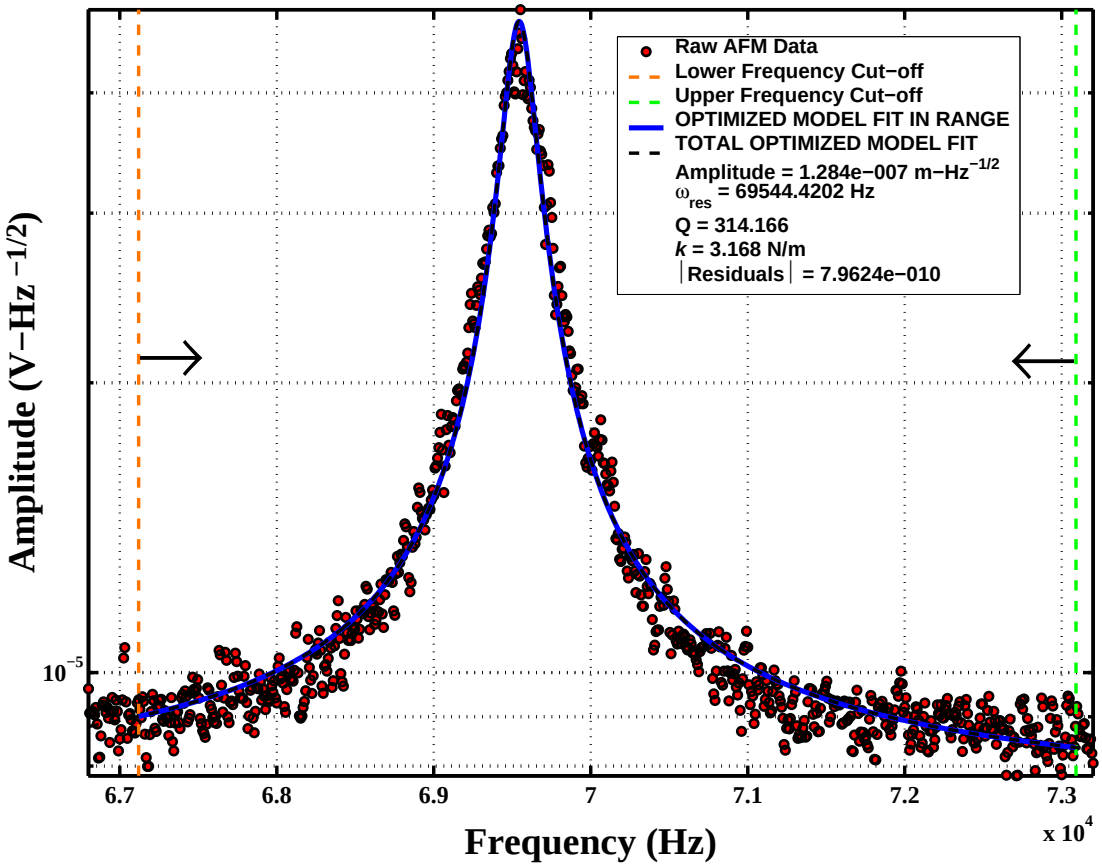

Figure 29: Output of MATLAB GUI for Sader's Method stiffness determination.

frequency, which, coupled with a MATLAB code to calculate the imaginary portion of the hydrodynamic function of Equation 99, allowed determination of the beam stiffness. Figure 29 is the output of a custom MATLAB GUI developed for this work, which shows the thermal spectra data and fit curve, the stiffness, the first resonance frequency, and data associated with the fitting process used for determining the quality of fit. One advantage of Sader's method is that it does not require that the actual deflection of the microcantilever be calculated (one will note that the units of the ordinate in Figure 29 are in volts, the direct output of the AFM), an advantage not showed by the next method employed.

4.2.1.2 The Method of Hutter and Bechhoefer: Experimental Details

Another characterization approach employed was that of Hutter and Bechoefer, also known as the sensitivity method (discussed in §3.3.5.1), which employs the equipartition theorem to equation the mean value of the energy of the microcantilever to a temperature dependent value; the AFM was used for thermal spectrum acquisition. While this method requires determination of the sensitivity, it requires no other experimental information except for the temperature of the fluid which engulfs the microcantilever. A thermal spectrum fitting process is carried out, as in Sader's method, to fit Equation 98 to the thermal spectra data that is now scaled by the sensitivity (to put the data into units of deflection– see §4.2.1 for a discussion of the sensitivity). f_1 and Q are determined by the curve fitting process and calculation of the mean-squared amplitude (i.e., the $\langle A^2 \rangle$ of Equation 97) via numerical integration allows for determination of the beam stiffness via Equation 97. Sader's method (§4.2.1.1) and the method of Hutter and Bechhoefer provide two means to determine stiffness, both of which necessitate the use of an AFM. The next method discussed negates the need for an AFM but is not capable of determining resonance frequency information.

4.2.2 Experimental Approach Two: Nanoindenter

The nanoindenter approach (briefly introduced in §2.4.4) is more direct in terms of stiffness determination than the techniques described in §4.2.1.1 and §4.2.1.2 at the expense of increased time consumption. An MTS Nanoindenter XP was used (MTS Systems Corporation, Eden Prairie, MN) to deflect the end of various microcantilevers while logging force-deflection data, the slope of which is equal to the stiffness. Figure 30 shows a CAD drawing of the experimental setup. The indentation motion (i.e., actuation) of the nanoindenter tip (① in Figure 30) in the direction normal to the lateral motion stage (② in Figure 30) is controlled by a coil/magnet assembly (③

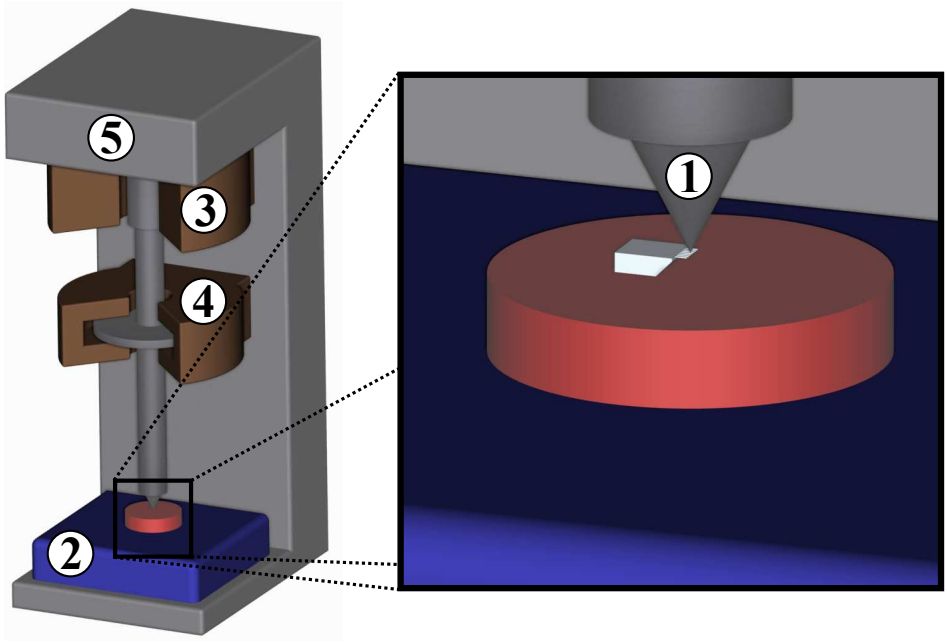

Figure 30: Nanoindenter configuration: ①=nanoindenter tip, ②=lateral motion stage, ③=coil/magnet assembly, ④=capacitance gauge, and ⑤=load frame.

in Figure 30) and is measured by a capacitance gauge (④ in Figure 30). The load frame of the nanoindenter (⑤ in Figure 30) has a stiffness of roughly 1×10^7 N/m, the machine has a force resolution of 50 nN, a displacement resolution (in the direction of indentation) of <0.01 nm, a lateral stage resolution of 45 nm, and a claimed lateral positioning accuracy of $\pm$ 1.5 μm [3]. The nanoindenter tip is a so-called Berkovich type, with the geometry of a three-sided pyramid as shown in Figure 31 (this geometry is shown as it becomes important for the injection-molded SPM probes discussed in Chapter 5).

To determine the microcantilever stiffness, the nanoindenter is used to deflect the end of a microcantilever while logging data of the force applied to the beam tip and the amount of deflection. The slope of a force versus distance plot is the stiffness, and the plot should be linear if the microcantilever obeys the linear elastic assumption.

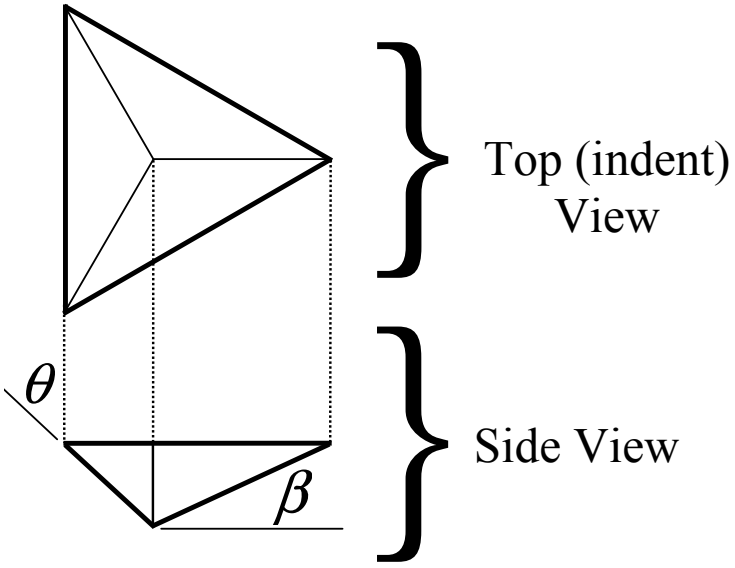

Figure 31: Nanoindenter tip geometry, $\theta = 65.3°$, $\beta = 12.95°$, and the tip radius is approximately 40-60 nm [3].

Figure 32 shows an actual force-distance curve produced from the nanoindenter data, and it is very close to straight, as indicated by the R^2 value of nearly one. It is obvious from Figure 32 that the initial portion of the force-distance curve is nonlinear, and this is attributed to possible indenter tip-microcantielver surface slippage. However, the initial region is hardly influential; by performing a linear least squares fit of the data in Figure 32 from 1 μm to 4.5 μm gives a fit of $F = 5.752\delta - 1.1$ with $R^2 = 0.999956$, which correlates to a difference in stiffness of roughly -0.6% as compared to the least squares fit on the entire data set.

Obviously, the indenter tip cannot be placed at the extreme end of the microcantilever, but the stiffness value calculated when pressing at a distance ΔL from the tip of a beam of length L ($k_{\Delta L}$), can be used to calculate the stiffness for an end load, k, by Equation 102.

$$k = k_{\Delta L} \left(\frac{L - \Delta L}{L} \right)^3 \tag{102}$$

See the inset of Figure 32 for nomenclature. By using data from multiple points along

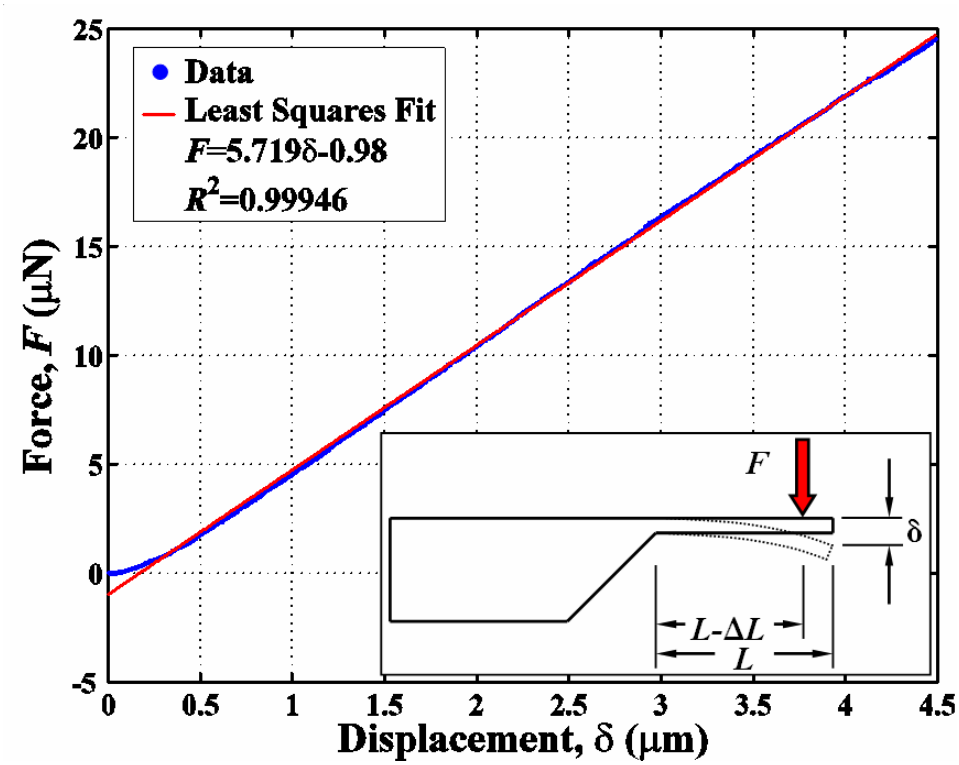

Figure 32: Nanoindenter data output (roughly 4,500 points) and least squares fit curve.

the beam length, the nanoindenter method allows one to reduce the uncertainty in k. For this work, all the microcantilevers measured were deflected roughly 5 microns[7] and 350 data points[8] were obtained over the roughly 30 seconds that the beam is deflected.

4.2.2.1 Nanoindenter Error

There are many sources of error when using the nanoindenter method to determine microcantilever stiffness:

- The load frame compliance,
- Thermal drift,
- Curvature of the microcantilever about its length due to the applied load,
- Protrusion of the indenter tip into the microcantilever surface,
- Force and deflection calibration error,
- Measurement and positioning error,
- Off-axis loading by the nanoindenter, and
- Inaccurate alignment between nanoindenter tip and nanoindenter camera.

These error sources now will be dealt with in turn.

The load frame stiffness (k_{lf}) is on the order of 1×10^7 N/m, so by modeling the nanoindenter-microcantilever as a pair of springs in series, the system stiffness (k_{sys}) equals $(k_{lf}^{-1} + k^{-1})^{-1}$, using $k = 1$ N/m yields $100[(k - k_{sys})/k] \approx 1 \times 10^{-5}\%$, showing that the error due to load frame compliance is negligible.

[7] $\approx$5 μm is a high estimate of the deflection that the microcantilevers will see in actual use as sensors.

[8] One data point consists of a measurement of both force and displacement.

The thermal drift error is due to any thermally-induced expansion or contraction of the sample and indentation machinery during data acquisition. The nanoindenter software corrects for this by holding the indenter at a small constant load for roughly 1 minute after a microcantilever load-deflection data set is obtained. During this holding time, the displacement is recorded to obtain a thermal drift rate in nm/sec, and then the deflection data is corrected. Usually, thermal drift is roughly 0.05 nm/sec, so in this case for a 30 second test of $\approx$5 μm deflection, the thermal accounts for for roughly 0.1% of the total deflection, making this error negligible even if the deflection were not adjusted by the nanoindenter.

Microcantilever curvature-induced deflection can be approximated by looking to thin-plate elasticity theory (see Equation 103), which predicts the deflection of a thin plate in the thickness direction, z_{mp} due to a point-load P applied at the center of the microcantilever (i.e., at mid-width and sufficiently far from any boundary constraints in a Saint-Venant sense) [59]

$$z_{mp} = \frac{6Pw^2(1-2/\pi)(1-\nu^2)}{Et^3\pi^3} \tag{103}$$

where w is the beam width, t is the thickness, ν is the Poisson's ratio, and E is the elastic modulus. By using a "generic" beam and loading (i.e., L, w, t, E, P, and ν equal to 500 μm, 100 μm, 10 μm, 3 GPa, 25 μN, 0.3, respectively), the percent difference in the measured deflection with and without the point-load curvature effects is less than 0.05%. Similar values are obtained for all geometries presented in this work, indicating that this source of error is negligible.

To estimate the amount of deformation that the nanoindenter tip-sample surface experiences, a Hertzian contact model is employed, which examines the elastic deformation that two spheres coming into contact under a load (P) will see. Here, the reference point where the two spheres meet is considered, with the top sphere representing the nanoindenter tip and the bottom sphere representing the microcantilever surface, as seen in the left hand side of Figure 33. u_z^{tip} and u_z^{surf} will denote the

deflection away from this tangent plane of contact that the points M and N will see, in the z_1 and z_2 directions, respectively. R_1 and R_2 denote the radii of curvature for the tip and surface, respectively. Equation 104 shows the total deflection that the nanoindenter would measure, $u_z^{tip} + u_z^{surf}$, and shows how taking the limit as the radius of curvature and the inverse of coordinate position (r) of the microcantilever sphere goes to infinity (to simulate a flat surface) [243]

$$u_z^{tip} + u_z^{surf} = \lim_{R_1, 1/r \to \infty} \sqrt[3]{\frac{9\pi^2}{16} \frac{P^2(k_1+k_2)(R_1+R_2)}{R_1 R_2}} - \beta r^2 = \sqrt[3]{\frac{9\pi^2}{16} \frac{P^2(k_1+k_2)^2}{R_1}} \tag{104}$$

where $k_i = (1-\nu_i^2)/\pi E_i$ and β is a constant that is irrelevant in this case because $r = 0$.[9] Using "generic" values of $P = 25$ μN, $R_1 = \infty$ (to simulate a flat surface), $R_2 = 50$ nm (i.e., the nanoindenter tip radius of curvature), $E_1 = 3$ GPa, $E_2 = 50$ GPa, $\nu_1 = \nu_2 = 0.3$ gives $u_z^{tip} + u_z^{surf} \approx 50$ nm, which is about 0.5-1% of the total deflection and translates into a roughly $0.5 - 1\%$ error in stiffness. As the Hertzian model of Equation 104 assumes an *entirely* spherical indentation, it greatly underestimates the amount of material that must be deformed, as shown in the right hand side of Figure 33, so the estimate of a $\approx 0.5 - 1\%$ error in stiffness is considered conservative.

The measurement error in this nanoindenter approach encompasses two "error-prone" processes (when compared to the other error sources). The first error source is the determination of beam length L, (to use with Equation 102), which is accurate to roughly $\approx \pm 3\mu$m (as explained by the standard deviation of the measured plan geometry values in Chapter 5). The second error source is the position of the nanoindenter when it depresses the microcantilever (i.e., the determination of ΔL). To estimate the error in stiffness due to the errors in measuring L and ΔL, it is assumed that both of these uncertainties are the same, which is reasonable as they are both measured

[9] $\beta = r^2 \left(\frac{1}{2R_1} + \frac{1}{2R_2} \right)$

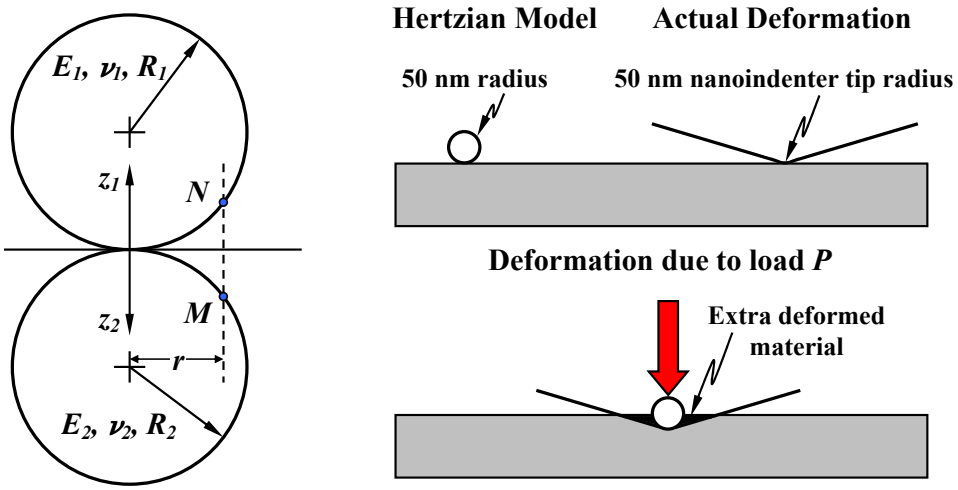

Figure 33: Hertzian contact model (left) and nanoindentation schematic (right).

using a optical microscope at the same magnification. Figure 34 shows the percent error in stiffness as a function of the microcantilever length and the uncertainty in the measurement of the length and ΔL, (i.e., as a function of δL).[10] Figure 34 shows that the measurement uncertainty causes the largest amount of error in this method, but with a δL of roughly 5 μm, the greatest uncertainty for the beams of this work is below 6%, and, based upon the data of Chapter 5 (e.g., the microcantilever geometries), roughly 80% of the beams measured will have an error of less than 3% of the nanoindenter-determined stiffness due to the measurement uncertainty.

The error due to off-axis loading by the nanoindenter (i.e., loading at points other than those along the mid-width of the beam) have been quantified via a finite element analysis, again using the generic beam values with the stiffnesses measured at numerous points on the top surface of the microcantilever. The simulation results are shown in Figure 35, and indicate that, so long as the nanoindenter is positioned

[10] δL is the measurement uncertainty, so it is a $\pm$ value, but the percent errors shown in Figure 34 were calculated as a worst case scenario by defining: $k_{correct}/k_{\Delta L} = [(L-\Delta L)/L]^3$ (i.e., without any uncertainty), $k_{+uncert}/k_{\Delta L} = \{[(L+\delta L)-(\Delta L-\delta L)/(L-\delta L)]\}^3$ (i.e., worst-case scenario of uncertainty, maximizing the numerator and minimizing the denominator), and finally arriving at the definition of the % Error in Figure 34, %Error$= 100\{[(k_{correct}/k_{\Delta L})-(k_{+uncert}/k_{\Delta L})]/(k_{correct}/k_{\Delta L})\} = 100[(k_{correct}) - (k_{+uncert})/k_{correct}]$.

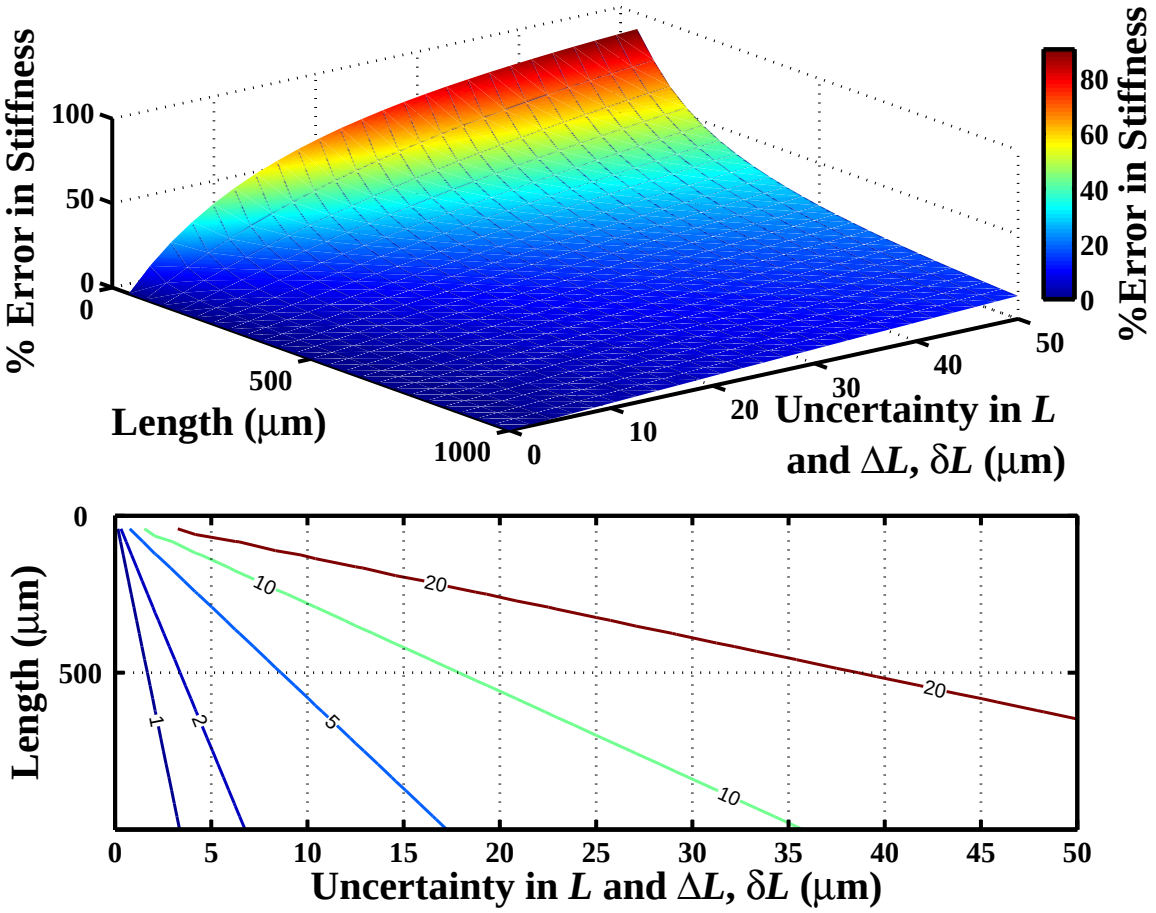

Figure 34: Surface (top) and contour (bottom) plot of percent error in stiffness as a function of microcantilever length (L) and measurement uncertainty (δL) (numbers in the contour lines of the bottom plot denote percent error in stiffness).

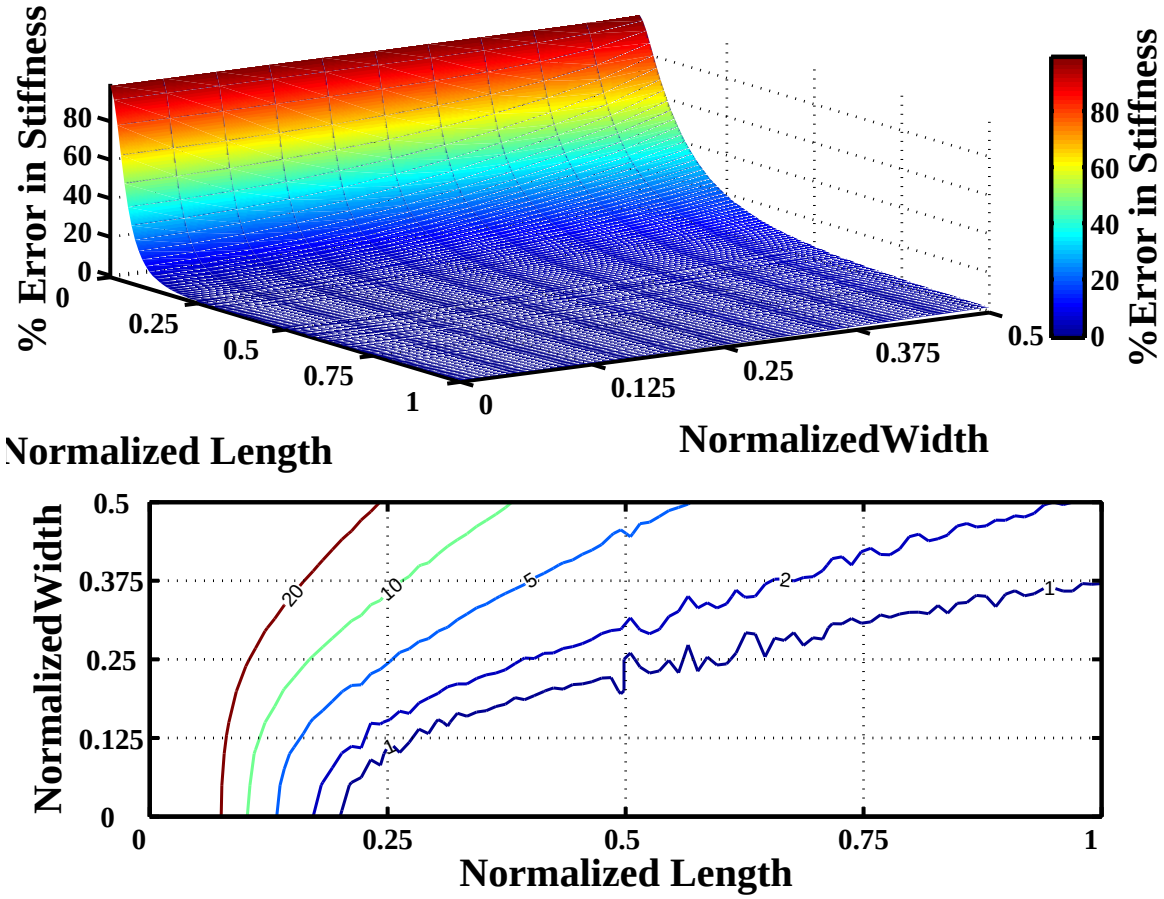

Figure 35: Surface (top) and contour (bottom) plot of percent error in stiffness as a function nanoindenter offset in the microcantilever width and length directions (numbers in the contour lines of the bottom plot denote percent error in stiffness).

anywhere from the half length to the free end of the beam and within ±25% of the beam mid-width, the error should be below roughly 0.5-1%. This result is commensurate with similar analyses in the literature [56, 220]. Figure 35 is logical in that, for a given position along the length, the error is higher at the edges of the beam (i.e., at normalized width equal to ±0.5) due to increased torsional deformation, and, for a given position along the normalized width, the error increases as the normalized length tends toward zero due to Saint-Venant effects present at the microcantilever base.

To align the camera that the nanoindenter machinery uses to position the tip to the tip itself, a "tip-to-sample" calibration is performed. This is a standard procedure where the nanoindenter tip is instructed to make five shallow indentations in a pattern resembling the five-dotted side of a playing die. Figure 36 details the procedure, where the initial alignment (assumed to be inaccurate) immediately after the indent alignment pattern is created is shown in ①. After this series of indentations is made, the user is instructed to align the cross mark of the camera screen with the center mark of the indent pattern, as shown in ② of Figure 36. To check the alignment the user translates the bulls eye to a fresh area (③ of Figure 36) and instructs the nanoindenter to make a new series of alignment marks. After the marks are created, the nanoindenter positions the camera above the marks and, if properly aligned (as shown in ④ of Figure 36), the cross mark will be right over the center indent. The distance from the center indent to any of the satellite indents is roughly 50 μm, but Figure 36 was created (for illustrative purposes) with a low magnification lens (10×) whereas for an experimental calibration one would use a higher magnification lens (e.g., 40×) to zoom in on the center indent much closer, hence making the alignment error roughly equal to ± 1 μm. With this type of error, the induced stiffness error (calculated via Equation 102) will be less roughly 0.5%.

4.2.2.2 Why Use the Nanoindenter?

The reader may be wondering why such a large amount of effort was expended to explain the process and errors involved in nanoindentation-based microcantilever stiffness determination. The reason is that this approach is considered, both by the author and generally in the literature, to be among the most accurate methods. This conclusion is germane to the current work as the length-scale dependent stiffnesses of Chapter 3 were examined experimentally in this work, with the results discussed in

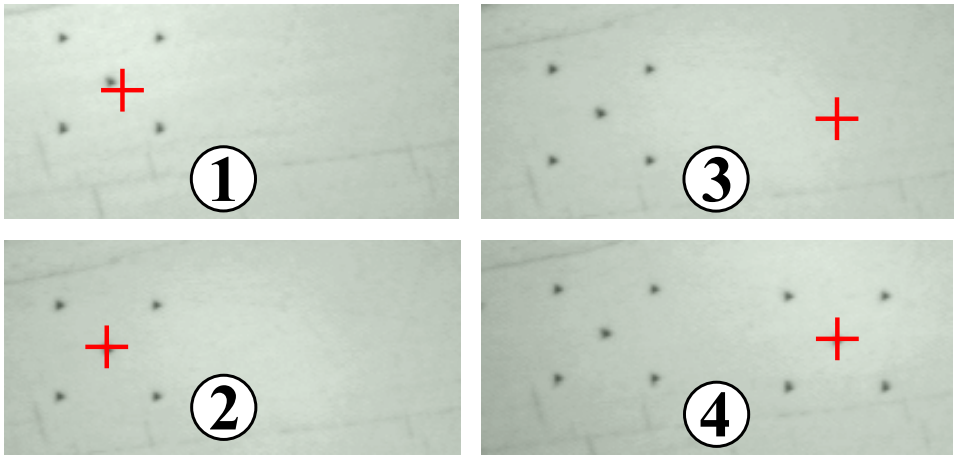

Figure 36: Nanoindenter alignment procedure.

the next chapter. By comparison to other test methods that have a $\pm 10 - 15\%$ *test-to-test* variability in measuring the stiffness of *the same beam* with the tests run only *minutes apart*, nanoindentation, while tedious and time-consuming, is a very enticing approach; hence it was chosen when an accurate stiffness determination was needed.[11]

To determine the test-to-test variation of the nanoindentation approach, five different microcantilevers were measured ten times each, with two of the beams being measured ten times consecutively (i.e., ten measurements of the first beam and then ten measurements of the second) and the third beam was measured ten times "randomly" over the course of two days. For a given beam, the test-to-test variation in stiffness was less than 2% indicating that this is the most repeatable and accurate experimental method (in terms of repeatability) of those available for this work; this type of repeatability also has been demonstrated in the literature [100]. Saying that the nanoindentation approach is superior to AFM methods is not meant to imply that the AFM-based methods are not useful, indeed they are employed later in this work for some microcantilever parts and are used profusely in the literature. However,

[11] This type of variation was observed for this work using both Sader's method of §4.2.1.1 and the sensitivity method of §4.2.1.2.

Table 5: Nanoindenter error sources summary.

ERROR SOURCE/DESCRIPTION	INDUCED STIFFNESS ERROR
Load frame compliance	$\approx 1\times10^{-5}$%
Thermal drift	≈0.1%
Curvature of the microcantilever about its length	≈0.05%
Elastic/plastic protrusion of the indenter into the microcantilever surface	≈1%
Force and deflection calibration error	≈3%
Measurement/positioning error	≈3-6%
Off axis loading by the nanoindenter	≈0.5-1%
Inaccurate alignment between nanoindenter tip and nanoindenter camera	≈0.5%

when this work explores the length-scale dependent stiffness, the superior stiffness determination of the nanoindenter is relied upon, as more accuracy is desired. Table 5 lists the different error sources for the nanoindenter, which sum up to roughly 8-12% for the various beam geometries of this work; this value is commensurate with the literature values for the nanoindentation method [37]. This is the "total" accuracy though, and not the test-to-test variation. The AFM-based methods have similar "total" accuracy *and* larger test-to-test variations, making them less accurate as a stiffness determination tool. Keep in mind that this is error in the *stiffness*, and the AFM is used extensively in this work and the literature to determine resonance frequency behavior (with a repeatability of less than 0.5%), while the nanoindenter cannot accomplish this. In short, the nanoindenter can determine stiffness to a high accuracy (as compared to all the other available techniques), while the AFM (or the Scentris system of §4.2.3) can determine the resonance frequency (and frequency shifts) to a high accuracy.

4.2.3 Experimental Approach Three: Scentris System

The Scentris system (Veeco Instruments Inc., Woodbury New York) was used for this project and is able to monitor the deflection and resonance behavior of up to

eight microcantilevers simultaneously. The system can actuate the microcantilevers (piezoelectrically at a given resonance which is limited to under roughly 400 kHz) to increase the quality factor for sensing in fluids, an application which the Scentris is particularly well-suited for. The general scheme is that an eight-fiber optic bundle has one fiber focused upon each beam, and light reflects onto a photodiode. Each of the fiber optic leads is illuminated from a laser source in turn (i.e., 1-2-3-4, etc.) with only one lead active at any time (see Figure 39). This is essentially a serial application of the optical lever as seen in Figure 39, with the laser scanning consecutively over the eight beams (for an eight beam part), and then starting back at the first beam. The machine scans over the eight beams in roughly one fifth of a second. If parts with less than eight beams are used, the optic fiber leads corresponding to the absent beams are not activated in the scanning sequence. The only caveat is that the beams (for an eight beam part) must be on a 250 μm pitch, so there are eight precise locations that can be scanned. Therefore, parts with less than eight beams must have the microcantilevers residing in one of the eight spots to be sensed (because the pitch of the lasers *is not* adjustable).

Figure 37 shows an overall view of the Scentris system, and the camera looks "down" upon the microcantilevers (i.e., a plan view as seen in the camera output in Figure 37). The microcantilever mounting unit is the piece shown in Figure 38, and a mirror reflects the laser light from the fiber optic source shown in Figure 39 to the microcantilever surfaces, where the light is finally reflected to the photodiode. To properly position the laser spots relative to the microcantilever beams (i.e., at the ends of the beams), the camera output is used in conjunction with positioning knobs which move the lasers.

To calibrate microcantilevers (i.e., determine resonance frequencies and stiffnesses), the Scentris can use either thermal (k and f_i information) or piezoelectric actuation (f_i information only). For stiffness determination (under thermal actuation only), an

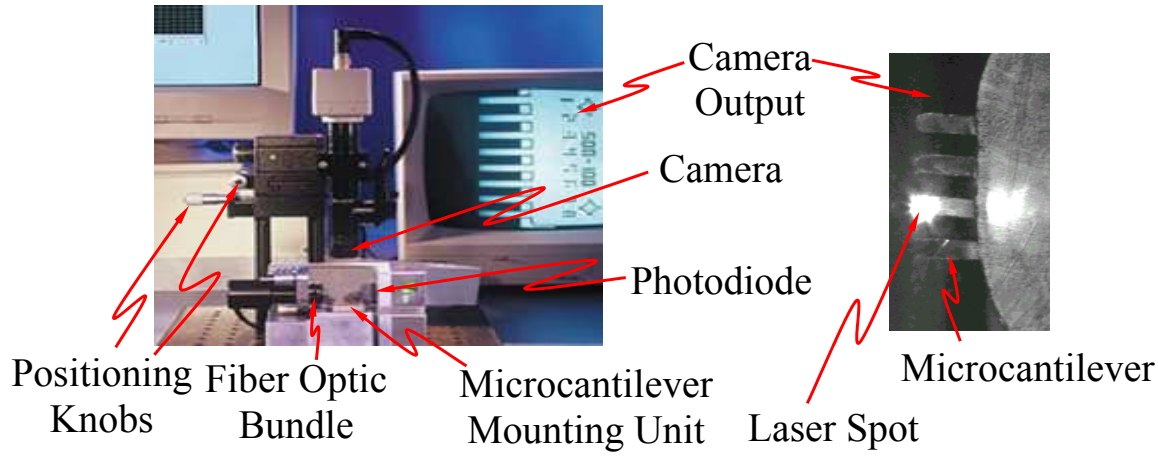

Figure 37: Scentris system– the picture on the right hand side is a four cantilever, polypropylene part showing the active laser spot on the third microcantilever.

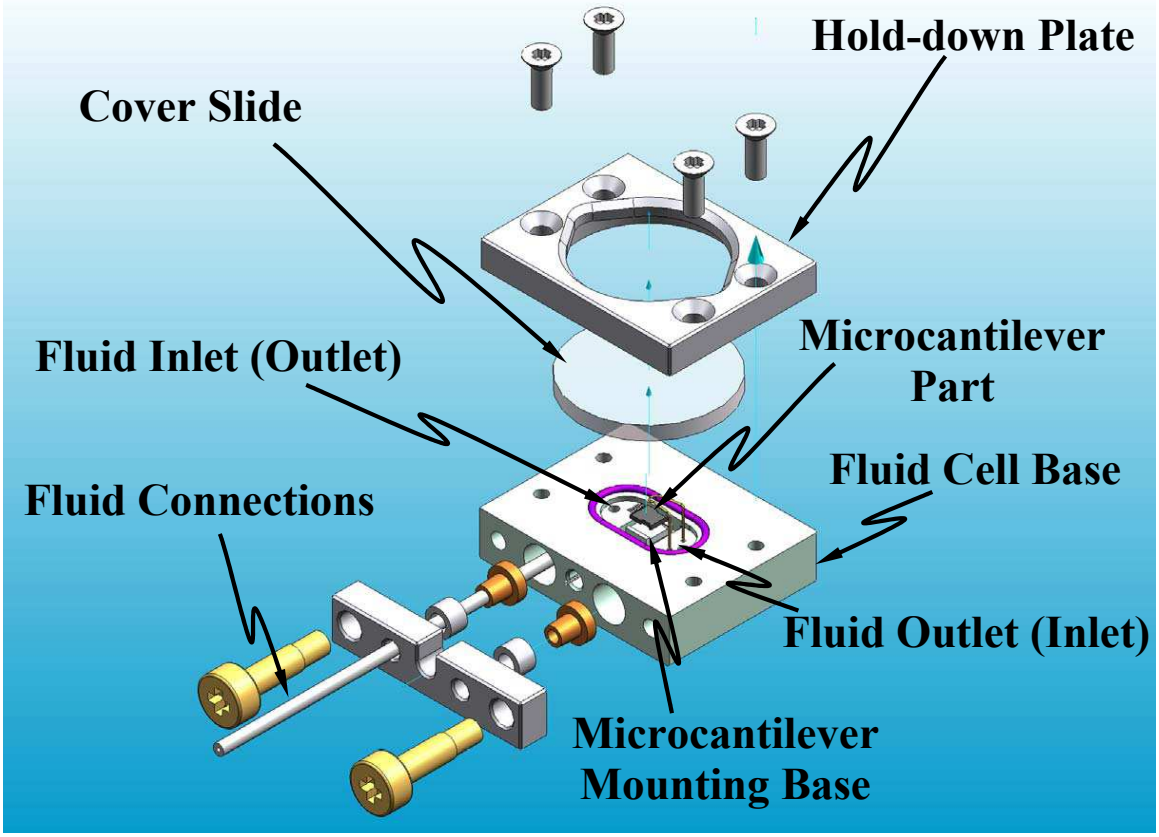

Figure 38: Scentris system fluid cell setup [6].

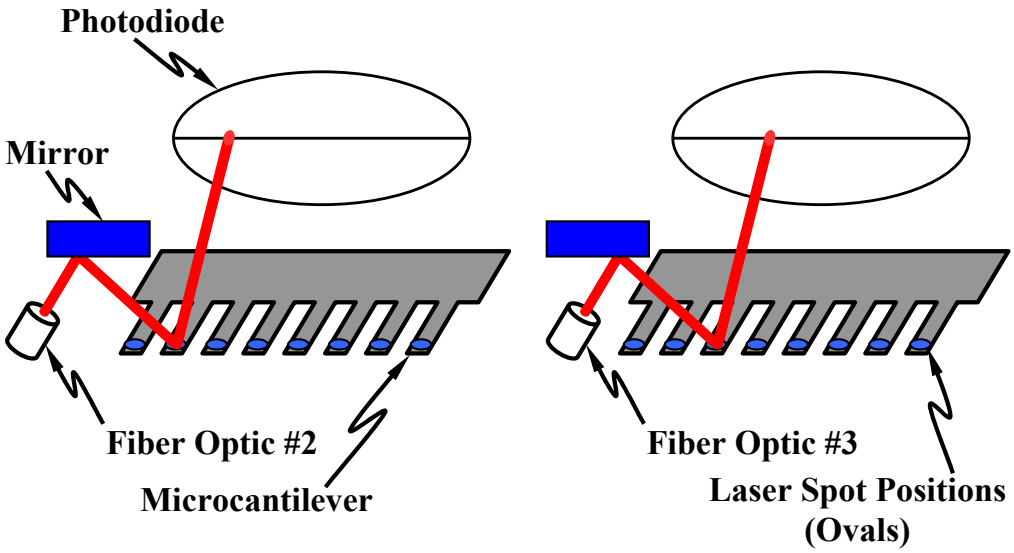

Figure 39: Picture of the Scentris system microcantilever scanning approach.

analytic form (similar to Equation 98) is fit to the data and the software uses the method of Hutter & Bechhoefer (see §4.2.1.2) to calculate k.

To calibrate the Scentris machine itself (i.e., to ensure that the deflections read by the Scentris are accurate), a custom-made piezoelectric setup was used. A 2×2×2 mm cube piezoelectric stack was purchased (PL022.31, Physik Instrumente, Auburn, MA). An AFM was used to determine the voltage-displacement curve for the piezoelectric element, which is shown in Figure 40. Then, the piezo piece was placed in the Scentris system and used to actuate a microcantilever part while the Scentris system recorded the beam tip deflection (ΔS), as shown in Figure 41. There is certainly a component of drift in Figure 41 (i.e., the deflection baseline is not flat), but this is considered negligible as the rapid height jump (ΔS) is the important parameter for calibration. This approach allowed the Scentris's deflection measurement to be calibrated.

The Scentris is designed for fluid-based sensing, and as such comes with an integrated fluid cell setup shown in Figure 38. Two fluid connections (only one shown) deliver fluid to and from the cell, while the laser bundles emit light through the cover

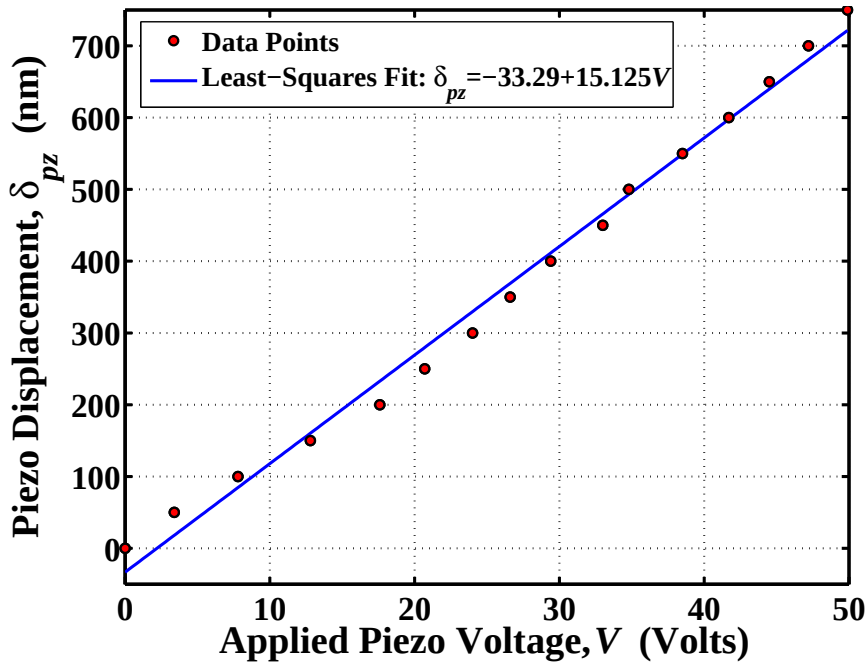

Figure 40: AFM-determined piezoelectric piece displacement versus applied voltage plot and linear regression ($R^2 = 0.9913$).

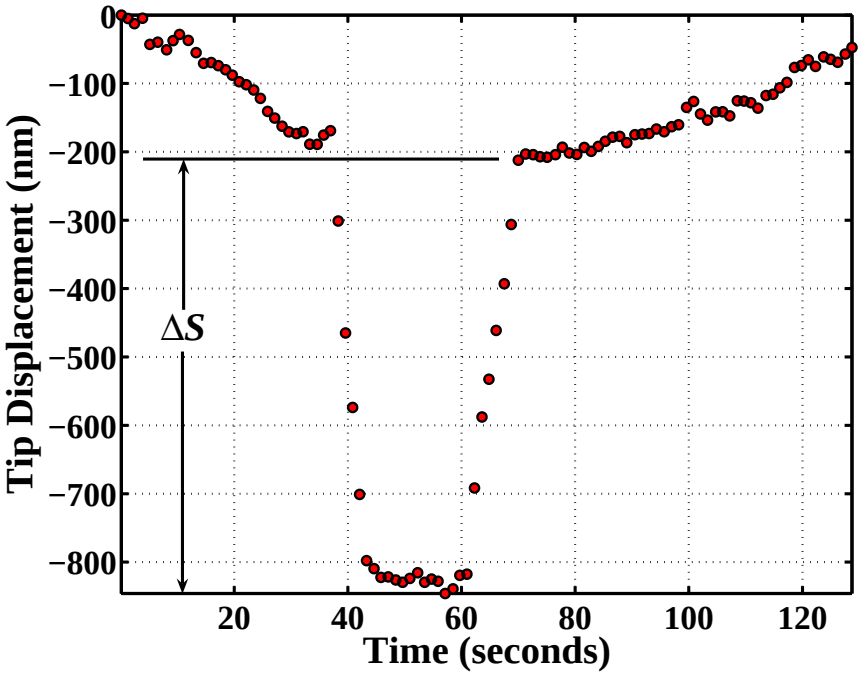

Figure 41: Scentris system-determined tip displacement versus time plot (≈ 30 volts applied to the piezoelectric piece). ΔS is the tip deflection due to the piezoelectric actuator.

slide onto the back of the microcantilever parts. The mounting base for the microcantilevers is fixed upon a piezoelectric stack so that all of the microcantilevers can be actuated at one time while fluid is flowing through the cell increasing the beam Q, making resonance tracking much easier. The hold-down plate is attached with four screws as shown in Figure 38, and effectively seals the cover slide to the fluid cell base via an O-ring. The Scentris system is used in this work both for characterization of microcantilevers (in air and water) and for chemical sensing. Specifically, it is used to monitor the generation of surface stresses to examine the validity of the surface stress-induced resonance-shift modeling of §3.3.3.6.

In AC mode (i.e., for resonance-based experiments), the microcantilevers are first "tuned" in the Scentris so the machine software knows what the resonant frequency of each beam is. The software automatically tracks the frequency shifts upon demand, and can track any mode so long as the frequency is under approximately 400 kHz. The Scentris can simultaneously monitor deflection during the resonance shift acquisition time, although the dual-monitoring capability has seen limited success as will be discussed in Chapter 5.

This concludes the discussion of the microcantilever characterization details and equipment; the discussion now turns to the computer simulation.

4.3 Simulation Details

This section details the finite element simulations, which were used to examine the validity of certain theories and equations proposed in Chapter 3.

4.3.1 Solid Finite Element Analyses

There were numerous solid finite element analyses carried out for this work, mainly to verify some of the theoretical resonance modeling of Chapter 3 (§3.3.3.6), to examine the off-axis error of the nanoindenter discussed in §4.2.2.1,[12] and to simulate the different resonance modes (e.g., bending, lateral, and torsional) of §3.3.4. All simulations, (both two- and three-dimensional) were carried out by the ANSYS 7.1 package.

The two-dimensional modal analyses (used to verify the results of §3.3.3.6, specifically the effect of surface stress on the resonance frequency of a beam), modeled a microcantilever as a line,[13] with one endpoint of the line having displacement and rotation fixed at zero as shown in the left hand side of Figure 42. Two sets of simulations were run to examine the end force model or the axially distributed model of §3.3.3.6. The simulations applied an end-force at the free end of the microcantilever (to test the end force model) or an axially distributed force (to test the axially distributed force model) from the buckling load in compression ($\hat{\sigma} = -\pi^2/4$ for the end force model and $\hat{\sigma} = -\pi^2/2$ for the axially distributed force model) to different positive values (chosen to be much higher than any seen in experiment) in equal increments over 100 different finite element analyses.

For all 2D analyses the p-method was employed,[14] which uses a specific criterion to judge if a simulation has sufficient mesh density. For this work a change in global strain energy, global RMS stress, and resonant frequency between the ith and $(i+1)$

[12] All analyses used a "generic" material and beam with $E = 3$ GPa, $\nu = 0.3$, and L, w and t equal to 500, 100, and 10 μm, respectively.

[13] Subparametric, Euler-Bernoulli based ANSYS "BEAM3" elements were used, which have degrees of freedom of in-plane displacement and rotation about the direction out of plane at each of their two nodes, along with nonlinear capabilities.

[14] To increase simulation accuracy, the p-method alters the polynomial used for approximating the geometry and the primary variable over an element, whereas the n-method (not used for this work) keeps the approximation order of each element constant but increases the number of elements to increase simulation accuracy.

iteration of less than 1% was considered to be a satisfactory solution. The p method eliminates the need for explicit mesh refinement by the user, and accomplishes the mesh refinement by adding nodes to elements which are deemed to be insufficient. The model for these 2D simulations started with 500 elements; this mesh was adaptively refined once (the minimum) to satisfy the three convergence criteria, resulting in a final model with approximately 1000 elements.

One set of three dimensional analyses was used to verify the results of §3.3.3.6, similar to the 2D simulations and another set was used to simulate the different resonance modes (i.e., bending, lateral, and torsional) as discussed in §3.3.4. Solid elements and the standard cantilever boundary conditions of zero slope and displacement at the cantilevered end were used.[15] For the surface stress investigations (when the surface stress is modeled as an end force), a force was applied at the free end of the microcantilever (as an evenly-distributed surface stress, shown in the right hand side of Figure 42) along the length direction of the geometry and varied to shift the structure from compression (at the Euler buckling load of $\pi^2/4$ for the end force model and $\pi^2/2$ for the axially distributed force model) to tension (the maximum tensile value was chosen to coincide with values much higher than any seen experimentally) in equal increments over the course of 100 finite element analyses. For the surface stress investigations (when the surface stress is modeled as a uniformly distributed axial force), a uniform axial force was applied along the top surface of the microcantilever from the Euler buckling load (for the end load or the axially distributed load) to a tensile load chosen to be much higher than any loading yet seen experimentally. For all 3D modal simulations, the same p-method criteria as used for the 2D frequency analyses were again employed (i.e., 1% or less change in global strain energy, global RMS stress, and resonant frequency between subsequent analyses). For all of the

[15] ANSYS "SOLID95" elements were used, which are 8-node, isoparametric, 3D elements with degrees of freedom of displacement in three directions at each node.

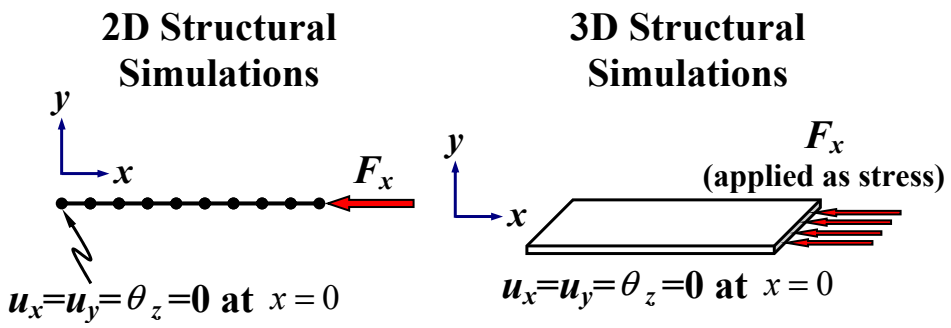

Figure 42: General scheme for 2D (left) and 3D (right) modal frequency finite element analyses.

modal solid finite element analyses (2D and 3D), the geometries undergoing simulation were simple enough that they were created within the ANSYS package (i.e., no CAD package was necessary). The model for the 3D modal simulations started with 8,000 parallelepiped elements (100 along the beam length, 40 along the beam width, and two along the beam thickness) and this mesh was adaptively refined once (the minimum) yielding roughly 15,000 elements, which satisfied the three convergence criteria.

The difference between the modal 3D simulations discussed in the last paragraph and the analyses used to simulate the off-axis loading error of the nanoindenter was only in the manner of loading (i.e., the mesh, boundary condition, and convergence criteria were equivalent), which was changed from the length-direction of the microcantilever to the thickness direction. The top of the microcantilever was viewed as a grid, and individual finite element analyses were run at numerous grid points, as shown in Figure 43. Half-symmetry was used to reduce computing times, and the percent error results were calculated as a function of position on the beam surface, with the results (as discussed in §4.2.2.1) shown in Figure 35.[16] The stiffness at the

[16]It was decided to present the results of Figure 35 in this chapter as opposed to the next as they are simply employed to show that the nanoindenter error is acceptable so long as the nanoindenter tip is positioned sufficiently close to the mid-width of the microcantilevers.

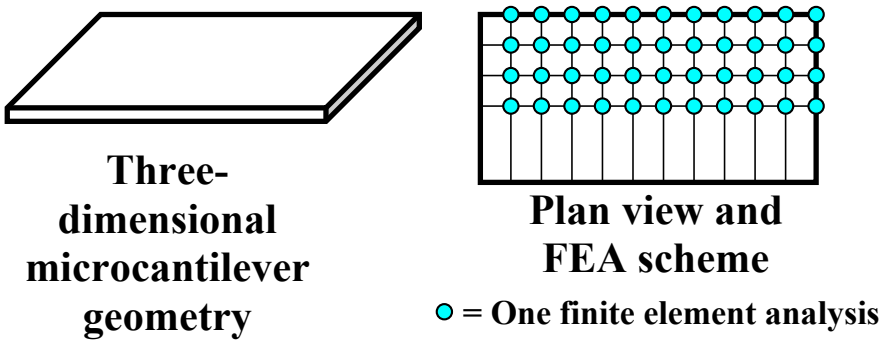

Figure 43: Generic scheme for 3D off-axis nanoindenter error finite element analyses, the actual scheme consisted of 2,100 individual finite element analyses.

mid-width and full length (i.e., that of a true, end-loaded cantilever structure) was considered the "correct" value (k_{cor}), and then was used to scale the stiffnesses of non-end loads by using Equation 102 and the percent errors of Figure 35 were calculated by using % Error= $100(k_{oa} - k_{cor})/k_{cor}$, where k_{oa} was the FEA-calculated off-axis stiffness (which was scaled by k_{cor} and Equation 102). Two hundred finite element analyses were performed (i.e., 200 grid points as in Figure 43 were used).

4.4 Summary

This chapter opened with explanation of the approaches and equipment used to produce the polymeric microcantilever parts, along with associated details. The experimental equipment used in the characterization of microcantilever parts were then covered, and the chapter closed by detailing the simulations used to investigate the validity of certain predictions discussed in Chapter 3. Chapter 5 now presents the experimental results obtained using the methods of this chapter, and compares some of these results to the theoretical predictions of Chapter 3.

CHAPTER V

RESULTS

This chapter discusses the experimental results in a two-pronged approach; the first details the manufacturing goal-related results, such as the demonstration of successful microcantilever production via solvent casting and injection molding. Then, the chapter turns to the scientific goal-related results, such as the investigation of the length scale dependent bending stiffness and the work on new microcantilever operational modes developed for this project. After the results and findings are discussed, the chapter closes and leads into Chapter 6, which discusses the overall conclusions of this dissertation in the context of the experimental results and comparison with theory, along with some of the new applications enabled by this work and recommendations for future work.

5.1 Manufacturing Goal-Related Results

The manufacturing goals were accomplished mainly using the injection molding (IM) process, but solvent casting also proved feasible. This section will briefly cover the limited solvent casting results, which were mainly a feasibility study, and then discuss the more robust IM results, which were used to examine the theories proposed in Chapter 3.

5.1.1 Solvent Casting

For the solvent casting approach, the only material used was a single polystyrene (see §4.1.2.7 for the material properties). One hundred PS single-cantilever parts were produced, thirteen of which were characterized. The results are presented in Table 6, where Q and f_1 were obtained by fitting Equation 98 to thermal spectra

data, and the method of Hutter and Bechhoefer was used to determine the stiffness (see §4.2.1.2). These data show a stiffness range from approximately 0.001 N/meter to 0.1 N/meter- these values are commensurate with those of existing, silicon-type microcantilevers currently in use. With this solvent casting technique, there is little trouble producing beams with stiffnesses greater than 0.3 N/meter as the solvent-cast solution simply can be made to a different mixture ratio (e.g., five parts solvent to one part polymer), hence producing thicker, stiffer beams. The solvent casting technique also was used to produce films of submicron thickness, however no attempts were made to transform these films into microcantilevers, as the desired stiffness goals were reached with film thicknesses roughly equal to one and one-half microns. The process presented herein could be used with virtually any soluble polymer that can be cast into a smooth film. Figure 44 shows an "average" part (in terms of width), whereas Figure 45 shows the part produced with the smallest width– recall that length and thickness are not difficult to control with this technique making width *only* the size scale-limiting dimension. The microcantilevers have roughly 40 nm of gold evaporated onto their top surface.

5.1.1.1 Durability of Solvent Cast Microcantilevers

The strain to fracture (STF) for many thermoplastic polymers is higher than it is for ceramic materials (e.g., STF of PS ≈2% [40], STF silicon ≈1.2% [112]). This implies that a PS microcantilever can undergo more deformation without fracture (as its STF is higher) compared to a silicon-based cantilever. This prediction was tested experimentally by subjecting the PS microcantilevers to severe tip deflections (roughly 350 microns), and found that they returned to their initial configuration upon unloading (see Figure 46). However, the deflections encountered in use of microcantilever sensors are usually less than 5 microns. In addition, extremely severe deflections (essentially bending the beam at 90° at the beam base) do not break the PS cantilevers.

Table 6: Solvent cast microcantilever figures of merit, ordered by increasing stiffness.

Beam Number	Stiffness, k (mN/m)	Quality Factor, Q	1st Resonant Frequency, f_1 (kHz)
1	3.1	8.75	2.67
2	10	8.97	2.31
3	11	11.1	3.51
4	14	9.13	5.88
5	15	12.5	3.02
6	17	10.7	3.93
7	17	13.0	4.03
8	18	14.1	8.37
9	34	5.68	10.8
10	34	15.0	6.30
11	43	6.70	7.57
12	140	30.17	5.29
13	250	32.37	9.45

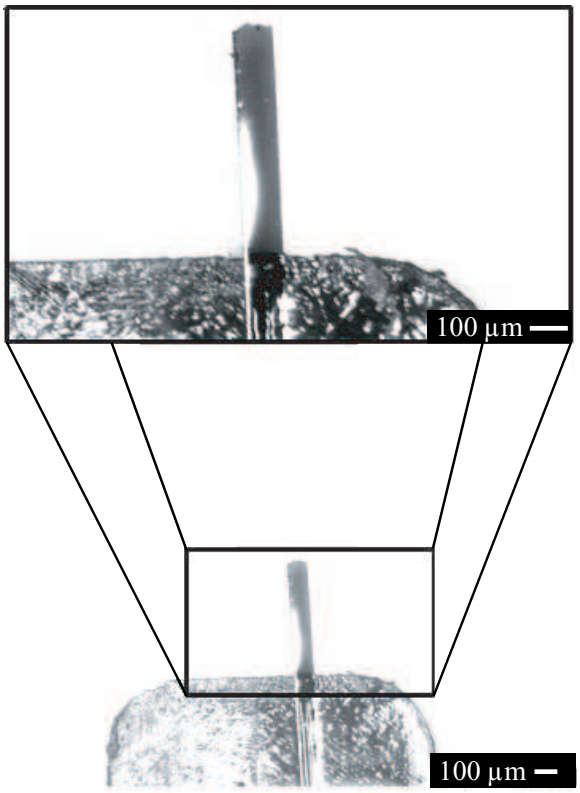

Figure 44: Polystyrene (both beam and base) single-cantilever part.

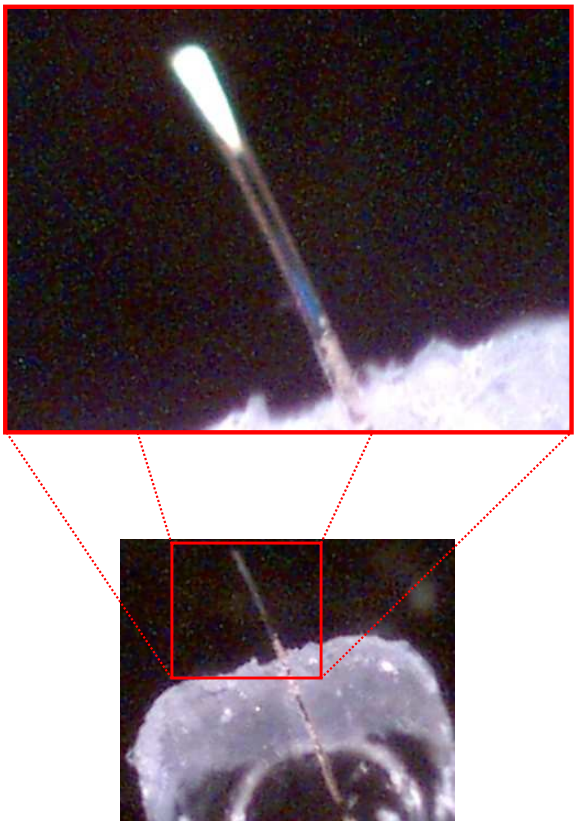

Figure 45: Polystyrene (both beam and base) single-cantilever part with width of ≈ 25 μm.

The beams can be formed back into a relatively flat structure after such 90° bending and are still feasible for characterization. One should note that two or three cycles of this bending will cause the microcantilever to fatigue and fracture at the base of the beam. This beam flexibility makes the solvent cast microcantilevers less susceptible to breakage, a phenomenon common with silicon-type cantilevers that are handled too roughly. Solvent cast polymeric cantilevers can be dropped on the ground without breaking (from roughly 3 feet), a feat that usually destroys silicon-type beams.

5.1.1.2 Multiple-cantilever Parts via Solvent Casting

Some rudimentary work was performed to produce multiple cantilever parts via solvent casting. The procedure was the same as that discussed so far, except that the spacing of the cuts was now chosen to have multiple beam strips left on the glass substrate, as shown in Figure 47. The same xylene gluing, water soaking procedure then yielded multiple-beam parts, shown in Figure 48. It is apparent from Figures 47 and 48, that the technique is by no means elegant or refined, but future work could make this technique feasible. Some of the beams were clearly separated (as shown in the inset of Figure 48 with the 50 μm scale bar) while others were not (as shown in the inset of Figure 48 with the 40 μm scale bar). Higher quality, sharper cutting blades could remedy this. None of the microcantilevers from the multiple-beam, solvent cast parts were characterized as the technique was aborted in favor of injection molding, which showed much better results for multiple beam parts and is the next topic covered.

5.1.2 Injection Molding

This subsection presents the bulk of the experimental results obtained from injection-molded polymeric microcantilevers. A feasibility study is presented first, which was performed as proof-of-concept and to examine the range of geometries that could be injection molded, using PS as a test material (§5.1.2.1). Using the geometry

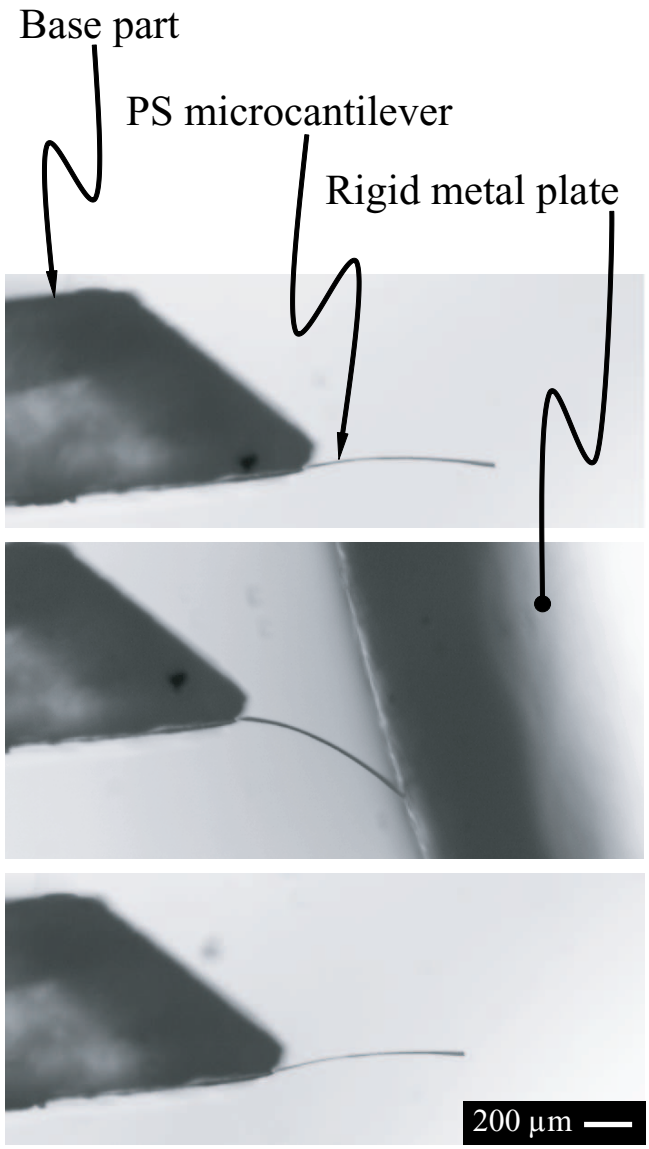

Figure 46: Polymer beam ductility- the top picture shows a PS microcantilever (fixed to a PS base) that is resting freely, the middle picture shows a rigid metal plate that has been brought into contact with the microcantilever and hence transversely deflected the tip of the beam roughly 350 μm, and the bottom picture is of this same beam after unloading, showing the final position to be nearly identical to the starting position.

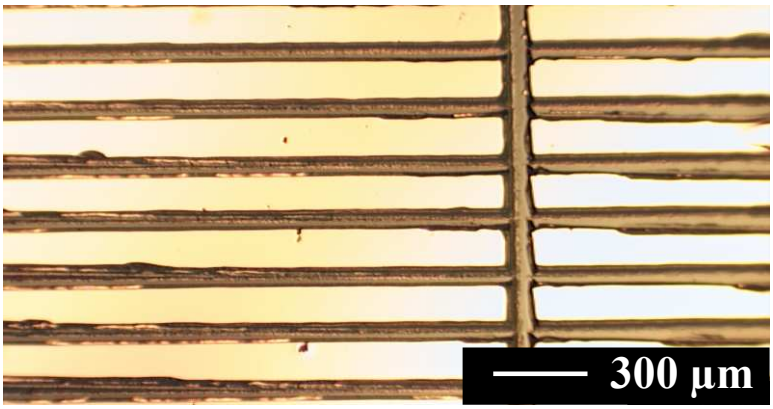

Figure 47: Cut PS film for production of multiple-beam parts.

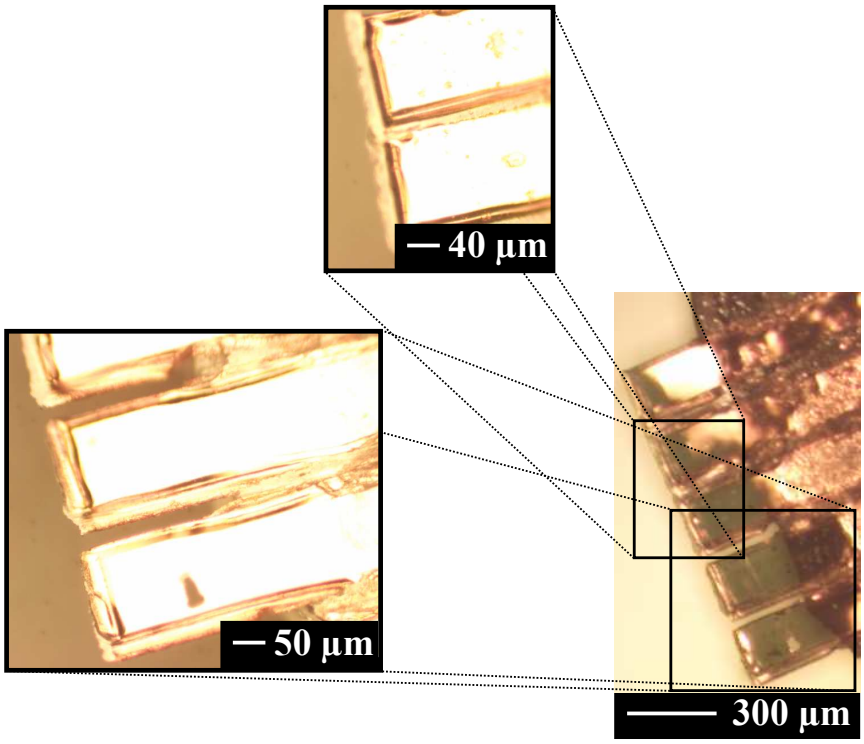

Figure 48: Polystyrene (both beam and base) multiple-cantilever part.

information gleaned from the feasibility study, molds were fabricated as discussed in §5.1.2.2. A repeatability analysis (using microcantilevers made from the materials of Table 3) discussion follows (§5.1.2.3), then the results from a minimum injection moldable-thickness study are presented (§5.1.2.4) and are followed by the results from composite microcantilevers made using the materials of Table 4 (§5.1.2.5). A brief study of the durability of injection molded cantilevers (§5.1.2.6) closes the discussion on the manufacturing goal-related results and attention turns to the scientific goal-related results in §5.2.

5.1.2.1 Feasibility Analysis

The feasibility analysis sought (*i*) to determine the proper cutting conditions to produce acceptable microcantilever channels, (*ii*) to employ molds to produce microcantilever parts from polystyrene as a proof of concept (e.g., IM is feasible and the parts are produced with minimal flash and similar mechanical behavior as their silicon-type counterparts) as this work had not been done before, (*iii*) to get a preliminary estimate of the agreement between theory (e.g., Equation 21 and Equation 54) and experimental values of f_1 and k, and (*iv*) to see if the IM process warrants a rigorous repeatability analysis. One of these four goals is now dealt with, in turn, in each of the next four paragraphs.

The analysis began with the production of roughly twenty different molds, the microcantilever cavities of which were made with end mills having a range of diameters (25-200 μm) operated at different spindle speeds (10 kRPM to 50 kRPM) and different linear feed rates (0.1 mm/minute to 5 mm/minute); this determined which cutting conditions produced quality microcantilever channels while avoiding premature tool failure. No rigorous design of experiments was employed as it was determined relatively quickly that maximum spindle speed (50 kRPM[1]) with a feed rate

[1]The maximum spindle speed of the equipment was actually 60 kRPM, but previous users had described strange vibration behavior dangerous to the experimental apparatus at that spindle speed,

less than roughly 2.5 mm/minute and a tool diameter greater than 75 μm produced acceptable microcantilever cavities.

A subset of the molds produced showed promise for actual injection molding (e.g., minimum cutting-edge burrs, acceptable microcantilever cavity size and shape) and were used with the Sesame machine (§4.1.2.5) to injection mold polystyrene microcantilever parts. Some of these molds proved successful while others did not. A subset of the mold cavities that produced acceptable parts were measured (using the same technique detailed in §5.1.2.2) and some polystyrene parts from these molds were characterized via Sader's method using the measured mold length and width values to determine the stiffness and the first-mode resonance frequency and quality factor; these three parameters allow for a comparison between silicon-type parts and the PS parts. Table 7 shows the measured mean mold geometry values followed by the bracketed standard deviations. Figure 49 shows a successful mold and a part produced from it with little flash and complete microcantilever cavity filling (the cavities from top to bottom in Figure 49 correspond to cavities D, E, and F of Table 7). Indeed, the k, f_1, and Q values of listed in Table 7 are commensurate with those of various silicon-type microcantilevers [7, 5]. As the mechanical behavior and geometry of the PS microcantilevers are commensurate with their silicon-type counterparts, PS beams are likely feasible for sensing applications (this claim is proven in this chapter).

For comparison to experiment, the mold geometries of Table 7 were used to calculate the predicted stiffnesses (using Equation 21) and first mode resonant frequencies (using Equation 54) with the manufacturer-provided material property data of Table 3; the results of these calculations are shown in Table 8 along with percent difference between theory and experiment; k Percent Difference=$100\left[\left(k_{\text{calc}} - k_{\text{exp}}\right)/k_{\text{calc}}\right]$ and similarly for f_1 Percent Difference. The disagreement between theory and experiment for the resonance behavior is less than 10% for all geometries, indicating that

so the 50 kRPM speed was designated (by the owner of the equipment) to be the maximum.

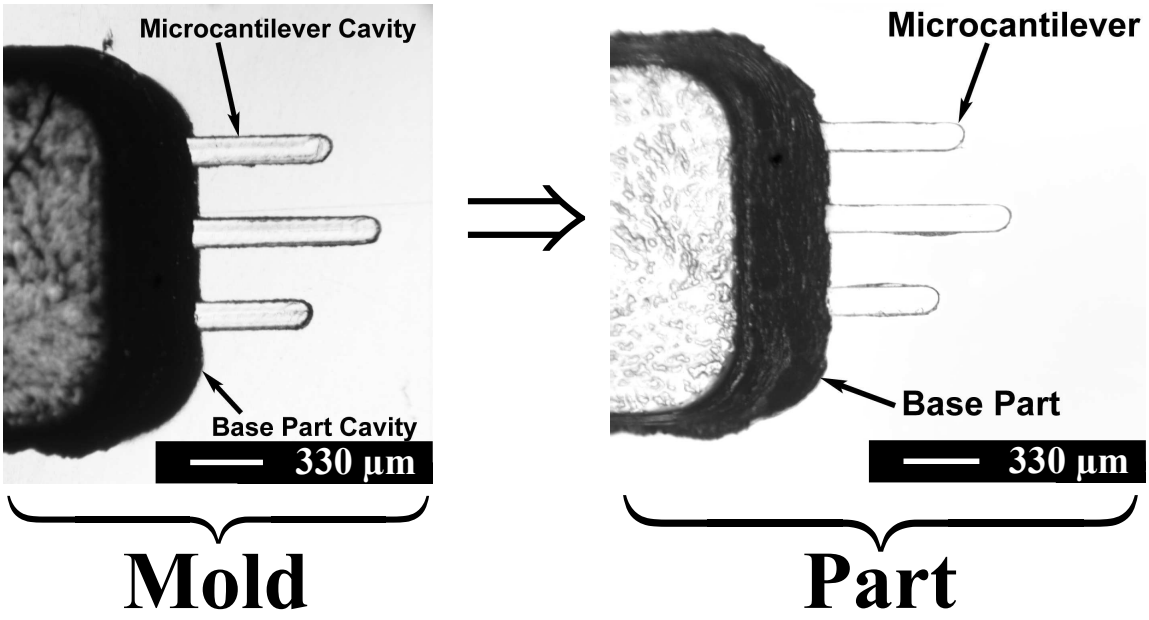

Figure 49: Mold and produced PS part.

the theory is a reasonably accurate predictor of resonance frequency. Conversely, the disagreement between theory and experiment for the stiffness values is larger, which indicates that either Sader's method (or the data acquisition involved) is not an accurate indicator of stiffness or that the theory is flawed. The trend of better agreement (of experiment versus theory) for frequency than for stiffness (when determined via Sader's method or the method of Hutter and Bechhoefer) holds true in the vast majority of measurements obtained for this work; the literature has noted this as well [37].

Before beginning the full-fledged repeatability analysis discussed in §5.1.2.3, a group of resonance frequency measurements were taken (on the Scentris system) from 26 PS parts, each made from the same mold with the same processing conditions and gold-coated with roughly 25 nm of gold at a rate of 0.5 Å per second. While this

Table 7: Feasibility study microcantilever cavity geometries. The microcantilever cavities were arbitrarily sorted in order of decreasing cavity thickness. The cavities are labeled by letter to avoid confusion with molds presented later, which are numbered. The mean geometry value is followed by the bracketed standard deviation.

Cavity Letter	Length (μm)	Width (μm)	Thickness (μm)
A	560 [8]	77 [3]	43.92 [1.0]
B	537 [14]	131 [5]	35.82 [0.4]
C	572 [9]	128 [2]	8.91 [0.2]
D	543 [13]	130 [3]	8.62 [0.3]
E	755 [7]	131 [3]	7.52 [0.3]
F	464 [14]	132 [2]	6.21 [0.3]
G	370 [12]	168 [2]	3.68 [0.3]
H	365 [8]	163 [8]	2.58 [0.3]
I	374 [5]	157 [8]	2.20 [0.3]

Table 8: Experimental and calculated microcantilever beam stiffnesses (k_{exp} and k_{calc}), stiffness percent difference, experimental and calculated first mode resonant frequency (f_1^{exp} and f_1^{calc}), resonance percent difference, and quality factor. The "Beam Letter" parts were made in the "Cavity Letter" cavities of Table 7. [a]The high stiffness of beams 1 and 2 in Table 8 pushed their thermal resonance amplitude below the white noise floor, therefore the beams were actuated piezoelectrically to measure their resonance but their stiffness was only tenable via Equation 21.

Beam Letter	k_{exp} (N/m)	k_{calc} (N/m)	k Percent Difference	f_1^{exp} (kHz)	f_1^{calc} (kHz)	f_1 Percent Difference	Quality Factor, Q
A	N/A[a]	27.7	N/A[a]	35.0	37.4	6.4	N/A[a]
B	N/A[a]	29.1	N/A[a]	35.9	33.2	-8.1	N/A[a]
C	0.25	0.36	31.1	7.4	7.8	5.6	68.8
D	0.21	0.39	46.5	7.2	7.3	1.0	57.5
E	0.07	0.10	25.3	3.5	3.5	0.1	37.0
F	0.16	0.23	28.7	8.3	7.6	-9.9	42.4
G	0.078	0.12	37.1	7.1	7.1	1.0	24.5
H	0.042	0.043	2.7	5.4	5.2	2.7	19.9
I	0.013	0.024	45.4	4.2	4.2	-0.2	9.1

amount of data cannot prove repeatability, it was obtained to possibly *disprove* repeatability; wildly varying data would suggest that the process is unrepeatable, making the more rigorous analysis discussed in §5.1.2.3 unnecessary.[2] Figure 50 presents the mean (dashed, horizontal lines) and standard deviation (μ and σ) of the resonance data along with each resonance measurement itself. Group 1 of Figure 50 consists of the 26 parts made from the first cantilever cavity, and similarly for Groups 2 and 3. For each group, Figure 50 shows a uniform data spread about the mean, a small standard deviation (less than 3% of the mean in all cases) and a constant mean for each group, which indicates that the IM process could be repeatable, hence a rigorous repeatability analysis was employed. A mold dedicated to the repeatability analysis along with two other molds are now discussed.

5.1.2.2 Main Mold Production Results

As discussed in §4.1.2.8, many different mold geometries were selected to produce microcantilevers, however three were focused upon. To refresh the reader's memory of §4.1.2.8 and introduce this nomenclature, mold number one was used to test the limits of the thinnest possible beams that could be injection molded, mold number two was designed to produce cantilevers with "standard" resonance- or deflection-based sensing properties (i.e., resonance frequencies of roughly 20-25 kHz and a stiffness of roughly 1 N/m), and mold number three was used to test the length scale-dependent bending stiffness of §3.3.1.3. In terms of feasible sensing, mold two should be considered the most useful.

The geometries of the first mold sought to produce the thinnest feasible microcantilevers. Mold number one was produced using a 150 μm diameter end mill operated at a 50 kRPM spindle speed with a linear feed rate of 1 mm/min. While this resulted in very wide microcantilevers as compared to commercially-available silicon parts,

[2]Resonance measurements were used as they are the simplest and most rapid to obtain– nonetheless, poor resonance data would indicate poor repeatability.

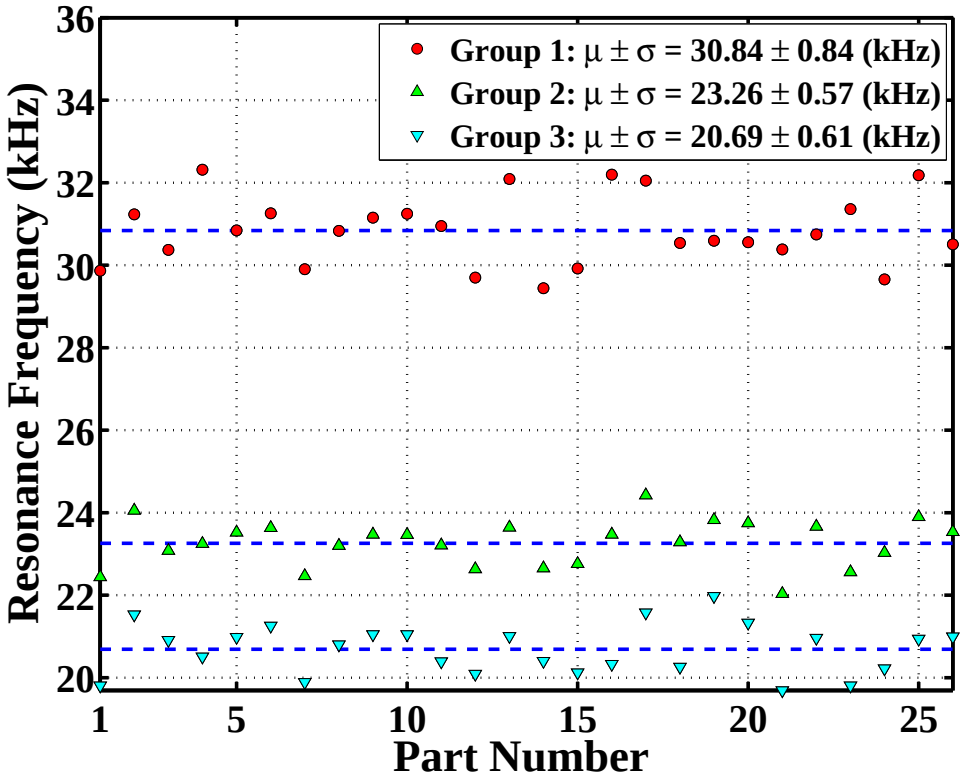

Figure 50: Resonance frequency data over 26 PS parts, each made the same mold with three cantilever cavities; the horizontal, dashed lines represent the mean value for each of the three different cantilever cavity geometries (i.e., for Groups 1, 2, and 3).

the larger end mill produced higher quality cavities than smaller diameter end mills at these small depths of cut ($\approx 2\mu$m).[3] Molds two and three were produced using the cutting conditions (50 kRPM spindle speed and 1 mm/min linear feed rate) and end mills (100 μm diameter) which made the highest quality cavities of proper depth ($\approx 10\mu$m) and a more reasonable width ($\approx 100\mu$m).

Table 9 shows the dimensions of the different cavity geometries, which are pictured in Figure 51 (the "thickness mold"), Figure 52 (the "useable mold"), and Figure 53 (the "length scale mold"– the mold of a long, thick cantilever used to test the length scale dependent stiffness of §3.3.1.3). Mold number one has a varying thicknesses (with relatively constant length and width) to explore the thinnest possible micro-cantilever while mold number two shows very similar geometries; for mold number two it was desired to make four cavities of as similar geometry as possible. Previous work had shown that the four cantilever cavities could be cut with a 100 μm end mill before tool breakage (hence the four cavities of the useable mold) while the 150 μm end mill was more robust (hence the five cavities of the thickness mold). The microcantilever numbering scheme shown in Figures 51 through 53 and Table 9 will be used throughout the rest of this dissertation.

To obtain the measured values of Table 9, ten different measurements for cavity width and thickness were taken in the parting plane at equal intervals along the cavity length direction, while five different measurements for cavity length were taken in the parting plane at equal intervals in the cavity width direction; a white light interferometer was used. Figure 54(a) and (b) shows an image output by the white light interferometer with and without line traces. The horizontal line in Figure 54(b) generates the data shown in Figure 55, which are used to determine a generic length

[3]For the smaller diameter end mills at micron-scale depths of cut, the resulting channels were almost parabolic in cross-section and left significant edge burrs, indicating that a plowing action had occurred instead true chip formation; this type of poor cutting below a threshold value has been seen in the literature and is probably due to a highly negative rake angle unavoidable as cutting depth become smaller (due to a nonzero tool cutting edge radius) [203, 76, 75].

Table 9: Microcantilever mold cavity geometries for the thickness mold (cavity numbers one through five), the useable mold (cavity numbers six through nine), and the mold used to examine the length scale dependent bending stiffness (cavity number ten). The mean geometry value is followed by the bracketed standard deviation.

Cavity Number	Length (μm)	Width (μm)	Thickness (μm)
1	374 [5]	157 [8]	2.20 [0.3]
2	365 [8]	163 [8]	2.58 [0.3]
3	370 [12]	168 [2]	3.68 [0.3]
4	381 [15]	170 [2]	3.91 [0.3]
5	405 [19]	172 [3]	5.10 [0.5]
6	417 [2]	122 [5]	12.23 [0.5]
7	396 [5]	117 [4]	12.29 [0.4]
8	387 [8]	119 [6]	12.44 [0.5]
9	379 [7]	114 [4]	12.93 [0.4]
10	836 [6]	125 [5]	29.37 [0.1]

measurement. Similarly, the vertical line in Figure 54(b) generates the data shown in Figure 56, which are used to determine a generic width and thickness measurement. The blue lines in Figures 55 and 56 are plotted on distorted axes showing the profiles while the red dots above the axes in these two figures are the equally-scaled data points (i.e., the red dots are a scaled-up description of the cantilever cavities in the actual cavity aspect ratio). The mean geometric dimensional values, obtained from these types of line traces with the different mold geometries, are shown followed by the bracketed standard deviations in Table 9. With the mold geometry results detailed, attention now turns to the repeatability of the microcantilevers produced using these molds with various polymeric materials.

5.1.2.3 Repeatability Analysis

The useable mold (Figure 52 and cavities six through nine of Table 9) was used with the four material of Table 3. Of the four materials that were employed for the

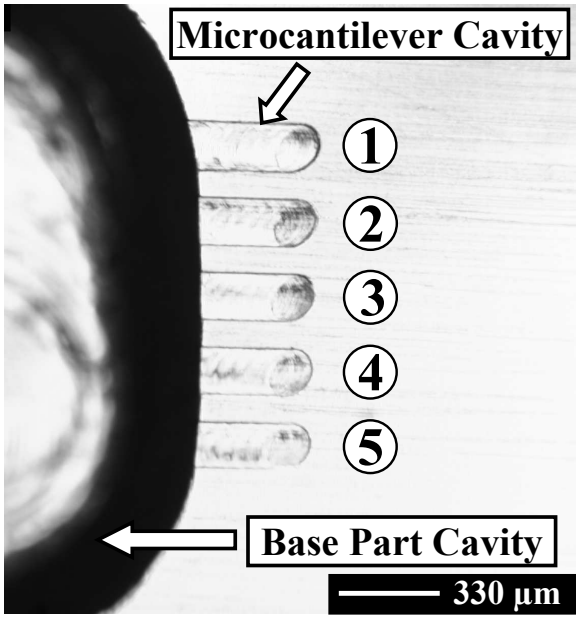

Figure 51: Optical micrograph of the "thickness mold" and the "Cavity Number" scheme of Table 9.

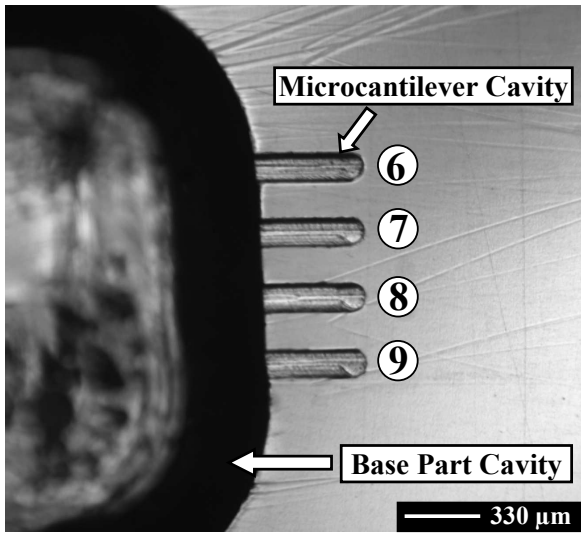

Figure 52: Optical micrograph of the "useable mold" and the "Cavity Number" scheme of Table 9.

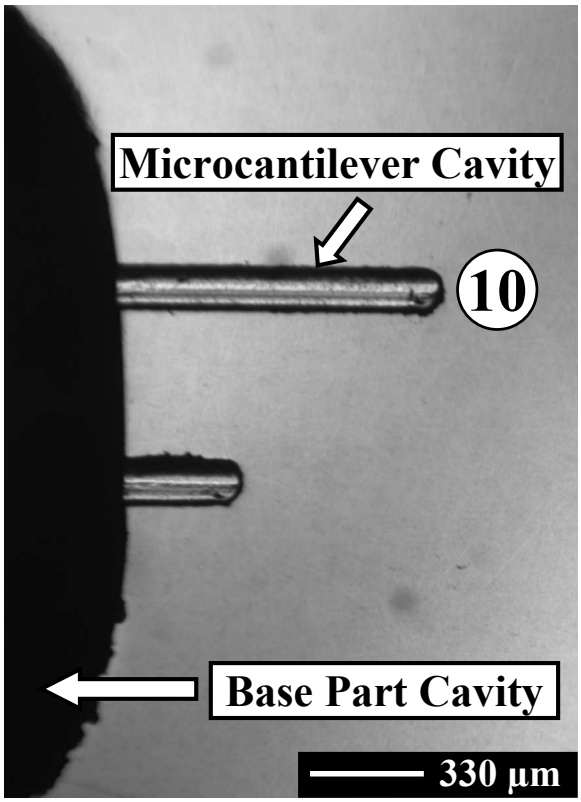

Figure 53: Optical micrograph of the mold used to test the length scale dependent bending stiffness of §3.3.1.3 and the "Cavity Number" scheme of Table 9. The shorter cavity shown below was not used for this work.

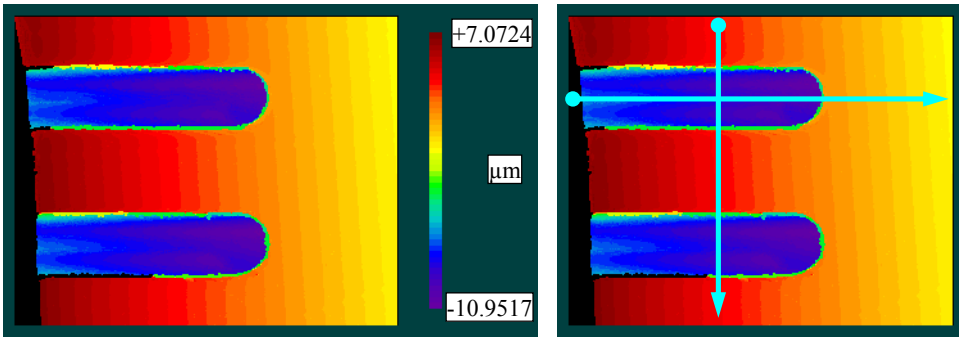

Figure 54: White light interferometer graphical output of a mild surface showing two microcantilever cavities.

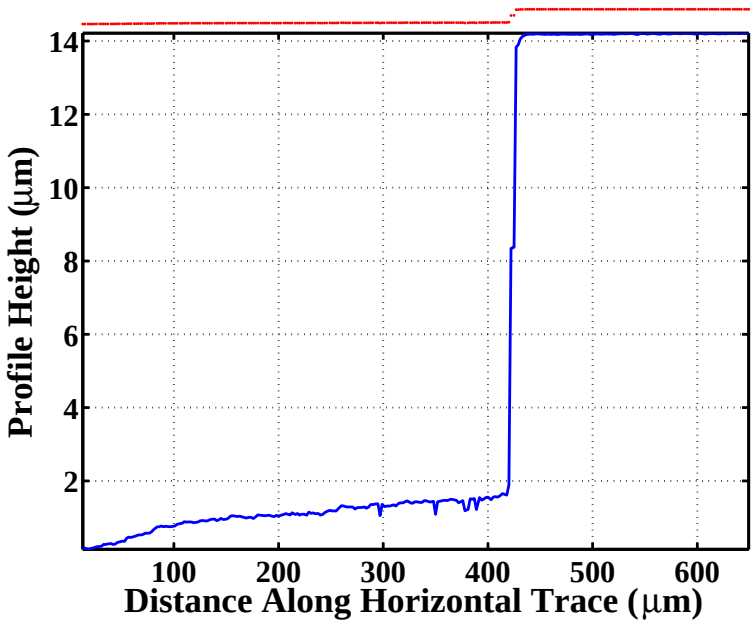

Figure 55: Output data of the horizontal line trace in Figure 54(b) (roughly 225 points, the blue lines are plotted on distorted axes showing the profiles while the red dots above the axes in are the equally-scaled data points).

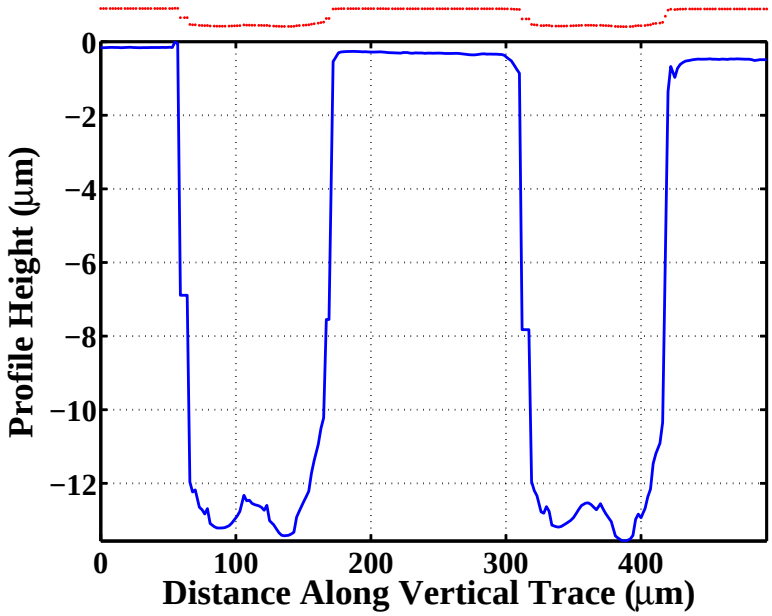

Figure 56: Output data of the vertical line trace in Figure 54(b) (roughly 225 points, the blue lines are plotted on distorted axes showing the profiles while the red dots above the axes in are the equally-scaled data points).

repeatability analysis (e.g., the PS, PP, LCP, and NN6 of Table 3), only three yielded useful parts– the PS, PP, and NN6. The first problem encountered when using the LCP was significant flash, as shown in Figure 57. This was due to the high melt flow index of the material (MFI $\approx$ 100, $\approx 10\times$ that of the PS, PP, and NN6) and excessive holding pressure. This amount of flash was extreme, and much greater than any observed with the other three materials. By reducing the holding pressure, the flash problem was resolved, but a new problem presented itself. Specifically, the microcantilever cavities would fill, but would not empty upon part removal (i.e., the cantilever cavities became clogged). The left hand side of Figure 58 shows a picture of the mold after one shot of the LCP material (i.e., the mold was cleaned to clear the cantilever cavities and then one part was made), and it is apparent that two of the four cantilevers were clogged.[4] The right hand side of Figure 58 shows the part that was removed from the mold in the left hand side of Figure 58, and none of the four cantilevers were fixed to the part after removal; two of the cantilevers were obviously stuck in the mold and the other two presumably were ripped off during removal. Of roughly 100 parts attempted, not one LCP part had a full length cantilever upon removal from the mold, and all four cantilever cavities of the mold became clogged after production of roughly four parts. Therefore, it was concluded that the fiber-filled LCP material was not feasible to produce the microcantilever parts.

Conversely to the LCP, the PS, PP, and NN6 materials produced parts with acceptable flash. The PS parts showed the most flash, as shown in Figure 59; even with this amount of flash, the PS parts were feasible sensors and showed good repeatability (as will be discussed subsequently).[5] The PP and NN6 parts exhibited minimal flash,

[4]Note that the color of the mold in Figure 58 is slightly blue (initially the mold was chrome-colored); this is due to a phase transformation induced by the high mold temperatures (as compared to the other three materials used) of roughly 250 °C dictated by the LCP. The LCP material was used last so that all measured parts were made before the mold steel was blued.

[5]The flash thickness was determined via white light interferometry to be roughly 150-200 nm, indicating that true nano-scale injection molding may be possible if the mold cavities could be manufactured in a controlled fashion at the nanoscale, via EDM for example.

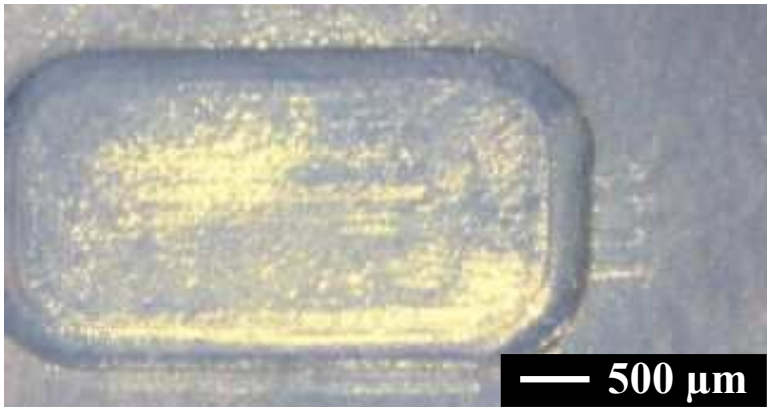

Figure 57: Optical micrograph of a completely flashed LCP microcantilever part (this part was made with the mold shown in Figure 52).

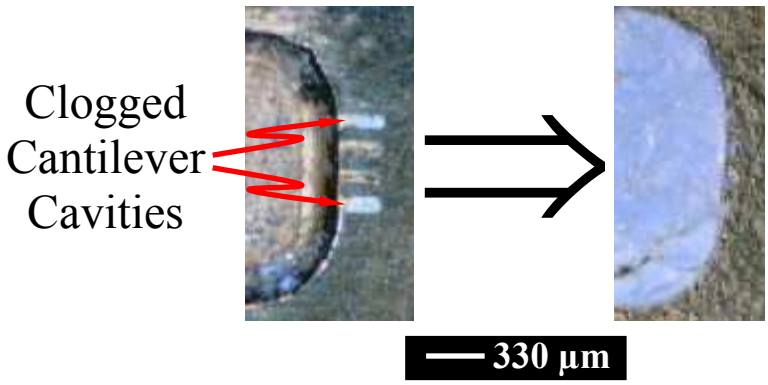

Figure 58: Optical micrographs of the partially clogged useable mold (left) and the resulting part (right); this is the mold pictured in Figure 52.

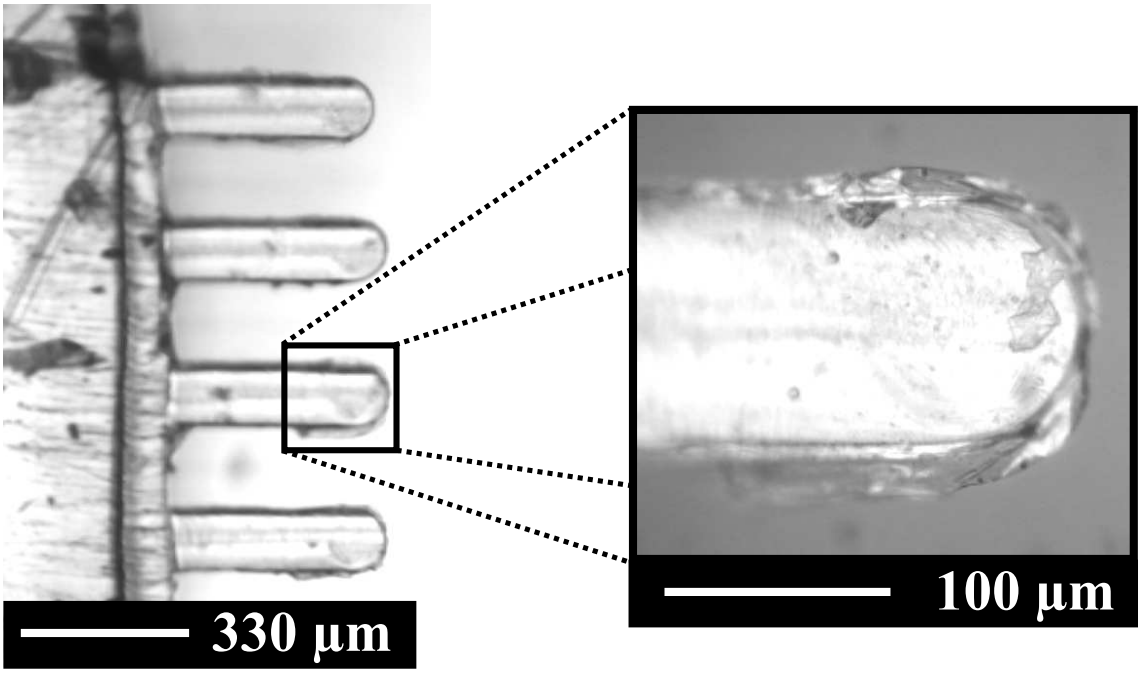

Figure 59: Optical micrographs of a representative PS part with flash.

and representative beams are shown in Figure 60 for PP (top) and NN6 (bottom). It should be noted that during the feasibility study it was learned that as the molds are used more, the amount of flash for a given polymer diminishes somewhat, most likely due to the top mold insert repeatedly being pressed upon the bottom insert (with roughly 8 kN of force) which decreases, in an attritional fashion, any burrs that exist around the parting plane edges of the microcantilever cavities. Therefore, the flash exhibited by the PS is probably due to youth of the useable mold, because PS was the first material used. Unfortunately, the production attempts with the LCP material warped (due to excessive temperatures) the useable mold so it could not be used after some wear to make PS parts and test this theory. However, work of the feasibility analysis with different molds showed this type of flash reduction with sufficient mold usage when using the PS material (see Figure 49). Nonetheless, the PS parts with flash were feasible sensors whose mechanical behavior was repeatable as will be shown in the remainder of this subsection.

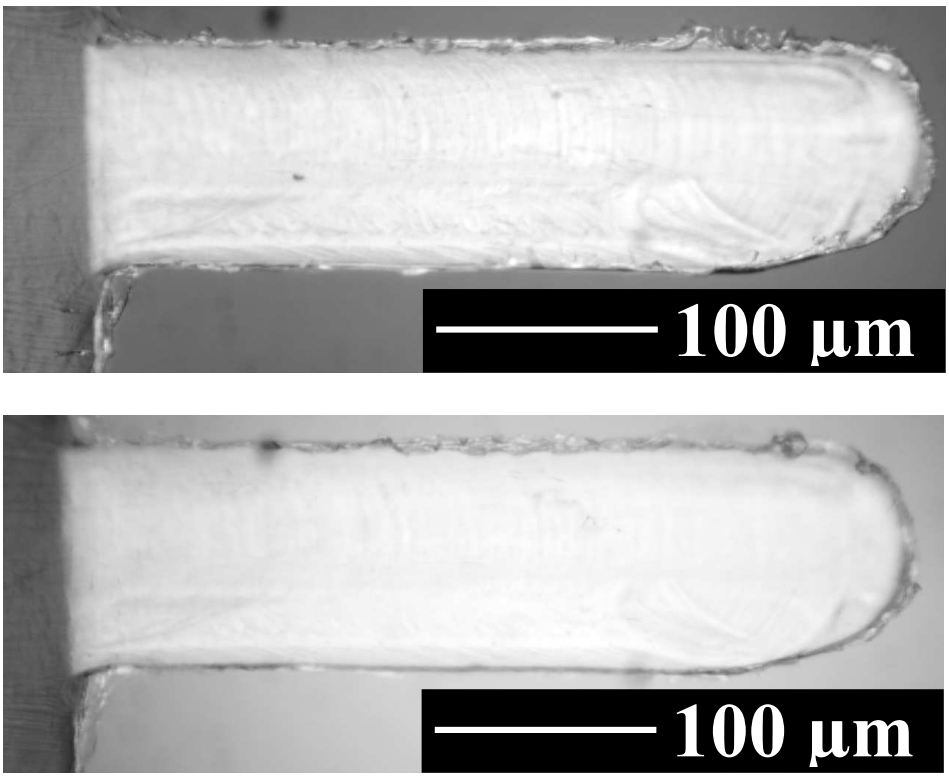

Figure 60: Optical micrographs of representative PP (top) and NN6 (bottom) microcantilevers.

The processing conditions and machine settings that varied from material to material are listed in Table 10 (see Table 2 for the constant machine settings). Similar to the solvent cast parts (§5.1.1), each injection molded part made from these three materials that was measured for the repeatability analysis was first coated with roughly 20 nm of gold at a rate of 0.25 Å per second so that sufficient laser energy would be reflected off of the microcantilevers for use in the Scentris system. The resonance frequency was used as the parameter to judge repeatability and the state of process control (i.e., in or out of control); the criteria for which are now discussed.

One approach to quantifying repeatability and control status of the IM cantilever production process would be to manufacture X number of microcantilever parts and calculate statistical values such as the mean and standard deviation of measured parameters (e.g., k and f_1) of the X parts, and use these statistical values to gauge

Table 10: Processing conditions for the PS, PP, and NN6 parts made for the repeatability analysis.

VARIABLE	POLYSTYRENE (PS)	POLYPROPYLENE (PP)	NYLON COMPOSITE (NN6)
MOLD COOL TIME (SECONDS)	30	30	45
MAXIMUM INJECTION PRESSURE (MPA)	22.5	22.5	30
1ST HOLDING PRESSURE (MPA)/TIME (SECONDS)	22.5/10	22.5/10	30/15
2ND HOLDING PRESSURE (MPA)/TIME (SECONDS)	22.5/10	22.5/10	30/15
MOLD TOP INSERT TEMPERATURE (°C)	162.8	162.8	190.6
MOLD BOTTOM INSERT TEMPERATURE (°C)	148.9	148.9	176.6
HEATED CENTRAL BLOCK TEMPERATURE (°C)	218.3	218.3	248.9
NOZZLE TEMPERATURE (°C)	218.3	218.3	248.9

repeatability and process control. While this approach is valid, this work sought to produce a more rigorous repeatability judgement, and statistical process control (SPC) was used.[6] The theory behind SPC is to take subsets of all the produced products, measure certain parameter(s) of interest, and then use this data to draw reasonable conclusions about the entire lot of parts produced, even though the desired parameter(s) of each part have not been measured. SPC allows for these conclusions to be drawn from a lot of parts produced over a larger time frame without measuring each part, hence speaking to repeatability in a larger sense than just measuring the first X number of parts produced. The reader may see Appendix C for a review of SPC and the rules used in this work to determine control and repeatability.

The SPC analysis was employed for the useable mold (i.e., that shown in Figure 52) using the three feasible materials (PS, PP, and NN6; see Table 3 of §4.1.2.7

[6]SPC is a technique commonly used in manufacturing and business to determine whether or not the production of specific part or service, so long as quantifiable performance measures exist, is repeatable and in control [230, 42].

for material description). The scheme was to produce 230 parts from the mold from each material. A subgroup size of five with a total of ten subgroups was chosen, and Western Electric Company Zone Rules (WECO rules) were employed to produce X-bar charts (see Appendix C for details). This is a total of (one mold)$\times$(ten subgroups per mold)$\times$(five parts per subgroup)$\times$(four microcantilevers per part)$\times$(one measurement per microcantilever per material)$\times$(four materials) equals 800 measurements (see Appendix E for the individual measurements). The subgroups consisted of parts 1-5, 26-30, 51-55, 76-80,..., 226-230, for each cantilever made from each material. The Scentris system of §4.2.3 was used and each measurement consisted of determining the first bending mode resonance frequency. The Scentris was operated in AC tuning mode, which means that the cantilever parts were actuated piezoelectrically in a frequency sweeping fashion to locate the first-mode resonance frequency. The repeatability was determined only for the useable mold as it is experimentally valid, whereas the thickness and length-scale testing mold were used only to determine filling feasibility of the different polymers and to test the length scale-dependent bending stiffness theory of Chapter 3.

Figure 61 shows the X-bar plot for f_1 with the useable mold (cavities numbered six through nine in Table 9) using polystyrene. None of the so-called Western Electric Company Zone Rules, which dictate the control and repeatability status of a system, were violated (see Appendix C), indicating that the IM production of the PS parts from the useable mold in terms of f_1 is repeatable and in control. The process was also repeatable and in control for the other two materials used (i.e., PP and NN6), but the X-bar charts for these materials are relegated to Appendix D (Figure 100 and Figure 101) for sake of brevity. Table 11 shows the overall means (μ), ranges, standard deviations (σ), and percent of the mean represented by the standard deviation for f_1 for the various materials made with the useable mold.[7]

[7]The $N = 50$ total measurements per cavity geometry per material are used to calculate the

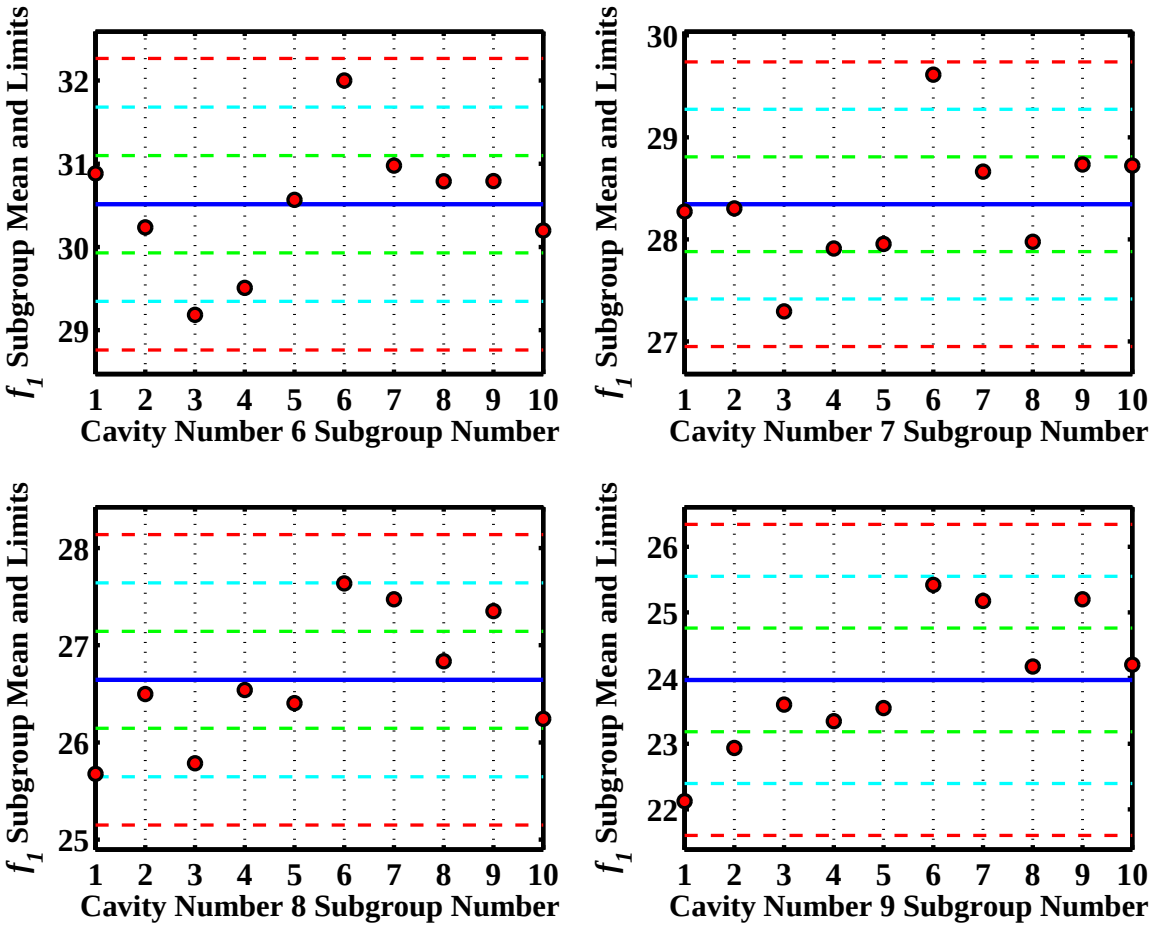

Figure 61: f_1 X-bar plots for the polystyrene parts (ordinate values are in kHz).

Table 11: Total mean, range, standard deviation, and percent of the mean represented by the standard deviation f_1 over fifty measurements per material taken from each of the microcantilever geometries from the useable mold (cavities six through nine) made from three materials (see Table 3 for material description).

Cavity Number	Material Number	f_1 Mean, μ (kHz)	f_1 Range (kHz)	f_1 Standard Deviation, σ (kHz)	Percent of μ Represented by σ
6	PS	30.51	3.94	0.97	3.18
6	PP	27.09	5.21	1.00	3.70
6	NN6	31.48	6.74	0.82	2.61
7	PS	28.34	3.99	0.95	3.35
7	PP	19.43	9.88	1.94	9.98
7	NN6	26.76	9.86	2.86	10.69
8	PS	26.64	4.81	1.02	3.83
8	PP	21.83	8.71	1.60	7.33
8	NN6	25.33	6.92	1.26	4.97
9	PS	23.97	5.74	1.38	5.76
9	PP	21.43	5.98	1.03	4.81
9	NN6	24.51	6.45	0.75	3.06

Before ending the repeatability analysis discussion, and its conclusion of IM being an in control, repeatable production process to make microcantilevers, the four main assumptions of the SPC analysis were investigated (see Appendix C) and are now discussed in turn. To determine randomness of the data, autocorrelation plots for all the mold geometries with the four materials were generated. Figure 62 shows the autocorrelation plot for the parts made from PS. Aside from one data point at a lag of three, Figure 62, the other autocorrelation plots (Figure 102 and Figure 103 in Appendix D), verify that the measured data are random. The data point suggesting

mean and standard deviation values in Table 11, values which are defined in the conventional sense of $\overline{X} = \mu = \frac{1}{N}\sum_{i=1}^{N} X_i$ and $\sigma = \left[\frac{1}{N-1}\sum_{i=1}^{N}\left(\overline{X} - X_i\right)^2\right]^{\frac{1}{2}}$ where the X_i represent a generic measurement of f_1.

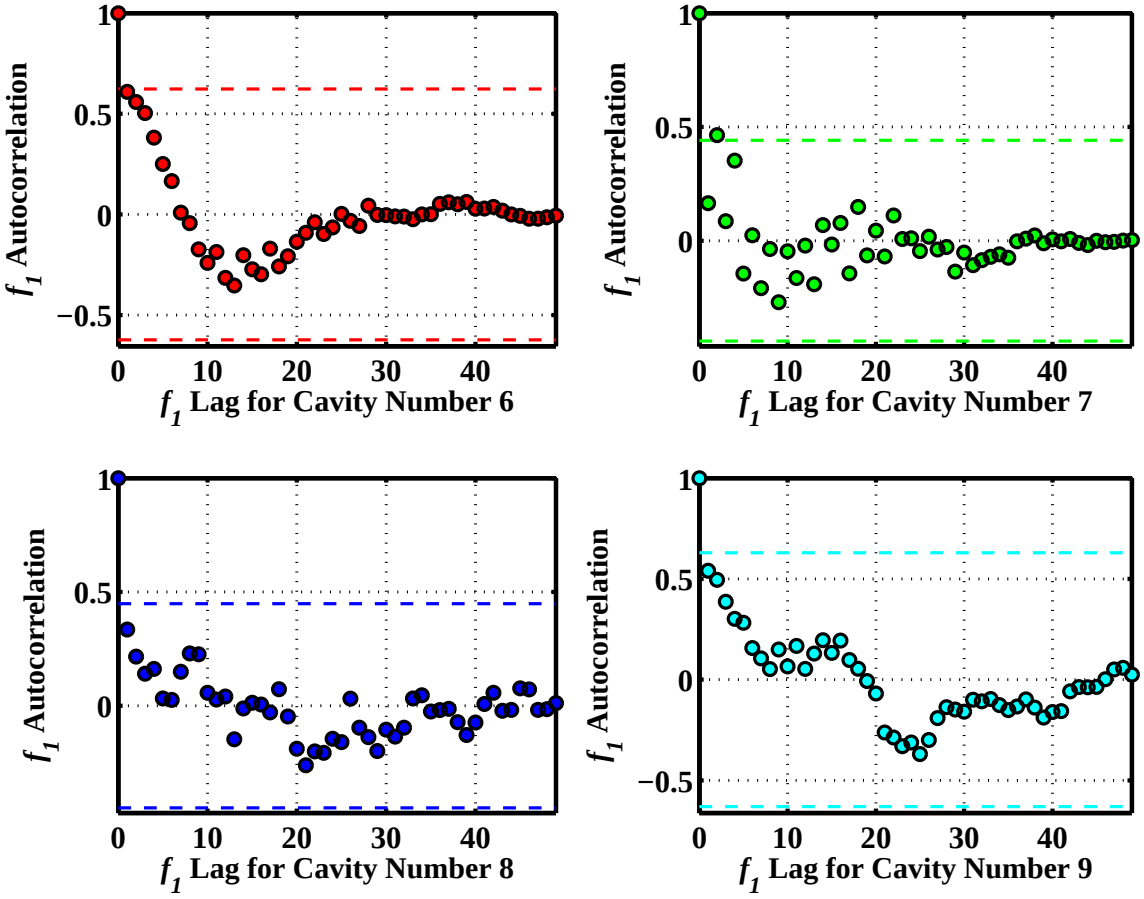

Figure 62: f_1 autocorrelation plots for the polystyrene parts.

non-random PS part data at a lag of three is considered negligible as it is very close to the bound, and occurs only in one instance.

To determine if the errors and measured values of the process are distributed normally, a linear regression is performed on each set of data (the $n = 50$ individual k measurements for a given beam geometry for a given polymer, for example) and a normal probability plot of the residuals was generated for each of the twelve resulting data sets (four mold cavities times three materials);[8] the N residuals will simply be

[8] A normal probability plot is constructed by plotting the theoretical residual values from a standard normal distribution versus their sorted values (small to large). Curvature or other severe deviations from a straight line imply that the random errors are not normally distributed [192].

the ith data point minus the overall mean (for $N = 1, 2, \ldots, 50$).[9] Figure 63 shows the residual normal probability plot for the PS parts for the measured first mode resonant frequency. In Figure 63, the residuals were normalized (i.e., for each of the four data series, each residual was divided by the maximum residual value in that respective series) to allow them to be plotted on the same graph; the normalization will only change the slope of the data, which is unimportant because linearity of the data points is the only item of interest. The data in Figure 63 show that the linearity description seems reasonable for f_1 and for the residuals of f_1 measured from PS parts from each of the four mold cavities.[10] Similarly, the remaining normalized residual probability plots for mold cavities numbered seven through nine for both of the other two materials used (shown in Figure 104 and Figure 105 in Appendix D) all display linearity as well. Therefore, all of the errors of the statistical repeatability analysis are assumed to be normally distributed.

To determine if the measured data sets had a constant mean (see Appendix C), run-sequence plots were generated. Figure 64 shows the run sequence plot for the measured f_1 values from the polystyrene parts and this plot, along with the others generated for the different materials (Figure 106 and Figure 107 of Appendix C), show that all the data sets do have a constant mean.

The final assumption that needs to be validated to validly employ SPC is that of homoscedasticity, or constant variance of the data, and autoregressional conditional

[9]From the definition of a linear regression one fits the data of $i = 50$ measurements of stiffness, k_i (for example) to the form: $k_i = X_i\mathbf{b} + \epsilon_i$ where $X = [1, 1, \ldots, 1]$ (length i) for this case (since the stiffnesses should not vary for a given polymer and cavity geometry); after least-squares minimization this results in $\mathbf{b} = (X^T X)^{-1} X^T k = ([1, 1, \ldots, 1][1, 1, \ldots, 1]^T)^{-1} X^T k = n^{-1}[1, 1, \ldots, 1][k_1, k_2, \ldots, k_{50}]^T = \bar{k} \Rightarrow \epsilon_i = k_i - X_i\mathbf{b} = k_i - \bar{k}$.

[10]If the errors of a univariate data set are normally distributed, then the data set itself is normally distributed; the equation for the data set will be the mean value plus the residuals, which is a uniform distribution (the mean is constant) plus normally distributed residuals and a uniform distribution plus a normal distribution is just a normal distribution with a shifted mean.

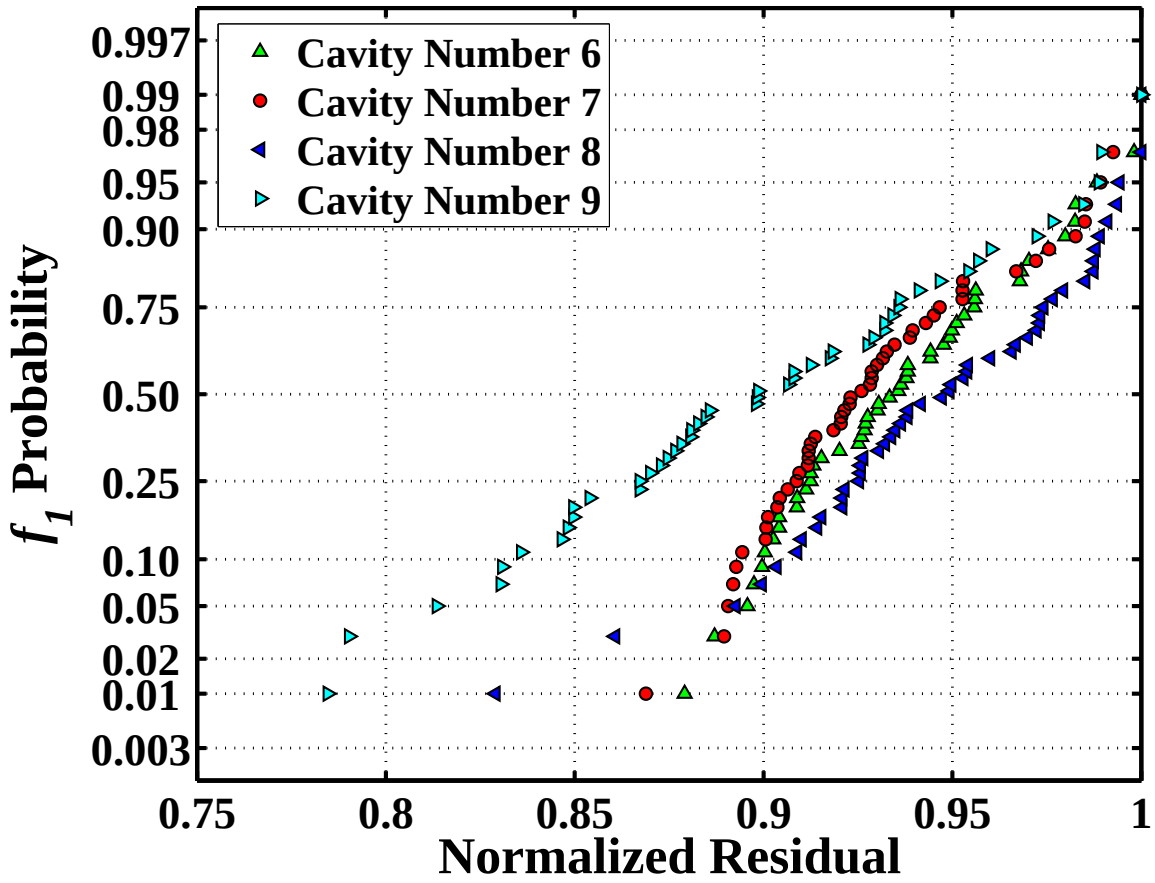

Figure 63: f_1 normalized normal probability plots for the polystyrene parts.

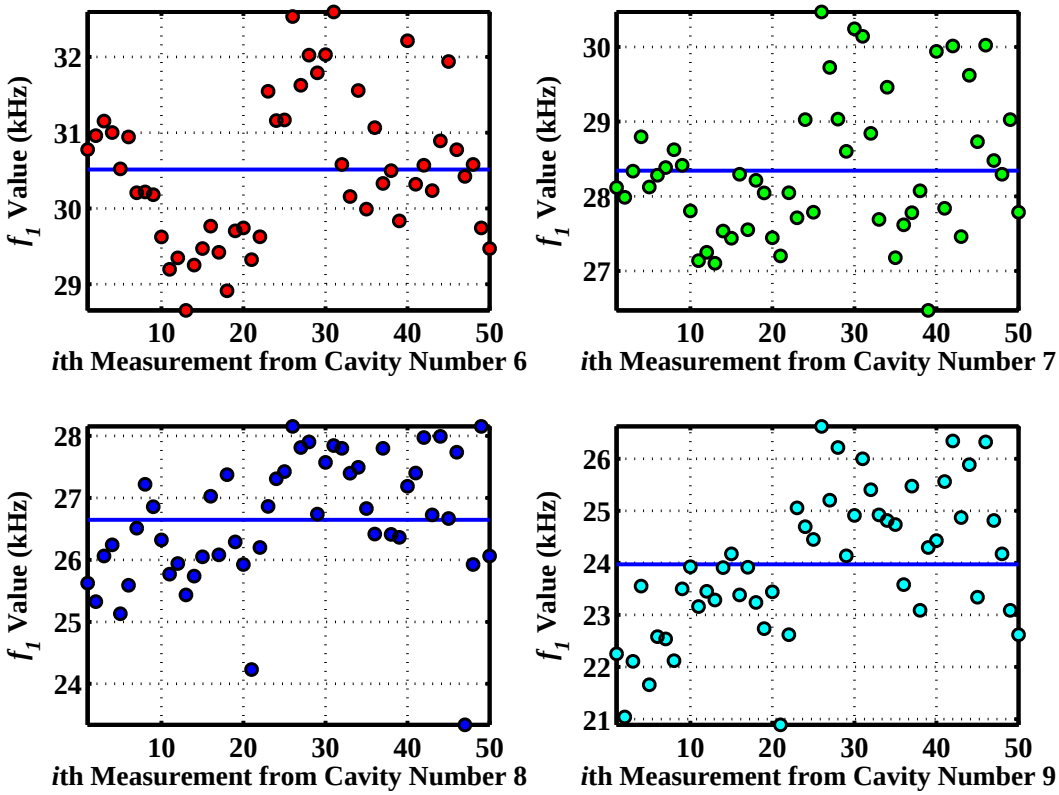

Figure 64: f_1 run sequence plots for the polystyrene parts (the horizontal line indicates the overall mean).

heteroscedasticity (ARCH) analysis was used (see Appendix C).[11] The ARCH analysis showed that, to a significance level of 0.001 (i.e., 99.9% confidence), all data sets measured showed homoscedasticity.[12]

As the assumptions of the SPC analysis are justified (random data from a normal distribution with constant mean and variance of the individual data sets), employment of the Western Electric Company Zone Rules with the X-bar charts is justified, and therefore so are the conclusions of these rules: the IM carried out for this work is a repeatable, in-control process for producing polymeric microcantilevers.

[11] One could use the more common, although less statistically rigorous SPC-based approach of R-charts, which are X-bar charts applied to the range of data of each subgroup. The range is used as an estimate of the standard deviation, so an R-chart used in conjunction with the WECO rules estimates whether or not the standard deviation, and equivalently the variance of the subgroups is repeatable and in control (e.g., if the variance is constant).

[12] The MATLAB archtest function was used for the ARCH analysis.

Before moving to the next manufacturing goal, a comparison between the theoretical first mode frequencies (obtained via Equation 54, the average mold geometry values in Table 9, and the material property data of Table 3) is given in Table 12. The first two columns identify the cavity number and material, while the last four columns identify the experimental mean, the predicted mean, and the percent difference between the two, which is defined as 100*(predicted value - experimental value)/predicted value. It is apparent that the theoretical values are all below the experimental values, and this is likely due to the high frequency of the motions that the beams are experiencing. The elastic modulus values in Table 3 are obtained using uniaxial tension tests, which are run at strain rates much lower than those experienced by the microcantilevers as they resonate. As discussed in §3.3.3.2, the elastic modulus will monotonically increase with strain rate for the polymers considered here (e.g., amorphous and semicrystalline polymers well below their T_g) so it is expected that the uniaxially-determined elastic modulus values would underestimate the resonance frequency (recall that $f_i \propto \sqrt{E}$). This is not a groundbreaking discovery though, resonance frequency and phase measurements have long been used to obtain the storage and loss modulus values for polymeric cantilever specimens [2, 31, 200]. The discussion and calculation of the structural damping (in polymers) in the context of the resonant behavior of polymeric microcantilevers is beyond the scope of this work.

With the production of microcantilevers proven feasible via solvent casting (§5.1.1) and injection molding, and the repeatability proven and justified for IM using three distinct classes of polymer, the first manufacturing goal of the project is met (see §1.2.1). The second manufacturing goal, the thinnest microcantilever possible produced via IM, is now discussed.

Table 12: Mean experimental f_1 values, theoretical f_1 values, and percent difference from fifty measurements per material taken from each of the microcantilever geometries from the useable mold (cavities six through nine) from three materials (see Table 3 for material description).

Cavity Number	Material Number	Mean Experimental f_1 (kHz)	Theoretical f_1 f_1(kHz)	Percent Difference
6	PS	30.51	25.09	-21.6
6	PP	27.09	18.75	-44.5
6	NN6	31.48	23.38	-34.7
7	PS	28.34	22.79	-24.4
7	PP	19.43	17.03	-14.1
7	NN6	26.76	21.23	-26.0
8	PS	26.64	21.50	-23.9
8	PP	21.83	16.07	-35.9
8	NN6	25.33	20.03	-26.4
9	PS	23.97	19.29	-24.2
9	PP	21.43	14.42	-48.6
9	NN6	24.51	17.98	-36.3

5.1.2.4 Results– Thickness Mold

The thickness mold (cavity numbers 1 through 5 in Table 9 and shown in Figure 51) was used for this portion of the work. The PS, PP, and NN6 (see Table 3) were the materials employed, and all three of them filled the microcantilever cavities with acceptable amounts of flash. It was discovered that the minimum thickness of the parts was limited by the inability to produce microcantilevers that were flat enough for characterization, due to warpage manifestation as the parts cooled in the mold cavity (i.e., microcantilever cavity filling and flash were not the limiting factors).[13] The PP and NN6 cantilevers that were made ended up so curled that they were unable to be characterized in the AFM or the Scentris system because the laser reflected off the beams to regions inaccessible to the photodiode. The PS parts, however, showed less, albeit still severe, warpage to the extent that they could be characterized in the AFM (the Scentris system could not be used because the gold-coating process causes severe curvature of the cantilevers). A representative PS part is shown in Figure 65. A repeatability or characterization analysis could ensue, but the goal of this section is merely to examine the thinnest microcantilevers possible. In terms of feasible sensing, the minimum thickness is concluded to be above two microns. However, it could be possible to use IM to produce thinner cantilevers if the warpage problem could be overcome; a true rapid thermal response mold design may be able to accomplish this and could be useful future work. The final manufacturing goal, production of composite parts, is now discussed.

5.1.2.5 Composite Microcantilevers with Varying Fillers and Filler Content

As mentioned in §4.1.2.7, PMMA-carbon nanofiber composite materials were employed for this work. This was done to satisfy the third manufacturing goal, which

[13]Many different combinations of processing conditions were implemented to reduce warpage, but the attempts were unsuccessful.

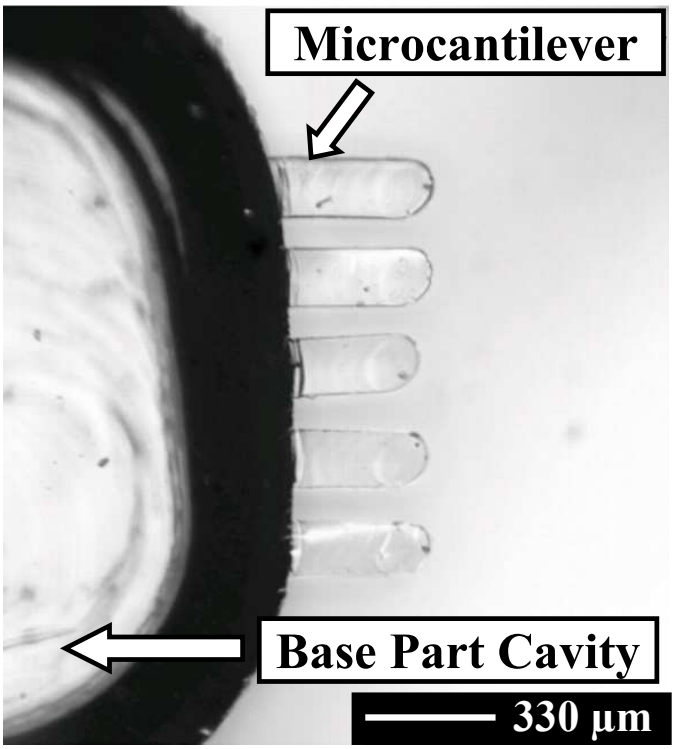

Figure 65: Optical micrograph of a PS thickness mold part.

sought to show the ability to tailor the microcantilever's mechanical behavior (quantified via resonance frequency measurements) for a given matrix material and a given mold geometry. A three-cantilever mold from the feasibility study was chosen (the useable mold was warped due to overheating when trying to inject the LCP material in the repeatability analysis), and ten, three-cantilever parts were made from this mold using the neat PMMA and the four PMMA-carbon nanofiber composites shown in Table 4.[14] Figure 66 shows a picture of the mold used along with the numbering scheme while Table 13 shows the mean and bracketed standard deviation values (obtained using the interferometry methods of §5.1.2.2) for the mold used.

No SPC repeatability analysis was performed for these parts as the work of §5.1.2.3

[14]The materials obtained for this work were donated by Dr. Satish Kumar of the School of Textile and Fiber Engineering department at the Georgia Institute of Technology. Only five grams (roughly two tablespoons) of each material was available, hence only ten parts were made from each material; the small volume of material was hedged by the large volume of advice, material property data, and reference material donated by Dr. Kumar.

Table 13: Microcantilever mold cavity geometries used to make the PMMA-CNF parts. The mean geometry value is followed by the bracketed standard deviation.

Cavity Number	Length (μm)	Width (μm)	Thickness (μm)
11	506 [14]	130 [10]	17.73 [0.4]
12	468 [12]	132 [9]	16.44 [0.5]
13	398 [10]	123 [6]	15.85 [0.4]

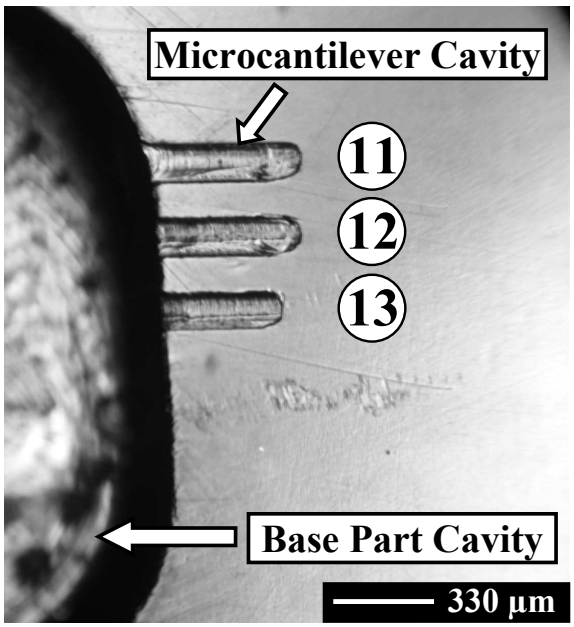

Figure 66: Optical micrograph of the mold whose geometry is the "Cavity Number" scheme of Table 13.

is considered sufficient to prove repeatability. However, as will be seen from the mean and standard deviation of the measured quantity (e.g., first-mode resonance frequency), production of the PMMA-CNF composite parts showed very little variation, and the variation was consistent with that shown in the overall mean and standard deviation of the parts made for the repeatability analysis of §5.1.2.3.

The PMMA-CNF parts showed interesting mold filling behavior. Parts could be made without flash that had incompletely filled cantilever cavities, or parts could be made with flash and filled cantilever cavities. It is hypothesized that the mold insert

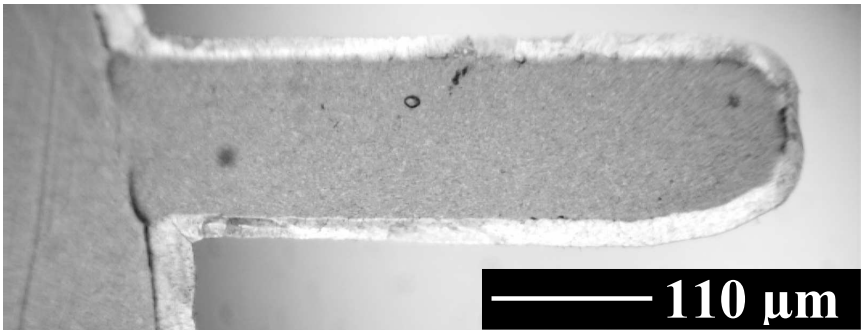

Figure 67: Optical micrograph of a representative PMMA-CNF part showing the PMMA flash and PMMA-CNF cantilever.

(top and bottom) flatness was such that it led to completely-filled cavities with flash consisting mainly of the PMMA matrix material and cantilevers consisting of the PMMA-CNF composite material, as shown in Figure 67 (this type of filling behavior was representative of all the PMMA-CNF composite materials). This would be due to the nanofibers decreasing the viscosity of the composite material as compared to the PMMA matrix material. There could be trace amounts of CNF in the flash, but due to the small size of the fibers (diameters of roughly 100-200 nm), they would be unobservable with the optical microscope. Even with the excessive flash, the parts made from the various PMMA-matrix materials showed high repeatability and statistically different mechanical behavior, as is now discussed.

Table 14 shows the mean and standard deviation of the f_1 values obtained from the ten different parts made from each of the five materials in Table 4 (see Appendix F for the complete data listing), and the percent of the mean represented by the standard deviation values, $100\frac{\mu(f_1)}{\sigma(f_1)}$. Although not to the degree demonstrated in the repeatability study (see Table 11), the values of Table 14 show small variation (quantified by the percent of the mean represented by the standard deviation), which indicates good repeatability. While this is reassuring, the goal of this subsection was not to show repeatability but to show statistically different mechanical behavior for some or all

Table 14: Total mean, range, standard deviation, and percent of the mean represented by the standard deviation of f_1 over ten measurements per material taken from each of three microcantilever geometries (arbitrarily numbered 10, 11, and 12) made from five materials. Material Number 1: Neat PMMA, Material Number 2: PR-21-PS 5%, Material Number 3: PR-21-PS 10%, Material Number 3: PR-21-PS 5%, Material Number 3: PR-24-PS 10% (see Table 4 for material description).

Cavity Number	Material Number	f_1 Mean, μ (kHz)	f_1 Range (kHz)	f_1 Standard Deviation, σ (kHz)	Percent of μ Represented by σ
11	1	40.46	8.28	2.45	6.0
11	2	42.67	5.85	1.92	4.5
11	3	42.16	4.19	1.31	3.1
11	4	43.68	10.44	2.74	6.3
11	5	44.73	13.02	3.82	8.5
12	1	31.40	7.00	2.37	7.5
12	2	34.99	9.19	2.67	7.6
12	3	32.90	3.05	1.24	3.8
12	4	33.84	10.07	2.72	8.0
12	5	34.52	11.11	3.41	9.9
13	1	26.79	4.64	1.49	5.6
13	2	32.10	7.51	2.54	7.9
13	3	28.23	5.58	1.81	6.4
13	4	28.94	11.03	3.44	11.9
13	5	30.65	9.70	3.15	10.3

of the different PMMA-based materials employed; the statistical approach to quantifying this goal is now presented and the final judgement on mechanical behavior disparity made.

To determine whether or not the different fillers gave a statistically significant difference in mean values for first-mode bending resonant frequency a so-called pairwise comparison was performed. One mean-comparison test is the one-way analysis of variance (ANOVA), where one compares the mean values of numerous groups and tests the hypothesis that they are all the same, against the null hypothesis that they are

not all the same. However, the null hypothesis (i.e., not all means are the same) is too general for this case as it is desired to specifically tell which individual pairs are statistically significantly different from each other. Another mean-comparison approach is to perform a t-test of one group mean against another (a standard approach), where the specified confidence (α) determines the cutoff value of the t statistic. For $\alpha = 0.025$, when there is no statistical difference between the means of two groups, one will incorrectly find a statistically significant difference no more than 2.5% of the time. When more than two groups exist, if the t-test (with $\alpha = 0.025$ for example) were applied to each group the chance of incorrectly finding a statistically significant difference would increase (as there is more than one comparison).

Due to the shortcomings of ANOVA and pairwise t-testing, a Tukey pairwise comparison was employed. The Tukey test compares the means of each sample (μ_i) group and provides a mean difference value (e.g., $\mu_1 - \mu_2$) and, more importantly, a confidence interval for the difference, at a given confidence level. If the confidence interval of the difference contains zero, then the difference is not statistically significant, and vice-versa if the interval does not contain zero.

Tukey comparisons of the data showed that, for all beam geometries, the neat PMMA showed a statistically significant difference from at least one of the composite materials, hence satisfying the manufacturing goal of this subsection. The comparisons between the PMMA/CNF parts of varying fillers and contents showed mixed results; for some of the geometries and composite material combinations there was a statistically significant difference while for others there was not. The results are presented as matrix formats in Figure 68. Note that there is no reason to assume that the different composite materials would be statistically different than each other, especially in light of their elastic modulus values (see Table 4).

(a)

	NEAT PMMA	PR – 21 – 5	PR – 21 – 10	PR – 24 – 5	PR – 24 – 10
NEAT PMMA	0	0	0	0	1
PR – 21 – 5		0	0	0	0
PR – 21 – 10			0	0	0
PR – 24 – 5		Symmetric		0	0
PR – 24 – 10					0

(b)

	NEAT PMMA	PR – 21 – 5	PR – 21 – 10	PR – 24 – 5	PR – 24 – 10
NEAT PMMA	0	0	1	0	0
PR – 21 – 5		0	0	0	0
PR – 21 – 10			0	0	0
PR – 24 – 5		Symmetric		0	0
PR – 24 – 10					0

(c)

	NEAT PMMA	PR – 21 – 5	PR – 21 – 10	PR – 24 – 5	PR – 24 – 10
NEAT PMMA	0	1	0	0	1
PR – 21 – 5		0	1	0	0
PR – 21 – 10			0	0	0
PR – 24 – 5		Symmetric		0	0
PR – 24 – 10					0

Figure 68: Multiple comparison matrices for (a) cavity number one, (b) cavity number two, and (c) cavity number three. An entry of zero in the (i, j) location indicates that the f_1 means for Group i and Group j are not statistically different, while an entry of one indicates that the f_1 means of the two groups are statistically different.

5.1.2.6 Durability of Injection Molded Microcantilevers

To investigate the durability of injection molded cantilevers, an experiment similar to that of §5.1.1.1 was conducted. An injection molded PS cantilever was deformed three times in manners that are extreme when compared to the actual deformation the parts would see in use. Figure 69 parts (a) through (h) show the events in chronological order. Part (a) is the beam as it comes out of the injection mold, (b) is the first deformation event, and (c) is the recovered shape. Figure 69 (d) shows the second, more extreme deformation event, along with the recovered shape in (e). Figure 69 (f) shows the most extreme situation, which is essentially a 90° bending of the cantilever, with the recovered shape shown in (g). Finally, Figure 69 (h) shows the "flattened" shape, obtained by manually flexing the microcantilever of Figure 69 (g) in a downward fashion so that it is somewhat flat again. It should be noted that the configurations of Figure 69 (c), (e), and (h) are flat enough for use in an AFM or the Scentris system. Similar results are seen for the other types of polymers employed (see §4.1.2.7 for a listing of materials used). That the microcantilevers are still feasible for use after this type of deformation implies that the plastic beams are durable– on numerous occasions plastic beams were dropped on the floor and stepped on without damage, a feat that would likely destroy silicon-type beams.

5.1.3 Injection Molded Microcantilevers as Sensors

This subsection presents experimental results obtained when using injection molded microcantilever parts as scanning force microscopy probes (§5.1.3.1) and as both deflection- and resonance-based sensors (§5.1.3.2 through §5.1.3.4).[15] The purpose of this subsection is to show that polymeric cantilevers can produce results commensurate with those of commercially-available silicon type cantilevers in a variety of

[15]The resonance-based sensing of this section is only due to an adsorbed mass, as the experimental results of surface stress induced resonance shifts (a scientific goal) are discussed in §5.2.2, along with the other scientific goal-related results.

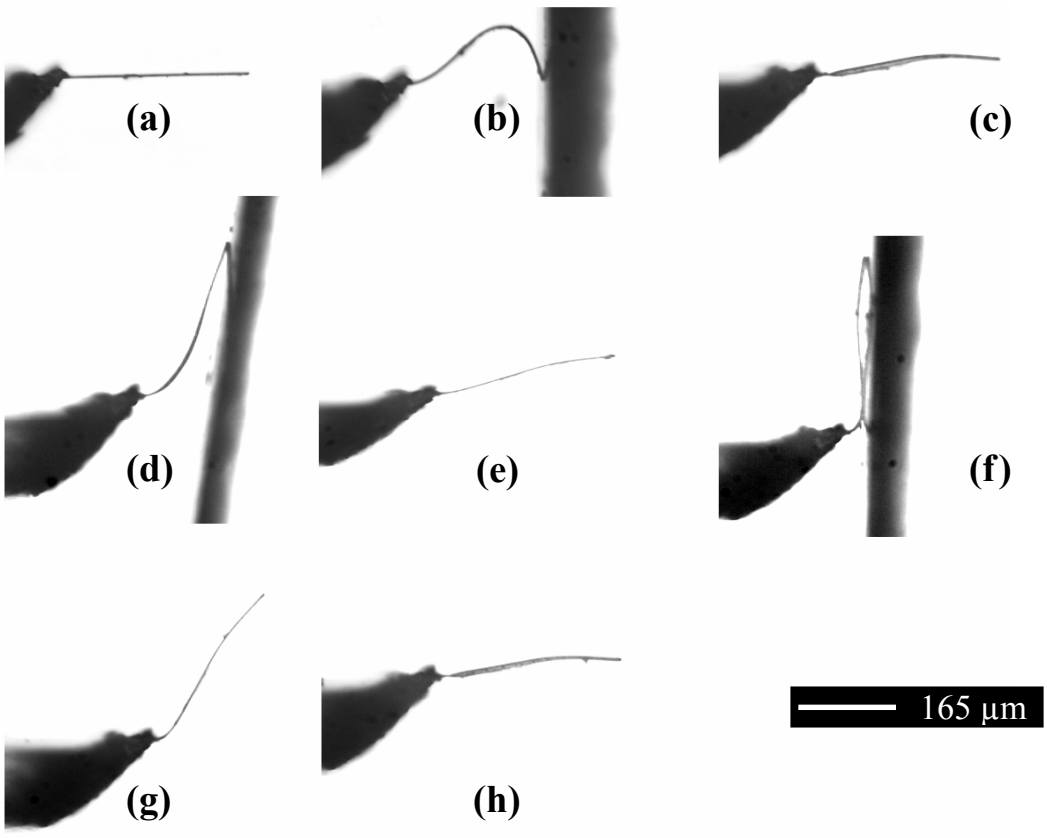

Figure 69: Optical micrographs of deformation events of an injection molded PS microcantilever.

commonly-used fields.

5.1.3.1 New Measurement Application– Polymeric SFM Probes with Integrated Tips

The main difference between microcantilever parts used for force spectroscopy applications and the "diving board" type beams for sensing is the inclusive probe tip of the SFM parts; this tip, as used in scanning force microscopy, allows for interrogation of sample surface topography. To produce these tips, a nanoindenter was employed to make indentations in the injection molds, which, when filled by the polymer during the IM process, become the SFM probe tips. The radius of curvature of the nanoindenter tip is roughly 50 nm [3], which is a value commensurate with "unsharpened", silicon-type SFM probes [7, 5]. So, whereas the polymeric parts are not feasible in situations where their sharpened, silicon-type brethren are, there is still a large number of applications where the polymeric parts are useful. Polystyrene was chosen as the material for use mainly due to its high elastic modulus in comparison to other polymers, which will reduce tip deformation and increase image resolution. The size of the microcantilever is roughly 300 by 75 by 10 microns (length-width-thickness). An optical picture of a microcantilever with the integrated tip is shown in the bottom of Figure 70. The top of Figure 70 shows a closer view of the tip itself (circled).

The mold was heated to 175 °C prior to injection and to heat the melt to 205 °C. The mold heaters were shut off immediately after the cavity was filled (i.e., at the end of injection). The injection was pressure-limited to 50 MPa, and the total injection time was roughly 1 second. The holding time was set at 30 seconds total, and then the fluid (water) cooling was active for 15 seconds after the holding period. At this time the mold halves were opened and the part removed manually. Roughly 25 parts were made but only five were used for this work. To measure the injection molded tip geometry, one of the polymer cantilevers was mounted (tip-face up) onto a steel AFM specimen disk using double-sided tape. A CSC 12 Tapping Mode™

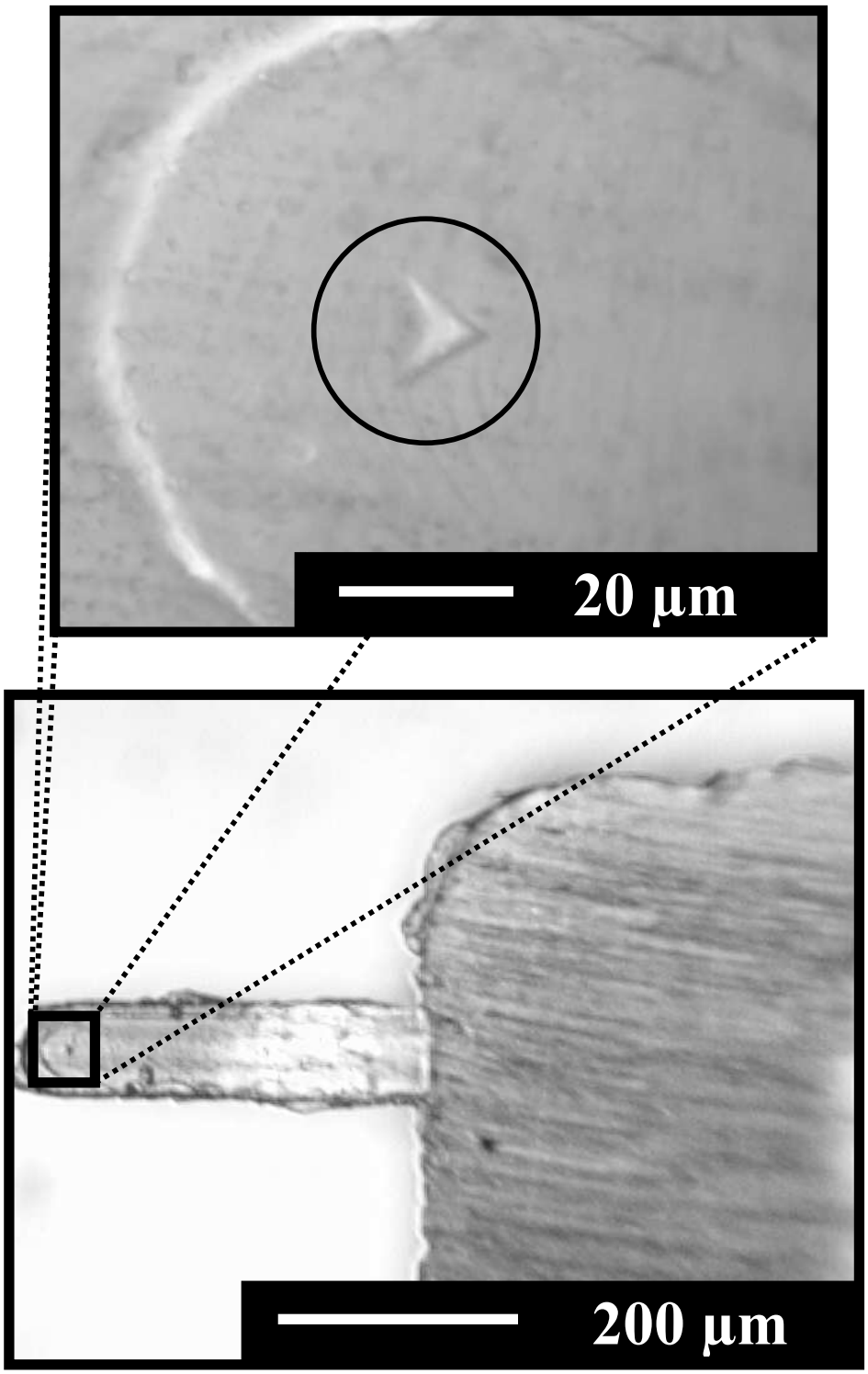

Figure 70: Optical micrographs of an injection molded SFM part (bottom), with a higher magnification view of the circled, pyramidal tip (top).

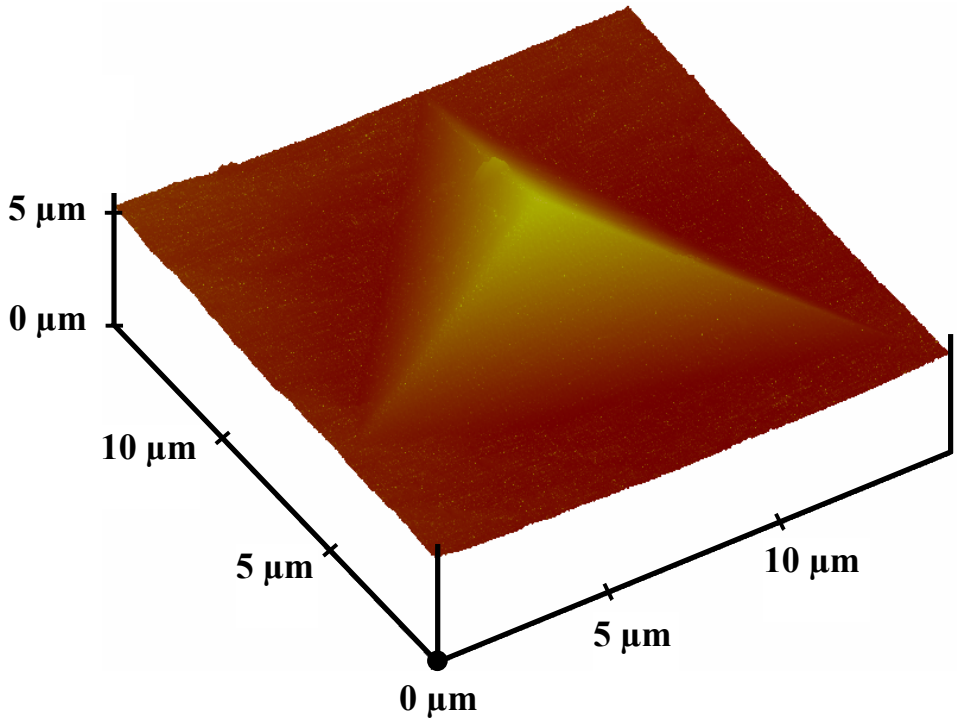

Figure 71: AFM-acquired image of an injection molded SFM tip, the tip height is roughly 1.45 μm.

cantilever (MikroMasch) that resonated at approximately 360 kHz was used to image the polymeric tip. Both the drive amplitude of the imaging cantilever and the setpoint (i.e., the point of contact between the imaging silicon tip and the imaged PS tip) values were optimized so as to minimize distortions of the polymer during imaging. As can be seen from the image presented in Figure 71, the portion of the mold that yields the tip appears to fill completely with polymer during the injection of the polystyrene into the mold.

With the SFM tips appearing promising (via examination of Figure 71), the next step was to attempt an imaging procedure using the polystyrene SFM parts. When used in the AFM, the polystyrene beams were smooth enough that the laser reflected off of the backside of the cantilever without any metal coating (the AFM has a higher laser power than the Scentris system, which required metal coating of microcantilevers for use).

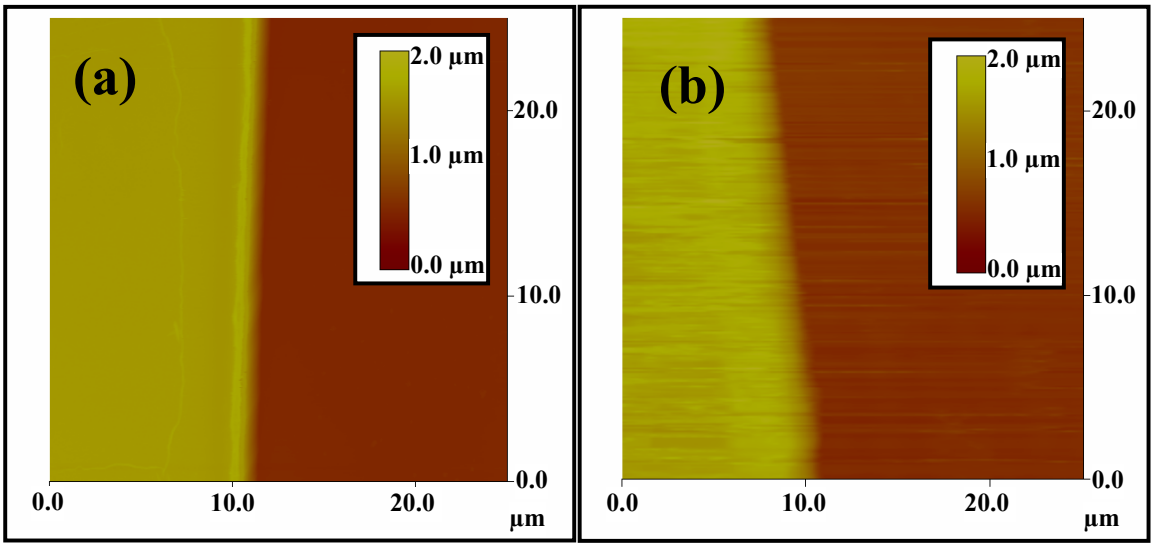

Figure 72: (a) Contact mode AFM image of a silicon grating acquired using a commercially available silicon cantilever and (b) Contact mode AFM image of the same silicon grating using a polystyrene injection-molded cantilever.

The imaging quality of this injection molded AFM probe was compared to the imaging capabilities of a commercially available Microlever™ AFM probe (Part Number MLCT-AUHW, Veeco Metrology) possessing a spring constant of approximately 0.03 N/m and a tip radius of curvature of approximately 15 nm. An optical grating was chosen as this has "sharp" ($\approx 90°$) edges to allow for examination of the wear characteristics of the PS SFM parts. Contact mode images of the microfabricated silicon/silicon nitride grating were acquired using both the silicon and polystyrene cantilever. Using a profilometer (Alpha-Step 500, KLA-Tencor, San Jose, CA), the step height of the grating was initially measured to be 1.06 μm. Prior to image acquisition the AFM was toggled into "Force Curve" mode so that a minimum contact force could be established, to minimize the amount of deformation experienced by the plastic tip during imaging. Figure 72(a) shows the resulting image obtained using the silicon-type part while Figure 72(b) shows the analogous image obtained using the PS part. A bearing analysis (i.e., a surface height analysis) for the silicon part-obtained image showed an average step height of 1.018 μm, while the bearing analysis of the

PS part-obtained image showed an average step height of 1.057 μm, which is roughly a 4% difference, indicating that the PS parts provide accurate height information. It is worth mentioning that the image presented in Figure 72(b) is the fifth sequential image that was obtained using the polystyrene cantilever, each of which consisted of 512 up-down, step height traversals by the polystyrene SFM part tip. By minimizing the imaging force the tip itself seems to have been unaltered during imaging, evidenced by the similarity of all five images. The agreement between the step heights that were measured with each probe (silicon vs. plastic) shows that the plastic is not undergoing any noticeable deformation that may lead to loss in image resolution or height accuracy in the z-direction. While the image quality was slightly higher for the silicon parts, this rudimentary study does indicate that injection molded polymeric SFM probes could be used for certain applications and it should be noted that silicon-type SFM probes cost in the range of 40 to over 200 dollars [7, 5]. With the injection molded SFM parts shown to be feasible for at least one application, attention now turns to a different field of microcantilever application, chemical sensing.

5.1.3.2 New Measurement Application– Deflection-based Polymeric Microcantilever Sensors: Vapor Phase

This subsection details the results of deflection-based chemical was performed using the injection molded polymeric microcantilevers made using the three materials of the repeatability analysis of §5.1.2.3 (i.e., PS, PP, and NN6). The first experiment chosen is somewhat of a benchmark for microcantilever sensors– the self-assembly of 6-alkanethiol monolayers on a gold surface– it was first studied with microcantilevers in 1996 and has been investigated by many others [22, 108, 89, 97, 98].[16] The general result from these works is that the surface stress induced on the gold coated surface is compressive at saturation (i.e., causes a deflection away from the gold surface),

[16] An n-alkanethiol has the chemical composition: $HS(CH_2)_nX$ where X is a tail group- the alkanethiols used for this work had $n = 6$ and hence were slender and cylindrically-shaped.

is proportional to thiol chain length, and has a magnitude on the order of 0.001-10 N/m, depending upon chain length and amount of surface coverage (i.e., if complete surface saturation is reached).[17]

To perform the experiment, a vapor-borne ethane-thiol was diffused into the Scentris system fluid flow cell (laboratory air-filled) where a gold-coated, four-beam, polymeric microcantilever part resided. The microcantilever deflection as a function of time was recorded while the thiol diffused into the flow cell. The measured mold geometry values of Table 9 and the material properties of Table 3, along with the surface stress-induced deflection modeling of Sader (discussed in §3.3.2 and not to be confused with Sader's stiffness determination of §3.3.5.2), allowed for calculation of the surface stress evolution as a function of time. As a representative result, the top of Figure 73 shows the raw deflection data (for a PS part) while the bottom of Figure 73 shows the calculated surface stress evolution.[18] The four different microcantilevers in Figure 73 show good agreement with each other and with previously published reports of 0.082 ± 0.02 N/m obtained using the same experimental methods [22].

Figure 73 shows a macro-scale view of the surface stress generation process. At the outset of SAM formation, the thiols compete with contaminants already present upon the gold surface of the microcantilever, contaminants whose source is the laboratory air. There is an initial process of contaminant desorption, followed by thiol adsorption and SAM formation. A two-parameter Langmuir model has been used to describe the thiol adsorption process, and Figure 74 shows a (polymeric part-representative) closer

[17]The cited work of Godin *et al.* ([89]) found surface stresses with orders of magnitude of 0.1 and 10 N/m (for self-assembly of dodecanethiol) when the gold coating is deposited via E-beam (*i*) at room temperature and (*ii*) at elevated temperature (roughly 300 °C), respectively. As the gold deposition of this work was performed at room temperature, the surface stress value on the order of 0.1 N/m should be used as the comparison for the work of Godin *et al.*

[18]The astute reader will realize that the work of surface stress-deflection relation of Sader (Equation 46)is for a homogeneous plate (i.e., without gold coating), but one assumption used in the derivation of Stoney's relation (e.g., the w_{free} of Equation 42) is that the film thickness (e.g., the gold layer), t_f, is so much smaller than the substrate thickness (e.g., the microcantilever) that t_f is neglected. Therefore, it is appropriate to neglect t_f for use with Equation 46.

view of the initial stages of contaminant desorption, thiol adsorption, and a LM fit obtained with a low concentration thiol to amplify the desorption region; it is apparent that, similar to the previous thiol adsorption works cited, the desorption process is evident and the LM is an accurate description of thiol adsorption. Rate constants can be calculated from this data but the purpose of this work is only to prove feasibility and accuracy of polymeric microcantilevers as vapor-phase, deflection-based sensors.

There are deflection influences aside from the surface stresses generated during monolayer formation. As pointed out in previous works, the effects of mass loading will cause a gravimetric deflection away from the gold surface, but assuming a densely packed monolayer (0.21 nm^2 per molecule [15, 16, 17]) and perfect bonding implies a loaded mass of roughly 1×10^{-14} to 1×10^{-13} kg, inducing a deflection of roughly 1×10^{-11} m, which is negligible compared to the roughly 50 nm (5×10^{-8} m) of deflection seen. Additionally, the release of thermal energy during the self assembly process will induce a deflection via a bimetallic effect (e.g., a difference of coefficients of thermal expansion between the polymeric microcantilever and the gold coating), but the released thermal energy (roughly 200 kJ/mol [195]) will add approximately 35 nJ of heat to the microcantilever (for 10^{10} molecules [22]); the effect of the heat on the beam tip displacement will be ≈ 1 nm [87], which is assumed negligible compared to the maximum deflection due to surface stresses (≈ 50 nm). Therefore, the bulk of the induced beam deflection can be attributed to surface stresses generated during the formation of a self assembled monolayer (SAM), as concluded by other works [22, 97].

To gauge accuracy and repeatability of the monolayer formation-induced surface stress experiments, the thiols were flowed over ten cantilever parts (each with four microcantilevers) made from PS, PP, and NN6 (a total of 30 parts with a total of 120 cantilevers). Data analogous to that in Figure 73 were obtained, and the surface stress values for each cantilever were when the surface stress versus time plots show

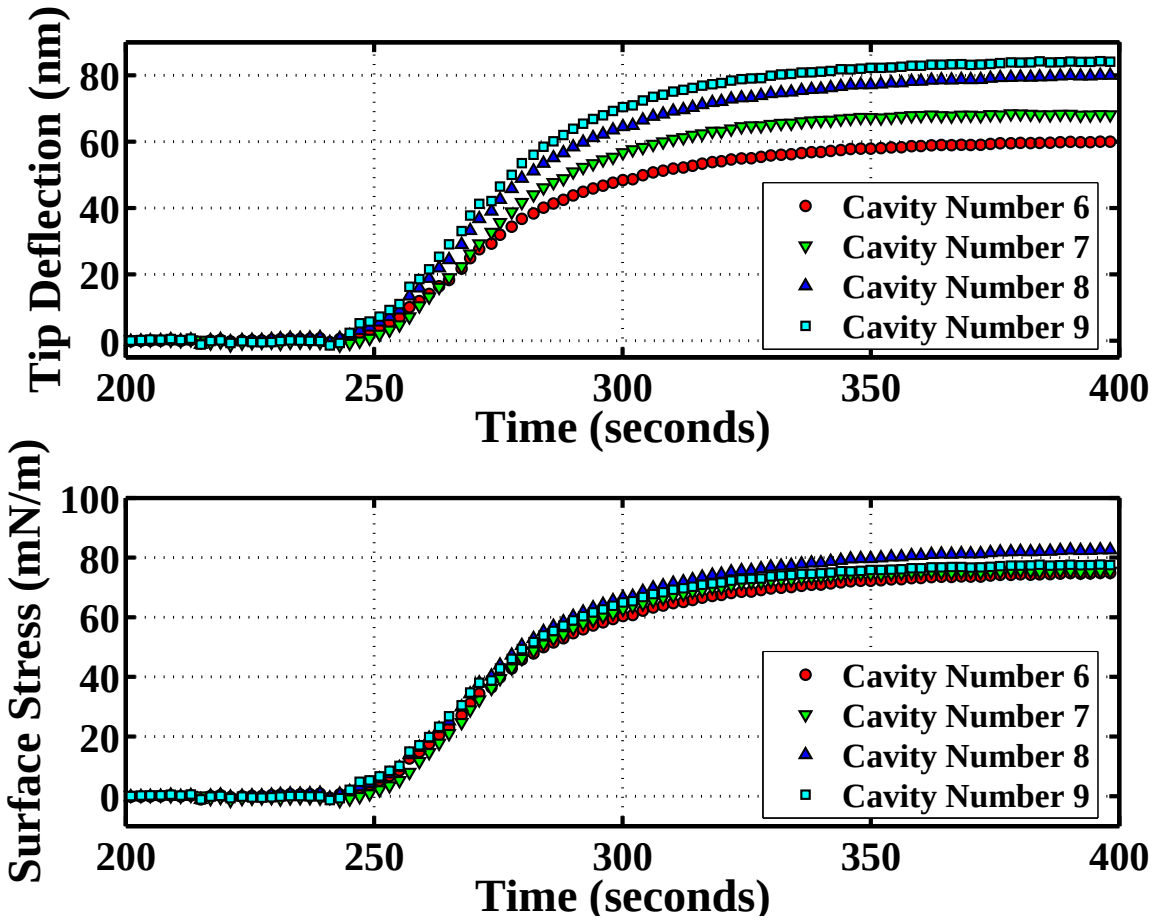

Figure 73: Deflection away from gold surface (top) and compressive surface stress generated (bottom) during monolayer self-assembly (from zero to 200 seconds the cantilever showed miniscule deflection).

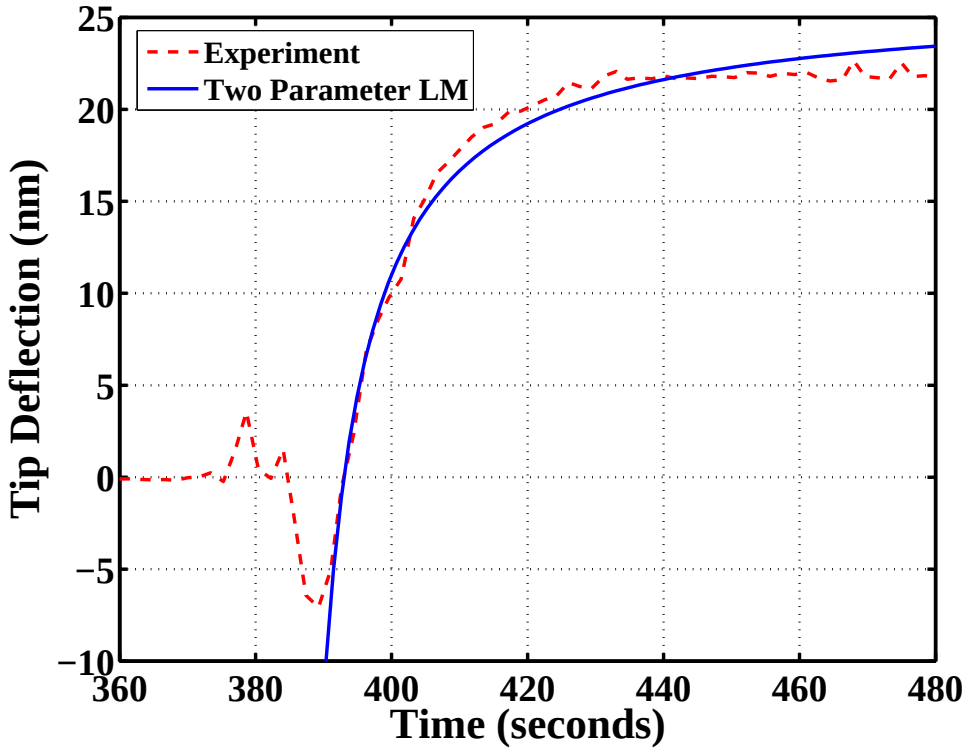

Figure 74: Surface stress plot showing desorption, adsorption and Langmuir model fit.

Table 15: Mean and standard deviation of measured surface stress values from deflection-based sensing.

Material Name	Mean Surface Stress (N/m)	Standard Deviation of Surface Stress (N/m)
PS	0.74	0.12
PP	0.83	0.16
NN6	0.64	0.11

a slope of roughly zero. Table 15 shows the mean and standard deviation values obtained from these tests for the different materials. The values in Table 15 (0.74, 0.83, and 0.64 N/m for the PS, PP, and NN6 parts, respectively) show that the saturation surface stress is in reasonable agreement (for the same thiol) with the literature values (0.082 ± 0.02 N/m [22], roughly 0.125 N/m [98]) for all cantilever materials. From these results, it is demonstrated that polymeric microcantilevers are feasible deflection-based, vapor phase sensors, which produced experimental results in agreement with literature values obtained with the same experimental methods. A logical next step is to employ polymeric microcantilevers as deflection-based sensors in the liquid phase, and this is now discussed.

5.1.3.3 New Measurement Application– Deflection-based Polymeric Microcantilever Sensors: Liquid Phase

The experiment chosen for the liquid phase, deflection-based sensing was the response of a self-assembled monolayer upon exposure to different pH levels. This experiment has already seen attention in the literature [82, 18]. The gold-coated cantilevers of a PS microcantilever part were incubated in capillaries (for roughly 15 min) filled with 10 μl of a 1 mM solution of mercaptohexadecanoic acid (MHA) in ethanol. Previous work has shown that MHA will form a dense, self-assembled monolayer on a sufficiently smooth gold surface, which the e-beam produced surfaces of the polymeric

microcantilevers are [15, 16, 17]. The cantilevers then were rinsed with ethanol and placed in the Scentris fluid cell. Phosphate buffer solutions with varying pH levels were flowed through the fluid cell, and the cantilever deflections were recorded over time. Figure 75 shows the thermal drift-corrected (i.e., a line of constant slope was subtracted from all of the data), surface stress results (calculated via Sader's work discussed in §3.3.2) for a PS microcantilever at different pH levels.[19]

The buffer pH was changed to 7.92, 9.06, and 10.04 at times in Figure 75 of roughly 500, 3,000, and 5,000 seconds, respectively. A buffer solution of pH 4.66 (which should cause no deflection [18]) was flowed in to the fluid cell at in Figure 75 of zero, 2,000, 4,000, and 6,000 seconds respectively. The literature values for MHA-coated cantilever beams (same experimental procedure) of similar plan geometry ($L \times w$ of roughly 400×120 μm for the PS parts and roughly 500×100 μm for the silicon-type parts) at pH values of 9 and 7 are 0.032 N/m and 0.008 N/m, respectively [18]. These values only marginally agree with the values obtained with the polymeric cantilevers of approximately 0.06 N/m (pH 9.06) and 0.05 N/m (pH 7.92), respectively.

Only limited experimental work was carried out for the liquid-phase, deflection-based sensing due to inability to control the thermal drift of the fluid-based process (the data shown was the best subset from approximately 20 experimental runs, all of which had significant drift problems) and the manifestation of large pressure spikes upon change of buffer solution pH. To gauge the influence of the thermal drift and surface stress effects from the opposite fluid-solid interface, silicon-type microcantilevers were used for the same experiment. Unfortunately, similarly unsatisfactory results were obtained, implying that the poor results could be due to either the experimental setup or equipment, but not inherent in the polymeric microcantilevers

[19] At pH values increasingly above roughly 5, the carboxy groups tethered to the gold surface increasingly deprotonate (i.e., become more negatively charged, $\mathrm{COOH} \rightarrow \mathrm{COO}^- + \mathrm{H}^+$) leaving an increasingly negatively charged layer on the gold surface. As the negative surface charge increases, the surface groups electrostatically repel each other more, increasing the surface stress and deflection as pH level increases.

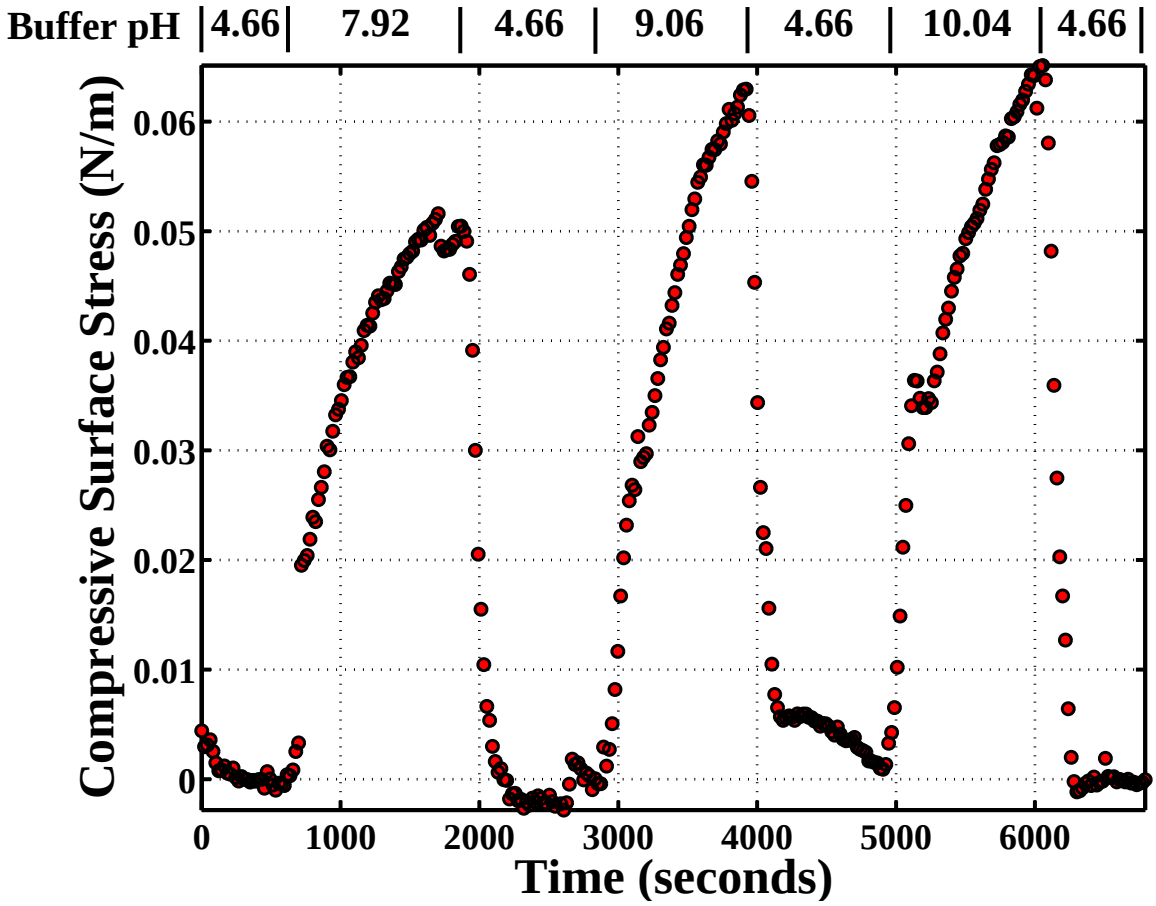

Figure 75: Compressive surface stress generated versus time during pH variation over MHA-functionalized, PS microcantilevers.

themselves. Nonetheless, some of the data (Figure 75) did produce reasonable results indicating that, if the experimental setup could be refined, polymeric microcantilevers could be feasible for fluid phase, deflection-based sensing applications. More satisfactory results were obtained for vapor phase, resonance-based sensing with polymeric microcantilevers, which is now discussed.

5.1.3.4 New Measurement Application– Resonance-based Polymeric Microcantilever Sensors: Vapor Phase

To validate the polymeric microcantilevers as feasible vapor phase, resonance-based sensors, an adsorption process had to be observed that would increase the effective

mass of a microcantilever while not significantly affecting the surface stress or deflection of the beam, because these two phenomena (i.e., surface stress and deflection) will also induce a change in the beam's resonance. These goals were most simply satisfied by using polymeric microcantilevers to measure air humidity. As humidity increases, more water is adsorbed on the surfaces of the microcantilever, hence reducing its resonance frequency without significantly effecting the state of surface stress or beam deflection [43, 241].

The experimental procedure was to take an injection molded polymeric microcantilever, mount it into the Scentris fluid flow cell, and measure the fundamental resonance frequency as a function of relative humidity of the fluid forced through the flow cell. Nitrogen was the carrier gas and was flowed over the beams after being bubbled in a water bath to increase the percent relative humidity (PRH), which was measured with a commercial hygrometer (RH62, Omega Engineering Inc., Stamford, CT). A plot of the resonance behavior as a function of time for a PP microcantilever (from a four cantilever part) is shown in Figure 76 along with the PRH values from the hygrometer. As expected, the added mass reduces the cantilever f_1 (see Equation 59); these results were typical of all polymeric parts. The adsorbed mass sensitivity (i.e., shift in Hz per unit increase in percent relative humidity) was roughly -5 Hz/PRH calculated from data obtained from 5 parts of each material (PS, PP, NN6).[20] With a quality factor of these cantilevers of roughly 40 in the humidified air, a frequency resolution of roughly 5 Hz is possible, indicating that the PRH resolution of these beams is roughly one PRH. The reader should note that higher bending modes, and different deformational modes (e.g., lateral and torsional modes [229]) can be monitored to significantly increase this sensitivity, as can lock-in amplifier schemes (via increasing the

[20]Water is known to affect the elastic modulus of nylon and nylon composites, but this effect is considered negligible over the short experimental time of roughly 100 minutes [259].

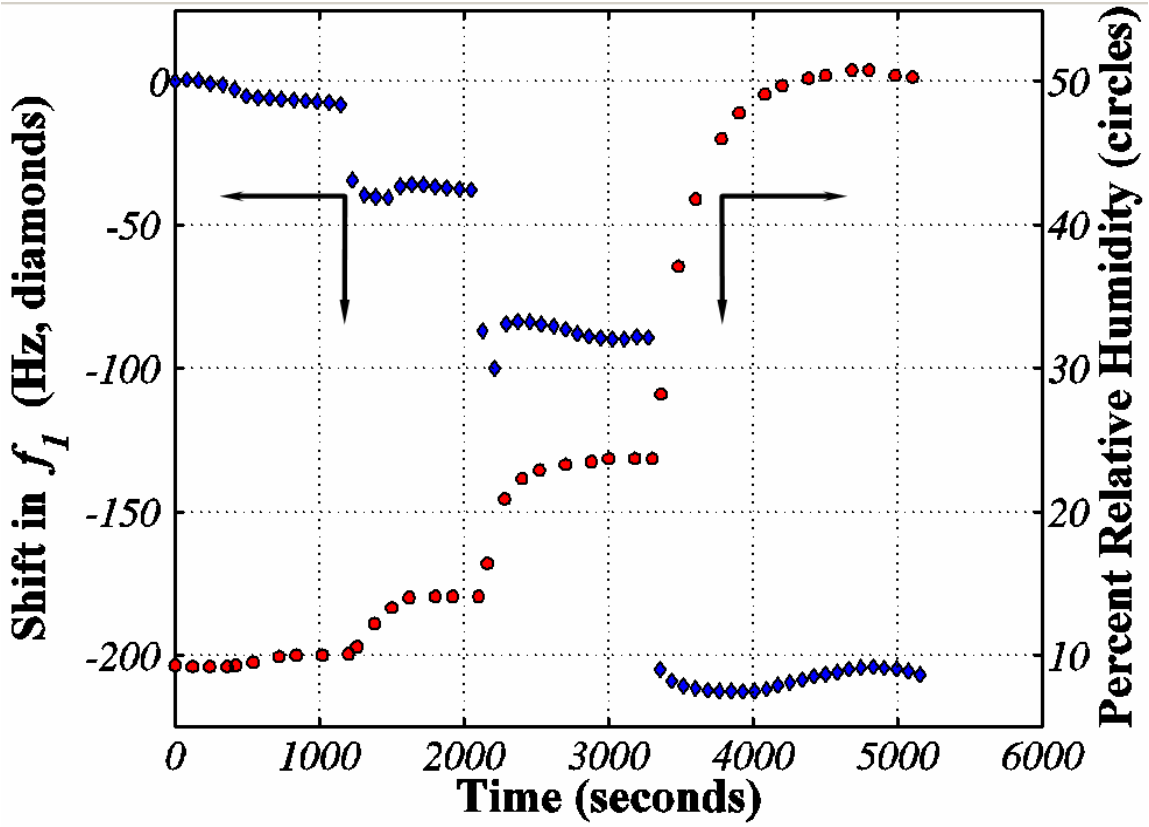

Figure 76: Variation of f_1 as a function of relative humidity (negative changes in f_1 imply a decrease in fundamental resonance frequency).

quality factor [238, 148]). While not revealing polymeric microcantilevers as an incredibly sensitive humidity sensor, this experiment does successfully demonstrate that polymeric beams are feasible for vapor phase, resonance-based sensing applications.

5.1.4 Manufacturing Goals: Summary and Conclusions

This concludes the discussion on the manufacturing goal related results. The first manufacturing goal (repeatable production of microcantilevers via non-IC methods from a variety of materials) was achieved as evidenced by the solvent cast parts of §5.1.1 and the IM parts of §5.1.2. The second goal (the thinnest IM cantilever possible) was examined in §5.1.2.4 and showed the limit to be roughly 2 μm, although the solvent casting approach can produce submicron thickness polymeric cantilevers.

The third manufacturing goal (production of composite microcantilevers) was accomplished as shown by the PMMA-carbon nanofiber composite injection molded microcantilevers of §5.1.2. The final manufacturing goal (proof of concept via use of injection molded microcantilevers as both deflection- and resonance-based sensors, and as contact mode scanning probe microscopy sensors) was detailed in §5.1.3.2 (vapor phase, deflection-based sensing), §5.1.3.3 (liquid phase, deflection-based sensing), §5.1.3.4 (vapor phase, resonance-based sensing), and §5.1.3.1 (polymeric SFM probes). With the exception of the liquid-phase, deflection-based sensing, all portions of the third manufacturing goal were met indicating that polymeric microcantilevers are feasible substitutes yielding comparable behavior to silicon-type parts in a variety of applications. With the manufacturing goals covered, attention now turns to the scientific goals of this work.

5.2 Scientific Goal-Related Results

This section discusses the scientific goal-related results, and more specifically covers the length-scale dependent bending stiffness of §3.3.1.3, the surface stress induced resonance shifts of §3.3.3.6, and a resonance-based beam geometry determination method (§5.2.3).

5.2.1 Length Scale Dependent Bending Stiffness

To estimate the presence (if any) of a length-scale dependence, EB beam theory stiffness values (which do not include the material length-scale parameter) were calculated and compared to nanoindenter-obtained stiffness values (which would include the material length-scale parameter) for numerous microcantilevers. The mathematics of the approach are discussed in §3.3.1.4. The approach was employed for microcantilevers made from PP (discussed in §4.1.2.7). The logic behind the selection of PP was its semi-crystalline structure. The Hooke's Law type constitutive model was derived by assuming a perfectly repeated crystal lattice, and hence for materials such as single

crystal silicon (which exhibits a very repeatable lattice structure) length scale effects are not observed in bending stiffness (e.g., the Hooke's Law model is sufficient) [59]. However, previous work has suggested that higher deviation from a perfect crystal structure will render the Hooke's law type models increasingly invalid, especially at small length scales, and a material with varying microstructure could have a more pronounced length-scale effect [84]. Human bone is a material of this type (e.g., a material with nonuniform microstructure) that has been shown to exhibit measurable length-scale effects [201, 267]. In this vein, the PP is an ideal candidate for length scale effects because it has a nonuniform crystal structure on both the molecular scale (e.g., amorphous and crystalline regions) and on the microscale (e.g. nonuniform spherulite formation). Therefore, the PP was used in hopes of observing a length-scale effect. A total of 20 microcantilevers were made and tested; 10 parts were made from mold cavity 13 of Table 13 ($t \approx 15$ μm, with an appearance commensurate with the top optical micrograph of Figure 60), and 10 parts were made from mold cavity number 11 of Table 9 ($t \approx 30$ μm, with a representative part shown in Figure 77). The theory of Chapter 3 predicts that the influence of the length-scale upon stiffness, if present, for these two geometries (for a given material) should show roughly a $4\times$ difference.

5.2.1.1 Elastic Modulus Determination

Euler-Bernoulli beam theory stiffness is a function of beam geometry, elastic modulus, and Poisson's ratio. The geometry of the beams is assumed to be close to that of the molds, so the measured mold geometry values were used for EB theory stiffness calculations.[21] A dynamic mechanical analysis (TA instruments Inc., DMA 2980 New Castle, DE, displacement resolution: 1nm, force resolution < 0.001 N [1])

[21]Thermal shrinkage of the cantilevers in the molds during the IM cooling phase will result in dimensional changes of roughly one part per thousand, or roughly 0.5, 0.1, and 0.01 μm for L, w, and t, respectively. This is a small number relative to the geometry itself and also serves to slightly *decrease* the stiffness of the microcantilever ($k \propto L^{-3}, t^3, w$), so the length-scale effects would not be affected severely and would have to overpower the thermal effects. Therefore, if the length-scale effects are observed, then the thermal shrinkage can be excluded as a possible source.

machine was used in a static mode (as a uniaxial tension test apparatus) to determine the microcantilever elastic modulus of the same microcantilevers whose stiffness was determined in the nanoindenter. The microcantilever base part was mounted in a custom-made jig, which was gripped by the lower (moveable) clamp of the DMA machine and roughly 200 μm of the free end of the microcantilever was secured in the fixed top clamp of the DMA machine. To determine the effective length of the microcantilevers (i.e., the length of the cantilever not in the clamping device, necessary for strain calculations), white light interferometry was used; the clamping process produces a small amount of surface deformation in the gripped portion of the microcantilever which is measurable. This experimental setup has "extra" compliance when trying to determine E of the cantilever alone due to the base part of the cantilever being subject to tensile loading in addition to the microcantilever itself. The tensile stiffness of the base part (k_{bp}^{axial}) will be roughly 150 times higher than the tensile stiffness of the cantilever itself (k_{b}^{axial}), so the influence of the base part is considered negligible as it will result in a difference in the measured E of the cantilever of less than 0.5%; a value calculated with the cross sectional areas of the beams and the base parts (A_b and A_{bp}), and the effective lengths of the beam and base parts (L_b and L_{bp}), respectively where $k_{b}^{axial} = E_b A_b / L_b$ and $k_{bp}^{axial} = E_{bp} A_{bp} / L_{bp}$.

After mounting the parts in the DMA machine, a deformation ramp was applied to the microcantilevers at a specified rate (e.g., zero to x μm at a rate of y μm/minute).[22] As the elastic modulus of PP will be strain rate-dependent, the loading was applied such that the strain rate of the DMA testing was the same as the maximum strain rate experienced by the beams when deflected by the nanoindenter. According to the assumptions of Chapter 3, the strain rate will vary linearly and symmetrically about the mid thickness of the beam and evenly across the beam width. Therefore, the

[22]The DMA machine was calibrated to take into account the loadframe compliance and the mass of the movable clamp mechanism.

effective elastic modulus of the beam will be one half of the maximum elastic modulus, which occurs at the top and bottom surfaces of the microcantilever (it is assumed here that the beam behaves the same in tension and compression). Recall that the elastic modulus increases monotonically with strain rate for the beams considered here. As a conservative approach (i.e., one that mitigates the difference between the EB theory calculated stiffness values and the nanoindenter-determined stiffness values), the maximum elastic modulus was assumed to occur across the *entire* cross section of the beam hence making the EB stiffness values larger than they likely are. This maximum elastic modulus was was measured by the DMA, where the specified strain rate ($\dot{\epsilon}_{max}$) was calculated via Equation 105 (determined from the theory of §3.3.1.3 for a beam with zero slope or displacement at the fixed end and zero moment and a prescribed displacement, δ, at the free end),

$$|\dot{\epsilon}_{max}| = \frac{3t\delta}{2TL^2} \tag{105}$$

where T is time of the loading (both δ and T are prescribed to the nanoindenter). Recall that the nanoindenter is instructed to apply a given displacement over a specified time period, hence the displacement boundary condition at the beam end. With the beam geometry assumed to be the mold geometry listed in Table 13, and the nanoindenter parameters of $T = 30$ seconds and $\delta = 5$ μm known, the strain rate was calculated to be 2.5×10^{-5} sec^{-1} and 10.5×10^{-6} sec^{-1} for the thin ($t = 15.85$ μm) and thick ($t = 29.37$ μm) parts, respectively (using the mold geometry of cavity number 13 of Table 13 for the thin part and cavity number 10 in Table 9 for the thick part).

The relevant output from the DMA machine is the displacement of the moveable clamp, which is converted into an engineering strain via the effective length of the cantilevers, and the applied force, which is converted into an engineering stress via the cross-sectional area of the particular microcantilever being tested. Engineering stress strain plots were generated, the linear region of which yielded the elastic moduli of

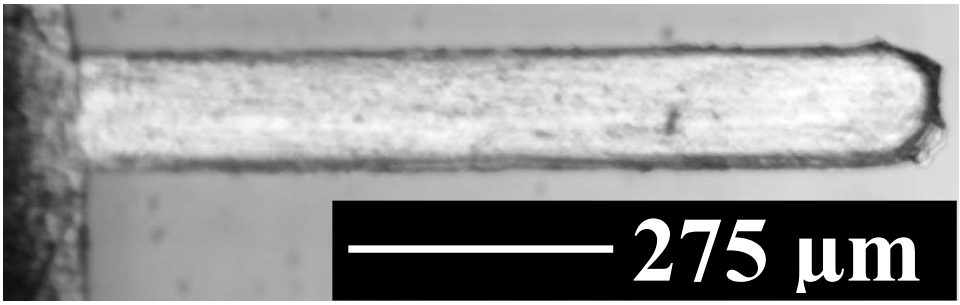

Figure 77: Representative thick PP part used for testing of the length-scale dependent bending stiffness.

the various cantilevers; the method is depicted in Figure 78. Also shown in Figure 78 are estimated uncertainties in E (DMA manufacturer-provided) and the 0.2 percent offset elastic modulus, which determines a yield stress of 35-45 MPa (for PP), a range which encompasses the literature values [40]. Table 16 shows the individual E measurements, the mean and standard deviation of the E measurements, and the stiffness values, k_{EB}, calculated via the EB theory Equation 21 using the mean DMA elastic modulus values, the Poisson's ratio (using to be the manufacturer-provided value),[23] and the measured mold geometries for the different geometry and cantilever combinations. Note that the elastic modulus values determined from the DMA at these strain rates are roughly 2× higher than the manufacturer values listed in Table 3 and the E values for the thick and thin parts (on average) are not very different, even though the strain rate for the for the thick parts was roughly 2× that of the thin parts. The stiffness values in Table 16 (k_{EB}) will be compared with the nanoindenter-determined stiffness values, k_{NI}, which are now discussed.

5.2.1.2 Nanoindenter-determined Stiffness Results

The nanoindenter was operated in continuous stiffness measurement (CSM) mode, which imposes a sinusoidal motion of specified amplitude and frequency (10 nm and 50

[23] In Equation 21, $\varphi = (1-\nu^2)$ owing to the plane strain situation exhibited by the microcantilevers.

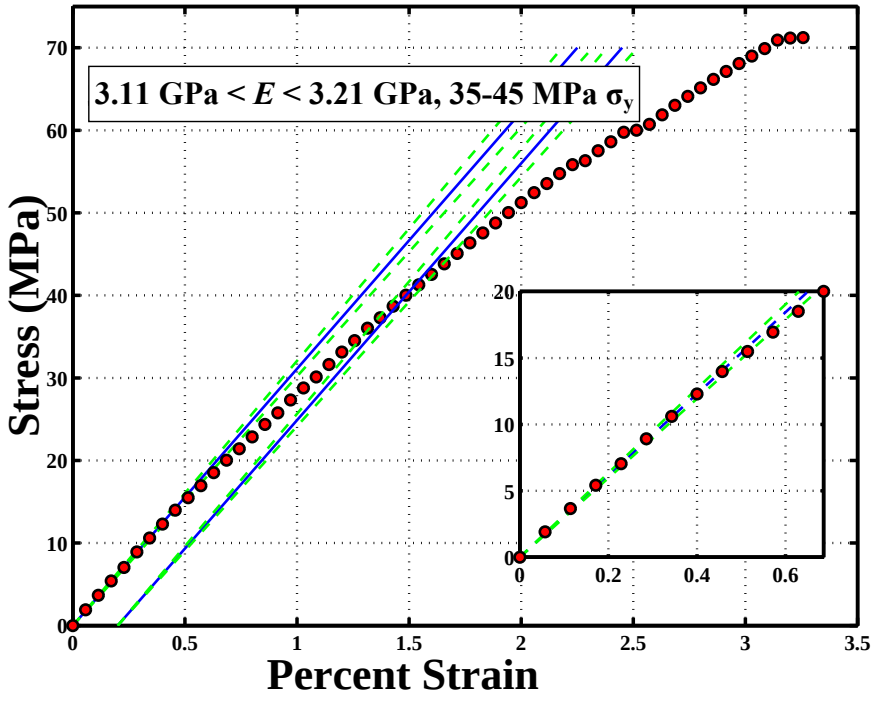

Figure 78: Engineering stress-strain plot of a PP microcantilever obtained from the DMA machine.

Table 16: DMA measured elastic modulus values for E and EB theory stiffness values (k_{EB}) calculated for the thick PP cantilevers ($t \approx 30$ μm) and the thin PP cantilevers ($t \approx 15$ μm), along with mean and standard deviation values.

Part Number	Thick PP Part E, (GPa)	Thin PP Part E, (GPa)	Thick PP k_{EB} (N/m)	Thin PP k_{EB} (N/m)
1	3.0	3.4	4.5	7.3
2	3.7	3.3	5.4	7.1
3	3.4	2.8	5.1	6.0
4	3.1	2.9	4.6	6.2
5	3.4	3.3	5.1	7.1
6	3.0	3.3	4.4	7.1
7	3.1	2.9	4.7	6.2
8	3.6	3.3	5.4	7.0
9	3.4	3.2	5.0	6.7
10	2.9	2.7	4.3	5.9
μ	3.3	3.1	4.9	6.7
σ	0.27	0.25	0.4	0.5

Hz for this work) in addition to the constant rate of displacement of the nanoindenter tip when the tip was approaching and indenting the sample surface. CSM mode allows for a more precise determination of tip-sample contact by monitoring the phase difference between the applied tip displacement and the measured signal from the force transducer. By setting the tip harmonic frequency slightly above the factory-determined resonant frequency of the indenter assembly (roughly 20 Hz), the phase will shift from $+\pi$ to $-\pi$ upon contact of the tip with the sample, so the phase change will indicate tip-sample contact. The phase monitoring technique, as opposed to monitoring the slope of the force-deflection behavior of the indenter tip, is especially important for tip-sample contact determination when indenting compliant samples, and the microcantilevers are *extremely* compliant compared to the bulk surfaces that the nanoindenter usually interrogates.

Linear regressions were performed on the force-deflection curves of the 40 microcantilever parts measured to obtain their k_{NI} values. Table 17 shows the individual measured stiffness values and the mean and standard deviation for the stiffnesses determined from the "thick" cantilevers (i.e., those with $t \approx 30$ μm) and the "thin" cantilevers (i.e., those with $t \approx 10$ μm). It is apparent that the average k_{NI} values are much larger than the average k_{EB} values of Table 16. However, before analyzing the length-scale effects, possible error sources which could be aliased as length-scale effects are discussed.

5.2.1.3 Reasons for Length-scale dependence

This subsection looks at phenomena which would affect the bending stiffness (through violation of the assumptions of Chapter 3) and shows that the various effects would increase the EB beam theory stiffness (hence mitigating the length scale effects), are not large enough to account for the stiffened bending as measured by the nanoindenter, or are not observed. These effects are as folows:

Table 17: Individual, nanoindenter measured stiffness values (k_{NI}) and the mean [$\mu(k_{NI})$] and standard deviation [$\sigma(k_{NI})$] for the stiffnesses determined from the thick PP cantilevers ($t \approx 30$ μm) and the thin PP cantilevers ($t \approx 15$ μm).

Part Number	Thick PP Part k_{NI}, (N/m)	Thin PP Part k_{NI}, (N/m)
1	19.8	35.9
2	21.2	35.9
3	22.6	33.2
4	19.7	33.3
5	23.4	31.8
6	21.5	32.7
7	20.1	36.0
8	22.4	33.0
9	21.3	35.4
10	20.6	33.1
$\mu(k_{NI})$	21.3	34.0
$\sigma(k_{NI})$	1.2	1.5

- departure from a plane strain condition,
- difference in polymeric residual stresses due to orientation effects (i.e., anisotropy due to flow-induced polymer chain orientation manifested during the injection molding process) or thermal shrinkage-induced residual stress effects,
- formation of a relatively hard "skin" on one or both sides of the microcantilever due to cooling asymmetries in the injection molding process, and
- Effect of microcantilever base support compliance.

Each will be dealt with in turn.

Deviation from a plane strain condition would lead to the EB beam theory-calculated stiffness values being reduced by the factor $(1 - \nu^2) \geq 0.75$ assuming a worst-case ν value of 0.5 (recall that, for an isotropic, homogeneous, and linear elastic material $-1 \leq \nu \leq 0.5$). The effect of moving from plane strain to plane stress in the EB beam theory calculation would *reduce* the calculated stiffness hence *increasing* the difference between the calculated value and the nanoindenter-determined value, making the length-scale effect seem larger. However, the calculations of this work were carried out using the plane strain assumption, which will mitigate this difference. Therefore, the plane strain calculation, while probably justified for the thin beam ($w/t \approx 8$) and possibly justified for the thick beam ($w/t \approx 4$), serve to reduce any length-scale effects and hence are a conservative approach.[24]

Any residual stresses or macro-scale orientation remaining in the microcantilevers upon cooling and removal from the mold could affect the stiffness as measured by the nanoindenter and the E values measured by the DMA. The PP parts should, assuming sufficiently fine spherulite formation, show no macro-scale orientation effects because their semi-crystalline nature will cause numerous spherulites to form

[24] As pointed out by others [225, 114] , the plane stress case may be a more accurate assumption at the 5 μm deflections experienced by the microcantilevers, however the plane strain analysis is more conservative (i.e., it mitigates length scale effects) and is therefore used.

with local anisotropies that cancel in the macro-scale; the PP parts (under cross-polarized light) under 50× magnification were completely lit (a close view of a beam is shown in Figure 79), indicating a "fine" crystalline structure as expected from the cooling time (which was set at roughly 30 seconds), longer cooling times from a given temperature will induce a finer crystal structure [145]. A higher-powered microscope could reveal the spherulite structure; spherulite size can range from submicron up to several hundred microns, depending upon processing conditions [40, 63]. Two main causes of residual stresses in injection molded parts are due to (*i*) melt flow-induced chain orientation which may or may not remain in the frozen the solidified part and (*ii*) thermally-induced polymer chain organization/disorganization and mechanical stresses induced by the thermal shrinkage of the part coupled with the viscoelastic nature of the polymeric material (e.g., tempered glass). The flat nature of the beams upon removal from the mold [see Figure 69 (a)] implies that there is no asymmetric residual stress about the mid-thickness of the beam, similar to the layer removal method [250].

Symmetric residual stresses, however, could exist and would result in an apparent increase in the elastic modulus at different points along the length and width of the beam (for a physical interpretation of residual stress effects upon hardness and elastic modulus, the reader may think of pressing upon a piece of unstressed rubber, and then stretching the rubber which will make it feel firmer). In a similar vein, a relatively hard "skin" could form on the entire top and bottom surfaces of the microcantilevers, or the center of the beams could have a relatively higher elastic modulus. To examine residual stress-induced asymmetry effects, the nanoindenter was used (in CSM mode) to determine the polymer elastic modulus as a function of beam thickness at the 15 length-width points of the microcantilever shown in Figure 80, with the *with the beams fixed to a rigid substrate*. While the nanoindenter cannot be used for valid comparison of E values with the DMA E values (mainly due to significant plastic

Figure 79: Optical micrograph of a PP microcantilever under cross-polarized light.

deformation during indentation and strain rate effects), the nanoindenter still can be used to examine uniformity of E along the plan geometry of the beams and as a function of penetration depth (it is assumed that E uniformity at one frequency implies E uniformity at all frequencies). Beams were also "flipped over" and secured to the substrate, so a complete variation of E as a function of penetration depth could be obtained. Figure 81 shows a representative plot of 15 E versus penetration depth traces (points are the individual data points and the line is the averaged E value as a function of indentation depth); the magnitude is not relevant in these plot only the uniformity of E as the depth increases.[25] According to CSM-mode nanoindentation theory, the region near the first 10% of indentation (i.e., from zero to roughly 0.8 μm in Figure 81 will not be accurate for larger indentation, so less attention should be paid to this region of Figure 81 [3]). It is seen from Figure 81 and the other plots (not shown) that the elastic modulus is reasonably uniform over the beam thickness and over the plan dimensions, but not acceptably uniform to neglect. However, even with this "large" variation in E (approximately $\pm$25%), it will be seen in the next subsection that the length-scale effects dominate.

Finally, the compliance of the base part during the nanoindenter stiffness determination tests would cause the nanoindenter k_{NI} value to be lower than the actual beam stiffness. This would lower the difference between the EB beam theory stiffness value and the nanoindenter-determined value (because k_{NI} is larger), hence mitigating a length-scale dependence. Therefore, base part compliance also leads to a conservative approach.

[25]There are more data points at lower indentation depth in Figure 81 because the sampling rate of the nanoindenter is constant but the indentation velocity increases as the indenter penetrates the surface.

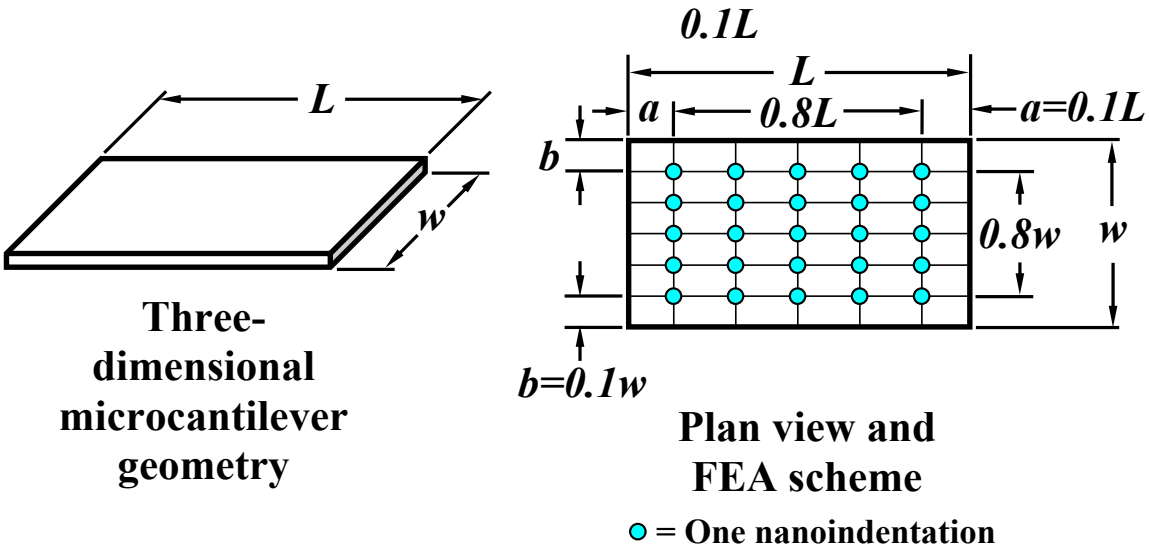

Figure 80: Nanoindentation scheme to test uniformity of elastic modulus.

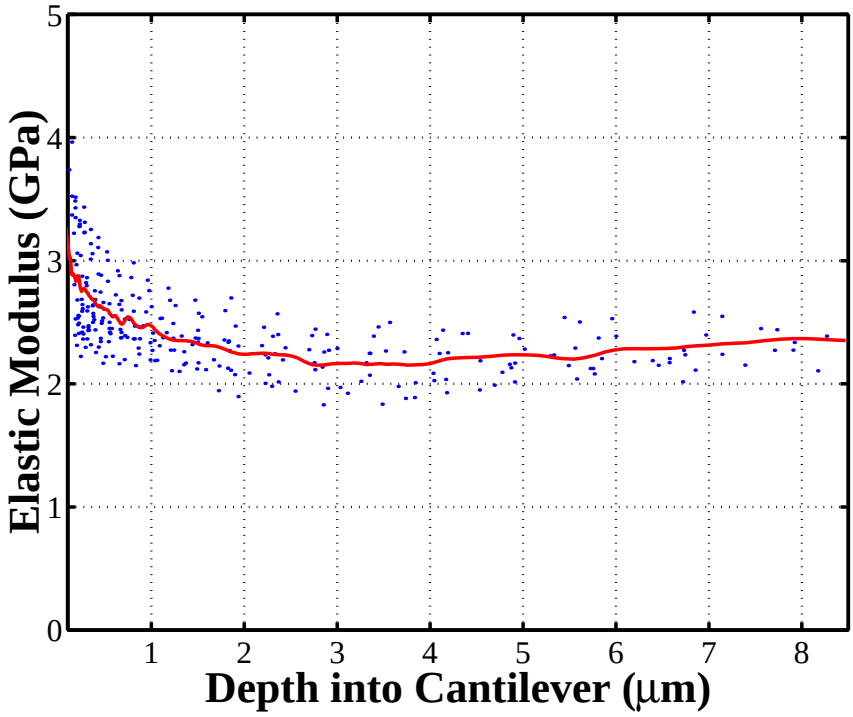

Figure 81: Data set from 15 nanoindentations taken at different locations along the length and width of a microcantilever (points) and an average (line) E versus indentation depth ($t \approx 16$ μm).

5.2.1.4 Why no Length-scale dependence in Resonance?

The length-scale effects could also be present in the resonance behavior of the microcantilever. Indeed, it was seen that the modeling of this work underestimates the resonance frequencies (see §5.1.2.3). Some or all of this underestimation is due to the increased elastic modulus at higher strain rates while any remainder could be accounted for by the length-scale effects. When attempting to experimentally examine this underestimation, two experimental problems present themselves: the strain rate and the magnitude of the forces. The maximum strain rate of the DMA (roughly 1-10 $\sec^{-1}$) was limited to roughly two orders of magnitude lower than the strain rate experienced by the beams when resonating, so the DMA could not be used measure E at such high frequencies. Additionally, (i) the total amount of tip displacement seen by the beams during resonance is roughly 100 nm implying an end force of roughly 100 nN (for a 1 N/m stiffness beam) so one is experimentally limited by the force resolution of the nanoindenter of 50 nN, and (ii) the maximum tip deflection rate of the nanoindenter would result in a strain rate that is 10-100 times lower than seen by the beams during resonance so the nanoindenter could not be used to examine length-scale effects upon resonance. Therefore, the length scale effects should, for this work, be seen as most important for microcantilever applications where force calculation is determined directly from a deflection multiplied by a stiffness, as it is in many situations [204]. From a scientific standpoint, useful future work could investigate the (possibly) strain-rate dependent material length scale parameter and investigation of E at very high strain rates for structures (particularly polymeric) on the micron scale.

5.2.1.5 Length-scale dependence: Conclusions

When using the mean nanoindenter- and EB theory-determined stiffness values, the bending length scale parameter ($\hat{b}_h$) of Chapter 3 was calculated to be roughly 54.9

μm and 32.3 μm for the thick and thin geometries, respectively. These values are commensurate with literature values of 24 μm for an epoxy (Bisphenol-A epichlorohydrin resin was mixed with 20 phr of diethylenetriamine hardener), roughly 10 μm (for steel and aluminum plates with a 50 μm thickness, and for a polystyrene foam plates with a thickness of 1 mm) [133, 67, 132], which is reassuring.

The bending stiffness as determined by the nanoindenter is larger than the EB beam theory value (roughly 7$\times$ larger), which is too large to be due to the elastic modulus scatter as a function of beam location and the other effects discussed in §5.2.1.3. Therefore, it is concluded that the increased bending stiffness is due to inadequacies in the Hooke's law type constitutive model and that, for PP especially, the length scale dependent bending stiffness model derived for this work is a more accurate constitutive model at this length scale. This result is particularly important for PP (and probably other polymeric and possibly non-polymeric) microcantilever systems, and could be important for future, polymer-based MEMS/NEMS applications. With the length-scale discussion concluded and the results showing a length-scale dependence, the second scientific goal is addressed.

5.2.2 New Measurement Mode– Surface Stress-Induced Resonance Shifts

As mentioned in §4.3, the analytic derivations of §3.3.3.6, which proposed a model predicting the resonance shift that would be induced for a given applied surface stress ($\bar{\sigma}$), were verified via finite element analysis. Additionally, experimental validation was explored and both the modeling and experimental aspects are now discussed in turn.

5.2.2.1 Simulation Results

The surface stress influence on microcantilever resonance was modeled via both 2D and 3D finite element analyses (the details of the simulations are discussed in §4.3). Figure 82 shows the theoretical variation of the first wavenumber as a function of

the applied dimensionless surface stress and dimensionless surface stress ($\hat{\sigma}$) for the first resonance mode (obtained via Equation 74) and the simulated values from the 2D and 3D FEA.[26] Figure 83 shows the percent difference between the 2D FEA and the theory of Equation 74 (analogous plots for the 3D simulations were practically indistinguishable). Figure 82 shows that at $\bar{\sigma} = \pi^2/4 \approx -2.467$, the wavenumber is zero (i.e., $\alpha_1 = 0$), which shows that, according to the FEA, the frequency goes to zero as the force acting on the beam end approaches the Euler buckling load. The errors in Figure 83 show good agreement for the experimentally valid (for these microcantilevers at least) region of surface stresses from -0.5 N/m to 0.5 N/m. Analogous simulations carried out up to surface stresses of 200 N/m (or a dimensionless surface stress of 1000)[27] showed a maximum percentage difference between simulation and Equation 74 of roughly 15, 4, 10, 12, and 9 percent for the first through fifth modes, respectively. Note that this amount of surface stress is *huge* and has not been remotely seen in experiment, so while the errors of 20% in the first mode may seem large, this is almost purely an academic exercise at these levels of surface stress. Nonetheless, the model of Equation 74 and the simulations show good agreement in an experimentally relevant region as shown in Figures 82 and 83.

The percent difference between 3D FEA-simulated squared wavenumber of the axially distributed force model and the predicted squared wavenumber [i.e., $(\underline{\alpha}_i^{\Delta\sigma})^2$ obtained from Equation 76] versus surface stress and dimensionless surface stress is shown in Figure 84. The first mode percent difference is larger at high compressive stresses but is low in the experimentally relevant range of approximately $-0.2 < \bar{\sigma} <$ 0.5 N/m (or $-1 < \hat{\sigma} < 2.5$). Using an axial force uniformly distributed along the length of the beam (i.e., application of X N/m along the beam length), simulations

[26] A generic polymeric cantilever geometry of $L - w - t = 500 - 100 - 10$ μm and $E = 3$ GPa were used to generate the dimensionless surface stress in this subsection.

[27] The surface stress is bounded from below by buckling, so simulations were carried out only for increasing surface stresses.

were carried out up to surface stresses of 200 N/m (or a dimensionless surface stress of 1000) and showed a maximum percentage difference from Equation 76 of roughly 14, 15, 30, 2, and 10 percent for the first through fifth modes, respectively. Again, these values are not seen experimentally so the simulations are exploratory while not applicable practically. The finite element modeling of this subsection showed good agreement with the theoretical modeling of Chapter 3, however the true test of the analytic modeling will be how it compares to experiment, which is now discussed.

5.2.2.2 Experimental Results and Comparison

The theoretical results of §3.3.2, namely Equation 46, give an entirely displacement-based approach to predict the magnitude of the surface stress acting on a microcantilever. Similarly, Equations 74 and 76 can be manipulated to give the surface stress acting on a microcantilever as a function of resonance frequency. Therefore, if both deflection and resonance frequency are monitored while surface stress is accumulated on a microcantilever, the two methods (i.e., the deflection-based approach and the resonance-based approach) yield two means to predict the amount of surface stress generated. In this manner, the resonance based approaches developed for this work (i.e., Equations 74 and 76) can be validated or rejected when compared to the deflection-based approach, which has been validated in the literature.

While monitoring both resonance and deflection during adsorption is possible with the Scentris system, the results were not satisfactory. In the dual monitoring mode, the Scentris piezoelectrically actuates the microcantilevers to track resonance peaks and this actuation, while only displacing the tip of the microcantilevers a distance on the order of 10 nm, leads to unacceptable deflection tracking; the deflection signal is very noisy and shows erratic jumps that are not physically reasonable. Additionally, when tracking resonance (either solely or while also tracking deflection) the software can (and does) jump from mode to mode as time progresses, resulting in resonance

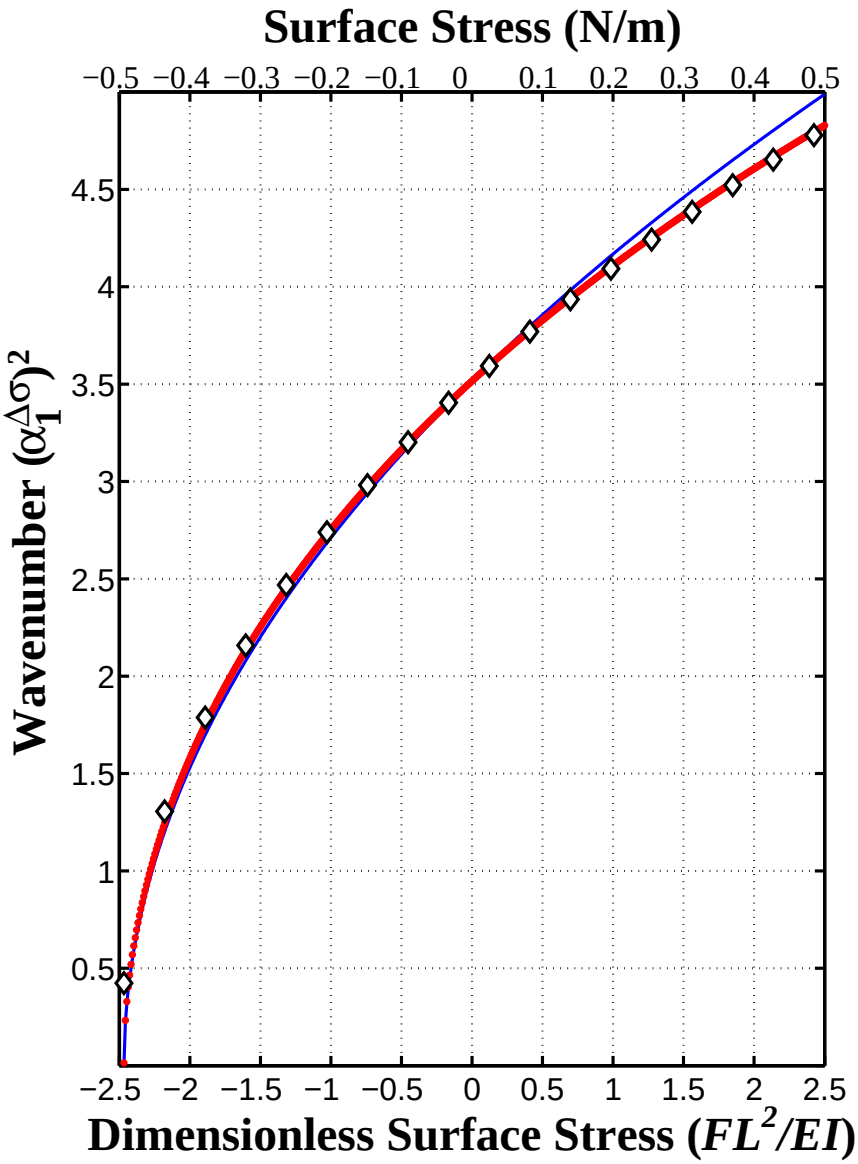

Figure 82: Theoretical (solid line), 2D (circular dots), and 3D (diamonds) simulated variation of squared wavenumber, $(\alpha_1^{\Delta\sigma})^2$, versus dimensionless surface stress, $\hat{\sigma} = FL^2/EI$ for the first resonance mode obtained with the model of a constant force acting axially at the free end of a cantilever.

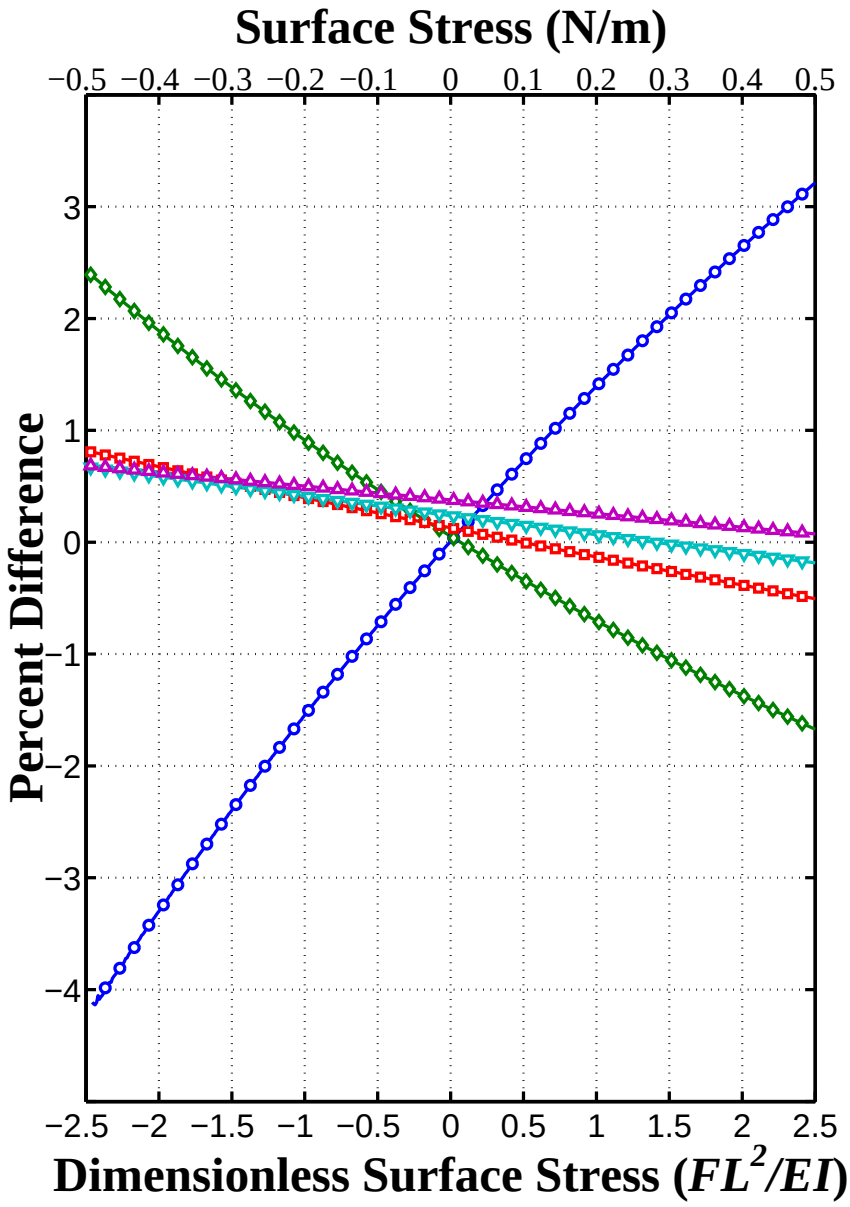

Figure 83: Percent difference between the finite element-simulated and theoretical (Equation 74) squared wavenumber $(\alpha_1^{\Delta\sigma})^2$ versus dimensionless surface stress for resonance modes one through five ($\circ$, $\Diamond$, $\square$, $\triangledown$, and $\triangle$, respectively), every tenth finite element simulation is shown for every mode.

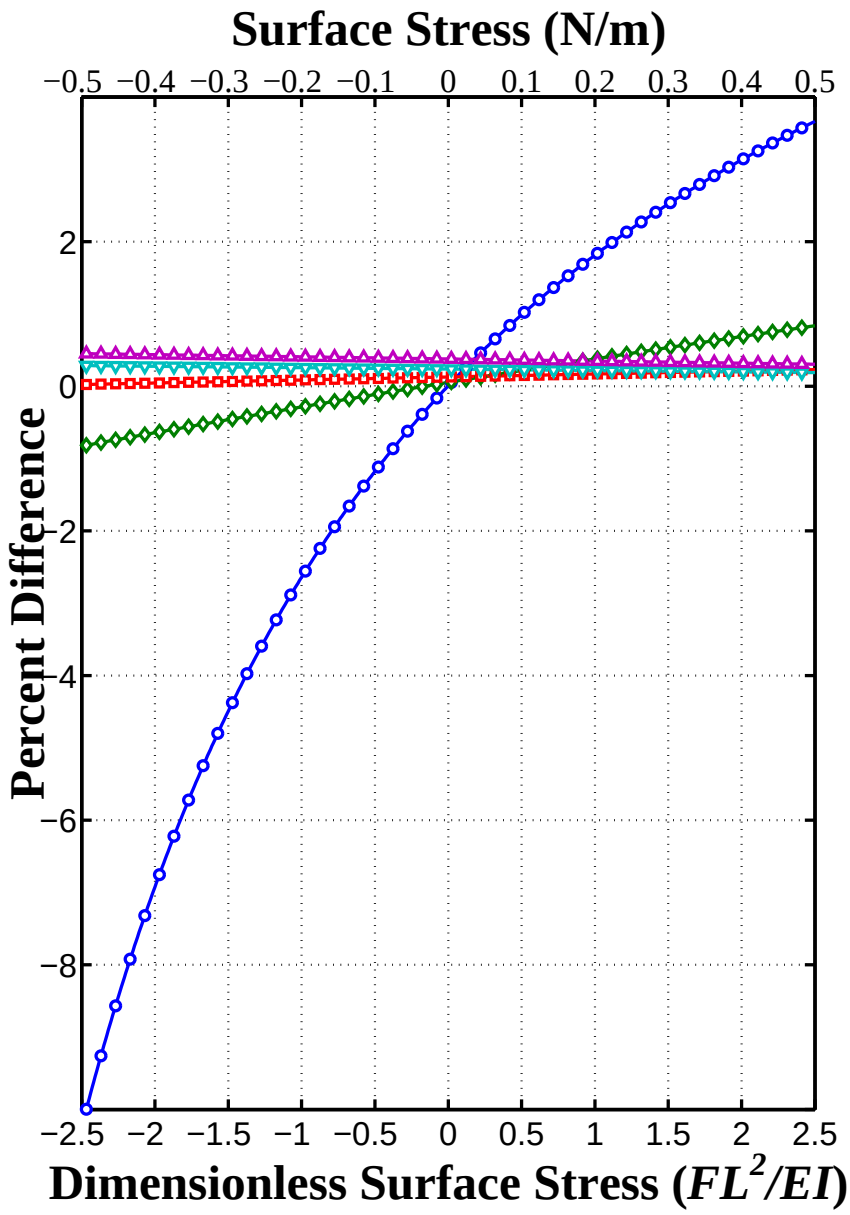

Figure 84: Percent difference between the finite element-simulated and theoretical squared wavenumber, $(\underline{\alpha}_i^{\Delta\sigma})^2$ versus dimensionless surface stress for the axially-distributed force model (Equation 76) for resonance modes one through five ($\circ$, $\Diamond$, $\square$, $\triangledown$, and $\triangle$ in the figure), every tenth finite element simulation is shown for each mode.

data that is not useful.[28] Therefore, a strategy was employed to take advantage of the Scentris system strengths (e.g., deflection-only tracking) while avoiding the weaknesses (e.g., simultaneous resonance and deflection tracking during an adsorption process).

The experimental procedure was to measure the bending resonant frequencies for numerous modes of many gold-coated microcantilevers in air (using the Scentris system). The cantilevers then were subjected to a fluid-phase thiol adsorption event during which the deflection was tracked by the Scentris system (but not the resonance), allowing for calculation of the surface stresses via the work of Sader discussed in §3.3.2. After the adsorption event is complete (and the saturation surface stress value is reached), the microcantilevers were rinsed in deionized water to remove excess thiols not bonded to the gold surfaces of the beams and were allowed to dry for 24 hours. The rinsing and drying processes leaves the thiol SAM on the surface of the beams (and the surface stress due to the SAM), while removing any extra matter that would cause a mass-induced resonance reduction. Finally, the resonant frequencies of the various modes measured before the adsorption event were measured again in the Scentris system to give numbers that will be shifted by the surface stress still present on the beam. This approach allows for a comparison between the deflection-predicted surface stresses and the resonance-predicted surface stresses obtained via the surface stress modeling of this dissertation (e.g., Equation 74 and Equation 76).[29]

The mathematical form used for calculation of the surface stress ($\bar{\sigma}$) based upon the resonant frequency before (f_i) and after the adsorption ($f_i^{+\Delta\sigma}$) obtained using the

[28] The Scentris system is not yet commercially available and our group is acting as a test site; new resonance-tracking software is being developed at Veeco to improve the machine, but this software is not available yet.

[29] An effective elastic modulus and second moment of the cross sectional area were calculated (for use with Equation 74 and Equation 76) using the effective composite theory discussed in §3.3.3.4, with an elastic modulus value for a nanoscale gold film of 69.1 GPa ([253]) and a gold layer thickness of 25 nm. The equations used were $\Delta f_1 = 2\pi \left[\sqrt{\frac{E_s I_s}{\rho_s A_s + \rho_f A_f}} - \sqrt{\frac{E_s I_s}{\rho_s A_s}} \right]$; the relevant parameters are defined in §3.3.3.4.

theoretical results of §3.3.3.6 (Equations 54, 73, and 75), is given by Equation 106

$$\bar{\sigma} = \left[\left(\frac{f_i^{+\Delta\sigma}}{f_i} \right)^2 - 1 \right] \frac{Ewt^3\pi^2}{12\hat{\beta}L^3} \tag{106}$$

where $\hat{\beta} = 4$ for the end force model (e.g., Equation 73) and $\hat{\beta} = 2$ for the axially distributed force model (e.g., Equation 75), which is used henceforth due to its more accurate description of the microcantilever loading induced by a surface stress.

By assuming a dense monolayer formation, which is justified by the previous work in the literature (≈ 0.21 nm^2 of surface area per molecule) [15, 16, 17], and using the area of the gold surface (known) and molecular weight of the molecules bonded to it, the adsorbed mass was calculated to be roughly at most 1×10^{-13} kg,[30] which would reduce the bending mode frequencies of the cantilevers by less than 0.05%, which is assumed negligible.

As discussed in §5.1.3.2, the thiol will protonate forming a compressive surface stress which will tend to stretch the beams and increase their resonant frequencies. It is henceforth assumed that the various modal frequency increases are due solely to the formation of a compressive surface stress. There will be negligible density damping effects upon the resonance modes due to the height of the monolayer (≈ 2 nm [16, 15, 17]) as shown by Equation 80. It is also assumed that the monolayer itself will not significantly increase the structural stiffness of the microcantilevers (as in the effective elastic modulus and second moment of the cross sectional area effects discussed in §3.3.3.4).[31] Finally, it is assumed that the surface stress generated in the liquid phase will be unchanged once the solute agent (e.g., the water used to dilute the thiol) evaporates from the SAM. As the SAMs have been shown to form dense

[30] $(0.2\text{ kg/mole})(0.05\text{ mm}^2\text{ area})/[(0.21\text{ nm}^2\text{ area/molec.})(6.023\times10^{23}\text{ molec./mole})] \approx 1\times10^{-13}$ kg

[31] Previous work of Ricco *et al.* estimates the shear modulus of a thiol monolayer (obtained via a SAW) to be roughly 10 MPa [211]. Assuming a worst case Poisson's ratio value of 0.5 with a safety factor of 4 (this assumes a linear elastic isotropic model, which is incorrect, hence the large safety factor), $G = E/2(1+\nu) \Rightarrow 6G = 60$ MPa, which, coupled with the effective section properties and the 2 nm layer thickness predicts that the increased section properties due to the monolayer will change the resonance behavior by less than 0.001%, which is assumed negligible.

monolayers on gold surfaces, there should be little free area for any solute molecules to reside on the surface and hence the surface stresses should be unchanged upon solute evaporation.

The experiment was run on four different silicon-nitride (each with $L - w - t$ of approximately $499 - 97 - 0.80$ μm as determined via SEM) microcantilevers. The reason for using a silicon-nitride part (as opposed to a polymeric part) is that a reference beam can be used. Roughly 2 nm of titanium was evaporated upon the top (i.e., laser-striking) surface of the microcantilevers followed by roughly 25 nm of gold (both coating processes were carried out at 0.25 Å/sec.). The gold layer is chemically stripped from one of the cantilevers leaving one titanium-coated beam, which will not interact with the thiols. Therefore, any effects influencing the resonance (e.g., surface stresses generated by silicon-thiol bonding or any residual mass left on the beams after rinsing and drying) exhibited by the Ti-coated beam can be subtracted from the gold-coated beams in an attempt to isolate the surface stress generation effects. No suitable gold stripping agent could be devised that would not significantly or detrimentally interact with the polymeric microcantilevers and shadow masking (i.e., deposition of Ti onto one polymeric cantilever after others had been gold coated) attempts proved unsuccessful. The theoretical surface stress equations are only a function of the microcantilever geometry and material properties, so employing a silicon-nitride cantilever was seen as advantageous (due to ability to use a reference beam) and acceptable.

The first six bending modes of the four different microcantilevers were measured (one beam used as a reference) before and after liquid-phase adsorption of a water-diluted aminoethane-thiol (1 mM). This bonding event monitored via microcantilevers has previously shown a measurable increase (roughly 0.5 kHz) in first-mode bending resonant frequency for a cantilever resonating at roughly 70 kHz (before adsorption) [118] and hence was chosen for this work. Table 18 shows the measured resonance

frequencies before (f_i) and after the thiol species adsorption ($f_i^{+\Delta\sigma}$), the resonance shifts (Δf_i), and calculated surface stresses for the first six bending modes of the three non-reference beams ($\bar{\sigma}$). The reference beam (beam number four) shows slight decreases in resonant frequencies for each mode, likely due to residual mass remaining on the beam after rinsing and drying or moderate Ti-thiol surface stress effects.

Figure 85 shows the deflection response of the microcantilevers in the liquid phase. The flow cell, a buffer solution, and the thiol solution were set up and allowed to thermally equilibrate for six hours. Then the thiol solution is pumped into the fluid cell and completely displaces the buffer solution in roughly 15 seconds at which time the logging of data begins.[32] It is apparent from the Langmuir-type desorption and adsorption of this experiment that the rate constants of this liquid phase aminoethanethiol adsorption event are much smaller than the gas phase studies of §5.1.3.2 (note that the abscissa values are in *hours*). Due to this, any microcantilever deformation due to surface stresses during the roughly 15 seconds of buffer-thiol solution exchange is considered negligible. It is seen that the three non-reference microcantilevers deflect much more than the Ti-coated reference beam, as expected.[33] Additionally, Figure 85 shows that the three non-reference beams do not exhibit the same deflections indicating that the surface stresses generated are not the same on the three beams. Figure 86 shows the surface stress values for the three non-reference beams obtained from the resonance- and deflection-based techniques. The values show reasonable agreement and are considerably improved over the existing models in the literature whose prediction and theory disagree by roughly two orders of magnitude [135, 43].

There is an outlying point for the first mode of beam two and this could be due to the relatively low first-mode quality factor of this beam ($Q_1 \approx 50$ for beam two, whereas $Q_1 \geqslant 100$ for beams one and three); lower quality factors induce higher

[32]Due to the large number of data points (roughly 100,000), the deflection behavior during the thermal equilibriation stage was not monitored.

[33]Ti was used as it is known to not significantly interact with thiols [18].

uncertainties in the measured resonance frequencies. This lowered Q could be due to any lack of uniformity in the metal coating process, for example. The quality factors for all four of these beams for modes two through six were greater than ≈ 150, so the low Q_1 for beam number 2 is a likely source of surface stress calculation error.

Aside from the anomalous point of mode number one for beam two, the data in Figure 86 shows reasonable agreement. In light of this agreement, it is concluded that the surface stress modeling of this work is a reasonably accurate means to detect surface stress generation upon microcantilevers solely by monitoring bending mode resonance frequency, and this new modeling is much improved over existing methods. With the second scientific goal discussed, the third is dealt with in turn.

5.2.3 New Characterization Technique– Geometry Determination Obtained Solely by Resonance Behavior

As mentioned in §4.3, finite element analyses were employed to simulate the free resonance modes (bending, lateral, and torsional) to see how closely the equations of §3.3.4 match simulation. Additionally, the resonance behavior of a microcantilever was experimentally determined (using an AFM) and the resonance behavior used to determine the microcantilever geometry, which was compared to values obtained from an SEM. The simulation and experimental results now are discussed and compared.

5.2.3.1 Experimental Results and Comparison to Simulation

The nominal (i.e., manufacturer-provided) length, width, and thickness values of the microcantilever simulated were 500 μm, 100 μm, and 1 μm, respectively. The beam material is silicon-nitride (E = 170 GPa, ν = 0.23, and ρ_b = 2330 kg/m^3 [21], the cantilevers used for the cited work were made by the same group that produced the cantilevers used for this subsection, so the crystal orientation and hence material properties are known from the cited work). The SEM image-obtained microcantilever geometry was a length of 499 μm, a width of 97 μm, and a thickness of 0.80 μm (LEO

Table 18: Measured resonance frequencies before, (f_i), and after adsorption, ($f_i^{+\Delta\sigma}$), resonance shift (Δf_i), and calculated surface stresses for the three non-reference beams ($\bar{\sigma}$).

Beam Number and Quantity	Bending Mode 1	Bending Mode 2	Bending Mode 3	Bending Mode 4	Bending Mode 5	Bending Mode 6
1 f_i (kHz)	4.56	29.03	81.70	160.11	264.02	391.79
2 f_i (kHz)	4.55	29.10	81.82	160.18	263.91	391.45
3 f_i (kHz)	4.62	29.17	81.92	160.42	264.25	391.44
4 f_i (khz)	4.95	30.75	85.02	165.46	272.21	403.90
1 $f_i^{+\Delta\sigma}$ (kHz)	4.57	29.17	82.16	160.95	265.45	393.54
2 $f_i^{+\Delta\sigma}$ (kHz)	4.59	29.24	82.21	161.08	265.47	393.58
3 $f_i^{+\Delta\sigma}$ (kHz)	4.64	29.38	82.57	161.71	266.33	394.70
4 $f_i^{+\Delta\sigma}$ (kHz)	4.93	30.68	84.81	165.20	272.08	403.15
1 Δf_i (kHz)	0.01	0.14	0.46	0.84	1.43	1.75
2 Δf_i (kHz)	0.04	0.14	0.39	0.90	1.56	2.14
3 Δf_i (kHz)	0.02	0.21	0.64	1.29	2.08	3.26
4 Δf_i (kHz)	-0.02	-0.07	-0.21	-0.26	-0.13	-0.75
1 $\bar{\sigma}$ (mN/m)	0.33	0.42	0.48	0.40	0.35	0.37
2 $\bar{\sigma}$ (mN/m)	0.74	0.42	0.42	0.42	0.38	0.43
3 $\bar{\sigma}$ (mN/m)	0.56	0.57	0.61	0.57	0.49	0.60

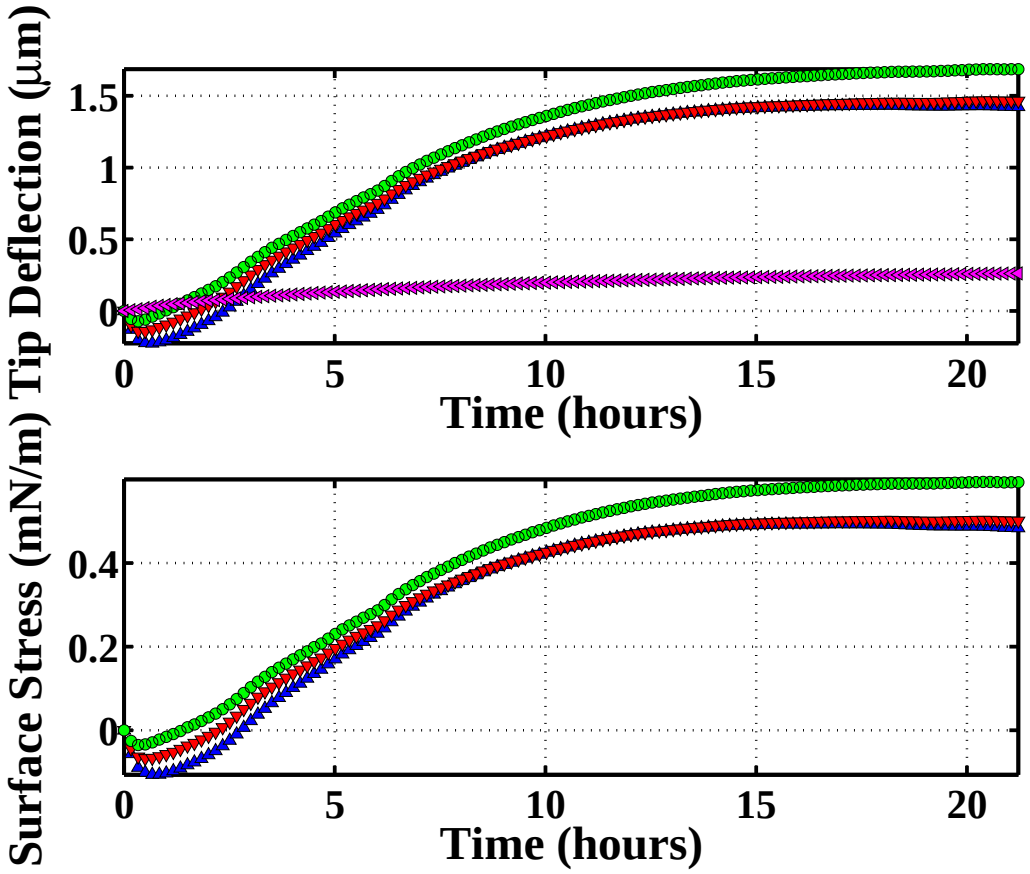

Figure 85: Deflection (top) and corrected (i.e., with the reference beam portion subtracted) surface stress (bottom) evolution for the four silicon beams ($\triangle$= Beam 1,$\triangledown$ = Beam 2, $\circ$ = Beam 3, $\triangleleft$ = Reference Beam) with roughly every thousandth data point shown.

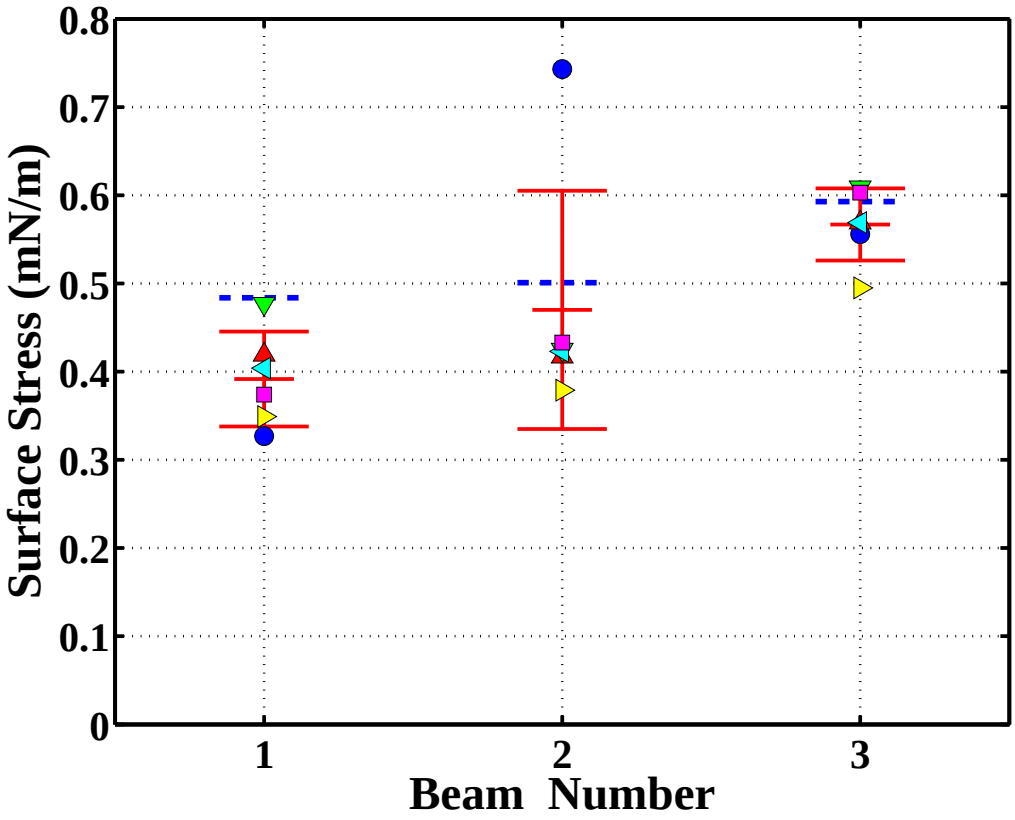

Figure 86: Deflection-based surface stress (the three thick, dashed horizontal lines) and resonance-based surface stress obtained with modes one through six ($\circ$, $\triangle$, $\triangledown$, $\triangleleft$, $\triangleright$, and $\square$, respectively) along with mean resonance-based surface stress values and error bars corresponding to one standard deviation (horizontal, red lines) for the three non-reference beams.

1530 Field Emission Scanning Electron Microscope). The 3D, modal finite element model was constructed using the SEM-obtained geometry and the material properties just listed; the details of the FEA are covered in §4.3.

To compare the geometry obtained from the SEM and that obtained from Equations 54, 87, and 95, the resonance behavior of a microcantilever was monitored via an AFM (§4.2.1). The two halves of the four-quadrant photodiode which preferentially detect the "vertical" beam motion (i.e., in the beam thickness direction) were monitored for one data set and the two halves of the photodiode which preferentially detect "horizontal" motion (i.e., twisting in the θ direction of Figure 8) were monitored to obtain a second set of data.

To assess the validity of using this new geometry determination technique as a valid approach to calculate beam stiffness, the microcantilever stiffness was determined in three fashions. The first two methods were that of Sader (theory in §3.3.5.2 and experimental approach in §4.2.1.1) and that of Hutter & Bechhoefer (theory in §3.3.5.1 and experimental approach in §4.2.1.2), which are commonly-used, accepted, and valid techniques. As required by these methods, the thermal spectra data were fit by an analytic form (terms for $1/f$ noise, white noise, and a simple harmonic oscillator) and the stiffnesses calculated using the published techniques [219, 217, 105]. Additionally, the stiffness was calculated using the EB beam theory-based expression, $k = Ewt^3/[4L^3(1-\nu^2)]$ (e.g., Equation 21), where the beam geometries used were those obtained by SEM and those determined by the resonance-based techniques of this work.

Table 19 shows the predicted bending, lateral, and torsional resonant mode frequencies as calculated by theory (i.e., the SEM-obtained geometries and Equations 54, 87, and 86) along with the corresponding values obtained from the FEA and experiment; the theoretical and FEA values were used to interpret the experimental thermal spectra data. It is seen from Table 19 that the theory and FEA agree well and, for

the modes listed in Table 19, the theory alone could be used to predict resonance frequencies for the various modes (one would use the manufacturer-provided micro-cantilever geometry estimates to predict the resonant modes). Figure 87 shows the normalized vertical displacement amplitude from zero to 400 kHz, and the first six bending mode frequencies are labeled along with the first, third, and what may be the fourth torsional mode. For the bending modes, the theory, FEA, and experiment agree well (see Table 19), so it is assumed that the labeled bending modes in Figure 87 are indeed f_1^b through f_6^b.[34] There was a very large disagreement between the theory, FEA, and experimental value for the fourth torsional mode (f_4^t theory: 311.7 kHz, f_4^t FEA: 320.8 kHz, f_4^t experiment: 360.1 kHz), hence its exclusion from Table 19. The value labeled f_4^t in Figure 87 was not used for calculations because it is not entirely certain that the mode labeled f_4^t in Figure 87 is actually the fourth torsional mode. It is also possible that it is the fourth mode, and that Equation 86 and the FEA are not accurate predictors of this mode.

Conversely to f_4^t, the first three torsional modes were determined with high confidence; f_3^t is apparent and labeled in Figure 87 while the first torsional mode is labeled and evident in Figure 88, which shows the normalized horizontal displacement spectra from zero to 400 kHz. Unfortunately, Figure 88 has large components of noise obscuring the second torsional mode. Figure 89 shows a subset of Figure 88 (i.e., zero to 150 kHz) where f_2^t is more evident. As the first three torsional mode frequencies predicted by theory and FEA agreed well with experiment, it is likely that these observed modes are f_1^t through f_3^t.

The first lateral mode frequency is predicted via finite elements and theory (i.e., Equation 87) to occur at roughly 540 kHz, which is above the frequency ceiling of the data card used (800 kHz maximum sampling rate implies a 400 kHz ceiling)

[34]The reader will recall from §3.3.4 that f_i^b, f_j^l, and f_s^t denote the ith bending, jth lateral, and sth torsional resonance modes, respectively.

Table 19: Theoretical, simulated, and experimental resonance frequency values.

Resonance Type	Mode Number	Theory (kHz)	FEA (kHz)	Experiment (kHz)
Bending	1	4.43	4.47	4.6
Bending	2	27.78	28.02	28.8
Bending	3	77.79	78.57	80.8
Bending	4	152.44	154.37	157.5
Bending	5	251.99	255.85	256.4
Bending	6	376.44	383.07	371.0
Lateral	1	537.52	523.64	576.3
Torsional	1	44.52	46.84	42.7
Torsional	2	133.57	142.97	131.6
Torsional	3	222.61	246.21	220.2

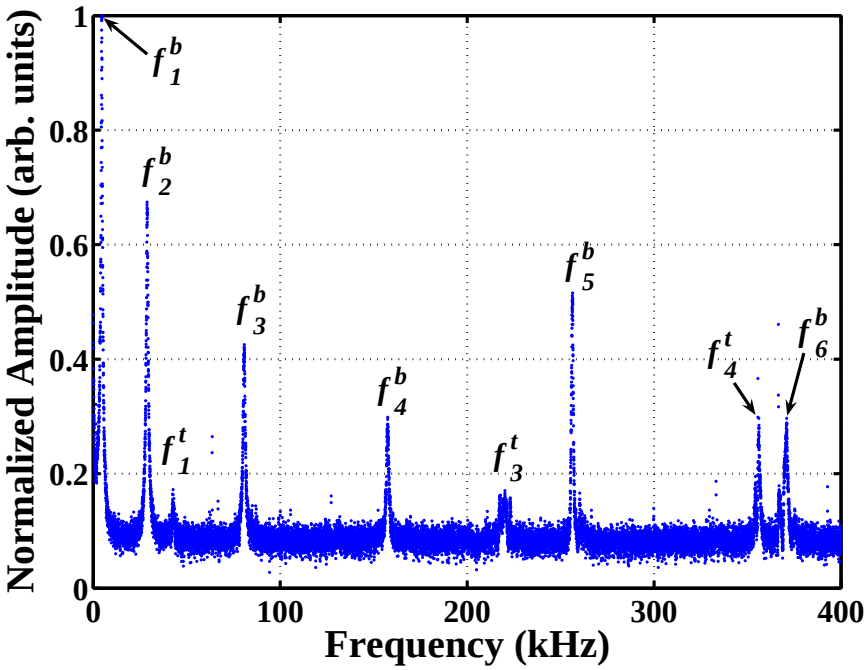

Figure 87: 0-400 kHz frequency response of the thermally-driven cantilever while monitoring the "vertical" segments of the photodiode.

in conjunction with the AFM. However, the AFM used is capable of piezoelectrically actuating the cantilever at any prescribed frequency below roughly 4 MHz and monitoring for frequencies corresponding to large (as compared to the noise floor) amplitude motion. Therefore, the AFM was used to excite the microcantilever in a range from 520-600 kHz, and two large-amplitude motions were detected, one motion at 576.3 kHz and another motion at 579.3 kHz. The Scentris system (not used for exclusively for this work due to inferior deflection sensitivity and a high noise floor as compared to the AFM) was used to obtain a graphical output of these two motions (the AFM is not capable of outputting this data), which is shown in Figure 90. The bending and torsional modes nearest $\approx$ 580 kHz were f_7^b (theory: 525.8 kHz, FEA: 535.9 kHz) and f_7^t (theory: 578.8 kHz, FEA: 606.8 kHz). f_7^b was ruled out as a candidate for the observed motions (i.e., those at 579.3 kHz or 576.3 kHz) because $\approx$ 530 kHz is not very close to $\approx$ 580 kHz, and all other theoretical-FEA-experimental bending mode comparisons (see Table 19) showed close agreement. Therefore, it is assumed that the higher mode in this 520-600 kHz neighborhood (i.e., 579.3 kHz) was f_t^7, (because this matches the theory and FEA values better than the predicted f_1^l of roughly 540 kHz), so f_l^1 was chosen to be 576.3 kHz. However, even if 579.3 kHz is used as f_l^1, the calculated geometries will change by less than 1%.

Table 20 shows experimental geometry (e.g., the length, width, and thickness values obtained from the resonance technique of this work) and the stiffnesses (k_M^{ijs}), which were calculated using the experimental geometry values in Table 20 and $k_M^{ijs} = Ewt^3/4L^3(1-\nu^2)$. Table 21 shows the percent difference between the experimentally-determined values for length, width, thickness, and stiffness (k_M^{ijs}), and the SEM-obtained length, width, thickness, and stiffness [$k_{SEM} = Ewt^3/4L^3(1-\nu^2)$, calculated with the SEM-obtained geometries]. Table 22 shows the mean and first standard deviation for the length, width, and thickness determined from the eighteen independent sets of modal information in Table 20 (i.e., the various *i-j-s* combinations), the

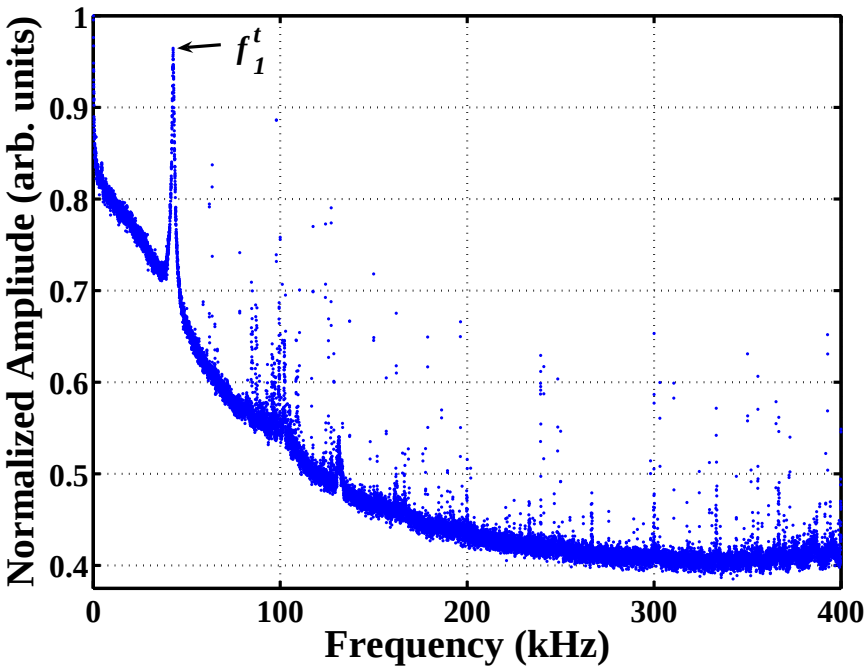

Figure 88: 0-400 kHz frequency response of the thermally-driven cantilever while monitoring the "horizontal" segments of the photodiode.

SEM-obtained geometry, and the percent difference between the two. Table 23 shows the stiffness values obtained via Sader's method (with the SEM-obtained length and width) k_S, the method of Hutter & Bechhoefer k_{HB}, EB beam theory (using the SEM-obtained geometry) k_{SEM}, and the percent difference between these three stiffness values and the stiffness value obtained using EB beam theory and the mean length, width, and thickness values from Table 22, $k_M^{mean} = Ewt^3/4L^3(1-\nu^2) = 0.018$ N/m.

The values in Table 20 and the corresponding percent differences in Table 21 show reasonable agreement, particularly for the first four bending modes. At many of the higher mode numbers (i.e., frequencies), the percent error in length, thickness, and stiffness becomes increasingly significant (see Table 21). This may be due to increased damping effects (which are neglected by Equations 54, 87, and 86) as the resonance frequency of a particular mode is increased, and inability of Equations 54, 87, and 86 to accurately predict certain higher resonance modes. Therefore,

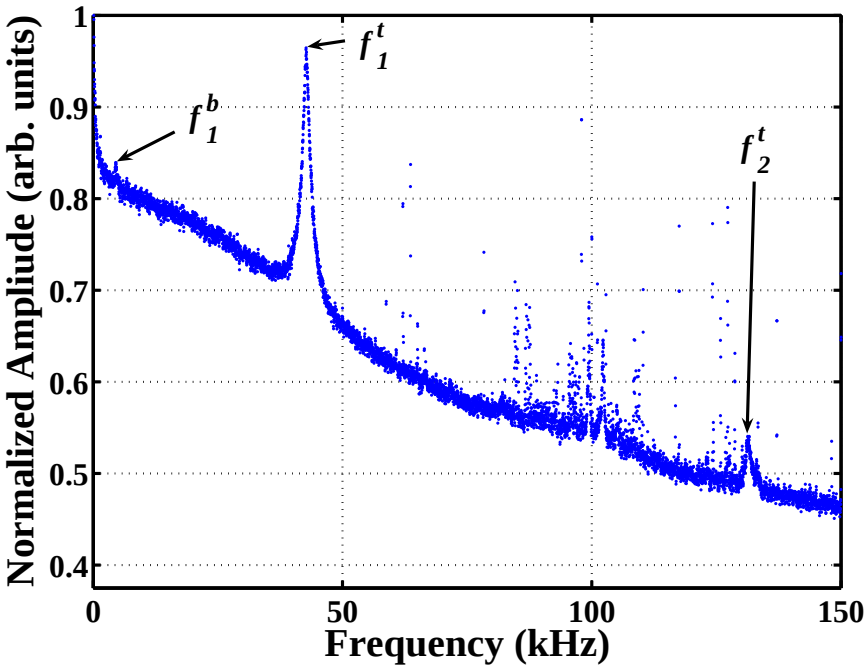

Figure 89: 0-160 kHz Frequency response of the thermally-driven cantilever while monitoring the "horizontal" segments of the photodiode.

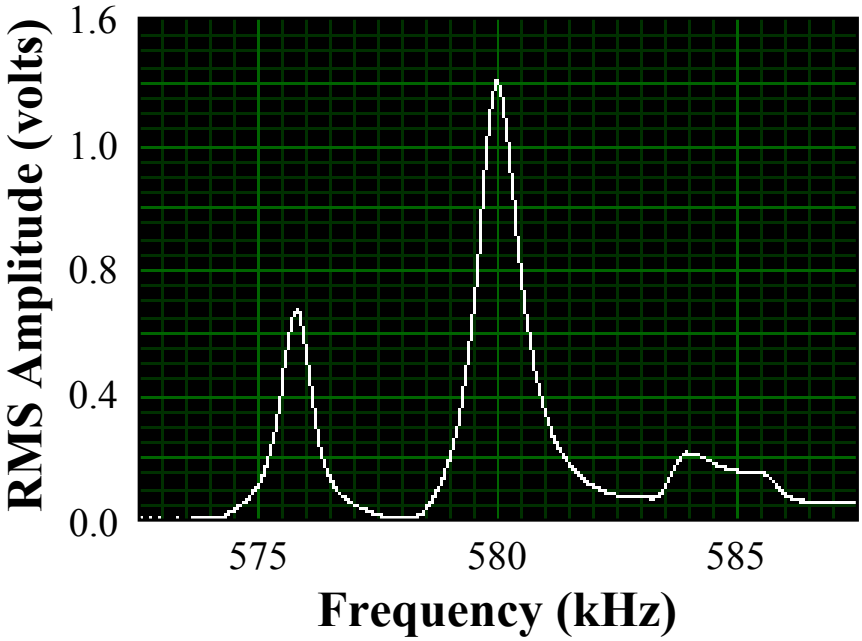

Figure 90: RMS amplitude versus frequency plot of the two large amplitude motions found in the 520-600 kHz range sweep (570-590 kHz range shown).

Table 20: Modal information used (i, j, and s refer to bending, lateral, and torsional mode number, respectively), experimentally determined length, width, thickness, and stiffness values (recall that the SEM-obtained values for length, width, and thickness were 499.2 μm, 97.2 μm, and 0.80 μm, respectively).

Modal Information (i, j, s)	Length (μm)	Width (μm)	Thickness (μm)	Stiffness, k_M^{ijs} (N/m)
1, 1, 1	503.6	105.9	0.85	0.021
1, 1, 2	490.2	100.4	0.80	0.019
1, 1, 3	488.3	99.6	0.79	0.018
2, 1, 1	503.1	105.7	0.84	0.021
2, 1, 2	489.7	100.2	0.80	0.018
2, 1, 3	487.8	99.4	0.79	0.018
3, 1, 1	504.1	106.1	0.85	0.021
3, 1, 2	490.7	100.6	0.80	0.019
3, 1, 3	488.8	99.8	0.80	0.018
4, 1, 1	501.5	105.0	0.83	0.021
4, 1, 2	488.1	99.5	0.79	0.018
4, 1, 3	486.2	98.7	0.78	0.018
5, 1, 1	493.8	101.9	0.80	0.018
5, 1, 2	480.7	96.5	0.76	0.016
5, 1, 3	478.8	95.8	0.75	0.016
6, 1, 1	478.4	95.6	0.72	0.014
6, 1, 2	465.7	90.6	0.69	0.012
6, 1, 3	463.8	89.9	0.68	0.012

one should be cautious when using this technique if no lower-mode frequencies are available. Nonetheless, the mean geometry values as determined by this new method show very good agreement with the SEM-obtained geometry, as shown in Table 22.

The percent differences in Table 23 between k_M^{mean}, k_{SEM}, and k_S are very small. However, the difference between k_M^{mean} and k_{HB} is markedly larger. One possible source of this error could be any inaccuracies in the displacement calibration, which relates the photodiode voltage to the actual displacement seen by the tip of the cantilever via the sensitivity. This type of inaccuracy would lead to an incorrect mean-squared cantilever tip displacement value, which is used in conjunction with the equipartition theorem to calculate k_{HB}. However, if this calibration error did exist, it would not induce any change in k_S as only the *voltage output* of the photodiode is used to calculate k_S (i.e., the thermal spectra output is not scaled by the sensitivity for Sader's method). Similarly, a displacement calibration would not affect the calculation of k_{SEM}, as only the SEM-obtained geometry is used. The reader should note that the agreement between EB beam theory and the experimental methods show no length-scale effects on bending stiffness, which is expected as the silicon material is close to the "perfect" structure assumed when deriving a Hooke's law type constitutive model, which is used to derive the EB beam theory equation.

The agreement between the values shown in Tables 22 and 23 indicate that the resonance-based technique developed for this work produces accurate estimates of beam geometry and stiffness. The stiffness estimates are similar to those of commonly-used, existing techniques (e.g., EB beam theory, Sader's method and the method of Hutter & Bechhoefer). The new approach of this work requires no invasive techniques, no *a priori* knowledge of any beam geometry, no curve fitting, is comparatively fast (i.e., the theoretical equations can predict the resonance frequencies rapidly so no FEA would be necessary), and allows for multiple data points from a single beam, which reduces uncertainty in the geometry and stiffness estimates. The only caveats

Table 21: Modal information used (i, j, and s refer to bending, lateral, and torsional mode number, respectively), and percent difference between the experimentally determined length, width, thickness, and stiffness values, and the measured values. Here the percent difference equals 100×[(SEM-obtained value - measured value)/SEM-obtained value].

Modal Information (i, j, s)	Length % Diff.	Width % Diff.	Thickness % Diff.	Stiffness % Diff.
1, 1, 1	−0.9	−9.2	−5.7	14.9
1, 1, 2	1.8	−3.5	−0.1	2.7
1, 1, 3	2.1	−2.7	0.7	0.7
2, 1, 1	−0.8	−9.0	−5.4	14.3
2, 1, 2	1.9	−3.3	0.2	1.9
2, 1, 3	2.2	−2.6	0.9	−0.1
3, 1, 1	−1.0	−9.5	−6.0	15.6
3, 1, 2	1.7	−3.7	−0.4	3.5
3, 1, 3	2.1	−2.9	0.3	1.5
4, 1, 1	−0.5	−8.3	−4.3	12.0
4, 1, 2	2.2	−2.6	1.1	−0.7
4, 1, 3	2.6	−1.8	1.9	−2.7
5, 1, 1	1.0	−5.0	0.3	0.5
5, 1, 2	3.7	0.5	5.6	−13.8
5, 1, 3	4.0	1.3	6.3	−16.1
6, 1, 1	4.1	1.5	9.4	−28.3
6, 1, 2	6.7	6.6	14.2	−46.8
6, 1, 3	7.0	7.4	14.8	−49.8

Table 22: Mean and standard deviation values for length, width and stiffness determined by the technique of this work (i.e., the values from Table 20), along with the SEM-obtained values and the percent difference between the mean values and the SEM-obtained values.

Dimension	Mean (μm)	Standard Deviation (μm)	Percent Difference
Length	488.0	11.6	-2.2
Width	99.5	4.7	2.6
Thickness	0.79	0.05	-1.9

Table 23: Stiffness values obtained via Sader's method (k_S), the method of Hutter & Bechhoefer (k_{HB}), and EB beam theory using the SEM-obtained geometry (k_{SEM}) and the percent difference between these three stiffness values and the stiffness value obtained using EB beam theory and the mean geometry values from Table 22, $k_M^{mean} = 0.018$ N/m.

Method	Stiffness (N/m)	Percent Difference
k_S	0.0178	-2.2
k_{HB}	0.0143	24.0
k_{SEM}	0.0181	-0.4

are that an estimate of the beam geometry is available, which nearly always is from the manufacturer [7, 5], and that the beam elastic modulus, density, and Poisson's ratio are known. While not covered in this work, the torsional stiffness, which is an important experimental parameter for certain microcantilever applications (e.g., lateral force microscopy), is also tenable via this new approach once the beam geometry in known.

5.2.4 Scientific Goals: Summary and Conclusions

This section presented the results used to test the length-scale dependent bending stiffness (§5.2.1), the influence of surface stress upon microcantilever bending resonant frequencies (§5.2.2), and the purely resonance-based approach to determining beam geometry (§5.2.3). The length-scale dependence modeling is new to the literature because it takes a different approach (e.g., micropolar theory) to arrive at an expression obtained by another work [133], which used a different elasticity model (e.g., strain gradient theory) and a circuitous power series expansion; a length scale dependence was clearly observed experimentally. The surface stress work is new to the literature in that it extends existing resonance modeling and shows good agreement with theory and allows a new microcantilever measurement mode – surface stress determination solely via resonance monitoring. The resonance-based approach to beam geometry determination is a novel application of existing theory that yields a new means to ascertain microcantilever stiffnesses (bending and torsional), and hence could be valuable in future microcantilever works where other stiffness determination methods are difficult or impossible to employ. In light of the findings of this section, the scientific goals as outlined in Chapter 1 [to (*i*) examine the influence of effects that may become more influential as characteristic length scales decrease, (*ii*) develop a new microcantilever experimental mode, and (*iii*) to develop a new microcantilever characterization technique] were satisfied.

5.3 Summary

This chapter first presented the manufacturing goal-related results, which mainly dealt with repeatable microcantilever production via injection molding using various materials and mold cavity geometries. The scientific goal-related results then were detailed, and the theories of Chapter 3 were compared to experimental values. Both sets of goals were satisfied as evidenced by the data and comparisons presented in

this chapter. Chapter 6 closes this dissertation with an overall summary of the work conducted, along with suggestions for future work.

CHAPTER VI

CONCLUSIONS AND RECOMMENDATIONS

This chapter summarizes the results of this dissertation along with suggesting improvements for, and shortcomings of, the work performed. The chapter also discusses suggestions for future work. The goals of this dissertation were broken into a manufacturing group and a scientific group, and the summaries are discussed in order of the goal groups.

6.1 Summary of Manfacturing Goal-Related Results

The first manufacturing goal was repeatable production of microcantilevers via non-IC methods from a variety of materials and two techniques were developed. The solvent casting approach of §5.1.1 produced feasible parts, but was abandoned after minimal work in favor of injection molding (§5.1.2.3), which was capable of repeatable microcantilever production from amorphous, semi-crystalline, and filled polymeric materials (PS, PP, and NN6) but not from a liquid crystal polymer.

The second manufacturing goal– the thinnest IM cantilever possible– was examined in §5.1.2.4. The result was a minimum thickness part of roughly 2 μm (for the PS, PP, and NN6 materials), which was limited not by flash or difficulties in mold filling, but by warpage developed in the microcantilevers during the cooling phase of the IM cycle.

The third manufacturing goal– the production of composite microcantilevers using polymers with the same matrix material and varying types and weight percent of

fillers– was investigated by producing the PMMA-carbon nanofiber composite injection molded microcantilevers of §5.1.2.5. The mean values of the measured resonant frequencies for the five different materials showed a statistically significant difference between the neat material and at least one of the composite materials for each of the three different mold geometries used, hence satisfying the goal.

The final manufacturing goal was to to show that polymeric microcantilevers were not only mechanical equivalents to silicon-type parts, but were experimental equivalents as well in a variety of applications. Vapor phase, deflection-based sensing of thiol adsorption on the gold-coated microcantilevers was shown feasible and produced surface stress values commensurate with the literature, as discussed in §5.1.3.2. Liquid phase, deflection-based sensing of pH variation-induced surface stress changes was not feasible due to inaccurate results, as discussed in §5.1.3.3. The poor results could be inherent in the beams themselves but experimental evidence suggests that shortcomings in the experimental equipment are likely culprits. Vapor phase resonance-based sensing was shown feasible and accurate and compared to a commercial hygrometer in §5.1.3.4 where the microcantilevers were used to monitor relative humidity. Probably the most fruitful experimental mode of this work was the demonstration of injection-molded SPM probes, which were shown to give reasonable results as compared to a silicon-type part in §5.1.3.1.

6.1.1 Manufacturing Goal-Related Results: Shortcomings, Improvements, and Future Work

While all of the manufacturing goals were met, there were certain shortcomings of the work, one of which was the poor results from the liquid phase, deflection-based sensing work. As pointed out, this is likely due to the poor fluid phase deflection tracking of the Scentris system with the polymeric microcantilevers. Another shortcoming on the manufacturing side was the large, but acceptable, amount of flash on the PS parts (see §5.1.2.3), and this could possibly be reduced or eliminated by "breaking in" the

molds through extended use, using EDM to produce the mold cavities without any burr formation, or increasing the clamping pressure of the molding machine.

The curling of the microcantilevers examined in the minimum thickness study was disappointing, but not disastrous. A rapid thermal response mold may reduce the warpage by cooling the polymer melt in a shorter amount of time. This would probably preclude the formation of semi-crystalline materials but may allow for feasible, submicron cantilevers to be injection-molded. From the dimensions of the flash seen in this work, thicknesses on the order of 100-200 nm may be possible; for scale, this is the thickness of roughly ten stacked lamellar layers of a crystalline polymer.

While the injection-molded SPM probes showed accurate results, the tips, which were produced in the mold with the nanoindenter, have such a low aspect ratio that the parts are not feasible for many SPM applications. While tip compliance will obviously become an issue at higher tip aspect ratios, a focused ion beam machine is an ideal candidate for production of very high aspect ratio pits in the injection molds themselves. Another option may be some type of electrochemical machining using an existing, silicon SPM probe as the cathode.

6.2 Summary of Scientific Goal-Related Results

The scientific goals for this work were three fold. The first sought to produce a length scale-dependent bending stiffness, which was accomplished theoretically in §3.3.1.3 and explored experimentally in §5.2.1. A length scale dependence was exhibited, as evidenced by the disagreement between the nanoindenter-determined stiffness values, which were roughly 7× larger than the EB beam theory values. Sources of error were examined and it was concluded that the errors were not significant enough to explain the larger stiffness difference. The length scale bending parameter was found to be commensurate with literature values for other materials, hence the length scale effect was concluded to exist, which could be particularly important for polymeric (and

possibly non-polymeric) microcantilever systems, and could be important for future, polymer-based MEMS/NEMS applications.

The second scientific goal sought to produce an entirely new microcantilever experimental mode, and the influence of surface stress upon microcantilever bending resonant frequencies (§5.2.2) is one such mode. The experimental results showed acceptable agreement with theory for the axially-distributed force model, and this model was concluded to be a reasonably accurate one. While the experiment did not match theory exactly, this model is still at least an order of magnitude improvement over the current model. This technique could be useful because it allows surface stress determination by monitoring resonant behavior alone, hence eliminating the need for a deflection calibration routine, which some new microcantilever experimental apparatus do not have (e.g., the Scentris system used in this work).

The final scientific goal was to develop a new microcantilever characterization technique, and this was accomplished with the purely resonance-based approach to determining beam geometry (§5.2.3). The experiment and theory agreed well for this new approach (geometry agreed to within 3%), hence proving to be a valid approach. Similar to the second scientific goal, this technique could be useful because it allows beam geometry (and subsequently bending and torsional stiffness and mass) determination by monitoring resonant behavior alone, hence eliminating the need for a deflection calibration routine.

The agreement between the experiment of Chapter 5 and the theory of Chapter 3 imply that the scientific goals as outlined in Chapter 1 [to (*i*) examine the influence of effects that may become more influential as characteristic length scales decrease, (*ii*) develop a new microcantilever experimental mode, and (*iii*) to develop a new microcantilever characterization technique] were met.

6.2.1 Scientific Goal-Related Results: Shortcomings, Improvements, and Future Work

One shortcoming of the scientific goals was the inability to directly measure the modulus at the strain rates seen by the microcantilevers as they resonate (see §5.2.1.4). This could be fruitful experimental ground to investigate a (possibly) strain-rate dependent material length scale parameter and E at very high strain rates for structures (particularly polymeric) on the micron scale. At these length scales and with polymeric materials, little experimental work has been performed.

If an experimental device could be devised to determine E at high frequencies, or if a resonance-based E determination was sufficient, one could use resonance information (e.g., bending mode frequencies) to determine the storage and loss moduli of polymeric materials at the microscale to examine any length scale effects. Additionally, one could look at the effect that species adsorption (e.g., water vapor adsorption into nylon) and temperature variation have upon resonance behavior. This approach has seen experimental validation at the macroscale, but little examination at the microscale [77].

A new force spectroscopy mode could be possible by using the end force model of §5.2.2, Equation 73 (e.g., determining the axial force acting on a tipped-cantilever as it scans over a surface, solely by monitoring resonant frequency). This idea was not explored for this work, but the mathematical modeling could be applicable. In a similar vein, one could examine the influence, if any, of a surface stress on the torsional resonant frequencies of a microcantilever as these modes show higher sensitivity [229].

APPENDIX A

CANTILEVER SURFACE STRESS FREQ. EQUATION

This appendix details the steps leading to Equations 74 and 73. The mode shapes and derivatives of §3.3.3.6 may be written as Equations 107 through 107 [208]. Here V is the transverse deflection of the beam as a function of position x, $\hat{T}$ is used to denote a function of position, to distinguish it from the time label (T) of §3.3.3.6. Here p and q are defined as they are in Equation 65 but the subscripts denoting the modenumber are left out for simplicity; the reader must keep in mind that the following derivations hold for each mode. Also, $d_x^i = \partial^i/\partial x^i$, ω is the resonant frequency (again the modenumber subscripts are left out for simplicity), $b = F/EI$ (as in §3.3.3.6), and the primes indicated differentiation with respect to x.

$$V = \{(d_x^3 - bd_x)V(0) + d_x^2V'(0) + d_xV''(0) + [V'''(0) - bV'(0)]\}\hat{T}(x) \tag{107}$$

$$V' = \{\omega^2V(0) + d_x^3V'(0) + d_x^2V''(0) + d_x[V'''(0) - bV'(0)]\}\hat{T}(x) \tag{108}$$

$$V'' = \{\omega^2d_xV(0) + (bd_x^2 + \omega^2)V'(0) + d_x^3V''(0) + d_x^2[V'''(0) - bV'(0)]\}\hat{T}(x) \tag{109}$$

$$V''' - bV' = \{(\omega^2d_x^2 - b\omega^2)V(0) + \omega^2d_xV'(0) + \omega^2V''(0) + (d_x^3 - bd_x)[V'''(0) - bV'(0)]\}\hat{T}(x) \tag{110}$$

where

$$\hat{T}(x) = \frac{1}{pq(p^2+q^2)}(q\sinh px - p\sin qx)$$

Imposition of the boundary conditions upon the mode shapes, which are now in terms of the transfer function $\hat{T}(x)$, facilitates the solution. It is seen that $\hat{T}(0) = 0$, so

the conditions of zero displacement and zero slope at the cantilevered end are satisfied (i.e., Equations 107 and 108 equal zero). The remaining two boundary conditions at $x = 1$ (x is normalized by L) permit formation of a matrix equation of the form $\hat{\mathbf{T}}\mathbf{V} = \mathbf{0}$, where $\hat{\mathbf{T}}$ is a function of the transfer function only, and $\mathbf{V}$ is a function of the eigenfunctions only.

$$V'' = \{\omega^2 d_x \cancelto{0}{V(0)} + (bd_x^2 + \omega^2)\cancelto{0}{V'(0)} + d_x^3 V''(0) + d_x^2[V'''(0) - b\cancelto{0}{V'(0)}]\}\hat{T}(1) = 0 \quad (111)$$

$$V''' - bV' = \{(\omega^2 d_x^2 - b\omega^2)\cancelto{0}{V(0)} + \omega^2 d_x \cancelto{0}{V'(0)} + \omega^2 V''(0) \quad (112)$$
$$+ (d_x^3 - bd_x)[V'''(0) - b\cancelto{0}{V'(0)}]\}\hat{T}(1)$$

$$\begin{bmatrix} d_x^3\hat{T}(1) & d_x^2\hat{T}(1) \\ \omega^2\hat{T}(1) & (d_x^3 - bd_x)\hat{T}(1) \end{bmatrix} \begin{Bmatrix} V''(0) \\ V'''(0) \end{Bmatrix} = \begin{bmatrix} 0 \\ 0 \end{bmatrix} \Rightarrow \hat{\mathbf{T}}\mathbf{V} = \mathbf{0} \quad (113)$$

The determinant of $\hat{\mathbf{T}}$ must vanish, which implies Equation 114.

$$|\hat{\mathbf{T}}| = 0 = \frac{d^3\hat{T}(1)}{dx^3}\left(\frac{d^3\hat{T}(1)}{dx^3} - b\frac{d\hat{T}(1)}{dx}\right) = \omega^2\hat{T}(1)\frac{d^2\hat{T}(1)}{dx^2} \Rightarrow \quad (114)$$

$$\left[p^3 q\cosh(p) + pq^3\cos(q)\right]\left\{\left[p^3 q\cosh(p) + pq^3\cos(q)\right] - r_1\omega^2\left[pq\cosh(p) - pq\cos(q)\right]\right\}$$

$$-\omega^2\left[q\sinh(p) - p\sin(q)\right]\left[p^2 q\sinh(p) + pq^2\sin(q)\right] = 0$$

Equation 114 is unwieldy (mainly in the two variables, p and q, and recall that Equation 114 must hold for each mode of vibration), so a computer symbolic algebra code (written in MATLAB) was used in conjunction with the buckling-resonance analogy of §3.3.3.6 (i.e., the observation that, at the buckling load, the resonance frequency should become zero) to obtain the final forms of Equations 74 and 73.

APPENDIX B

NON-IDEAL BOUNDARY CONDITIONS

This appendix presents analytic justification for the assumed boundary conditions used in this dissertation. As in §3.3.3.2, by employing the method of assumed modes we obtain the general solution of the equations of motion, Equation 50 (i.e., $X_i = A_i \sin s_i x + B_i \cos s_i x + C_i \sinh s_i x + D_i \cosh s_i x$). Looking at the beam setup in Figure 91, the boundary conditions to be satisfied are given as Equations 115 through 118.

$$V|_{x=0} = EIX_i'''|_{x=0} = k_1 X_i|_{x=0} \tag{115}$$

$$M|_{x=0} = EIX_i''|_{x=0} = k_2 X_i'|_{x=0} \tag{116}$$

$$V|_{x=L} = EIX_i'''|_{x=L} = k_3 X_i|_{x=L} \tag{117}$$

$$M|_{x=L} = EIX_i''|_{x=L} = k_4 X_i'|_{x=L} \tag{118}$$

Substitution of the general solution (i.e., Equation 50) into these boundary conditions, manipulation of the resulting set of equations into a matrix form of $\mathbf{MC} = \mathbf{0}$, followed by setting the determinant of $\mathbf{M}$ equal to zero will give the so-called wave relation. To examine the effect of the beam support influence for a cantilevered beam, this was done with $k_3 = k_4 = 0$ (i.e., a free end condition), and the resulting expression is Equation 119

$$s_i^3(\sin\alpha_i \cosh\alpha_i + \cos\alpha_i \sinh\alpha_i) + EIs_i^4(\cos\alpha_i + \cosh\alpha_i - 1)$$

$$-\frac{k_1 k_2}{EI}(1 + \cos\alpha_i \cosh\alpha_i) + k_1 s_i(-\cos\alpha_i \sinh\alpha_i + \sin\alpha_i \cosh\alpha_i) = 0 \tag{119}$$

where $s_i = (\omega_i^2 \rho_b wt/EI)^{1/4}$. Notice that in the limit as $k_1, k_2 \to \infty$, Equation 119 reduces to the wave relation for a cantilevered beam (e.g., $\cos\alpha_i \cosh\alpha_i + 1 = 0$) as

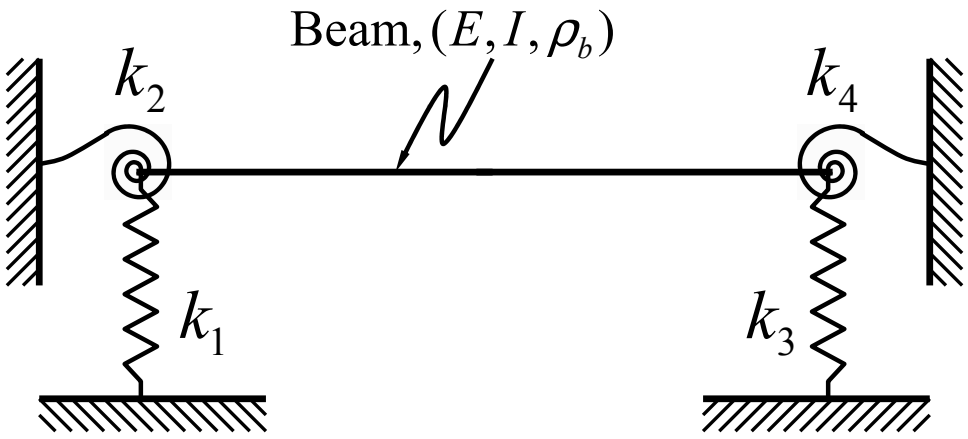

Figure 91: Beam with non-ideal boundary conditions.

expected. Figures 92 and 93 show the effect that a non-infinite base stiffness will have on the resonance frequencies (here the microcantilever geometry was chosen to be length-width-thickness of 500-100-10 μm and elastic modulus of 3 GPa). It is seen that the effect of support compliance lessens with increasing mode number, and that after a certain threshold stiffness for k_1 and k_2, the percent error in the frequencies of any mode is negligible. To model the rotational support stiffness (k_2), the microcantilever is treated as a two-beam system, as shown in Figure 94; this geometry was chosen to mimic the actual geometry of the microcantilevers as they are supported in the AFM and Scentris systems for characterization. The rotational stiffness of beam 1 [i.e., $\partial M/\partial u_z'(L)$] is obtained by differentiating the beam deflection equation and then solving for the moment as shown in Equation 120.

$$u_z(x) = \frac{PL}{EI}\left(\frac{x^2}{2} - \frac{x^3}{6L}\right) \Rightarrow u_z'(x) = \frac{PL}{EI}\left(x - \frac{x^2}{2L}\right) \Rightarrow u_z'(L) = \frac{PL^2}{2EI} \Rightarrow$$
$$u_z'(L) = \frac{ML}{2EI} \Rightarrow M = \frac{2u_z'(L)EI}{L} \Rightarrow k_2 = \frac{2EI}{L} \tag{120}$$

By using the values of 500 μm, 100 μm, 10 μm, and 3 GPa, for L, w_1 t_1, and E for beam 1 of Figure 94, $k_2 = 0.0125$ N-m/radian, which, in conjunction with Equation 119 (with $k_1 = \infty$) shows that $k_2 = 0.0125$ N-m/radian will cause a less than 0.01% error in f_i, which is considered negligible.

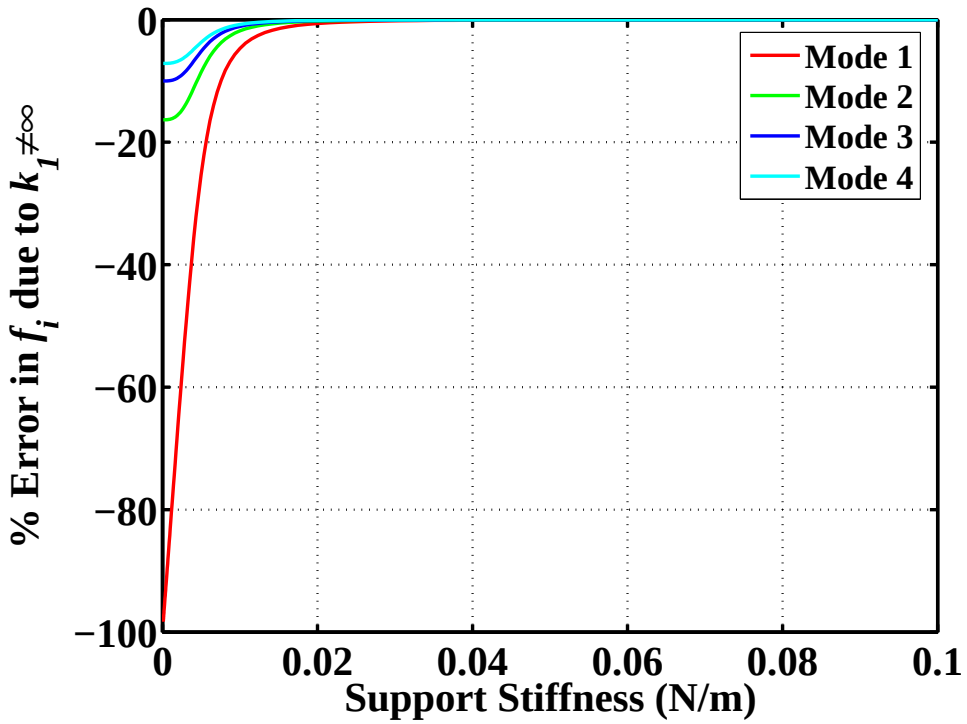

Figure 92: Influence of non-infinite k_1 upon the first through fourth mode resonance frequencies.

To determine k_1 it is assumed that a prismatic, square cross sectioned bar is supporting the load, with a length of 500 μm and an edge length (a) of 100 μm, as shown in Figure 95. The axial stiffness is determined via Hooke's law in Equation 121.

$$\frac{\text{Force}}{\text{Area}} \approx \text{stress} = E \times \text{strain} \Rightarrow \frac{P}{a^2} = E\frac{\delta L}{L} \Rightarrow \frac{P}{\delta L} = k_1 = \frac{Ea^2}{L} \tag{121}$$

In this case, $k_1 = Ea^2/L = 60$ kN/m, which, in conjunction with Equation 119 (with $k_2 = \infty$) shows that $k_1 = 60$ kN/m will cause a less than 0.01% error in f_i, which is considered negligible.Hence, the assumptions of zero slope and displacement used in this dissertation are justified.

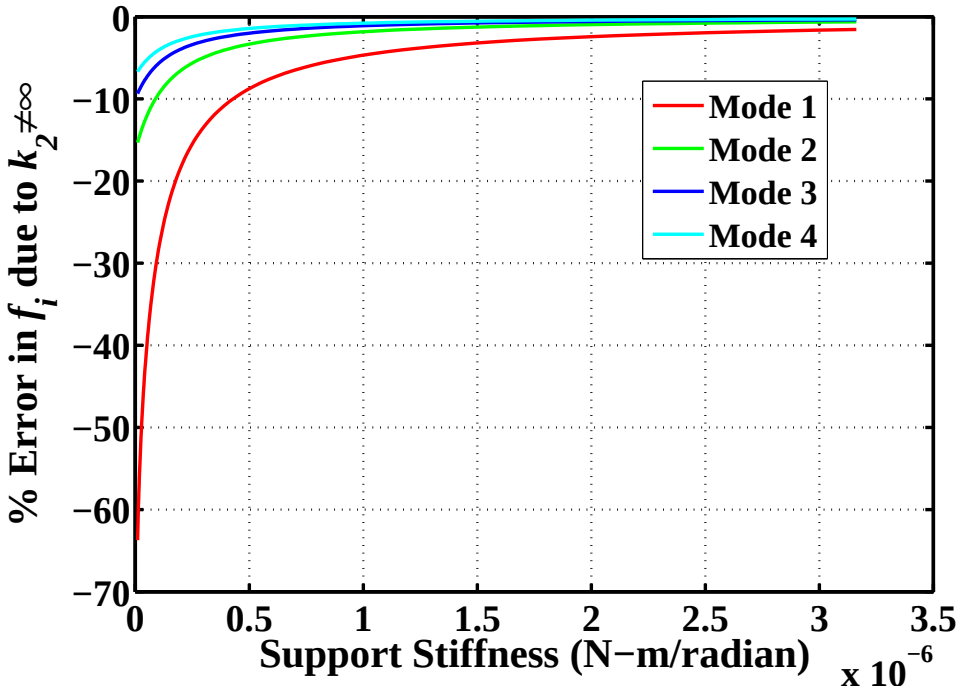

Figure 93: Influence of non-infinite k_2 upon the first through fourth mode resonance frequencies.

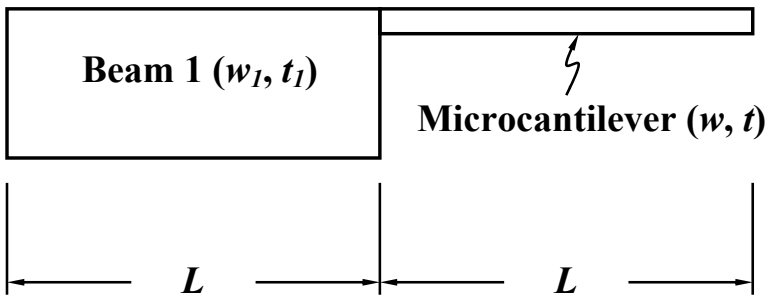

Figure 94: Two-beam model for estimating support rotational stiffness, k_2.

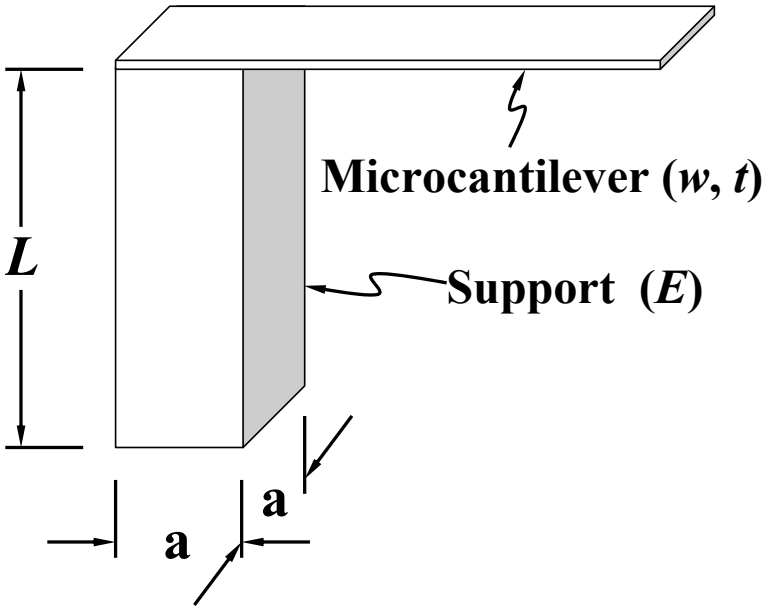

Figure 95: Model for representing support displacement stiffness, k_1.

APPENDIX C

STATISTICAL PROCESS CONTROL

Statistical process control (SPC) is elucidated in this appendix because it is used in Chapter 5 to determine the state of the injection molding process used to produce microcantilevers. In the 1920's, Walter Shewhart was the first to employ statistical procedures for quality control of manufactured products [230]. This approach is now called statistical process control and it is commonly used to determine whether or not a certain process is *in control* or *out of control*. An *in control* process is repeatable, and the errors present are assumed to inherent in the process and cannot be eliminated with redesign of the process itself. An *out of control* process is one which either has (*i*) an excess of uncontrollable error which cannot be reduced without process redesign, or (*ii*) correctable process error which is causing uncontrollable results.

The theory behind SPC is to take subsets of all the products produced, measure certain parameter(s) of interest, and then use this data to draw reasonable conclusions about the entire lot of parts produced, even though the desired parameter(s) of each part have not been measured. SPC was employed for this work as it was not possible to measure the entire set of microcantilever parts due to time constraints, yet a logical, industry and academe-accepted indicator of process control and repeatability was desired. However, before SPC can be applied legitimately, the data must be shown to follow certain assumptions.

C.1 SPC Assumptions

There are four assumptions underlying the measurement processes and SPC analysis used in §5.1.2.3, and these are as follows:

1. The measurements are random and independent.

2. The measurements and errors are each from a fixed (possibly distinct) distribution(s).

3. The measurement distribution has a fixed location (i.e., constant mean).

4. The measurement distribution has a fixed scale (i.e., constant variance).

Assumptions 1 and 2 are the so-called independent and identically distributed assumptions (IID) in statistics terms.

C.1.1 Randomness of Data

To test the randomness assumption for this work (assumption 1), "autocorrelation" plots are used, which plots autocorrelation coefficient versus different lags.[1] The autocorrelation plot shows the sample autocorrelation coefficient (or simply autocorrelation[2]) on the ordinate and the lag on the abscissa, as shown in Figure 96. The autocorrelation for lag equal to one is always one, because each measurement is completely correlated with itself. The error bounds (the horizontal lines in Figure 96) are drawn at $\pm z_{1-\alpha/2}/\sqrt{N}$ where N is the sample size and z is the percent point function of a standard normal distribution [i.e., $N(0,1)$]. If any of the points lie outside of the bounds for a given lag, then it is likely (95% confidence for $\alpha = 0.1$ for example) that the data is not random with respect to that particular lag. The data in Figure 96 are random (they were generated randomly from a $N(0,1)$ distribution, so this isn't surprising).

[1] A "lag" is the difference in number between data points; the lag between X_i and X_{i-5} is 5.

[2] The correlation coefficient is defined as: $C_h/C_0 = \left[\sum_{i=1}^{N-h}(X_i - \overline{X})(X_{i+h} - \overline{X})\right]\left[\sum_{i=1}^{N}(X_i - \overline{X})^2\right]^{-1}$ where h is the lag and note that $C_h/C_0 \in [-1, 1]$.

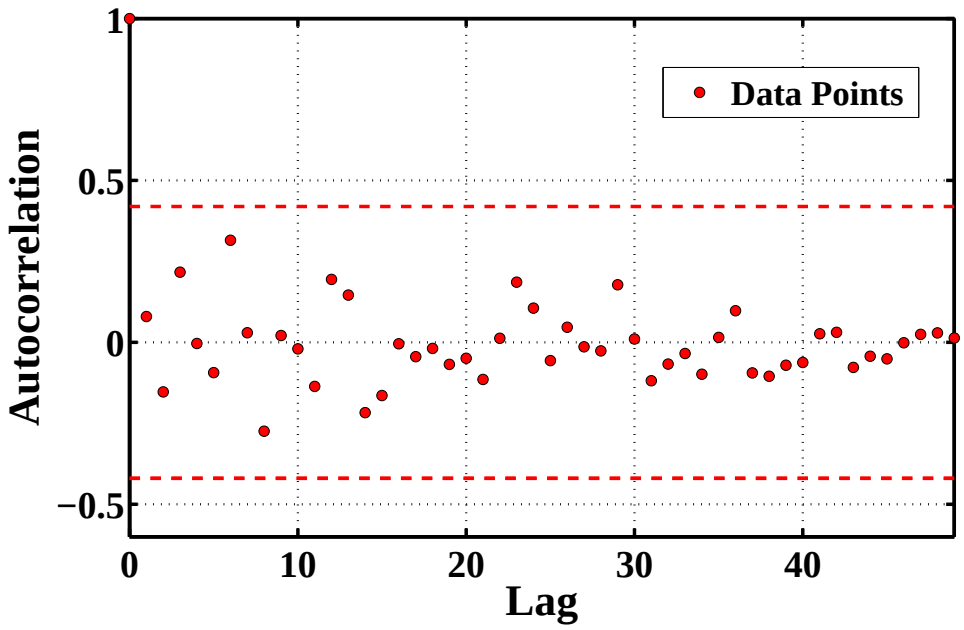

Figure 96: Generic autocorrelation plot.

C.1.2 Normal Distribution of Data

Normal probability plots, in which the data are plotted against a theoretical normal distribution in such a way that the points should form an approximately straight line, are used in this work to determine if the data sets (i.e., the individual f_1 and k measurements) and the errors (the residuals from a linear regression on the individual f_1 and k measurement sets) are normally distributed (assumption 2). Figure 97 shows a normal probability plot of a data set randomly generated from an $N(1, 1)$ distribution, and it is seen that the plot is close to linear. However, one should note that the ordinate axis in scaled nonlinearly and the data linearity conclusion should be drawn mainly from the bulk of the data points; for Figure 97 this would be within a probability of 0.5 ± 0.4 as that encompasses roughly 80% of the data.

C.1.3 Constant Mean of Data

Run-sequence plots (i.e., the X_i measurements versus i) are used in this work to determine if the data exhibits a shift in location (i.e., a constant mean). Figure 98

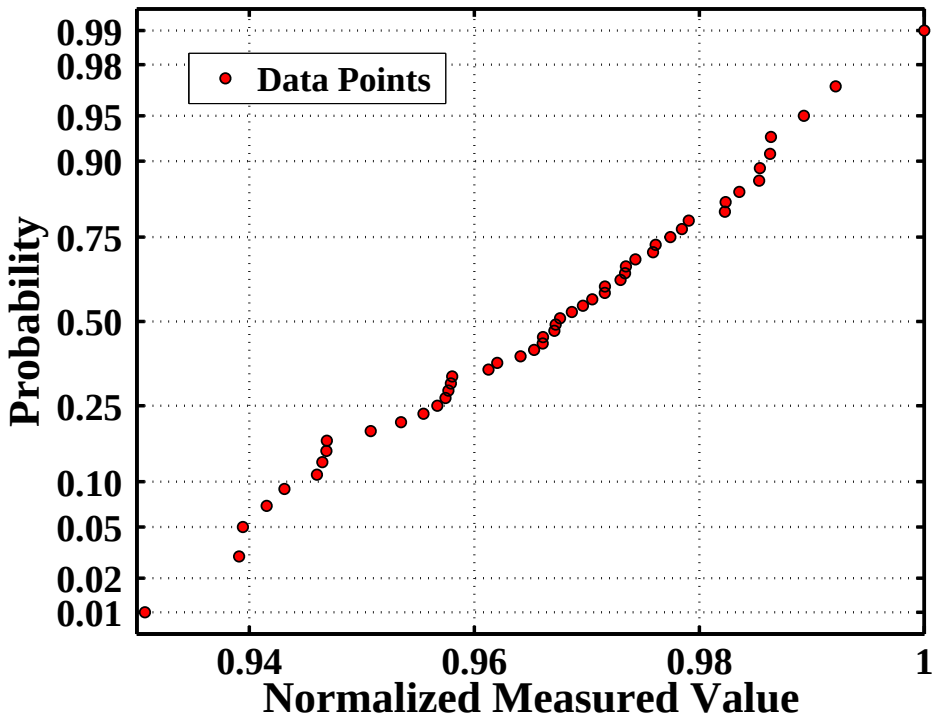

Figure 97: Generic normalized normal probability plot.

shows a run-sequence plot from a set of data derived from an $N(0,1)$ distribution. It is seen that the mean line does not change significantly as i increases, so this data set shows no shift in location.

C.1.4 Constant Variance of Data

The last assumption to be verified in order to employ SPC theory is that the measured data exhibit a constant variance. To verify this, autoregressive conditional heteroscedastic theory (ARCH) is employed.[3] ARCH was originally developed by Engle in the late 1970's and early 1980's to estimate the means and variances of economic inflation in the United Kingdom using prior time-history data. Engle showed that an ARCH effect of nonconstant variance can have dramatic repercussions upon

[3]Heteroscedasticity can be thought of as time-varying variance or volatility in statistical terms. A conditional process exhibits a dependence of current observations upon the past observations, and autoregressive denotes a scheme that incorporates the past observation-dependence into the present observations.

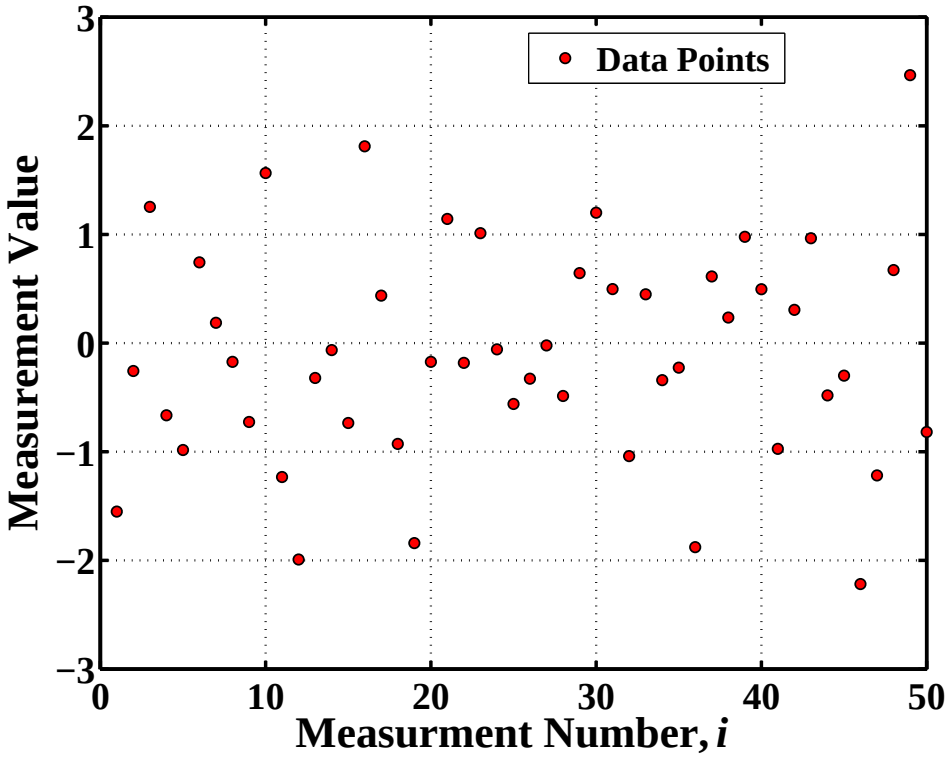

Figure 98: Generic run-sequence plot.

the future inflation behavior.

The approach taken here used Engle's theory to prove the converse of heteroscedasticity, or homoscedasticity (i.e., constant variance of a data set). To accomplish this, one looks at the conditional effect of a measurement taken "today", X_i, as drawn from a conditional density funtion, $f(X_i|X_{i-j})$, whose variance will be $V(X_i|X_{i-j})$ [68].[4] By employing ARCH theory (via the MATLAB package with the archtest function), the presence or absence of an ARCH effect can be quantified at a specific significance level and at different lags.[5] The MATLAB code takes sample residuals obtained from

[4]Here "conditional" notation is used, where $g(X_i|X_{i-j})$ denotes that the value of g evaluated at the ith measured value (X_i), is also a function of some known previous measurement value (or values) X_{i-j}, for an arbitrary function g, and j such that $1 \leq i-j \leq n-1$), where there are n total measurements and j is the lag.

[5]The significance level is the probability of type I error, or assuming that ARCH effects are not present when, in fact, they are. For example, an α of 0.05 gives a 5% chance of falsely concluding that no ARCH effects are present.

the univariate linear regression of the data curve fit (e.g., the same curve fits used to generate the normalized residual normal probability plots discussed in §C.1.2), and tests for the presence of jth order ARCH effects by regressing the squared residuals on a constant and the lagged values of the previous j squared residuals. If the data exhibits homoscedasticity (i.e., a constant variance), the asymptotic test statistic, $(j+1)R^2$, is asymptotically chi-square distributed with j degrees of freedom [35].[6]

A Boolean decision vector, $\mathbf{H}$, is returned from the computer code, where an entry of zero indicates that no ARCH effects exist at the corresponding element of a lags vector (nonzero integers representing the lag values examined), $\mathbf{L}$, and an entry of one indicates heteroscedasticity at the corresponding lag; the length of $\mathbf{H}$ is the same as the length of $\mathbf{L}$. If all elements of $\mathbf{H}$ are zero, then one can conclude (at significance level α) that the variance is constant at *all lags*, or $V(X_i|X_{j-1}) = V(X_i)\ \forall\ 1 \leq i \leq n$ and at all possible lags (i.e., all possible j values). In short, if $\mathbf{H} = \mathbf{0}$ for a particular data set, then that data set is homoscedastic and the constant variance-assumption necessary to employ the SPC techniques is justified. For this work all possible lags were examined (i.e., $j = 0, 1, 2, \ldots, 49$) over the fifty measurements of stiffness and first resonance frequency acquired for each of the eight different cantilever geometries and the four different polymeric materials (i.e., all the repeatability measurements discussed in §5.1.2.3). With the SPC measurement assumptions and their physical validation scheme (e.g., the autocorrelation, normal probability, and run-sequence plots) explained, attention turns to the SPC tools that can be employed for data sets satisfying such assumptions, and what information these tools can divulge about the

[6] R^2 is the sample multiple correlation coefficient determined from the jth order ARCH effects regression equation, which is as follows:

$$\begin{bmatrix} Y_1 \\ Y_2 \\ \vdots \\ Y_n \end{bmatrix} = \mathbf{X}\bar{\beta} = \begin{Bmatrix} \begin{bmatrix} 1 & \left(R_i^2 - R_{i-1}^2\right) & \left(R_i^2 - R_{i-2}^2\right) & \cdots & \left(R_i^2 - R_{i-j}^2\right) \end{bmatrix}_1 \\ \begin{bmatrix} 1 & \left(R_i^2 - R_{i-1}^2\right) & \left(R_i^2 - R_{i-2}^2\right) & \cdots & \left(R_i^2 - R_{i-j}^2\right) \end{bmatrix}_2 \\ \vdots \\ \begin{bmatrix} 1 & \left(R_i^2 - R_{i-1}^2\right) & \left(R_i^2 - R_{i-2}^2\right) & \cdots & \left(R_i^2 - R_{i-j}^2\right) \end{bmatrix}_n \end{Bmatrix} \begin{bmatrix} \beta_0 \\ \beta_1 \\ \beta_2 \\ \vdots \\ \beta_j \end{bmatrix}.$$

data sets.

C.1.5 SPC Techniques

The main SPC tool employed for this work (in Chapter 5) is the X-bar chart, which allows for a reasonable judgement to be made about the control status and repeatability of a process. The procedure for constructing these charts is to take a sequence of measurement subsets from a group of parts. For example, if ten thousand parts were made, parts numbered 1-50, 101-150, 201-250,..., 10,901-10,950 could be measured giving a total of one hundred subgroups ($N = 100$) of fifty parts each ($n = 50$). Then, the mean of the measured value for the jth subgroup ($\overline{X}_j$) is calculated from Equation 122.

$$\overline{X}_j = \frac{\sum_{i=1}^{n} X_i}{n} \tag{122}$$

This will yield one hundred (i.e., N=100) different $\overline{X}_j$ values corresponding to each subgroup of fifty parts. The total mean is calculated from Equation 123.

$$\overline{\overline{X}} = \frac{\sum_{j=1}^{N} \overline{X}_j}{N} \tag{123}$$

The next step is to produce a value for the standard deviation of each subgroup and one can employ (i) an estimator (or a "guess") for the standard deviation, derived from the subgroup sample data or (ii) decide whether there is adequate evidence to support a statement about the value of the standard deviation (i.e., hypothesis testing resulting in a confidence interval on the standard deviation). One advantage of SPC is that a small number of measurements per subgroup can be used (to get subgroup means), so the estimator approach is natural in the context of SPC because no additional measurement needs to be made (i.e., the subgroup size to calculate the subset mean and the subset standard deviation estimator can be of the same size, a size usually not large enough to allow for use of the definition of the standard

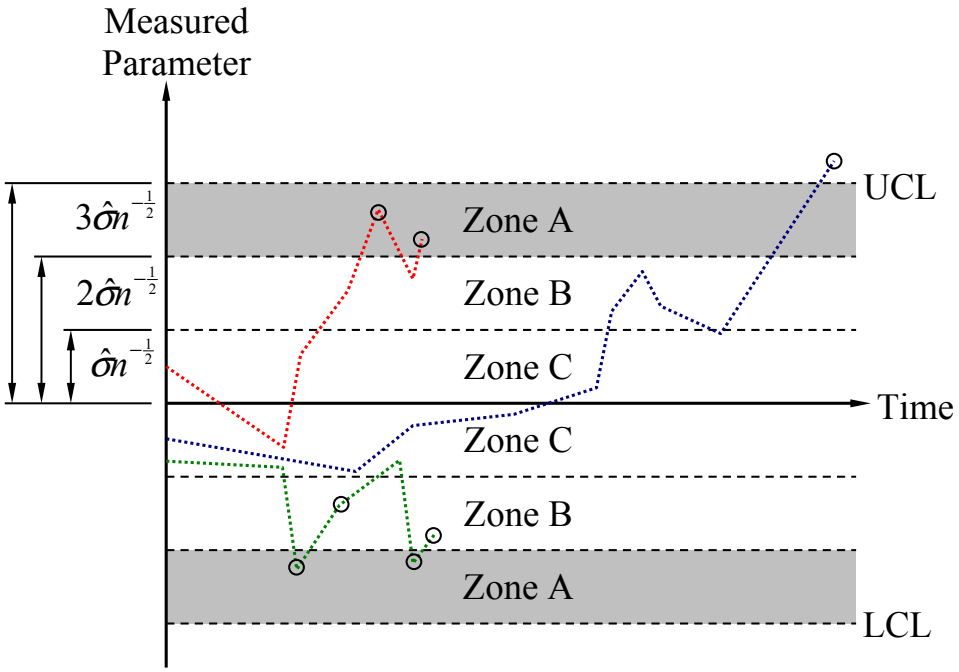

Figure 99: Generic X-bar chart (vertices on each of the three dotted lines represent sample subgroups).

deviation). Following standard SPC rules, Equation 124 is used to calculate the standard deviation estimator, $\hat{\sigma}$,

$$\hat{\sigma} = \frac{\overline{R}}{d_2} \tag{124}$$

where d_2 is a constant given in statistical tables[7] and $\overline{R}$, which is the mean of the ranges for the j individual subgroups, is given by Equation 125.

$$\overline{R} = \frac{\sum_{j=1}^{N} [\max(X_j) - \min(X_j)]}{N} \tag{125}$$

To construct the X-bar chart, the total mean value, $\overline{\overline{X}}$, is plotted as the centerline, and then lines are drawn at $\overline{\overline{X}} \pm \hat{\sigma} n^{-\frac{1}{2}}$, $\overline{\overline{X}} \pm 2\hat{\sigma} n^{-\frac{1}{2}}$, and $\overline{\overline{X}} \pm 3\hat{\sigma} n^{-\frac{1}{2}}$ as shown in Figure 99, where UCL and LCL denote the upper and lower control limits, respectively.

[7] d_2 is equal to 2.326 for the subgroup size used in this work (i.e., $n = 5$) [4].

Once the X-bar control chart is constructed, there are certain rules which dictate the control status of the process (i.e., in-control or out-of-control, to a reasonable uncertainty). By examining the so-called Western Electric Company Zone Rules (WECO rules), the X-bar chart is broken into three zones, labeled A, B, and C, as shown in Figure 99. Table 24 shows what constitutes a violation indicating that the process is out of control. These rules were defined by examining the reasonableness of certain observations. For example, a single point falling outside of Zones A, B, and C should happen with a probability of roughly 0.3% if a normal error distribution is assumed.[8] Similarly, the probability of observing two points out of three in a row in Zone A (on the same side of the mean line) and the probability of observing four points out of five in a row in Zones A and B (on the same side of the mean line) also are about 0.3%. With these observation probabilities known under the specific assumptions, the Western Electric Company Zone Rules of Table 24 were established [42]. These rules are used in Chapter 5 to determine whether or not the injection molding manufacturing of microcantilevers is an in- or out-of-control process. This control chart-based determination speaks to repeatability in a larger sense than just stating that the mean value is some μ and the standard deviation is some σ.

[8]Recall that, under a normally distributed spread, $\approx 99.73\%$ of the data will fall within plus-or-minus three standard deviations.

Table 24: Western Electric Company Zone Rules.

Rule Number	Symptom
1	One point falling outside of Zone A (blue line in Figure 99)
2	Two out of three successive points falling on the same side of the centerline in Zone A or beyond (red line in Figure 99)
3	Four out of five successive points falling on the same side of the centerline in Zone B or beyond (green line in Figure 99)
4	Seven successive points falling above or below the centerline
5	Seven successive points monotonically increasing (or monotonically decreasing)
6	Fourteen successive points alternating in an up-down pattern
7	Fifteen successive points in Zone C

APPENDIX D

X-BAR CHARTS AND NORMAL PROBABILITY PLOTS

This appendix first presents the X-bar charts in terms of stiffness (k) and first-mode resonance frequency (f_1), generated from the repeatability analysis of §5.1.2.3, for the polypropylene, neat liquid crystal polymer, and the nanoclay-nylon 6 composite of Table 3 (pages 263 through 264). All X-bar charts presented in this appendix are in control according to the Western Zone Control Rules of Appendix C, as are those presented in §5.1.2.3, indicating that the IM process is repeatable and in control in terms of k and f_1 for all four polymers of Table 3. Next, the autocorrelation plots (pages 265 through 266), residual normal probability plots (pages 267 through 268), and run-sequence plots (pages 269 through 270) discussed in §5.1.2.3 and Appendix C are presented. All autocorrelation plots show randomness in the data, all normal probability plots show linearity indicating that the data and errors are roughly normally distributed, and all the run-sequence plots show that the data show constant location and scale; these results indicate that employment of the Western Zone Control Rules of Appendix C is justified. All mold cavity numbers used in this appendix are those of Table 9.

D.1 X-Bar Charts

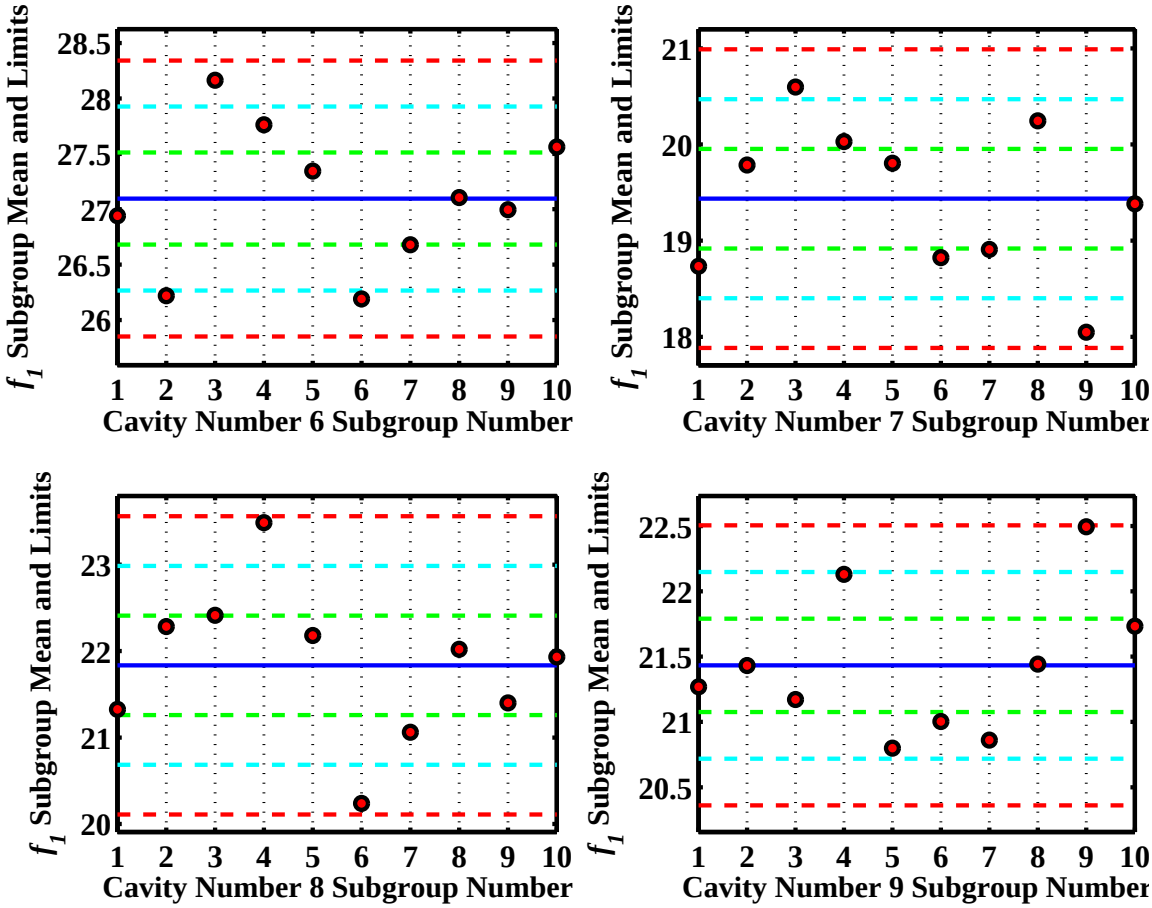

Figure 100: f_1 X-bar plots for the resonance mold with polypropylene parts (ordinate values are in kHz).

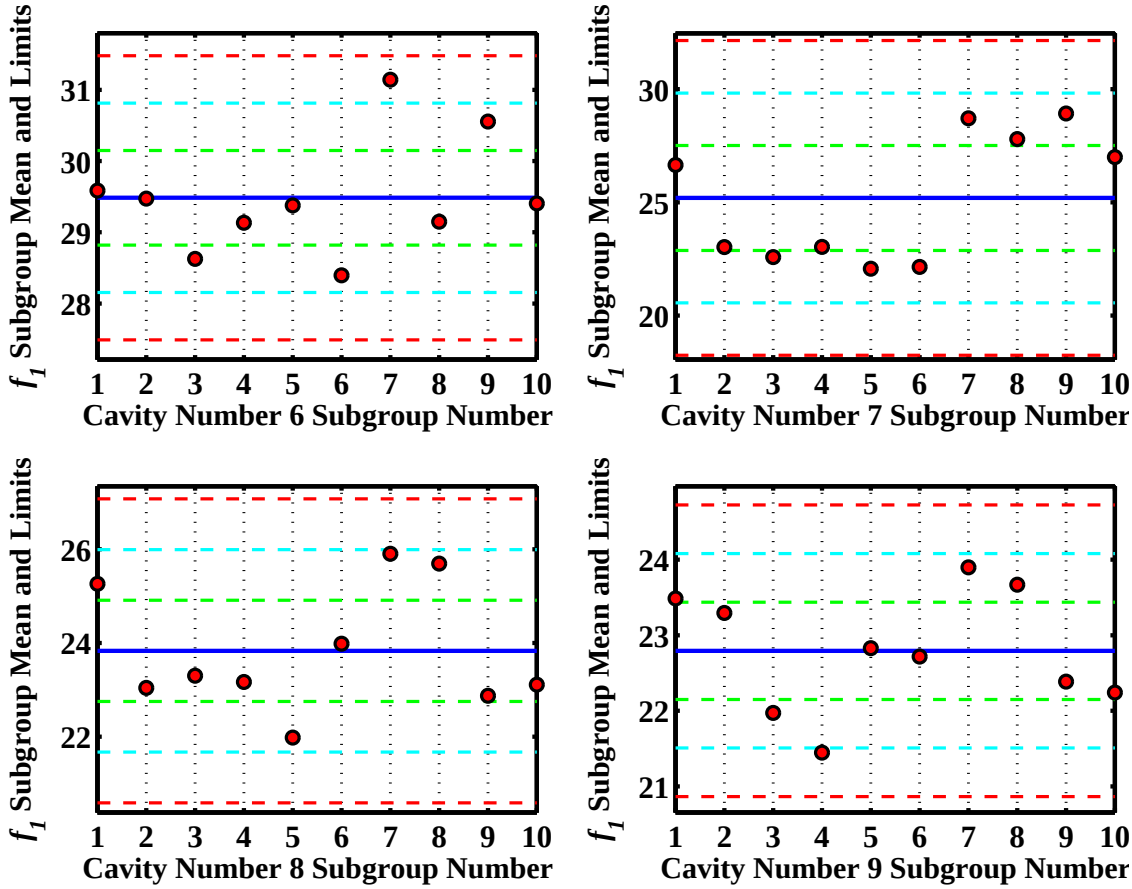

Figure 101: f_1 X-bar plots for the resonance mold with nanoclay-nylon 6 composite parts (ordinate values are in kHz).

D.2 Autocorrelation Plots

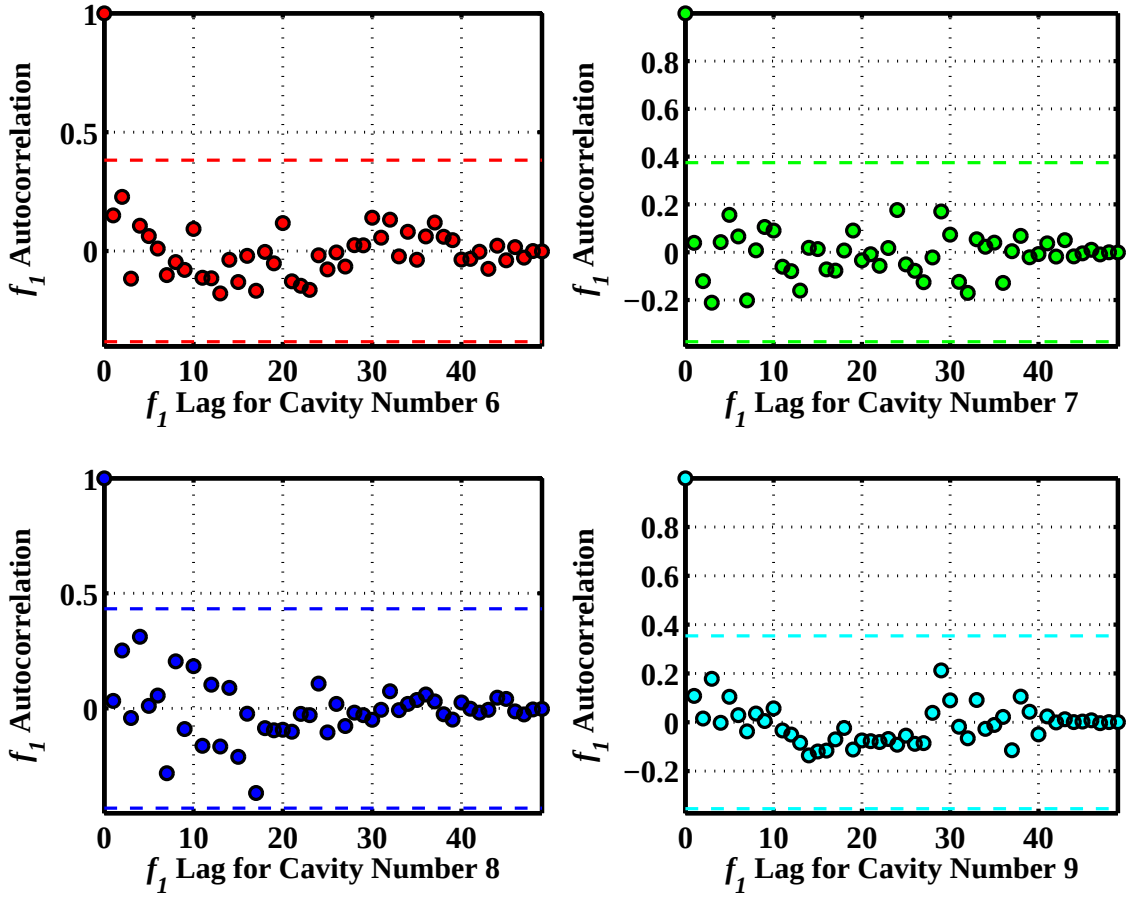

Figure 102: f_1 autocorrelation plots for the polypropylene parts.

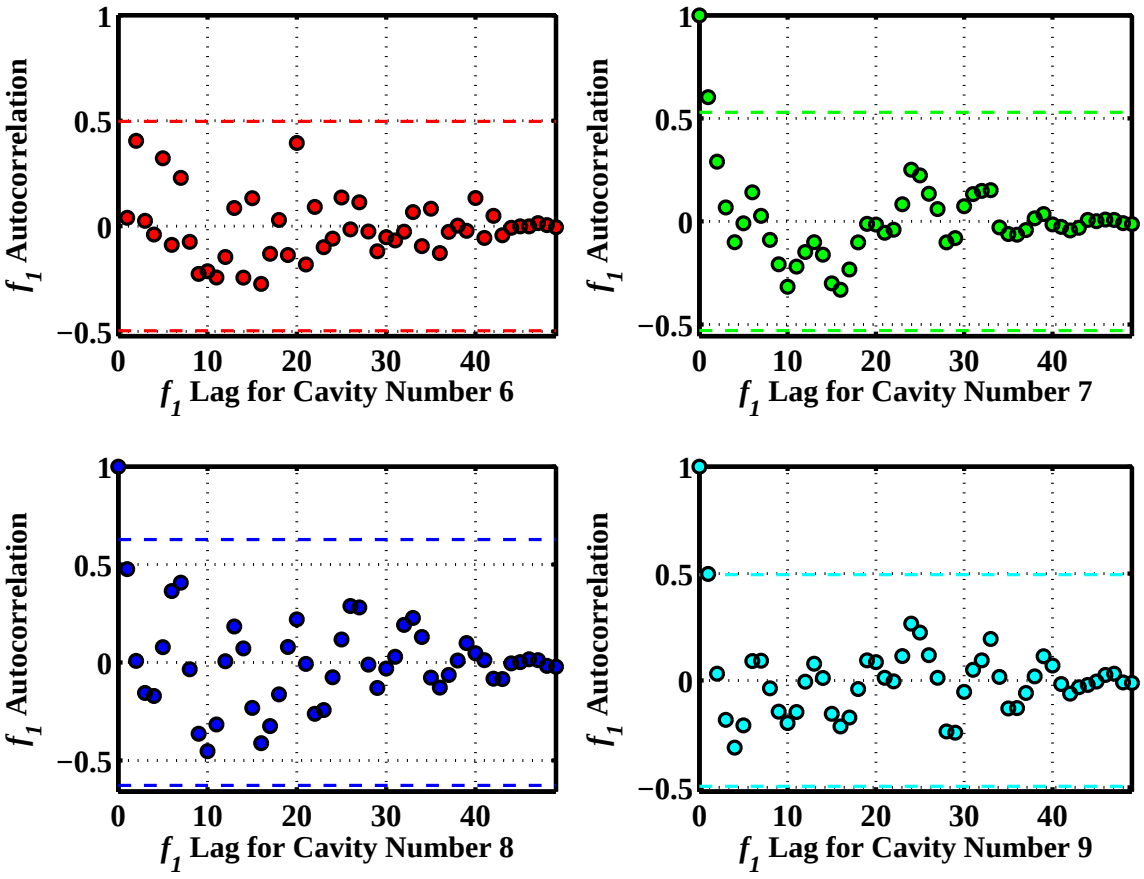

Figure 103: f_1 autocorrelation plots for the nylon composite parts.

D.3 Residual Normal Probability Plots

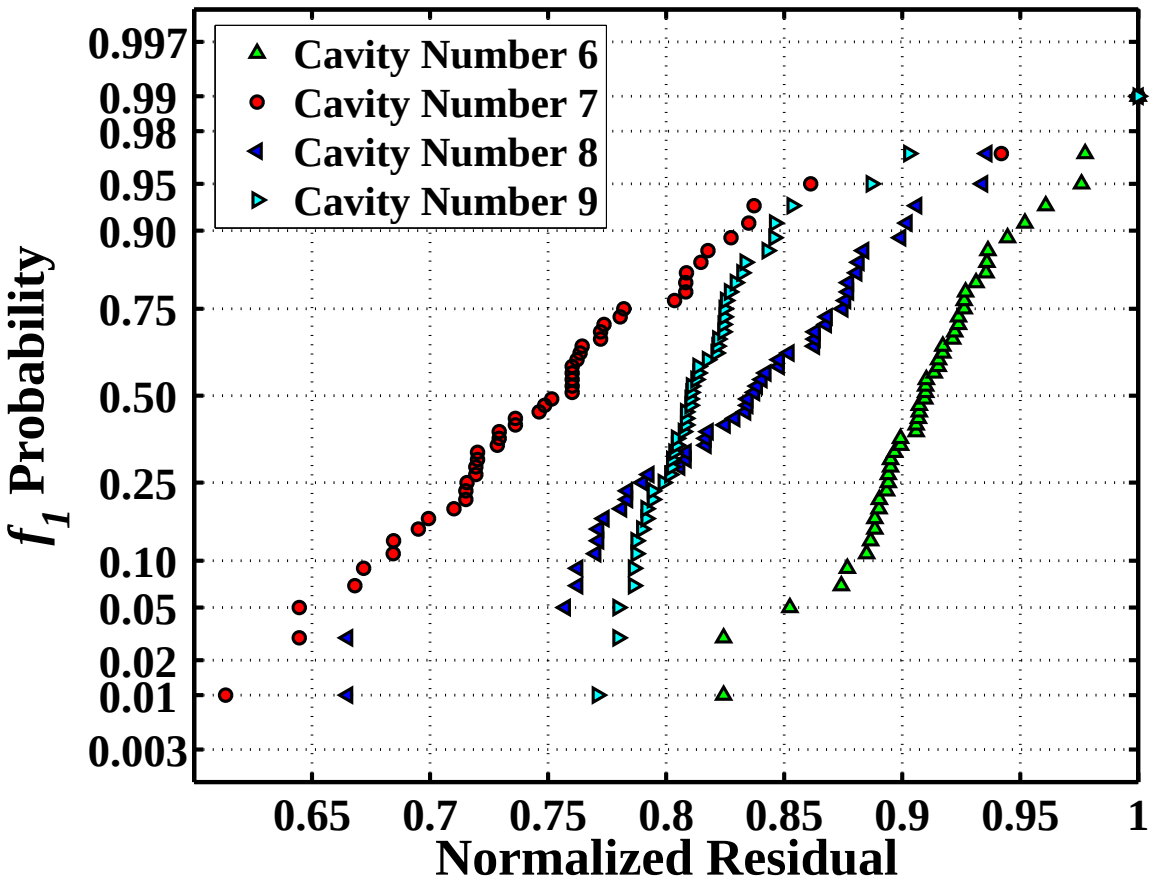

Figure 104: f_1 normalized normal probability plots for the polypropylene parts.

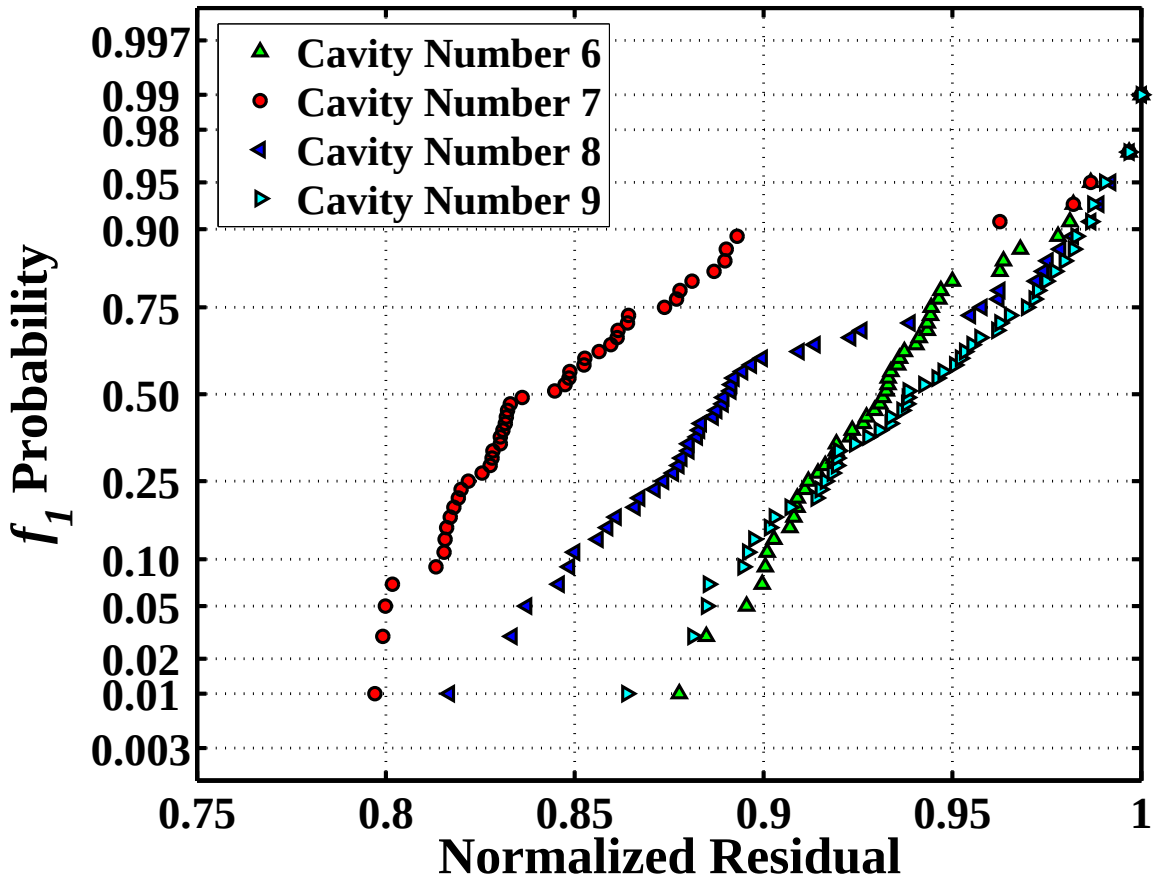

Figure 105: f_1 normalized normal probability plots for the nylon composite parts.

D.4 Run-sequence Plots

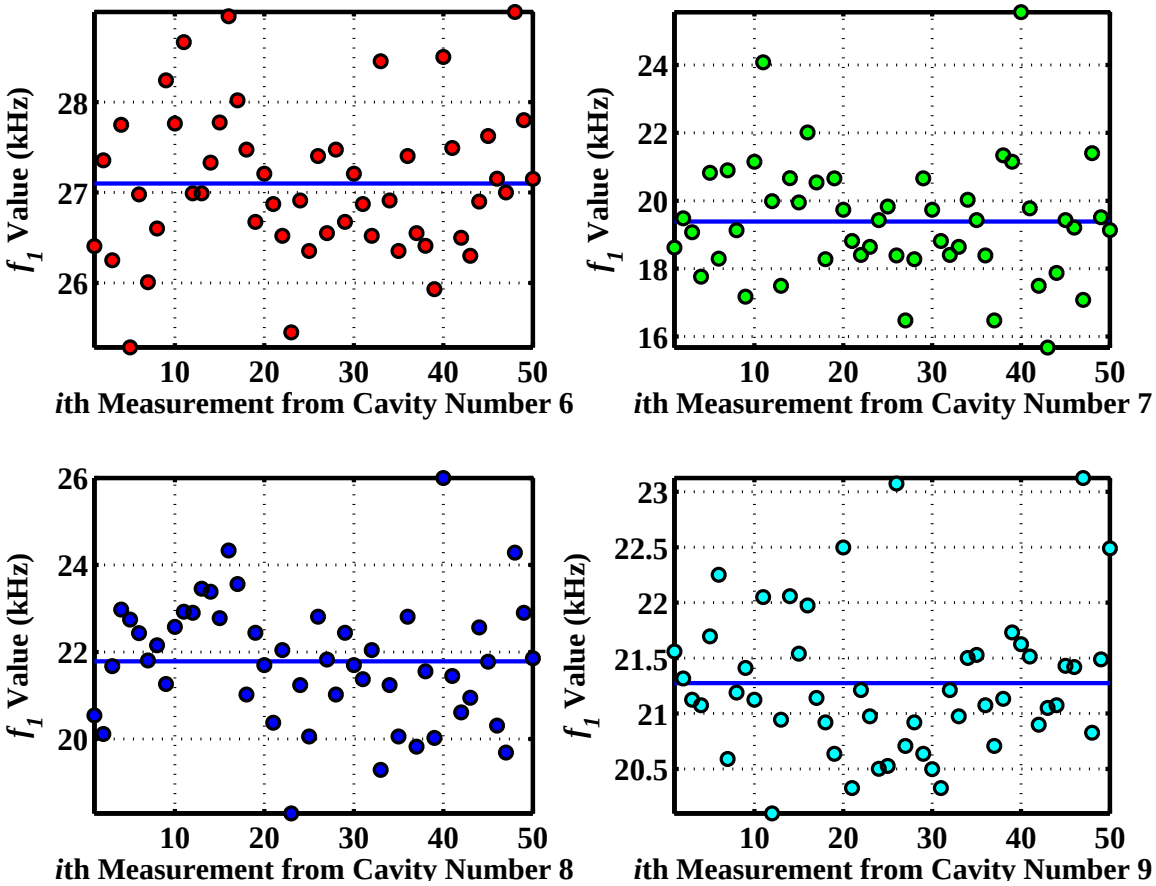

Figure 106: f_1 run sequence plots for the polypropylene parts (the horizontal line indicates the overall mean).

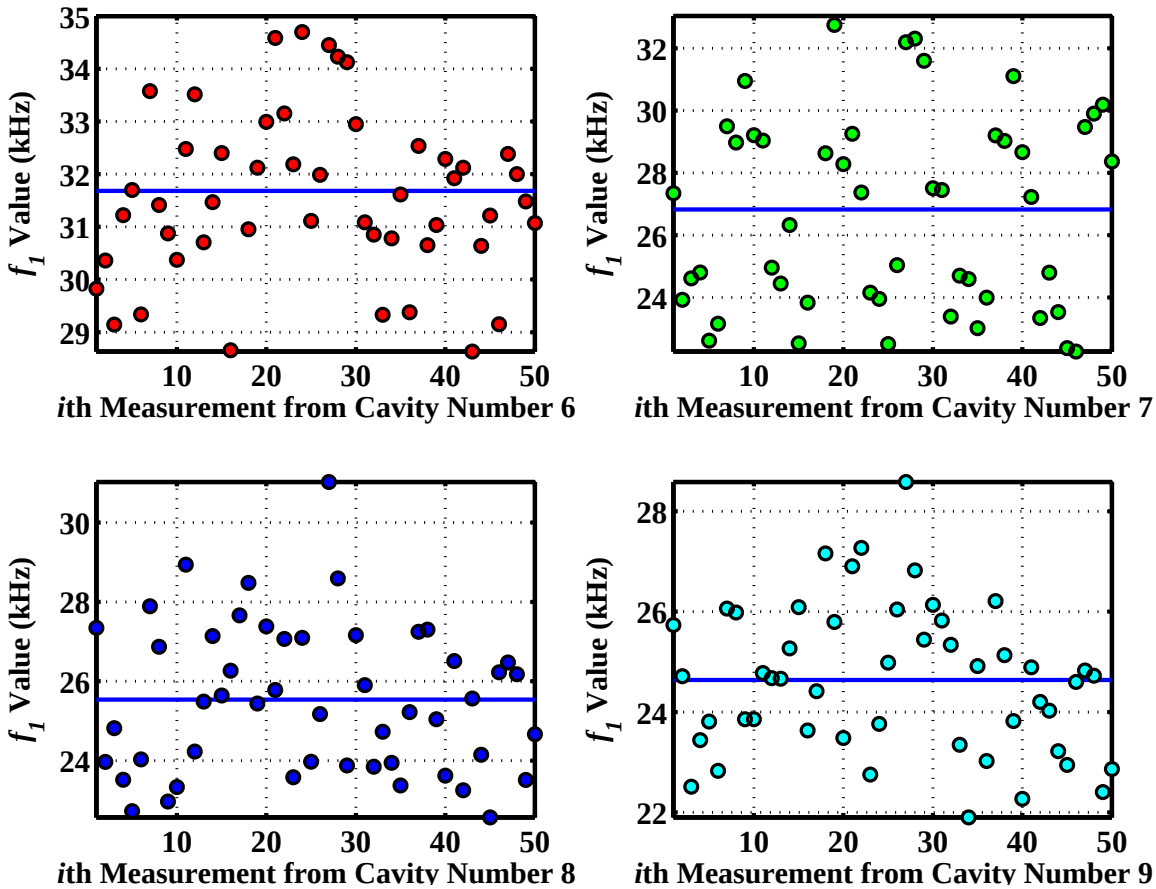

Figure 107: f_1 run sequence plots for the nylon composite parts (the horizontal line indicates the overall mean).

APPENDIX E

REPEATABILITY ANALYSIS PARTS DATA CHARTS

This appendix presents the experimental values obtained from the parts of §5.1.2.3. The individual f_1 values are presented for the neat PS, PP, and NN6 parts (see Table 3 for material descriptions), made from mold cavities 11, 12, and 13 (see Table 9 for cavity geometries).

Table 25: Individual f_1 values for the PS parts.

Measurement Number	f_1 Cavity Number 6	f_1 Cavity Number 7	f_1 Cavity Number 8	f_1 Cavity Number 9
1	30.78	28.12	25.62	22.25
2	30.96	27.99	25.33	21.04
3	31.15	28.34	26.06	22.11
4	31.00	28.80	26.24	23.55
5	30.52	28.12	25.13	21.66
6	30.94	28.28	25.59	22.58
7	30.21	28.39	26.51	22.54
8	30.22	28.63	27.22	22.12
9	30.18	28.42	26.86	23.50
10	29.62	27.80	26.32	23.93
11	29.20	27.14	25.77	23.16
12	29.35	27.25	25.94	23.45
13	28.66	27.10	25.44	23.29
14	29.25	27.54	25.74	23.91
15	29.47	27.44	26.05	24.17
16	29.77	28.30	27.03	23.38
17	29.42	27.55	26.08	23.92
18	28.91	28.21	27.37	23.24
19	29.70	28.05	26.29	22.74
20	29.74	27.45	25.93	23.45
21	29.32	27.20	24.23	20.89
22	29.63	28.05	26.20	22.62
23	31.55	27.71	26.86	25.06

Table 25: continued...

Measurement Number	f_1 Cavity Number 6	f_1 Cavity Number 7	f_1 Cavity Number 8	f_1 Cavity Number 9
24	31.16	29.03	27.31	24.70
25	31.17	27.79	27.43	24.45
26	32.53	30.47	28.15	26.63
27	31.63	29.73	27.81	25.21
28	32.03	29.03	27.90	26.22
29	31.79	28.60	26.74	24.14
30	32.03	30.24	27.57	24.91
31	32.60	30.14	27.84	26.00
32	30.58	28.84	27.80	25.41
33	30.16	27.69	27.40	24.92
34	31.56	29.46	27.49	24.81
35	29.99	27.18	26.83	24.74
36	31.07	27.62	26.42	23.58
37	30.33	27.78	27.80	25.48
38	30.50	28.07	26.41	23.09
39	29.84	26.47	26.36	24.30
40	32.21	29.94	27.19	24.43
41	30.32	27.84	27.40	25.56
42	30.57	30.01	27.97	26.34
43	30.24	27.46	26.72	24.87
44	30.89	29.62	27.99	25.89
45	31.94	28.73	26.67	23.34
46	30.78	30.02	27.74	26.33

Table 25: continued...

Measurement Number	f_1 Cavity Number 6	f_1 Cavity Number 7	f_1 Cavity Number 8	f_1 Cavity Number 9
47	30.42	28.48	23.34	24.81
48	30.58	28.30	25.93	24.17
49	29.74	29.03	28.15	23.09
50	29.47	27.79	26.06	22.62

Table 26: Individual f_1 values for the PP parts.

Measurement Number	f_1 Cavity Number 6	f_1 Cavity Number 7	f_1 Cavity Number 8	f_1 Cavity Number 9
1	26.41	18.62	20.54	21.56
2	27.36	19.48	20.12	21.32
3	26.25	19.07	21.68	21.13
4	27.75	17.76	22.98	21.08
5	25.29	20.83	22.75	21.70
6	26.98	18.29	22.43	22.25
7	26.01	20.90	21.81	20.59
8	26.60	19.13	22.15	21.19
9	28.24	17.17	21.26	21.41
10	27.76	21.15	22.58	21.13
11	28.66	24.08	22.93	22.05
12	26.99	19.99	22.90	20.10
13	26.99	17.49	23.45	20.95
14	27.33	20.67	23.38	22.06
15	27.78	19.95	22.78	21.54
16	28.95	22.01	24.33	21.98
17	28.02	20.54	23.56	21.14
18	27.48	18.28	21.02	20.92
19	26.68	20.66	22.44	20.64
20	27.21	19.74	21.70	22.50
21	26.87	18.82	20.38	20.33
22	26.52	18.41	22.05	21.21
23	25.45	18.64	18.29	20.98

Table 26: continued...

Measurement Number	f_1 Cavity Number 6	f_1 Cavity Number 7	f_1 Cavity Number 8	f_1 Cavity Number 9
24	26.91	19.43	21.24	20.50
25	26.35	19.83	20.06	20.53
26	27.40	18.39	22.81	23.07
27	26.55	16.48	21.83	20.71
28	27.48	18.28	21.02	20.92
29	26.68	20.66	22.44	20.64
30	27.21	19.74	21.70	20.50
31	26.87	18.82	21.38	20.33
32	26.52	18.41	22.05	21.21
33	28.45	18.64	19.29	20.98
34	26.91	20.03	21.24	21.50
35	26.35	19.43	20.06	21.53
36	27.40	18.39	22.81	21.07
37	26.55	16.48	19.83	20.71
38	26.41	21.34	21.56	21.13
39	25.93	21.15	20.03	21.73
40	28.50	25.56	26.00	21.63
41	27.49	19.78	21.45	21.52
42	26.50	17.50	20.61	20.90
43	26.30	15.68	20.95	21.05
44	26.90	17.88	22.57	21.08
45	27.63	19.43	21.78	21.43
46	27.15	19.21	20.31	21.42

Table 26: continued...

Measurement Number	f_1 Cavity Number 6	f_1 Cavity Number 7	f_1 Cavity Number 8	f_1 Cavity Number 9
47	27.00	17.08	19.69	23.13
48	29.00	21.40	24.29	20.83
49	27.80	19.52	22.90	21.49
50	27.15	19.14	21.86	22.49

Table 27: Individual f_1 values for the NN6 parts.

Measurement Number	f_1 Cavity Number 6	f_1 Cavity Number 7	f_1 Cavity Number 8	f_1 Cavity Number 9
1	32.40	28.29	25.41	23.52
2	30.15	24.85	23.85	25.04
3	30.37	24.67	25.20	22.95
4	30.55	24.73	23.19	23.45
5	32.00	22.46	22.29	23.89
6	30.56	23.05	24.47	23.67
7	32.56	31.40	26.42	25.92
8	29.20	30.35	27.24	24.91
9	33.06	30.11	23.49	22.84
10	30.71	29.41	23.57	23.74
11	34.54	27.68	27.77	26.90
12	29.59	26.17	27.19	24.74
13	32.53	23.95	27.13	25.66
14	31.34	25.53	26.16	23.88
15	34.27	22.74	25.58	24.52
16	31.25	25.24	27.15	25.91
17	35.56	30.89	27.67	26.51
18	31.65	32.58	27.18	25.77
19	32.42	33.87	24.43	25.49
20	30.52	30.20	25.58	25.00
21	34.29	27.38	28.21	24.47
22	35.11	23.08	24.99	25.07
23	31.62	26.62	25.70	25.41

Table 27: continued...

Measurement Number	f_1 Cavity Number 6	f_1 Cavity Number 7	f_1 Cavity Number 8	f_1 Cavity Number 9
24	34.26	23.95	24.71	24.37
25	30.39	23.39	23.88	24.93
26	33.96	25.08	25.07	25.30
27	32.83	30.35	28.90	27.70
28	30.62	30.41	29.60	23.95
29	35.91	29.30	25.30	25.08
30	33.74	32.34	26.07	22.46
31	30.81	27.22	26.99	24.55
32	30.37	24.51	23.53	23.40
33	31.13	23.31	25.26	22.03
34	29.18	25.24	24.62	22.12
35	31.63	23.67	22.27	22.86
36	31.15	23.06	24.48	23.59
37	34.23	30.85	27.47	25.53
38	31.45	28.54	27.31	23.89
39	31.89	30.20	23.72	22.46
40	30.87	29.52	24.44	23.60
41	31.39	26.88	25.57	24.03
42	29.52	24.07	24.08	23.85
43	28.67	23.58	24.97	22.08
44	29.69	23.85	25.24	21.62
45	31.10	22.41	22.58	24.29
46	28.56	23.64	24.60	23.15

Table 27: continued...

Measurement Number	f_1 Cavity Number 6	f_1 Cavity Number 7	f_1 Cavity Number 8	f_1 Cavity Number 9
47	32.29	30.72	28.14	25.92
48	30.99	29.82	26.29	24.08
49	32.75	30.31	24.71	22.77
50	31.44	28.50	25.21	24.45

APPENDIX F

PMMA-CNF PARTS DATA CHARTS

This appendix presents the experimental values obtained from the PMMA-CNF parts of §5.1.2.5. The individual f_1 values are presented for the neat PMMA, PR-21-5, PR-21-10, PR-24-5, and PR-24-10 materials (see Table 4 for material descriptions), made from mold cavities 11, 12, and 13 (see Table 13 for cavity geometries).

Table 28: Individual f_1 values for the Neat PMMA parts.

Part Number	Cavity 11 f_1 (kHz)	Cavity 12 f_1 (kHz)	Cavity 13 f_1 (kHz)
1	38.30	29.80	25.48
2	46.58	32.65	28.26
3	39.98	29.06	26.03
4	41.23	30.10	27.35
5	39.88	30.02	26.35
6	39.21	31.03	27.46
7	40.03	34.34	25.49
8	38.30	33.29	24.30
9	42.00	35.35	28.94
10	39.12	28.34	28.23

Table 29: Individual f_1 values for the PR-21-5 parts.

Part Number	Cavity 11 f_1 (kHz)	Cavity 12 f_1 (kHz)	Cavity 13 f_1 (kHz)
1	44.16	36.72	35.76
2	39.68	38.16	37.35
3	42.88	33.60	30.48
4	41.84	35.09	31.76
5	45.53	34.31	30.21
6	39.78	29.57	29.84
7	44.41	36.29	32.05
8	41.83	38.76	32.62
9	42.90	33.86	30.47
10	43.66	33.49	30.43

Table 30: Individual f_1 values for the PR-21-10 parts.

Part Number	Cavity 11 f_1 (kHz)	Cavity 12 f_1 (kHz)	Cavity 13 f_1 (kHz)
1	43.67	34.10	29.57
2	44.13	34.22	29.40
3	43.40	34.07	29.78
4	42.44	34.01	29.77
5	41.35	32.57	28.31
6	41.31	33.04	28.61
7	41.22	31.17	26.66
8	39.94	31.48	24.20
9	42.50	33.11	26.83
10	41.66	31.21	29.20

Table 31: Individual f_1 values for the PR-24-5 parts.

Part Number	Cavity 11 f_1 (kHz)	Cavity 12 f_1 (kHz)	Cavity 13 f_1 (kHz)
1	43.58	33.32	25.97
2	41.60	32.87	27.33
3	39.34	29.90	27.17
4	45.26	34.91	30.89
5	42.81	32.24	26.52
6	45.29	34.90	30.71
7	43.38	31.32	25.89
8	42.93	34.07	27.30
9	42.88	34.85	30.75
10	49.78	39.97	36.92

Table 32: Individual f_1 values for the PR-24-10 parts.

Part Number	Cavity 11 f_1 (kHz)	Cavity 12 f_1 (kHz)	Cavity 13 f_1 (kHz)
1	47.51	37.79	33.57
2	44.20	36.81	29.39
3	45.74	34.99	31.22
4	39.79	27.65	25.37
5	49.96	36.32	31.61
6	46.25	32.92	30.39
7	44.61	35.89	35.07
8	36.94	30.70	26.38
9	44.82	33.41	29.57
10	47.44	38.76	33.95

REFERENCES

[1] *DMA 2980 Dynamic Mechanical analyzer manual*, pp. 1–18. TA instruments, 1996.

[2] *ASTM E756-98, Standard test method for measuring vibration-damping properties of materials*. American Society for Testing and Materials, 1998.

[3] *Nanonindenter XP User Manual*, p. 56. MTS Systems Corp., 1999.

[4] *Manual on presentation of data and control chart analysis, 7th Edition*. American Society for Testing and Materials Committee E-11 on Quality and Statistics, 2002.

[5] *MikroMasch Cantilevers and Gratings Catalog (www.spmtips.com)*. MikroMash, February 2004.

[6] *Personal Communication (email)*. Veeco Instruments, 2004.

[7] *Veeco Probes Catalog, (www.veecoprobes.com)*. Veeco Instruments, 2004.

[8] Adams, D. P., Vasile, M. J., Benavides, G., and Campbell, A. N., "Micromilling of metal alloys with focused ion beam-fabricated tools," *Precision Engineering*, vol. 25, pp. 107–113, 2001.

[9] Adams, J. D., Parrott, G., Bauer, C., Sant, T., Manning, L., Jones, M., Rogers, B., McCorkle, D., and Ferrell, T. L., "Nanowatt chemical vapor detection with a self-sensing, piezoelectric microcantilever array," *Appl. Phys. Lett.*, vol. 83, pp. 3428–3430, 2003.

[10] Adams, R. D. and Bacon, D. G. C., "Measurement of the flexural damping capacity and dynamic youngs modulus of metals and reinforced plastics," *J. of Phys. D*, vol. 6, p. 2741, 1973.

[11] Agarwala, M., Klosterman, D., Osborne, N., Lightman, A., Dzugan, R., Rhodes, G., and Nelson, C., "Rapid fabrication of metal tooling using rapid prototyped ceramic pre-forms," in *American Ceramic Society 101st Annual Meeting and Exposition*, 1999.

[12] Ahmed, N., Nino, D. F., and Moy, V. T., "Measurement of solution viscosity by atomic force microscopy," *Rev. Sci. Instrum.*, vol. 72, pp. 2731–2734, 2001.

[13] Ahn, S. H., Montero, M., Odell, D., Roundy, S., and Wright, P. K., "Anisotropic material properties of fused deposition modeling ABS," *Rapid Prototyping*, vol. 8, pp. 248–257, 2002.

[14] Albrecht, T. R., Akamine, S., Carver, T. E., and Quate, C. F., "Microfabrication of cantilever styli for the atomic force microscope," *J. Vac. Sci. Technol. A*, vol. 8, pp. 3386–3396, 1990.

[15] Bain, C. D., Evall, J., and Whitesides, G. M., "Formation of monolayers by the coadsorption of thiols on gold: variation in the head group, tail group, and solvent," *J. Am. Chem. Soc.*, vol. 111, pp. 7155–7164, 1989.

[16] Bain, C. D., Troughton, E. B., Tao, Y. T., Evall, J., Whitesides, G. M., and Nuzzo, R. G., "Formation of monolayer films by the spontaneous assembly of organic thiols from solution onto gold," *J. Am. Chem. Soc.*, vol. 111, pp. 321–335, 1989.

[17] Bain, C. D. and Whitesides, G. M., "Formation of monolayers by the coadsorption of thiols on gold: variation in the length of the alkyl chain," *J. Am. Chem. Soc.*, vol. 111, pp. 7164–7175, 1989.

[18] Baller, M. K., *Microcantilever Sensor Arrays: Nanomechanics, Electronic Noses and DNA Chips*. PhD thesis, University of Basel, 2001.

[19] Bardeen, J. and Brattain, W. H., "The first transistor, a semiconductor triode," *Phys. Rev.*, vol. 74, p. 230, 1948.

[20] Barnes, J. R., Stephenson, R. J., Welland, M. E., Gerber, C., and Gimzewski, J. K., "Photothermal spectroscopy with femtojoule sensitivity using a micromechanical device," *Nature*, vol. 372, pp. 79–81, 1994.

[21] Battiston, F. M., Ramseyer, J. P., Lang, H. P., Baller, M. K., Gerber, C., Gimzewski, J. K., Meyer, E., and Güntherodt, H. J., "A chemical sensor based on a microfabricated cantilever array with simultaneous resonance-frequency and bending readout," *Sens. and Act. B*, vol. 77, pp. 122–131, 2001.

[22] Berger, R., Delamarche, E., Lang, P., Gerber, C., Gimzewski, J. K., Meyer, E., and Güntherodt, H. J., "Surface stress in the self-assembly of alkanethiols on gold," *Science*, vol. 276, pp. 2021–2023, 1997.

[23] Berger, R., Gerber, C., Gimzewski, J. K., Meyer, E., and Güntherodt, H. J., "Thermal analysis using a micromechanical calorimeter," *Appl. Phys. Lett.*, vol. 69, pp. 40–42, 1996.

[24] Bertsch, A., Jiguet, S., and Renaud, P., "Microfabrication of ceramic components by microstereolithography," *J. Micromech. Microeng.*, vol. 14, pp. 197–203, 2004.

[25] Binnig, G., Despont, M., Drechsler, U., Häberle, W., Lutwyche, M., Vettiger, P., Mamim, H. J., Chui, B. W., and Kenny, T. W., "Ultrahigh-density atomic force microscopy data storage with erase capability," *Appl. Phys. Lett.*, vol. 74:9, pp. 1329–1331, 1999.

[26] Binnig, G., Quate, C. F., and Gerber, C., "Atomic force microscope," *Phys. Rev. Lett.*, vol. 56, pp. 930–933, 1986.

[27] Binnig, G. and Rohrer, H., "Scanning tunneling microscopy– from birth to adolescence," *Rev. Mod. Phys.*, vol. 59:3, pp. 615–630, 1997.

[28] Binnig, G., Rohrer, H., Gerber, C., and Weibel, E., "Tunneling through a controllable vacuum gap," *Appl. Phys. Lett.*, vol. 40, pp. 178–180, 1982.

[29] Binning, G., Rohrer, H., Gerber, C., and Weibel, E., "Surface studies by scanning tunneling microscopy," *Phys. Rev. Lett.*, vol. 49, pp. 57–61, 1982.

[30] Bischoff, B. S. L. and Teichert, J., "Writing FIB implantation and subsequent anisotropic wet chemical etching for fabrication of 3D structures in silicon," *Sens. Act. A*, vol. 61, p. 369, 1997.

[31] Bland, D. R. and Lee, E. H., "Calculation of the complex modulus of linear viscoelastic materials from vibrating reed measurements," *J. Appl. Phys.*, vol. 26, pp. 1497–1503, 1955.

[32] Bohart, A., Collins, P., Faulk, S., Halvorson, C., McClellean, M., and Shillito, K., "Affordable, compact, research single point diamond turning machine," in *Proceedings of the ASPE*, vol. 22, pp. 184–186, 2000.

[33] Boskovic, S., Chon, J. W. M., Mulvaney, P., and Sader, J. E., "Rheological measurements using microcantilevers," *J. Rheol.*, vol. 46, pp. 891–899, 2002.

[34] Bowden, N., Terfort, A., Carbeck, J., and Whitesides, G. M., "Self-assembly of mesoscale objects into ordered two-dimensional arrays," *Science*, vol. 276, pp. 233–235, 1997.

[35] Box, G. E. P., Jenkins, G. M., and Reinsel, G. C., *Time Series Analysis: Forecasting and Control, 3rd Edition*. Prentice-Hall Inc., 1994.

[36] Brugger, J., Beljakovic, G., Despont, M., de Rooij, N. F., and Vettiger, P., "Silicon micro/nanomechanical device fabrication based on focused ion beam surface modification and KOH etching," *Microelectron. Eng.*, vol. 35, p. 401, 1997.

[37] Burnham, N. A., Chen, X., Hodges, C. S., Matei, G. A., Thoreson, E. J., Roberts, C. J., Davies, M. C., and Tendler, S. B., "Comparison of calibration methods for atomic-force microscopy cantilevers," *Nanotechnology*, vol. 14, pp. 1–6, 2003.

[38] Büstgens, B., Bacher, W., Bier, W., Ehnes, R., Maas, D., Ruprecht, R., Schomburg, W. K., and Keydel, L., "Micromembrane pump manufactured by molding," in *Proc. Fourth Int. Conf. on New Actuators*, (Bremen), pp. 86–90, June 1994.

[39] Butt, H. J. and Jaschke, M., "Calculation of thermal noise in atomic force microscopy," *Nanotechnology*, vol. 6, pp. 1–7, 1995.

[40] Callister, W. D., *Materials Science and Engineering: An Introduction*. New York, NY: John Wiley & Sons, fourth ed., 1997.

[41] Chakraborty, A. K. and Golumbfskie, A. J., "Polymer adsorption-driven self-assembly of nanostructures," *Annu. Rev. Phys. Chem.*, vol. 52, pp. 537–573, 2001.

[42] Champ, C. W. and Woodall, W. H., "Exact results for shewhart control charts with supplementary runs rules," *Technometrics*, vol. 29, pp. 393–399, 1987.

[43] Chen, G. Y., Thundat, T., Wachter, E. A., and Warmack, R. J., "Adsorption-induced surface stress and its effects on resonance frequency of microcantilevers," *J. Appl. Phys.*, vol. 77, pp. 3618–3622, 1995.

[44] Chen, L. and S.-C. Wong and, S. P., "Fracture properties of nanoclay-filled polypropylene," *J. Appl. Pol. Sci.*, vol. 88, pp. 3298–3305, 2003.

[45] Cherian, S. and Thundat, T., "Determination of adsorption-induced variation in the spring constant of a microcantilever," *Appl. Phys. Lett.*, vol. 80, pp. 2219–2221, 2002.

[46] Chou, S. Y., Krauss, P. R., and Renstrom, P. J., "Imprint of sub-25 nm vias and trenches in polymers," *Appl. Phys. Lett.*, vol. 67, pp. 3114–3116, 1995.

[47] Chui, B. W., Stowe, T. D., Kenny, T. W., Mamin, H. J., Terris, B. D., and Rugar, D., "Low-stiffness silicon cantilevers for thermal writing and piezoresistive readback with the atomic force microscope," *Appl. Phys. Lett.*, vol. 69:18, pp. 2767–2769, 1996.

[48] Chung, S., Hein, H., Pantenburg, J. M. F.-J., and Wallrabe, U., "LIGA technology today and its industrial applications," in *Proc. SPIEs Int. Conf. on Microrobotics and Microassembly*, vol. 4184, (Boston), pp. 44–55, Nov. 2000.

[49] Clarke, M., Pierse, M., Knuefermann, M., and Read, R., "New technology and novel design make sub-micron production practical," in *Proceedings of the ASPE*, vol. 22, p. 187, 2000.

[50] Cleveland, J. P., Manne, S., Bocek, D., and Hansma, P. K., "A nondestructive method for determining the spring constant of cantilevers for scanning force microscopy," *Rev. Sci. Instr.*, vol. 64(2), pp. 403–405, 1993.

[51] Clough, R. W., "The finite element method in plane stress analysis," in *Proceedings of the ASCE, Second Conference on Electronic Computation*, pp. 345–378, 1960.

[52] Colchero, J., Bielefeldt, H., Ruf, A., Hipp, M., Marti, O., and Mlynek, J., "Scanning force and friction microscopy," *Phys. Stat. Sol. (a)*, vol. 131, pp. 73–75, 1992.

[53] Cosserat, E. and Cosserat, F., *Theorie des Corps Deformables*. Hermann et Fils, 1909.

[54] Courant, R., "Variational method for the solution of problems of equilibrium and vibrations," *Bulletin of the American Mathematical Society*, vol. 49, pp. 1–23, 1943.

[55] Creigton, T. E., *Proteins: Structures and Molecular Properties*. Freeman, 1983.

[56] Cumpson, P. J., Clifford, C. A., and Hedley, J., "Quantitative analytical atomic force microscopy: a cantilever reference device for easy and accurate AFM spring-constant calibration," *Meas. Sci. Technol.*, vol. 15, pp. 1337–1346, 2004.

[57] Datskos, P. G., Thundat, T., and Lavrik, N. V., *Micro and nanocantilever sensors*. American Publishers, 2004.

[58] Delamarche, E., Bernard, A., Schmid, H., Michel, B., and Biebuyck, H. A., "Patterned delivery of immunoglobulins to surfaces using microfluidic networks," *Science*, vol. 276, pp. 779–781, 1997.

[59] Ding, J. N., Meng, Y. G., and Wen, S. Z., "Specimen size effect on mechanical properties of polysilicon microcantilever beams measured by deflection using a nanoindenter," *Materials Science and Engineering B*, vol. 83, pp. 42–47, 2001.

[60] Djurić, Z., "Noise sources in microelectromechanical systems," in *Proc. 22nd Int. Conf. on Microelctromechanical Systems*, vol. 1, pp. 85–96, 2000.

[61] Doiron, T. and Beers, J. S., *The Gauge Block Handbook*, pp. 13–15. NIST Monograph 180, U.S. Dept. of Commerce, National Inst. of Standards and Tech. (NIST), 1995.

[62] Döpper, J., Clemens, M., Kämper, W. E. K.-P., and Lehr, H., "Development of low-cost injection molded micropumps," in *Actuator96: Proc. Fifth Int. Conf. on New Actuators*, pp. 37–40, 1996.

[63] Dowling, N. E., *Mechanical Behavior of Materials 2nd Edition*. Upper Saddle River, NJ: Prentice Hall, 1999.

[64] Edvardsson, S., Ojamäe, L., and Thomas, J. O., "A study of vibrational modes in $Na^{(+)}$ beta-alumina by molecular dynamics simulation," *J. Phys. C.*, vol. 6, p. 1319, 1994.

[65] Ehrfeld, W., Bley, P., Götz, F., Hagmann, P., Maner, A., Mohr, J., Moser, H. O., Münchmeyer, D., Schelb, W., Schmidt, D., and Becker, E. W., "Fabrication of microstructures using the LIGA process," in *Proc. IEEE Micro Robots and Teleoperators Workshop- IEEE Catalogue Number 87TH02048*, (Hyannis, MA), 1987.

[66] Elkins, K., Janak, C., Nordby, H., Gray, R. W., Bøhn, J. H., and Baird, D. G., "Soft elastomers for fused deposition modeling," in *Proc. 8th. Solid Freeform Fabrication Symposium*, pp. 441–448, 1997.

[67] Ellis, R. W. and Smith, C. W., "A thin plate analysis and experimental evaluation of couple stress effects," *Experimental Mechanics*, vol. 7, pp. 372–380, 1968.

[68] Engle, R., "Autoregressive conditional heteroskedasticity with estimates of the variance of united kingdom inflation," *Econometrica*, vol. 50, pp. 987–1007, 1982.

[69] Ensz, M. T. and Griffith, M. L., "Critical issues for functionally graded material deposition by laser engineered net shaping (LENS)," in *Proc. of the 2002 MPIF Laser Metal Deposition Conference*, 2002.

[70] Eringen, A. C., *Mechanics of micromorphic continua*, pp. 18–33. Springer Verlag, 1968.

[71] Erlandsson, R., McClelland, G. M., Mate, C. M., and Chiang, S., "Atomic force microscopy using optical interferometry," *J. Vac. Sci. Tech. A*, vol. 6:2, pp. 266–270, 1988.

[72] Espinosa, H. D., Prorok, B. C., Peng, B., Kim, K. H., Moldovan, N., Auciello, O., Carlisle, J. A., Gruen, D. M., and Mancini, D. C., "Mechanical properties of ultrananocrystalline diamond thin films relevant to MEMS devices," *Experimental Mechanics*, vol. 43, pp. 256–268, 2003.

[73] Fahrenberg, J., Bier, W., Maas, D., Menz, W., Ruprecht, R., and Schomburg, W. K., "Microvalve system fabricated by thermoplastic molding," *J. Micromech. Microeng.*, vol. 5, pp. 169–171, 1995.

[74] Fan, T. H. and Fedorov, A. G., "Visualization of atomic force microscopy from molecular dynamics simulations," *ASME Journal of Heat Transfer*, vol. 123, p. 619, 2001.

[75] Fang, F. Z. and Liu, Y. C., "On minimum exit-burr in micro cutting," *J. Micromech. Microeng.*, vol. 14, pp. 984–988, 2004.

[76] Fang, F. Z., Wu, H., Liu, X. D., Liu, Y. C., and Ng, S. T., "Tool geometry study in micromachining," *J. Micromech. Microeng.*, vol. 13, pp. 726–731, 2003.

[77] Ferry, J. D., *Viscoelastic Properties of Polymers*, pp. 41–43. John Wiley & Sons, 1980.

[78] Feynman, R. P., *There's Plenty of Room at the Bottom.* Speech given at the Annual Meeting of the American Physical Society, Pasadena, CA., December 1959.

[79] Fleck, N. A. and Hutchinson, J. W., *Strain gradient plasticity*, vol. 33, pp. 295–361. Academic Press, 1997.

[80] Fleck, N. A. and Hutchinson, J. W., "A reformulation of strain gradient plasticity," *J. Mech. Phys. Solids*, vol. 49, pp. 2245–2271, 2001.

[81] Friedrich, C. R. and Vasile, M. J., "Development of the micromilling process for high aspect ratio microstructures," *J. Microelectromech. Sys.*, vol. 5, pp. 33–38, 1996.

[82] Fritz, J., Baller, M. K., Lang, H. P., Strunz, T., Meyer, E., Güntherodt, H. J., Delamarche, E., Gerber, C., and Gimzewski, J. K., "Stress at the solid-liquid interface of self-assembled monolayers on gold investigated with a nanomechanical sensor," *Langmuir*, vol. 16, pp. 9694–9696, 2000.

[83] Gardner, J. W., *Microsensors: Principles and Applications.* John Wiley & Sons, 1994.

[84] Gauthier, R. D., *Analytical and experimental investigations in linear isotropic micropolar elasticity.* PhD thesis, University of Colorado, 1974.

[85] Genolet, G., Brugger, J., Despong, M., Dreschler, U., Vettiger, P., Rooji, N. F. D., and Anselmetti, D., "Soft, entirely photoplastic probes for scanning force microscopy," *Rev. Sci. Instrum.*, vol. 70(5), pp. 2398–2410, 1999.

[86] Genolet, G., Despong, M., Vettiger, P., Anselmetti, D., and Rooji, N. F. D., "All-photoplastic, soft cantilever cassette probe for scanning force microscopy," *J. Vac. Sci. Tech. B.*, vol. 18(2), pp. 617–620, 2000.

[87] Gimzewski, J. K., Gerber, C., Meyer, E., and Schlittler, R. R., "Observation of a chemical reaction using a micromechanical sensor," *Chem. Phys. Lett.*, vol. 28, pp. 589–594, 1994.

[88] Göddenhenrich, T., Lemke, H., Hartmann, U., and Heiden, C., "Force microscope with capacitive displacement detection," *J. Vac. Sci. Tech. A*, vol. 8:1, p. 383, 1990.

[89] Godin, M., Williams, P. J., Tabard-Cossa, V., Laroche, O., Beaulieu, L. Y., Lennox, R. B., and Gruütter, P., "Surface stress, kinetics, and structure of alkanethiol self-sssembled monolayers," *Langmuir*, vol. 20, pp. 7090–7096, 2004.

[90] Goll, C., Bacher, W., Büstgens, B., Maas, D., Menz, W., and Schomburg, W. K., "Microvalves with bistable buckled polymer diaphragms," *J. Micromech. Microeng.*, vol. 6, pp. 77–79, 1996.

[91] Goll, C., Bacher, W., Büstgens, B., Maas, D., R, R. R., and Schomburg, W. K., "Electrostatically actuated polymer microvalve equipped with a movable membrane electrode," *J. Micromech. Microeng.*, vol. 7, pp. 224–226, 1997.

[92] Green, C. P., Lioe, H., Cleveland, J. P., Proksch, R., Mulvaney, P., and Sader, J. E., "Normal and torsional spring constants of atomic force microscope cantilevers," *Rev. Sci. Intrum.*, vol. 75, pp. 1988–1996, 2004.

[93] Griffith, M. L., Schlienger, M. E., Atwood, C. L., Romero, J. A., Smugeresky, J. E., Harwell, L. D., and Greene, D. L., "Tooling fabrication using laser engineered net shaping," in *ASME International Mechanical Engineering Congress and Exposition*, 1996.

[94] Hagan, M. F., Majumdar, A., and Chakraborty, A. K., "Nanomechanical forces generated by surface grafted DNA," *J. Phys. Chem. B*, vol. 106, pp. 10163–10173, 2002.

[95] Hagmann, P., W, W. E., and Vollmer, H., "Fabrication of microstructures with extreme structural heights by reaction injection molding," in *First Meeting of the European Polymer Federation European Symp. on Polymeric Materials–paper EPD05*, (Lyon, France), Sept. 1987.

[96] Hannan, R. B. W., Karlsons, D., and Lurie, M., "Embossed hologram motion pictures for television playback," *Appl. Opt.*, vol. 9, pp. 2283–2290, 1970.

[97] Hansen, A. G., Boisen, A., and Ulstrup, J., "Adsorption of biomolecules on microcantilevers," in *Tokyo-2001: Scanning Probe Microscopy, Sensors and Nanostructures*, 2001.

[98] Hansen, A. G., Mortensen, M. W., Andersen, J. E. T., Ulstrup, J., Kühle, A., Garnæs, J., and Boisen, A., "Stress formation during self-assembly of alkanethiols on differently pre-treated gold surfaces," *Probe Microscopy*, vol. 2, pp. 139–149, 2001.

[99] Hansen, O. and Boisen, A., "Noise in piezoresistive atomic force microscopy," *Nanotechnology*, vol. 10, pp. 51–60, 1999.

[100] Holbery, J. D., Eden, V. L., Sarikaya, M., and Fisher, R. M., "Experimental determination of scanning probe microscope cantilever spring constants utilizing a nanoindentation apparatus," *Rev. Sci. Instr.*, vol. 71, pp. 3769–3776, 2000.

[101] Hongming, M., Zengb, J., Realff, M. L., Kumar, S., and Schiraldi, D. A., "Processing, structure, and properties of fibers from polyester/carbon nanofiber composites," *Composites Science and Technology*, vol. 63, pp. 1617–1628, 2003.

[102] Huang, J. C., "Carbon black filled conducting polymers and polymer blends," *Advances in Polymer Technology*, vol. 21, pp. 299–313, 2002.

[103] Hull, C. W., "Apparatus for production of three-dimensional objects by stereolithography," *United States Patent Number 4,575,330*, 1985.

[104] Hutley, M. C., *Diffraction Gratings*. Academic, New York, 1982.

[105] Hutter, J. L. and Bechhoefer, J., "Calibration of atomic-force microscope tips," *Rev. Sci. Instr.*, vol. 64(7), pp. 1868–1873, 1993.

[106] Ikuta, K., Maruo, S., and Kojima, S., "New micro stereo lithography for freely movable 3d micro structure," in *Proc. of IEEE International Workshop on Micro Electro Mechanical Systems (MEMS98)*, pp. 290–295, 1998.

[107] Ilic, B., Czaplewski, D., Zalalutdinov, M., and Craighead, H. G., "Single cell detection with micromechanical oscillators," *J. Vac. Sci. Tech. B*, vol. 19, pp. 2825–2828, 2001.

[108] Itakuraa, A. N., Berger, R., Narushima, T., and Kitajima, M., "Low-energy ion-induced tensile stress of self-assembled alkanethiol monolayers," *J. Appl. Phys.*, vol. 80, pp. 3712–3714, 2002.

[109] Jeffrey, A., *Advanced Engineering Mathematics*, p. 799. Harcourt, 2001.

[110] Jia, Z. X., Zhang, J. H., and Ai, X., "Ultrasonic vibration pulse electro-discharge machining of holes in engineering ceramics," *J. Mater. Process. Technol.*, vol. 53, pp. 811–6, 1995.

[111] Jiang, J., Callender, C. L., Noad, J. P., Walker, R. B., Mihailov, S. J., Ding, J., and Day, M., "All-polymer photonic devices using excimer laser micromachining," *IEEE Photonics Technology Letters*, vol. 16:2, pp. 509–511, 2002.

[112] Johnson, G. C., Jones, P. T., and Howe, R. T., "Materials testing for MEMS: Needs, techniques, and results," *Proc. SPIE*, vol. 3874, pp. 94–101, 1999.

[113] Judson, E. A., Hill, D. N., Young, R. A., Cagle, J. R., Lackey, W. J., Carter, W. B., and Barefield, E. K., "An analysis of preferred orientation in yba2cu3o7-x superconducting films deposited by CVD on single-crystal and polycrystalline substrates," *Powder Diffraction*, vol. 9:4, pp. 250–259, 1994.

[114] Kaldor, S. K. and Noyan, I. C., "Differentiating between elastically bent rectangular beams and plates," *J. Appl. Phys.*, vol. 80, pp. 2284–2286, 2002.

[115] Kaschner, R., Schöne, M., Seifert, G., and Pastore, G., "Ab initio simulations of liquid systems: concentration dependence of the electric conductivity of nasn alloys," *J. Phys.: Condens. Matter*, vol. 8, pp. L653–L657, 1996.

[116] Kathuria, Y. P., "Microstructuring by selective laser sintering of metallic powder," *Surf. Coating Technol.*, vol. 116-119, pp. 643–647, 1999.

[117] Kawata, S., Sun, H. B., Tanaka, T., and Takada, K., "Finer features for functional microdevices," *Nature*, vol. 412, pp. 697–698, 2001.

[118] Khaled, A.-R. A., Vafai, K., Yang, M., Zhang, X., and Ozkan, C., "Analysis, control and augmentation of microcantilever deflections in biosensing systems," *Sens. Act. B*, vol. 94, pp. 103–115, 2003.

[119] Kiewit, D. A., "Microtool fabrication by etch pit replication," *Rev. Sci. Instrum.*, vol. 44, pp. 1741–1742, 1973.

[120] Kim, E., Xia, Y., and Whitesides, G. M., "Micromolding in capillaries: Applications in materials science," *J. Am. Chem. Soc.*, vol. 118, pp. 5722–5731, 1996.

[121] Klosterman, D., Chartoff, R., Agarwala, M., Fiscus, I., Murphy, J., Cullen, S., and Yeazell, M., "Direct fabrication of polymer composite structures with curved LOM," in *Solid Freeform Fabrication Symposium, University of Texas at Austin*, 1999.

[122] Knop, K., "Color pictures using the zero diffraction order of phase grating structures," *Opt. Commun.*, vol. 18, pp. 298–303, 1976.

[123] Kodama, H., "Automatic method for fabricating a three-dimensional plastic model with photo-hardening polymer," *Rev. Sci. Instr.*, vol. 52, pp. 1770–1773, 1981.

[124] Koiter, W. T., "Couple stresses in the theory of elasticity I and II," *Proc. K. Ned. Akad. Wet.(B)*, vol. 67, pp. 17–44, 1964.

[125] Kremer, D., Lebrun, J. L., Hosari, B., and Moisan, A., "Effects of ultrasonic vibrations on the performance in EDM," *Annals of the CIRP*, vol. 38:1, pp. 199–202, 1989.

[126] Kremer, D., Lhiaubet, C., and Moisan, A., "A study of the effects of synchronizing ultrasonic vibrations with pulses in EDM," *Annals of the CIRP*, vol. 40:1, pp. 211–214, 1991.

[127] Kröner, E., "On the physical reality of torque stresses in continuum mechanics," *Int. J. Engng. Sci.*, vol. 1, pp. 261–278, 1963.

[128] Kuo, C. L., Masuzawa, T., and Fujino, M., "High-precision micronozzle fabrication," *IEEE Micro Electro Mechanical Systems*, pp. 116–121, 1992.

[129] L. Ojamäe, K. H. and Probst, M., "The OH stretching frequency in liquid water simulations: The classical error," *Chem. Phys. Lett.*, vol. 191, p. 500, 1992.

[130] Lackey, W. J., Hanigofsky, J. A., Hardin, R. D., and Prasad, A., "Continuous fabrication of sic fiber tows by chemical vapor deposition," *J. Amer. Cer. Soc.*, pp. 1564–1570, 1995.

[131] Lackey, W. J., Vaidyaraman, S., and More, K. L., "Laminated c-sic matrix composites produced by CVI," *J. Amer. Cer. Soc.*, vol. 80:1, pp. 113–116, 1997.

[132] Lakes, R. S., "Size effects and micromechanics of a porous solid," *J. Materials Science*, vol. 18, pp. 2572–2581, 1983.

[133] Lam, D. C. C., Yang, F., Chong, A. C. M., Wang, J., and Tong, P., "Experiments and theory in strain gradient elasticity," *J. Mech. Phys. Solids*, vol. 51, pp. 1477–1508, 2003.

[134] Langen, H. H., Masuzawa, T., and Fujino, M., "Modular method for microparts machining and assembly with self-alignment," *Annals of the CIRP*, vol. 44, pp. 173–176, 1995.

[135] Lee, J. H., Kim, T. S., and Yoon, K. H., "Effect of mass and stress on resonant frequency shift of functionalized $\mathrm{pb(zr_{0.52}ti_{0.48})\ o_3}$ thin film microcantilever for the detection of c-reactive protein," *Appl. Phys. Lett.*, vol. 84, pp. 3187–3189, 2004.

[136] Lee, L. P., Berger, S. A., Liepmann, D., and Pruitt, L., "High aspect ratio polymer microstructures and cantilevers for biomems using low energy ion beam and photolithography," *Sens. Act. A*, vol. 71, pp. 144–149, 1998.

[137] Lee, M., Moon, S., Hatano, C. P., and Grigoropoulos, C. P., "Ultra-large lateral grain growth by double laser recrystallization of a-si films," *Appl. Phys. A*, vol. 73, pp. 317–322, 2001.

[138] Lee, S. H. and Dornfeld, D. A., "Precision laser deburring and acoustic emission feedback," *J. Manuf. Sci. Engng., Trans. ASME*, vol. 123:2, pp. 356–364, 2001.

[139] Li, J., Cassell, A. M., and Dai, H., "Carbon nanotubes as AFM tips: measuring DNA molecules at the liquid/solid interface," *Surf. Interf. Anal.*, vol. 28, pp. 8–11, 1999.

[140] Li, Y. Q., Tao, N. J., Pan, J., Garcia, A. A., and Lindsay, S. M., "Direct measurement of interaction forces between colloidal particles using the scanning force microscope," *Langmuir*, vol. 9, pp. 637–641, 1993.

[141] Lillehei, P. T., Poggi, M. A., Polk, B. J., Smith, J. A., and Bottomley, L. A., "Plastic tip arrays for force spectroscopy," *Anal. Chem.*, vol. 76, pp. 3861–3863, 2004.

[142] Lindholm, U. S., Kana, D. D., Chu, W. H., and Abramson, H. N. *J. Ship Res.*, vol. 9, p. 11, 1965.

[143] Lindsey, J. S., "Self-assembly in synthetic routes to molecular devices. biological principles and chemical perspectives: A review," *New J. Chem.*, vol. 15, pp. 153–180, 1991.

[144] Liu, F., Zhang, Y., and Ou-Yang, Z. C., "Flexoelectric origin of nanomechanic deflection in DNA microcantilever system," *Biosensors and Bioelectronics*, vol. 18, pp. 655–660, 2003.

[145] Lotz, B., "Phase transitions and structure of crystalline polymers," *Physical Sciences Information Gateway (http://www.psigate.ac.uk/roads/cgi-bin/psifullrecord.pl?handle=1007397971-15674)*, 2000.

[146] Lu, P., Shen, F., OShea, S. J., Lee, K. H., and Ng, T. Y., "Analysis of surface effects on mechanical properties of microcantilevers," *Mater. Phys. Mech.*, vol. 4, pp. 51–55, 2001.

[147] Lu, Z. and Yoneyama, T., "Micro cutting in the micro lathe turning system," *Int. J. Machine Tools Manufact.*, vol. 39, pp. 1171–1183, 1999.

[148] M, A., Cherian, S., Hedden, D., and Thundat, T., "Manipulation and controlled amplification of brownian motion of microcantilever sensors," *Appl. Phys. Lett.*, vol. 78, pp. 1637–1639, 2001.

[149] Madou, M., *Fundamentals of Microfabrication*. CRC Press, 1997.

[150] Maluf, N., *An Introduction to Microelectromechanical Systems Engineering*. Artech House, 1999.

[151] Malvern, L. E., *Introduction to the Mechanics of a Continuous Medium*, p. 280. Prentice-Hall, 1969.

[152] Mamim, H. J., "Thermal writing using a heated atomic force microscope tip," *Appl. Phys. Lett.*, vol. 69:3, pp. 433–435, 1996.

[153] Mananlis, S. R., Minne, S. C., Atalar, A., and Quate, C. F., "Interdigital cantilevers for atomic force microscopy," *Appl. Phys. Lett.*, vol. 69:25, pp. 3944–3946, 1996.

[154] Manias, E., Chen, J., Fang, N., and Zhang, X., "Polymeric micromechanical components with tunable stiffness," *Appl. Phys. Lett.*, vol. 79:11, pp. 1700–1702, 2001.

[155] Martin, J., Bacher, W., Hagena, O. F., and Schomburg, W. K., "Strain gauge pressure and volume-flow transducers made by hermoplastic molding and membrane transfer," in *Proc. Int. Workshop on Micro Electro Mechanical Systems, MEMS 1998*, (Heidelberg), pp. 361–366, Jan. 1998.

[156] Martin, Y., Williams, C. C., and Wickramasinghe, H. K., "Atomic force microscopeforce mapping and profiling on a sub 100-Å scale," *J. Appl. Phys.*, vol. 61:10, pp. 4723–4729, 1987.

[157] Marzolin, C., Smith, S. P., Prentiss, M., and Whitesides, G. M., "Fabrication of glass microstructures by micro-molding of sol-gel precursors," *Adv. Mater.*, vol. 10, pp. 571–574, 1998.

[158] Masuzawa, T., "Wire electro-discharge grinding for micro-machining," *Annals of the CIRP*, vol. 34, pp. 434–434, 1985.

[159] Masuzawa, T., Fujino, M., Kobayashi, K., and T, T. S., "Study on micro-hole drilling by EDM," *Bull. Jpn. Soc. Precis. Eng.*, vol. 20:2, pp. 117–120, 1985.

[160] Masuzawa, T., Kuo, C. L., and Fujino, M., "A combined electrical machining process for micronozzle fabrication," *Annals of the CIRP*, vol. 43, pp. 189–192, 1994.

[161] Masuzawa, T. and Tonshoff, H. K., "Three-dimensional micromachining by machine tools," *Annals of the CIRP*, vol. 46, pp. 621–628, 1997.

[162] Maxwell, J., Larsson, K., Boman, M., Hooge, P., Williams, K., and Coane, P., "Rapid prototyping of functional three-dimensional microsolenoids and electromagnets by high-pressure laser chemical vapor deposition," *Solid Freeform Fabrication*, pp. 529–536, 1998.

[163] McCormick, R. M., Alonso-Amigo, R. J. N. M. G., Benvegnu, D. J., and Hooper, H. H., "Microchannel electrophoretic separations of dna in injection-molded plastic substrates," *Ann. Chem.*, vol. 69, pp. 2626–2630, 1997.

[164] McDaniel, J. G., Dupont, P., and Salvino, L., "A wave approach to estimating frequency-dependent damping under transient loading," *Journal of Sound and Vibration*, vol. 231, pp. 433–449, 2000.

[165] McFarland, A. W., "Production and analysis of injection molded microoptics components," Master's thesis, The George W. Woodruff School of Mechanical Engineering, Georgia Institute of Technology, 2002.

[166] McFarland, A. W. and Colton, J. S., "Design and demonstration of a thermoplastic micromolding apparatus," *Journal of Microelectromechanical Systems*, submitted, 2004.

[167] McFarland, A. W. and Colton, J. S., "Investigation of length scale dependence in plate stiffness with relevance to microcantilever sensors," *Journal of Microelectromechanical Systems*, submitted, 2004.

[168] McFarland, A. W., Doyle, M. J., Bottomley, L. A., Poggi, M. A., and Colton, J. S., "Influence of surface stress on the resonant behavior of microcantilevers," *Applied Physics Letters*, submitted, 2004.

[169] McFarland, A. W., Poggi, M. A., Bottomley, L. A., and Colton, J. S., "Injection molded thermoplastic polymer scanning probe microscopy probes," *in prep.*, 2004.

[170] McFarland, A. W., Poggi, M. A., Bottomley, L. A., and Colton, J. S., "Injection molding of high aspect ratio micro-scale thickness polymeric microcantilevers," *Nanotechnology*, vol. 15, pp. 1628–1632, 2004.

[171] McFarland, A. W., Poggi, M. A., Bottomley, L. A., and Colton, J. S., "Plastic BIO-MEMS sensors," in *Proceedings of ANTEC2004*, (Chicago, IL), pp. 3717–3721, 2004.

[172] McFarland, A. W., Poggi, M. A., Bottomley, L. A., and Colton, J. S., "Production and characterization of polymer microcantilevers," *Rev. Sci. Instrum.*, vol. 75, pp. 2756–2758, 2004.

[173] McFarland, A. W., Poggi, M. A., Bottomley, L. A., and Colton, J. S., "Characterization of microcantilevers solely by frequency response acquisition," *J. Micromech. Microengng.*, submitted, 2004.

[174] McFarland, A. W. and Colton, J. S., "Production and analysis of injection molded micro-optics components," *Polymer Engineering and Science*, vol. 44, pp. 564–579, 2004.

[175] McKendry, R., Zhang, J., Arntz, Y., Strunz, T., Hegner, M., Lang, H. P., Baller, M. K., Certa, U., Meyer, E., Güntherodt, H.-J., and Gerber, C., "Multiple label-free biodetection and quantitative DNA-binding assays on a nanomechanical cantilever array," in *Proc. National Acad. Science*, vol. 99, pp. 9783–9788, 2002.

[176] McKeown, P. A., "From micro to nano-machining towards the nanometre era," *Sensor Review*, vol. 16:2, pp. 4–10, 1996.

[177] Meirovitch, L., *Elements of vibration analysis, 2^{nd} Edition*, pp. 125–126. McGraw Hill, 1986.

[178] Mindlin, R. D., "Micro-structure in linear elasticity," *Arch. Rational Mech. Anal.*, vol. 16, pp. 51–78, 1964.

[179] Mindlin, R. D., "Second gradient of strain and surface tension in linear elasticity," *Int. J. Solids Struct.*, vol. 1, pp. 417–438, 1965.

[180] Mindlin, R. D., "Stress functions for a cosserat continuum," *Int. J. Solids and Struct.*, vol. 1, pp. 265–271, 1965.

[181] Mindlin, R. D. and Tiersten, H. F., "Effects of couple-stresses in linear elasticity," *Arch. Rational Mech. Anal.*, vol. 11, pp. 415–448, 1962.

[182] Minne, S. C., Yaralioglu, G., Manalis, S. R., Adams, J. D., Zesch, J., Atalar, A., and Quate, C. F., "Automated parallel high speed atomic force microscopy," *Appl. Phys. Lett.*, vol. 72, pp. 2340–2342, 1998.

[183] Mishima, N., Ashida, K., Tanikawa, T., Maekawa, H., Kaneko, K., and Tanaka, M., "Micro-factory and a design evaluation method for miniature machine tools," in *Proc. of Int. Workshop on Microfactories*, pp. 155–158, 2000.

[184] Mishra, P. K., *Nonconventional Machining*, p. 89. Narosa Publishing House, 1997.

[185] Miyatani, T. and Fujihira, M., "Calibration of surface stress measurements with atomic force microscopy," *J. Appl. Phys.*, vol. 81, pp. 7099–7115, 1997.

[186] Mohr, J., "LIGA- a technology for fabricating microstructures and microsystems," *Sensors Mater.*, vol. 10, pp. 363–373, 1998.

[187] Monneret, S., C, C. P., and Gall, H. L., "Micro-scale rapid prototyping by stereolithography," *8th IEEE Int. Conf. on Emerging Technologies and Factory Automation (ETFA 2001)*, vol. 2, pp. 299–304, 2001.

[188] Moore, G. E., "Cramming more components onto integrated circuits," *Electronics*, vol. 38:8, 1965.

[189] Mühlhaus, H., *Continuum models for materials with micro-structure*, pp. 1–22. John Wiley & Sons, 1995.

[190] Nakano, M. and Nishida, N., "Contact printing method utilizing heated photoresist adhesive property for hologram copying," *Appl. Opt.*, vol. 18, pp. 3073–3074, 1979.

[191] Nakao, M. and Hatamura, Y., "A tabletop factory to fabricate micromachines, nano manufacturing world," in *Proceedings of the ASPE*, vol. 14, pp. 74–79, 1996.

[192] Neter, J., Kutner, M. H., Wasserman, W., and Nachtsheim, C. J., *Applied Linear Statistical Models, 4^{th} Edition.* R D Irwin Inc., 1996.

[193] Neubauer, G., Cohen, S. R., McClelland, G. M., Horn, D., and Mate, C. M., "Force microscopy with a bidirectional capacitance sensor," *Rev. Sci. Instrum.*, vol. 61, pp. 2296–2308, 1990.

[194] Nilsson, S. G., Sarwe, E. L., and Montelius, L., "Fabrication and mechanical characterization of ultrashort nanocantilevers," *Appl. Phys. Lett.*, vol. 83, pp. 990–992, 2003.

[195] Nuzzo, R. G., Dubois, L. H., and Allara, D. L., "Fundamental studies of microscopic wetting on organic surfaces. 1. Formation and structural characterization of a self-consistent series of polyfunctional organic monolayers," *J. Am. Chem. Soc.*, vol. 112, pp. 558–569, 1990.

[196] Oden, P. I., Chen, G. Y., Steele, R. A., Warmack, R. J., and Thundat, T., "Viscous drag measurements utilizing microfabricated cantilevers," *Appl. Phys. Lett.*, vol. 68, pp. 3814–3816, 1996.

[197] Oden, P. I., Datskos, P. G., Thundat, T., and Warmack, R. J., "Uncooled thermal imaging using a piezoresistive microcantilever," *Appl. Phys. Lett.*, vol. 69:21, pp. 3277–3279, 1996.

[198] Oesterschulze, E., "Novel probes for scanning probemicroscopy," *Appl. Phys. A*, vol. 66, pp. S3–S9, 1998.

[199] Okazaki, Y. and Kitahara, T., "NC micro-lathe to machine micro-parts," in *Proceedings of the ASPE*, vol. 22, pp. 575–578, 2000.

[200] Ouis, D., "Characterization of polymers by means of a standard viscoelastic model and fractional derivate calculus," *International Journal of Polymeric Materials*, vol. 53, pp. 633–644, 2004.

[201] Park, H. C. and Lakes, R. S., "Cosserat micromechanics of human bone: strain redistribution by a hydration-sensitive constituent," *J. Biomechanics*, vol. 19, pp. 385–397, 1986.

[202] Payne, M. C., Teter, M. P., Allan, D. C., Arias, T. A., and Joannopoulos, J. D., "Iterative minimization techniques for *ab initio* total-energy calculations: molecular dynamics and conjugate gradients," *Rev. Mod. Phys.*, vol. 64:4, pp. 1045–1097, 1992.

[203] Picard, Y. N., Adams, D. P., Vasile, M. J., and Ritchey, M. B., "Focused ion beam-shaped microtools for ultra-precision machining of cylindrical components," *Precision Engineering*, vol. 27, pp. 59–69, 2003.

[204] Poggi, M. A., Gadsby, E. D., Bottomley, L. A., King, W. P., Oroudjev, E., and Hansma, H., "Scanning probe microscopy," *Analytical Chemistry*, vol. 76, pp. 3429–3444, 2004.

[205] Pourovskii, L., *Ab Initio Simulations of Transition Metal Alloys: Towards the Multiscale Modeling.* PhD thesis, Uppsala University, 2003.

[206] Raiteri, R., Butt, H. J., and Grattarola, M., "Changes in surface stress measured with an atomic force microscope," *Scanning Microscopy*, vol. 12, pp. 243–251, 1998.

[207] Raiteri, R., Nelles, G., Butt, H.-J., Knoll, W., and Skladal, P., "Sensing of biological substances based on the bending of microfabricated cantilevers," *Letter to the Editor, Sens. Actuators B*, vol. 61, pp. 213–217, 1999.

[208] Rao, J. S., *Advanced theory of vibration*, p. 296. John Wiley & Sons, 1992.

[209] Reddy, J. N., *Energy and Variational Methods in Applied Mechanics.* John Wiley & Sons, 1984.

[210] Reyntjens, S. and Puers, R., "Focused ion beam induced deposition: fabrication of three-dimensional microstructures and youngs modulus of the deposited material," *J. Micromech. Microeng.*, vol. 10, pp. 181–188, 2000.

[211] Ricco, A. J., Staton, A. W., Crooks, R. M., and Kim, T., "Single-monolayer in situ modulus measurements using a SAW device: Photocrosslinking of a diacetylenic thiol-based monolayer," *Faraday Discuss.*, vol. 107, pp. 247–258, 1997.

[212] Rios, E. E., "Design and manufacturing of plastic micro-cantilevers by injection molding," Master's thesis, The George W. Woodruff School of Mechanical Engineering, Georgia Institute of Technology, 2003.

[213] Rodet, V. and Colton, J. S., "Properties of rapid prototype injection mold tooling materials," *Polymer Engineering and Science*, vol. 43:1, pp. 125–138, 2003.

[214] Rogers, B., York, D., Whisman, N., Jones, M., Murray, K., Adams, J. D., Sulchek, T., and Minne, S. C., "Tapping mode atomic force microscopy in liquid with an insulated piezoelectric microactuator," *Rev. Sci. Instrum.*, vol. 73, pp. 3242–3244, 2003.

[215] Rudnitsky, R. G., Chow, E. M., and Kenny, T. W., "Rapid biochemical detection and differentiation with magnetic force microscope cantilever arrays," *Sens. Act. A*, vol. 83, pp. 256–262, 2000.

[216] Rugar, D., Budakian, R., Mamin, H. J., and Chui, B. W., "Manipulation and detection of electron spins by magnetic resonance force microscopy," in *AIP Conference Proceedings*, vol. 696:1, pp. 45–52, 2003.

[217] Sader, J. E., "Frequency response of cantilever beams immersed in viscous fluids with applications to the atomic force microscope," *J. Appl. Phys.*, vol. 84:1, pp. 64–76, 1998.

[218] Sader, J. E., "Surface stress induced deflections of cantilever plates with applications to the atomic force microscope: Rectangular plates," *J. of App. Phys.*, vol. 89:5, pp. 2911–2921, 2001.

[219] Sader, J. E., Chon, J. W. M., and Mulvaney, P., "Calibration of rectangular atomic force microscope cantilevers," *Rev. Sci. Intrum.*, vol. 70:10, pp. 3967–3969, 1999.

[220] Sader, J. E., Larson, I., Mulvaney, P., and White, L. R., "Method for the calibration of atomic force microscope cantilevers," *Rev. Sci. Intrum.*, vol. 66:7, pp. 3789–3798, 1995.

[221] Schaller, T., Bohn, L., Mayer, J., and Schubert, K., "Microstructure grooves with a width of less than 50 cut with ground hard metal micro end mills," *Precision Engineering*, vol. 23, pp. 229–235, 1999.

[222] Schomburg, W. K., Martin, R. A. W. B. J., and Saile, V., "Amanda-surface micromachining, molding, and diaphragm transfer," *Sensors Actuators*, vol. A76, pp. 343–348, 1999.

[223] Schönenberger, C. and Alvarado, S. F., "A differential interferometer for force microscopy," *Rev. Sci. Intstrum.*, vol. 60, pp. 3131–3134, 1989.

[224] Schueller, O. J. A., Brittain, S. T., and Whitesides, G. M., "Fabrication of glassy carbon microstructures by soft lithography," *Sens. Act. A*, vol. 72, pp. 125–139, 1999.

[225] Searle, G. F. C., *Experimental Elasticity*, pp. 38–58. Cambridge University Press, 1920.

[226] Senden, T. J. and Ducker, W. A., "Experimental determination of spring constants in atomic force microscopy," *Langmuir*, vol. 10, pp. 1003–1004, 1994.

[227] Senturia, S. D., *Microsystem Design*. Kluwer, 2000.

[228] Shapiro, M. J., Lackey, W. J., Hanigofsky, J. A., Hill, D. N., Carter, W. B., and Barefield, E. K., "Chemical vapor deposition of silver films for superconducting wire applications," *Journal of Alloys and Compounds*, vol. 187, pp. 331–349, 1992.

[229] Sharos, L. B., Raman, A., Crittenden, S., and Reifenberger, R., "Enhanced mass sensing using torsional and lateral resonances in microcantilevers," *Appl. Phys. Lett.*, vol. 84, pp. 4638–4640, 2004.

[230] Shewhart, W. A., *Economic Control of Quality of Manufactured Product*. Van Nostrand, 1931.

[231] Soh, Y. A., Aeppli, G., Kim, C. Y., Mathur, N. D., and Blamire, M. G., "Magnetic domain structure and lattice distortions in manganite films under tensile strain," *J. Appl. Phys.*, vol. 93:10, pp. 8322–8324, 2003.

[232] Stoldt, C. R., Carraro, C., Ashurst, W. R., Gao, D., Howe, R. T., and Maboudian, R., "A low-temperature CVD process for silicon carbide MEMS," *Sens. Act. A*, vol. 97-98, pp. 410–415, 2002.

[233] Stoney, G. G., "The tension of metallic films deposited by electrolysis," in *Proc. R. Soc. London Ser. A*, vol. 82, pp. 172–175, 1909.

[234] Sun, C. and Zhang, X., "The influences of the material properties on ceramic micro-stereolithography," *Sens. Act. A*, vol. 101, pp. 364–370, 2002.

[235] Sun, X., Masuzawa, T., and Fujino, M., "Micro ultrasonic machining and its applications in mems," *Sensors and Actuators*, vol. A57, pp. 159–164, 1996.

[236] Sun, X., Masuzawa, T., and Fujino, M., "Micro ultrasonic machining and self-aligned multilayer machining/assembly technologies for 3d micromachines," in *Proceedings of the IEEE Micro Electro Mechanical Systems (MEMS)*, pp. 312–317, 1996.

[237] Takeuchi, Y., Yonekura, H., and Sawada, K., "Creation of 3d tiny statue by 5-axis control ultra precision machining," *Computer Aided Design*, vol. 35, pp. 403–409, 2003.

[238] Tamayo, J., Humphris, A. D. L., Malloy, A. M., and Miles, M. J., "Chemical sensors and biosensors in liquid environment based on microcantilevers with amplifed quality factor," *Ultramicroscopy*, vol. 86, pp. 167–173, 2001.

[239] Terfort, A., Bowden, N., and Whitesides, G. M., "Three-dimensional self-assembly of millimetre-scale components," *Nature*, vol. 386, pp. 162–164, 1997.

[240] Thaysen, J., Yalçinkaya, A. D., Vestergaard, R. K., Jensen, S., Mortensen, M. W., Vettiger, P., and Menon, A., "Su-8 based piezoresistive mechanical sensor," *Proc. MEMS*, pp. 320–323, 2002.

[241] Thundat, T., Warmack, R. J., Chen, G. Y., and Allison, D. P., "Thermal and ambient-induced deflections of scanning force microscope cantilevers," *J. Appl. Phys.*, vol. 64, pp. 2894–2896, 1994.

[242] Timoshenko, S. P. and Gere, J. M., *Mechanics of Materials, 4^{th} Edition.* PWS Publishing Co., 1997.

[243] Timoshenko, S. P. and Goodier, J. N., *Theory of Elasticity 3^{rd} Edition.* McGraw Hill, 1970.

[244] Timoshenko, S. P., Young, D. H., and Weaver, W., *Vibration Problems in Engineering, 4^{th} Edition*, pp. 416–420. John Wiley & Sons, 1974.

[245] Tortonese, M., Barrett, R. C., and Quate, C. F., "Atomic resolution with an atomic force microscope using piezoresistive detection," *Appl. Phys. Lett.*, vol. 62, pp. 834–836, 1993.

[246] Tortonese, M. and Kirk, M., "Characterization of application specific probes for SPMs," *Proc. SPIE*, vol. 3009, pp. 53–60, 1997.

[247] Toupin, R. A., "Elastic materials with couple stresses," *Arch. Rational Mech. Anal.*, vol. 11, pp. 385–414, 1962.

[248] Trau, M., Yao, N., Kim, E., Xia, Y., Whitesides, G. M., and Aksay, I. A., "Microscopic patterning of orientated mesoscopic silica through guided growth," *Nature*, vol. 390, pp. 674–676, 1997.

[249] Tseng, A. A., "Recent developments in micromilling using focused ion beam technology," *J. Micromech. Microeng.*, vol. 14, pp. R15–R34, 2004.

[250] Turnbull, A., Maxwell, A. S., and Pillai, S., "Residual stress in polymers– evaluation of measurement techniques," *Journal of Materials Science*, vol. 34, pp. 451–459, 1999.

[251] Uul, B. B., F T Shiokawa, T. O., and Fujihira, M., "Molecular dynamics simulation of non-contact atomic force microscopy of self-assembled monolayers on au(111)," *Nanotechnology*, vol. 15, pp. 710–715, 2004.

[252] Varadan, V. K., Jiang, X., and Varadan, V. V., *Microstereolithography and other Fabrication Techniques for 3D MEMS*. John Wiley & Sons, 2001.

[253] Vaz, A. R., Salvadori, M. C., and Cattani, M., "Young modulus measurement of nanostructured metallic thin films," *Journal of Metastable and Nanocrystalline Materials*, vol. 20-21, pp. 758–762, 2004.

[254] Vettiger, P., Cross, G., Despont, M., Drechsler, U., Dürig, U., Gotsmann, B., Häberle, W., Lantz, M. A., Rothuizen, H. E., Stutz, R., and Binnig, G. K., "The "millipede"– nanotechnology entering data storage," *IEEE Transactions on Nanotechnology*, vol. 1:1, 2002.

[255] Voigt, W., *Theoretische Studien uber die Elasticitatsverhaltnisse der Krystalle*, p. 34. Abh. Ges. Wiss., 1887.

[256] Wallenberger, F., "Inorganic fibers and microfabricated parts by laser assisted chemical vapor deposition (LCVD): Structures and properties," *Ceramics International*, vol. 23, pp. 119–126, 1997.

[257] Wallenberger, F., Nordine, P., and Boman, M., "Inorganic fibers and microstructures directly from the vapor phase," *Composites Science and Technology*, vol. 51, pp. 193–212, 1994.

[258] Wang, X., Ryu, K. S., Bullen, D. A., Zou, J., Zhang, H., Mirkin, C. A., and Liu, C., "Scanning probe contact printing," *Langmuir*, vol. 19, pp. 8951–8955, 2003.

[259] warburtin, F. L. and Hother-Lushington, J. F. P. J. S., "Some viseo-elastic properties of nylon," *British J. Appl. Phys.*, pp. 230–237, 1961.

[260] Weule, H., Hüntrup, V., and Tritschler, H., "Micro-cutting of steel to meet new requirements in miniaturization," *Annals of the CIRP*, vol. 50, p. 61, 2001.

[261] Whitesides, G. M., Simanek, E. E., Mathias, J. P., Seto, C. T., Chin, D., Mammen, M., and Gordon, D. M., "Noncovalent synthesis: Using physical-organic chemistry to make aggregates," *Acc. Chem. Res.*, vol. 28, p. 3744, 1995.

[262] Wojtowicki, J.-L., Jaouen, L., and Panneton, R., "New approach for the measurement of damping properties of materials using the Oberst beam," *Rev. Sci. Instrum.*, vol. 75, pp. 2569–2574, 2004.

[263] Wu, G., Datar, R. H., Hansen, K. M., Thundat, T., Cote, R. J., and Majumdar, A., "Bioassay of prostate-specific antigen (PSA) using microcantilevers," *Nature Biotech.*, vol. 19, pp. 856–860, 2001.

[264] Xia, Y. and Whitesides, G., "Soft lithography," *Annu. Rev. Mater. Sci.*, vol. 28, pp. 153–184, 1998.

[265] Yamataka, H. and Aida, M., "An *ab initio* MO study on the hydrolysis of methyl chloride with explicit consideration of 13 water molecules," *Chem. Phys. Lett.*, vol. 289, pp. 105–109, 1998.

[266] Yang, F., Chong, A. C. M., Lam, D. C. C., and Tong, P., "Couple stress based strain gradient theory for elasticity," *Int. J. Solids Struct.*, vol. 39, pp. 2731–2743, 2002.

[267] Yang, J. F. C. and Lakes, R. S., "Experimental study of micropolar and couple stress elasticity in bone in bending," *J. Biomechanics*, vol. 15, pp. 91–98, 1982.

[268] Yaralioglu, G. G. and Atalar, A., "Analysis and design of an interdigital cantilever as a displacement sensor," *J. Appl. Phys.*, vol. 83:12, pp. 7405–7415, 1998.

[269] Yu, Z. Y., Masuzawa, T., and Fujino, M., "Micro-EDM for three-dimensional cavities-development of uniform wear method," *Annals of the CIRP*, vol. 47, pp. 169–172, 1998.

[270] Zeng, J., Saltysiak, B., Johnson, W. S., Schiraldi, D. A., and Kumar, S., "Processing and properties of poly(methyl methacrylate)/carbon nano fiber composites," *Composites: Part B.*, In Press- Available online 31 October 2003.

[271] Zhao, X. M., Smith, S. P., Waldma, S. J., Whitesides, G. M., and Prentiss, M., "Demonstration of waveguide couplers fabricated using micro-transfer molding," *Appl. Phys. Lett.*, vol. 71, pp. 1017–1019, 1997.

[272] Zhao, X. M., Xia, Y., and Whitesides, G. M., "Fabrication of three-dimensional micro-structures: Microtransfer molding," *Adv. Mater.*, vol. 8, pp. 837–840, 1996.

VITA

Andrew W. McFarland was born in Walnut Creek, California on 27 October 1976. He attended San Ramon High School, in Danville, CA and obtained a B.S. degree in Mechanical Engineering from the University of California at Berkeley in May 2000. He headed East for graduate school at the Georgia Institute of Technology where he obtained an M.S. (2002) and Ph.D. (2004) in Mechanical Engineering.